DISSERTATION

PREDICTION AND MITIGATION STRATEGIES FOR THE TRANSIENT THERMAL PERFORMANCE OF LOW THERMAL RESISTANCE MICROCHANNEL EVAPORATORS

Submitted by

Caleb Del Anderson

Department of Mechanical Engineering

In partial fulfillment of the requirements

For the Degree of Doctor of Philosophy

Colorado State University

Fort Collins, Colorado

Summer 2024

Doctoral Committee:

Advisor: Todd M. Bandhauer

Karan Venayagamoorthy
Bret Windom
Daniel Wise

Copyright Caleb Del Anderson 2024

All Rights Reserved

ABSTRACT

PREDICTION AND MITIGATION STRATEGIES FOR THE TRANSIENT THERMAL PERFORMANCE OF LOW THERMAL RESISTANCE MICROCHANNEL EVAPORATORS

Microchannel flow boiling heat transfer offers an effective thermal management solution for high heat flux microelectronic devices such as laser diodes. The high heat transfer rates, nearly isothermal flow conditions, high surface area-to-volume ratios, and lower required pumping powers facilitate smaller component systems while more efficiently cooling devices and reducing packaging stresses associated with thermal expansion when compared with single-phase cooling systems. Although much study has been dedicated to optimizing steady state flow boiling performance, the typically highly transient operation of these microelectronic devices leads to unsteady spikes in heat flux and, subsequently, in device temperatures and may potentially exacerbate flow instabilities present at steady state. The low thermal capacitance of the package that often accompanies the low thermal resistance of microchannel evaporators increases the potential for device damage and failure since large temperature swings are more likely. Predicting and mitigating the transient response of a low thermal resistance microchannel evaporator is paramount to practical application as a thermal management technique.

In this work, temperature, pressure, and flow visualization measurements during stepped heat loads on two, low thermal resistance, microchannel evaporators revealed the presence of severe vapor backflow, large temperature overshoots, and impacted flow dynamics at the onset of nucleate boiling (ONB) despite the stability and high performance of the device under steady state

heating conditions. These overshoots were exacerbated with higher heating rates and reduced subcooling but were generally improved with higher flow rates. Applying a slower heating rate greatly improved the transient thermal response, reducing both peak temperature and vapor backflow. Channel and inlet orifice geometry were found to greatly impact the performance, with smaller channels and smaller orifice-to-channel restriction ratios resulting in intensified vapor backflow and temperature spikes, despite offering improved steady state performance. A computational model embedded in a reduced order design tool was created and validated with the experiments. Two separate models were created due to the different transient conditions observed between the two tested microchannel evaporators. The models allow predictive modeling of these evaporators to determine the impact of the transient heating behavior on microchannel evaporator devices.

The effect of incorporating gallium-based, solid-liquid Phase Change Materials (PCMs) was studied semi-empirically by simulating the performance of a virtual test section with predicted properties of a microchannel evaporator combined with gallium and gallium-composite foam PCMs. Properties of the PCMs were estimated and used to predict the test section thermal response under a range of PCM volumes. Models assuming single phase performance were conducted initially and the resulting predicted heat rate to the fluid applied experimentally to the test section heater to determine the temperature response. It was found that the simulated addition of the PCM slightly reduced the ONB temperatures but did not affect the peak temperature experienced by the device. The applied heating rate, however, did not consider the increased thermal resistance to the refrigerant fluid during the transient vapor backflow regime. The effect was most pronounced in the PCMs with the largest exposed surface area and with thermal conductivity-enhanced PCM composites comprised of gallium infiltrated in a copper foam matrix.

Additional PCM models utilizing the transient flow boiling model were subsequently run on a series of representative heat load test cases comparing the performance of a gallium-nickel and gallium-copper composite with similar dimensions to the earlier simulations. Key assumptions included the same ONB temperatures and vapor backflow conditions as the baseline cases without PCMs. The models predicted significantly lowered peak device temperatures due to the heat absorption into the PCM during the transient vapor backflow phase. The effect was dependent on the PCM thickness, latent heat, and thermal conductivity, reflecting trade-offs in material. In addition, peak temperature variability observed experimentally across multiple trials at the same nominal testing conditions was greatly reduced with the inclusion of a PCM.

ACKNOWLEDGMENTS

This PhD experience has been a wild roller coaster ride of highs and lows, and I would be remiss not thank those for whom I am incredibly grateful in shaping my journey for these past nearly six, highly formative years in my life.

First, I would like to express my sincerest gratitude to Dr. Todd Bandhauer for the enumerable ways with which he challenged and advised me on all facets of my research experience. His guidance provided not only a sturdy cornerstone for my research career but also honed my capability to persevere and adapt quickly in the face of tight deadlines or adversity, and for that I am incredibly grateful. His passion for and knowledge of the thermal sciences have been a kindling spark in my life towards pursuing a career in this field. I particularly appreciated the unique positioning of the lab as the liaison between research and end market. I would also like to offer my thanks to Dr. Charles Lewinsohn for his support and guidance on my research work in the final year of my program and for his patience in helping make this dissertation technically and grammatically sound.

I would like to thank my fellow coworkers in the REACH CoLab (though some of you may have known it by its old name, the ITS Lab) for making grad school as much of a blast as it could be and for all the great camaraderie: Josh Richey, thank you for showing me the lay of the dungeon land, teaching me to run the two-phase loop, and being someone I could bounce ideas or complain to about frustrating two-phase topics. Being a snowboarder takes away some brownie points though. David Hobby, thanks for being the guy I could go to for early help in my program, for collaborating with me on the LLNL work, and for those endless conversations in the dungeon about the most random things. Alex Grauberger, thanks for making fun of my Solar Shades that

one day at lunch; it kickstarted my interest in better fashion. Thanks for being a guy I could talk to about the challenges of graduate school. Shane Garland and Derek Young, thank you for the gnarly ski trips and for your invaluable assistance navigating the administrative part of the research world. Frederic Schmid, thank you for your humor and great knowledge of all things automotive and mechanical, and for hanging out in the basement dungeon lab with me. Ben Platt, thanks for all the fun times skiing and drinking beer, for the endless conversations about all things energy, and for your great recommendations on outdoorsy destinations in Colorado. Bella Amyx and Nicole Cassada, thank you for sticking with me on the LLNL project and for making the dungeon lab life more tolerable. And thanks for all the hiking and skiing trips we did! Maddy Siegel, thanks for explaining your Gen Z vernacular and for shredding the gnar with me. Katie Plese, thank you for being a sincere and understanding friend since nearly the beginning and for helping me out on research tasks as you could.

I would like to give a special shoutout to Sam Colosimo and Zach Gilvey who were with me from the start (though you both graduated well before me!). Sam, thank you for encouraging me to rekindle my skateboarding life and for the countless hours spent skating all over Northern Colorado. Thanks for being a conversational friend who I could just hang out with and discuss whatever. I am regretful we never were able to ski together; hopefully someday I can bask in your ski shadow. Zach, thank you for being my best friend from the start and for all the great times we spent together, whether it be hiking, skiing, road-tripping, movie-watching, beer-drinking, EISL, eating, or playing video games. Thanks for always bringing your fun goofiness to everything and inviting me to do everything with you. Thank you for the countless hours spent fixing our cars, it really helped me develop crucial skills in that area and save a terrific deal of money. And thank you for just being there for me and being someone who has been with me through this whole grad

school experience. I hope we can continue to remain such good friends even though you now live all the way down in Johnstown!

I would like to thank my housemates for making my home life such a pleasant experience and for being some of my best friends outside of school. Nathan, thanks for inviting me to go to Japan with you, for hosting such fun house parties, and for introducing me to the sprawling world that is the Cosmere. Kirsten, thanks for being such a conversational and pragmatic friend who was always there to talk about current challenges I was facing in grad school. Thanks for validating my thoughts and providing your helpful perspective. And I would be remiss if I did not thank you for bringing Buffy into my life! Katelyn, thanks for being such a kind friend, for inviting me to hang out with you and your friends so often, and for getting me outside my comfort zone.

I would like to express my immense gratitude to my partner Colleen. You have been such a gift in my life, and I am so elated that somehow our paths converged. I don't know where you were hiding all these years. Thank you for being so easy to talk with for hours and hours, for your positive and optimistic attitude, and for your fun outtake on life. Thank you for encouraging me to stand up for myself better and for helping me develop better planning skills for major, future events in my life. I appreciate your support so much in these last few critical months of my PhD program. You are my best friend and my favorite person.

Finally, I would like to offer my biggest thank you to my family. I love y'all so much: thank you for supporting me and standing by me from day one! Kylie and Luke, thanks for finally visiting me out here this year and for that crazy ski trip we caught ourselves in. Thank you for staying connected with me despite the vast distances between us now and for being the best brother and sister. I want to give a huge thank you to my parents for the immense understanding and support through my PhD experience. It has been such a long haul that is sometimes difficult to

explain, but I appreciate you trying your best to understand what I have been up to these past nearly six years. I would also like to thank my Aunt Laurie and cousins Derek, Athena, and Emily for their generosity and for allowing me to come down and visit for pretty much every holiday since I have lived out here. We have gotten much closer since I moved to Colorado, and I am so thankful to have y'all so close to me that I can go down and see you so often. Thanks for letting me become a larger part of your lives.

TABLE OF CONTENTS

ABSTRACT ii
ACKNOWLEDGMENTS v
LIST OF TABLES xii
LIST OF FIGURES xiii
CHAPTER 1. Introduction 1
1.1. Microchannel Flow Boiling for High Heat Flux Applications 1
1.2. Challenges for Microchannel Flow Boiling Under Transient Heating 5
1.3. Transient Thermal Buffering with Phase Change Materials 7
1.4. Research Objectives 10
1.5. Thesis Organization 11
CHAPTER 2. Literature Review 12
2.1. Transient Pool Boiling 13
2.2. Transient Flow Boiling 17
2.2.1. Macrochannels 18
2.2.2. Microchannels 21
2.3. Specific Aims of this Study 26
CHAPTER 3. Experimental and Computational Methods 29
3.1. Experimental Setup 29
3.1.1. Test Sections 29
3.1.1.1. 52 μm Hydraulic Diameter Microchannel Evaporator 30
3.1.1.2. 38 μm Hydraulic Diameter Microchannel Evaporator 32
3.1.2. Testing Facilities 33
3.1.2.1. Legacy Two-Phase Pumped Loop Test Facility 33
3.1.2.2. Transient Two-Phase Pumped Loop Test Facility 35
3.1.3. Experimental Testing Procedure and Test Matrix 38
3.1.3.1. Testing Procedure and Test Matrix for 52 μm Test Section 38
3.1.3.2. Testing Procedure and Test Matrix for 38 μm Test Section 39
3.1.3.3. Inlet Pressure Correction for 38 μm Test Section 40
3.1.4. Uncertainties and Calibrations 42
3.1.4.1. Uncertainties for 52 μm Test Section and Legacy Test Facility 43
3.1.4.2. Uncertainties for 38 μm Test Section and Transient Test Facility 44
3.1.5. Heat Losses 45
3.2. Computational Methods and Setup 48
3.2.1. ParaPower-NavyHHF Computational Design Tool 48
3.2.2. Model Setup and Configuration 52
3.2.3. Mesh Sensitivity Study 54
3.2.3.1. Mesh Sensitivity for 52 μm Test Section 55
3.2.3.2. Mesh Sensitivity for 38 μm Test Section 56
3.2.4. PCM Model Configuration and Setup 56
3.2.5. PCM Model Mesh Sensitivity 59
3.2.6. Semi-Empirical Parametric PCM Study at 35.4 W 60

CHAPTER 4. Preliminary Work Investigating a 52 µm Hydraulic Diameter Silicon Microchannel Evaporator 62
4.1. Stepped Heating Results 62
4.1.1. Transient Thermal Response with Flow Visualization 62
4.1.2. Effect of Peak Heat Load Magnitude 66
4.1.3. System Perturbations in Response to a Stepped Heat Load 67
4.2. Ramped Heating Results 68
4.2.1. Effect of Ramping Compared with Stepped Heating 68
4.2.2. Effect of Ramping Rate 70
4.2.3. Effect of Ramping on Fluid Flow Behavior 72
4.2.4. System Perturbations in Response to a Ramped Heat Load 73
4.3. Computational Modeling Approach and Results 74
4.3.1. Onset of Nucleate Boiling – Default Model Behavior 74
4.3.2. Onset of Nucleate Boiling – Preliminary Correlative Approach 76
4.3.3. Population Growth Model for Developing Boiling Heat Transfer Coefficient 78
4.3.4. Comparison with ONB Superheat Correlations from the Literature 81
4.4. Summary and Challenges with the Preliminary Approach 82
CHAPTER 5. Results, Discussion, and Model Development for 38 µm Hydraulic Diameter Silicon Microchannel Evaporator 85
5.1. Steady State Boiling Curve 85
5.2. Stepped Heating Results 86
5.2.1. Transient Thermal Response with Flow Visualization 86
5.2.2. Effect of Peak Heat Load Magnitude 89
5.2.3. Effect of Subcooling on Stepped Heat Loads 97
5.2.4. Effect of Mass Flow Rate on Stepped Heat Loads 103
5.2.5. Effect of Inlet Restriction on Device Behaviors 111
5.3. Flow Boiling Model for Stepped Heat Loads 113
5.3.1. Development of Model Framework within NavyHHF 114
5.3.2. NavyHHF Model for 35.4 W Case 117
5.3.3. NavyHHF Model for 37.5 W Case 120
5.3.4. NavyHHF Model for 55 W Case 122
5.4. Chapter Summary 124
CHAPTER 6. Impact of Phase Change Material on Microchannel Flow Boiling Under Stepped Heating… 127
6.1. General PCM Buffering Effects at 35.4 W 127
6.2. Effect of PCM on Heater Temperature at ONB 130
6.3. Effect of PCM on Peak Device Temperatures 133
6.4. NavyHHF Model with PCM 135
6.4.1. PCM Model at 35.4 W Peak Heat Load 136
6.4.1.1. Impact of Ga95/Ni5 Composite Foam PCM at 35.4 W 136
6.4.1.2. Impact of Ga60/Cu40 Composite Foam PCM at 35.4 W 139
6.4.1.3. Overall Comparison of PCM Impact at 35.4 W 141
6.4.2. PCM Model at 37.5 W Peak Heat Load 144
6.4.2.1. Impact of Ga95/Ni5 Composite Foam PCM at 37.5 W 145
6.4.2.2. Impact of Ga60/Cu40 Composite Foam PCM at 37.5 W 147
6.4.2.3. Overall Comparison of PCM Impact at 37.5 W 149

6.4.3. PCM Model at 55 W Peak Heat Load 152
6.4.3.1. Impact of Ga95/Ni5 Composite Foam PCM at 55 W 152
6.4.3.2. Impact of Ga60/Cu40 Composite Foam PCM at 55 W 155
6.4.3.3. Overall Comparison of PCM Impact at 55 W 158
6.5. Chapter Summary 161
CHAPTER 7. Conclusions and Recommendation for Further Work 164
7.1. Recommendations for Future Work 168
REFERENCES… 171
APPENDIX A. Arduino Synchronization Control Switch 178
APPENDIX B. Pressure Drop Correction Models 180
B.1. Model Equations and Assumptions 180
B.2. Inlet Plenum Pressure Drop Model 180
B.3. Inlet Restriction Pressure Drop Model 182
B.4. Outlet Plenum Pressure Drop Model 184
APPENDIX C. Derivation of Exponential Growth Model for Evolution of Flow Boiling Heat Transfer Coefficient 187

LIST OF TABLES

Table 2-1. Studies on microchannel flow boiling under transient heating.................................. 22
Table 3-1. Transient heat load test matrix for 52 µm microchannel evaporator.......................... 38
Table 3-2. Stepped heat load test matrix for 38 µm microchannel evaporator 39
Table 3-3. Inlet pressure transducer setpoints (in kPa) to maintain 20°C channel inlet saturation temperature (572 kPa)... 41
Table 3-4. Experimental uncertainties for 52 µm test section and legacy test facility. 44
Table 3-5. Experimental uncertainties for 38 µm test section and transient test facility. 45
Table 3-6. Heat loss parameters for both test sections. 47
Table 3-7. Material properties of solids used in NavyHHF models.. 52
Table 3-9. Mesh sensitivity study for 52 µm evaporator at 43 W... 55
Table 3-8. Mesh sensitivity study for 38 µm evaporator at 55 W... 55
Table 3-10. Properties of PCM materials investigated in this work. 59
Table 3-11. Mesh sensitivity for number of PCM vertical nodes by thickness. 60
Table 5-1. Vapor backflow decay rate as a function of flow rate. 111
Table 6-1. Temperature reduction range across PCM types and thicknesses at 35.4 W 144
Table 6-2. Temperature reduction range across PCM types and thicknesses at 37.5 W. 151
Table 6-3. Temperature reduction range across PCM types and thicknesses at 55 W. 160

LIST OF FIGURES

Figure 1-1. Comparison of heat fluxes experienced by high power density electronics with that of other high heat flux events. Adapted from [8]. 1
Figure 1-2. Effect of temperature on power conversion efficiency and peak wavelength for an in-house characterized laser diode device. 2
Figure 1-3. Comparison of a typical "conventional" cooling package with a more embedded package, where most layers have been removed, and the cooling channels are packaged directly into the device substrate. 3
Figure 1-4. Performance achieved in-lab for previous steady state microchannel flow boiling work across a range of channel and fin geometries. 4
Figure 1-5. Transient temperature profiles across regions in a high-power laser diode bar under 200 Hz pulses, from [29]. 5
Figure 1-6. Chip cooling architectures with increasing levels of integrated or embedded cooling, with their corresponding impact on transient temperature response [30]. 6
Figure 1-7. Comparison of cooling FOM versus latent heat for various material types. Adapted from [32]. 7
Figure 1-8. Previous studies demonstrating the impact of adding PCMs to high heat flux cooling packages. (Top) Comparison of various PCMs to buffering the thermal response of a surrogate device to a stepped heat load [35]. (Bottom) A study on a vehicular power electronics module with PCM experiencing lessened temperature excursions under an aggressive drive cycle [36]. 9
Figure 2-1. Typical temperature response for a ribbon heater experiencing an exponential heat input in time, from [38]. 14
Figure 2-2. Transient superheat curves showing large superheat and temperature overshoot at ONB, with stochasticity and temperatures dependent on peak heat flux [42]. 16
Figure 2-3. Typical transient temperature time series under a transient heat step from [50]. 19
Figure 2-4. Typical transient temperature response under a transient heat step from [54]. 23
Figure 2-5. Transient flow boiling temperature response compared across test sections with 2:1 and 4:1 inlet restriction ratios from [59]. 25
Figure 3-1. Detailed dimensions of 52 μm hydraulic diameter, silicon, microchannel evaporator investigated in this work. 30
Figure 3-2. Fluidic manifold for 52 μm hydraulic diameter microchannel test section which interfaces to two-phase pumped loop [12]. 31
Figure 3-3. Detailed dimensions of 38 μm hydraulic diameter, silicon, microchannel evaporator investigated in this effort. 32
Figure 3-4. Exploded schematic of fluidic interface manifold for 38 μm test section. 33
Figure 3-5. Simplified schematic of legacy testing facility from [62]. 34
Figure 3-6. Schematic of updated transient two-phase pumped loop testing facility. 35
Figure 3-7. Updated transient two-phase pumped loop testing facility and associated controls. 36
Figure 3-8. SolidWorks model used to calculate inlet plenum pressure drop. 41
Figure 3-9. Magnified optical microscopy image of inlet restrictor complex depth profile. 42
Figure 3-10. 1D thermal resistance loss networks from (a) the fluid side and (b) the heater side. 46
Figure 3-11. ParaPower thermal resistance network in matrix form from [66–68]. 48

Figure 3-12. Sample simplified block diagram for NavyHHF-ParaPower two-phase cold plate and boundary conditions. 49
Figure 3-13. Schematic for discretized solid and fluid with energy balance at interface and fin efficiency approach. 50
Figure 3-14. Model computational domain in NavyHHF-ParaPower showing fluid and solid regions and select dimensions. 53
Figure 3-15. Inlet and outlet boundary condition block dialog boxes for model fluid domain. 54
Figure 3-16. Example computational domain and naming convention for PCM study. 56
Figure 3-17. Sensitivity effect of number of vertical nodes on 35.4 W heat load and 2 mm thick gallium PCM during initial fast transient temperature rise. 59
Figure 3-18. Effect of different PCM material and volumes on the effective heat load to the fluid in the 35.4 W peak heat load simulations. 61
Figure 4-1. Transient heater temperature response to a stepped heat load, where numbers correspond to different flow visualization states. 63
Figure 4-2. Images from a 43 W stepped heat load. Flow is from left to right, and the white dotted line denotes the two-phase mixture/liquid interface in the upstream manifold: (1) Steady state single-phase. (2) Onset of boiling. (3) 0.1 seconds after ONB. (4) 0.2 seconds after ONB. (5) 0.4 seconds after ONB. (6) Steady state flow boiling. 64
Figure 4-3. Comparison of the transient temperatures of different peak stepped heat fluxes, where heat loads are applied at 0.5 s for ease in visualizing the rapid temperature response. 66
Figure 4-4. **(a)** Transient temperature and mass flux response to a pulsed heat load, applied at 0.5 s. **(b)** Test section inlet pressure and pressure drop response to same heat load. 67
Figure 4-5. Stepped heat load compared to ramped heat load at 50 W/s. Stochasticity in the ONB is observed but ramping results in a lower peak temperature in all cases. 69
Figure 4-6. Test section temperature compared across different heating rates with a peak heat load of 39 W. 71
Figure 4-7. Images for ramped heat load at 4 W/s (R1 – R3) and stepped heat load (P1 – P3), for a peak heat load of 39 W. (R1) and (P1) are at the ONB. (R2) and (P2) are 0.05 s (1 frame) after the ONB. Vapor backflow for the stepped test is much greater. (R3) coincides with the steady boiling time 0.15 s (3 frames) after the ONB for the ramped case. (P3) occurs at same time after the ONB for the stepped test and still shows vapor backflow and developing boiling dynamics. 72
Figure 4-8. **(a)** Inlet pressure and pressure drop time series, with pressure spikes coinciding with ONB. **(b)** Transient test section temperature and mass flux. Mass flux drop coincides with pressure drop spike and ONB. 74
Figure 4-9. Comparison of the default simulation behavior with the experimental data to a transient heat load that transitions to subcooled flow boiling, where the simulation fails to capture the overshoot. 75
Figure 4-10. Superheat-peak wall heat flux at ONB model embedded as interpolation table in NavyHHF-ParaPower tool. 76
Figure 4-11. Improved ONB model embedded in NavyHHF-ParaPower software, where ONB temperature matches experiment; however, the decay to steady state is too abrupt. 77
Figure 4-12. Plot depicting the exponential growth model equation bounded between the single-phase and two-phase heat transfer coefficients, with growth rate controlled by κ. 79
Figure 4-13. Resulting model combining exponential growth model with wall superheat correlation, showing adequate agreement with the experiment, especially during the transient. 80

Figure 4-14. Comparison of current ONB superheat results compared with selected correlations from the literature. 81
Figure 5-1. Steady state boiling curve at baseline flow conditions; ONB occurred at ~14.75 W. 85
Figure 5-2. Typical transient temperature profile with important points in time marked for accompanying flow visualization, with a peak stepped heat load of 35.4 W. 87
Figure 5-3. Flow visualization in the channels, with 1. Liquid only, 2. ONB, 3. Severe vapor backflow into inlet plenum, 4. Backflow lingers but is slowly pushed downstream, 5. Nearing steady state, 6. Steady state flow boiling with no vapor present in the inlet plenum. 88
Figure 5-4. Representative transient temperature responses across range of peak heat loads for given baseline flow conditions. Inset plot shows zoomed-in perspective for >35 W cases. 90
Figure 5-5. Time to onset of boiling for baseline fluid conditions across all heat loads and trials, where variability decreases greatly as q increases. 91
Figure 5-6. Characteristic sidewall scalloping associated with the DRIE etching process used to fabricate the microchannels. 92
Figure 5-7. Comparison of the steady state and peak temperatures for the baseline fluid conditions across all heat loads, with error bars reflecting 99% confidence intervals across multiple trials. 93
Figure 5-8. Comparison of the ONB temperature versus peak heat load for baseline flow conditions across all trials. 95
Figure 5-9. Comparison of the ONB temperature versus peak heat load across different inlet subcooling conditions. 97
Figure 5-10. Peak heater temperature comparison across heat loads and different inlet subcooling degrees. 99
Figure 5-11. Time to boiling incipience conditions across multiple trials compared by heat load and inlet subcooling. 100
Figure 5-12. Variability across trials, heat loads, and inlet subcooling scenarios in peak temperature as a function of the variability in time to ONB at the same conditions. 101
Figure 5-13. Effect of mass flow rate on average heater temperature at the ONB across heat loads. 103
Figure 5-14. Effect of mass flow rate on peak transient heater temperature across heat loads and trials. 105
Figure 5-15. Time to boiling inception across multiple trials compared at different peak heat loads and flow rates. 107
Figure 5-16. Schematic depicting various forces acting on fluid in a microchannel during the flow boiling process. 109
Figure 5-17. Comparison of transient behavior between both test devices at similar tested conditions. 112
Figure 5-18. Representative regime map for transient flow boiling model created in NavyHHF. 114
Figure 5-19. Process flow schematic for transient flow boiling model approach in NavyHHF. 115
Figure 5-20. Experimental results compared with transient boiling model in NavyHHF at 35.4 W peak heat load. 118
Figure 5-21. Zoomed-in view of Figure 5-19 to show comparison of backflow region, which experiences an additional dynamic that delays the temperature decay. 119
Figure 5-22. Model heater temperature synchronized with heat transfer coefficient following the exponential growth model for 35.4 W heat load. 120

Figure 5-23. Model heater temperature synchronized with heat transfer coefficient following the exponential growth model for 37.5 W heat load. 121
Figure 5-24. NavyHHF and experimental heater temperatures synchronized for 55 W heat load case. 123
Figure 5-25. Model heater temperature synchronized with heat transfer coefficient following the exponential growth model for 55 W heat load. 124
Figure 6-1. PCM cases studied under a 35.4 W heat step. **(a)** Average heater temperature versus time in simulation with different PCMs compared with baseline step response with black dashed line. **(b)** Amount of heat absorbed by PCMs versus time. 128
Figure 6-2. Linear trend observed in average ONB heater temperature and instantaneous heat load. 131
Figure 6-3. Peak temperatures versus ONB temperatures across baseline step and different PCM test cases. 133
Figure 6-4. Comparison of the GaNi-foam PCM impact on transient device temperatures with baseline case without a PCM at a 35.4 W peak heat load. 136
Figure 6-5. Comparison of the heat transfer into or out of the PCM in time across the different PCM thicknesses. 137
Figure 6-6. Comparison of the Ga60/Cu40 PCM impact on transient device temperatures. 139
Figure 6-7. Comparison of the heat transfer into or out of the Ga60/Cu40 composite across the different PCM. 140
Figure 6-8. Variation in transient temperature response and peak temperature observed across trials, with the worst-case and best-case trials identified. 141
Figure 6-9. Comparison of peak temperature ranges across the baseline and both PCM types at a 35.4 W peak heat load, at different PCM thicknesses, where the PCMs significantly reduce peak temperatures in the worst-case trial. 142
Figure 6-10. Comparison of peak temperature reductions with both PCM types at a 35.4 W peak heat load, at different PCM thicknesses, where the range in peak temperature reduction is large. 143
Figure 6-11. Comparison of transient temperatures across baseline case without PCM and with different Ga95/Ni5 PCM thicknesses, where the peak temperature drops sharply upon addition of PCM but with a lessened effect with further increases PCM thickness. 145
Figure 6-12. Transient heat rate into the PCM for a peak heat load of 37.5 W, showing the large amount of heat stored and then subsequently removed in the PCM during the vapor backflow regime. 146
Figure 6-13. Transient temperature comparison across baseline and Ga60/Cu40 PCMs at 37.5 W, showing the large reduction in peak temperatures. 147
Figure 6-14. Temporal heating rate to the PCM at 37.5 W of peak heating across the three different Ga60/Cu40 PCM cases, showing the rapid transfer of energy to and from the PCM during the backflow phase. 148
Figure 6-15. Comparison of peak temperature ranges obtained with a peak heat load of 37.5 W with best- and worst-case trials using both PCM types and across the thickness range, with significant reduction in peak temperature observed for all PCM cases. 150
Figure 6-16. Range of peak temperature reductions from baseline obtained with a peak heat load of 37.5 W with best- and worst-case trials using both PCM types and across the thickness range. 151

Figure 6-17. Transient heater temperatures at 55 W peak heat load across the baseline and Ga95/Ni5 PCMs with different thicknesses, showcasing the large peak temperature reduction effect due to incorporating a PCM. Numbers 1-4 correspond to specific states in time in Figure 6-19. 152
Figure 6-18. Transient heating rates into the PCM compared across the three PCM thicknesses for the Ga95/Ni5 PCM at a 55 W peak heating rate, where numbers 1-4 correspond to specific states with highlighted in Figure 6-19. 153
Figure 6-19. PCM melt fraction at selected instants in time from Figure 6-18. (1) ONB, PCM not fully melted, (2) peak temperature reached and PCM is still not fully melted, (3) intermediate state between peak temperature and fully developed two-phase state, (4) steady state flow boiling, PCM is fully melted. 154
Figure 6-20. Transient heater temperatures compared across the baseline and three different thicknesses of Ga60/Cu40 PCM at a peak heat load of 55 W. 155
Figure 6-21. Transient heating rates to the PCM across the three Ga60/Cu40 thicknesses for a peak heat load of 55 W. Numbers 1-4 correspond to specific states in Figure 6-22. 157
Figure 6-22. Nodal melt fractions and temperatures in PCM at 55 W peak heating with a 0.5 mm Ga60/Cu40 PCM. (1) PCM is fully melted at the ONB, (2) at the peak temperature, sensible heating has occurred in the PCM, (3) the PCM temperature drops as sensible heat is removed, (4) steady state is reached with fully melted PCM and a significantly lowered PCM temperature. 158
Figure 6-23. Comparison of peak temperature ranges obtained with best- and worst-case trials at a 55 W peak heat load using both PCM types and across the thickness range, with significant reduction in peak temperature observed for all PCM cases. 159
Figure 6-24. Comparison of peak temperature reduction ranges obtained with best- and worst-case trials at a 55 W peak heat load using both PCM types and across the thickness range, with significant reductions which depended heavily on PCM thickness and type. 160
Figure A-1. Schematic of Arduino-controlled synchronization and trigger switch. 178
Figure A-2. Arduino-controlled trigger and synchronization switch setup. 179
Figure B-1. Mesh sensitivity study for inlet plenum pressure drop model at 50 g/min. 181
Figure B-2. Example velocity streamline profiles for inlet plenum pressure drop model, where large velocity changes occur when moving from the inlet tube to the 90° bend with contraction into the five channels. 182
Figure B-3. Computational domain for half-channel inlet restriction and channel geometry. .. 183
Figure B-4. Determination of local pressure drop in inlet restriction model at 50 g/min. 183
Figure B-5. Mesh sensitivity study for inlet restriction model at 50 g/min. 184
Figure B-6. Mesh sensitivity study for outlet plenum model at 50 g/min. 185
Figure B-7. Example velocity streamline profiles for outlet plenum pressure drop model, where large velocity changes occur due to the contraction at the end of the supporting rib features, and due to expansion and a 90°-bend into the outlet tube. 186

NOMENCLATURE

Variable	Description	Units	Formula
A	Area	m^2	
Bo	Boiling number	-	$Bo = \frac{q''}{G i_{lv}}$
C_{th}	Thermal capacitance	J/K	
c_p	Specific heat capacity	J/kg-K	$D_h = \frac{4A_c}{PW}$
D_h	Hydraulic diameter	m	
F	Force	N	
FOM_q	Figure of Merit	$W/m^2s^{1/2}K^{1/2}$	$FOM_q = \sqrt{k i_{sl}}$
f	Friction factor	-	
G	Mass flux	kg/m^2-s	$G = \frac{\dot{m}}{A_c}$
g	Acceleration from gravity	m/s^2	
H	Height	m	
h	Heat transfer coefficient	W/m^2-K	
I	Electric Current	A	
i	Enthalpy	J/kg	
i_{lv}	Latent heat of vaporization	J/kg	
i_{sl}	Latent heat of fusion	J/kg	
k	Thermal conductivity	W/m-K	
K	Loss coefficient	-	
L	Length	m	
m	Fin parameter	1/m	$m = \sqrt{\frac{2h}{th_{fin}k}}$
$\dot{m}$	Mass flow rate	kg/s	
N	Number of or finite volume	-	
ΔP	Pressure drop	kPa	
P	Pressure	kPa	
PH	Heated perimeter	m	
Pr	Prandtl number	-	$Pr = \frac{\mu c_p}{k}$
PW	Wetted perimeter	m	
q	Heat load	W	
q''	Heat flux	W/m^2	
R	Electrical resistance	Ω	
R_{stab}	Stability Parameter	-	$R_{stab} = \sqrt{\frac{F_{back}}{F_{for}}}$
R_{th}	Thermal resistance	K/W	

Re	Reynolds number	-	$Re = \frac{GD_h}{\mu}$
S	Sample standard deviation	-	
T	Temperature	°C	
th	Thickness	m	
t	Time	s	
t_{stat}	99% two-tailed t-statistic	-	
U	Variability	-	
$\vec{u}$	Velocity field	m/s	
$\forall$	Volume	m^3	
ΔV	Potential difference, voltage	V	
v	Velocity	m/s	
W	Width	m	
We	Weber number	-	$We = \frac{G^2 D_h}{\rho_l \gamma}$
X	Generic dependent variable	-	
X_{tt}	Martinelli parameter	-	
x	Generic variable	-	

Greek and Latin

γ	Surface tension	N/m	
Δ	Difference	-	
δ	Uncertainty	-	
ε	Radiative emissivity	-	
η	Efficiency	%	
κ	Growth factor	1/s	
μ	Dynamic viscosity	kPa-s	
ν	Kinematic viscosity	m^2/s	
ρ	Density	kg/m^3	
σ	Stefan-Boltzmann constant	W/m^2-K^4	
τ_{th}	Thermal time constant	s	$\tau_{th} = R_{th} C_{th}$
ϕ	Porosity	-	$\phi = \frac{\forall_{Ga}}{\forall_{Ga} + \forall_{foam}}$
χ	Vapor quality	-	

Subscripts and Superscripts

amb	Ambient
avg	Average
back	Backward
base	Substrate base
bf	Backflow
bp	Biphasic
c	Cross-sectional
cb	Convective boiling
ch	Channel

conv	Convective
crit	Critical
DB	Dittus-Boelter
def	Default
dev	Developing region
e	Expansion
eff	Effective
EMT	Effective medium theory
f	Fluid
film	Mean air and surface temperature
fin	Fin wall between channels
foam	Porous metal foam
for	Forward
Ga	Gallium
geo	Geometric
glass	Borosilicate glass cap
h	Test section heater
i	Index in sum
in	In
l	Liquid
lo	Liquid-only
loss	Lost amount
lv	Liquid-to-vapor
max	Maximum
ME	Maxwell-Eucken
meas	Measurement
melt	Melting temperature
mp	Midpoint
nb	Nucleate boiling
net	Net value
ONB	Onset of nucleate boiling
ori	Inlet orifice/restriction
out	Out
par	Parallel
peak	Peak average heater value
plen	Plenum
rad	Radiative
s	Solid
samples	Samples collected
sat	Thermodynamic saturation
ser	Series
sl	Solid-to-liquid
sp	Single phase
ss	Steady State
stat	Statistical
sub	Subcooled

surf	Surface
tb	Transient boiling
tp	Two-phase
upstr	Upstream
v	Vapor
w	Perimeter wall of channel
weight	Weighted
x	Placeholder subscript

CHAPTER 1. Introduction

1.1. Microchannel Flow Boiling for High Heat Flux Applications

Electronic device miniaturization increases compactness and facilitates implementation into smaller systems with increased functionality and performance. For example, high power laser diodes, which are semiconductor devices that transform input electrical energy into a coherent beam of optical energy with a narrow wavelength band, are regularly employed across a diverse range of applications, including optical pumping of solid state lasers, industrial cutting and machining, directed energy applications, medical diagnostics and surgery, telecommunications, and inertial confinement fusion [1–5]. However, these devices can experience heat fluxes in excess of 1 kW/cm^2 (Figure 1-1), with package level volumetric heat loads surpassing 1 kW/cm^3, at

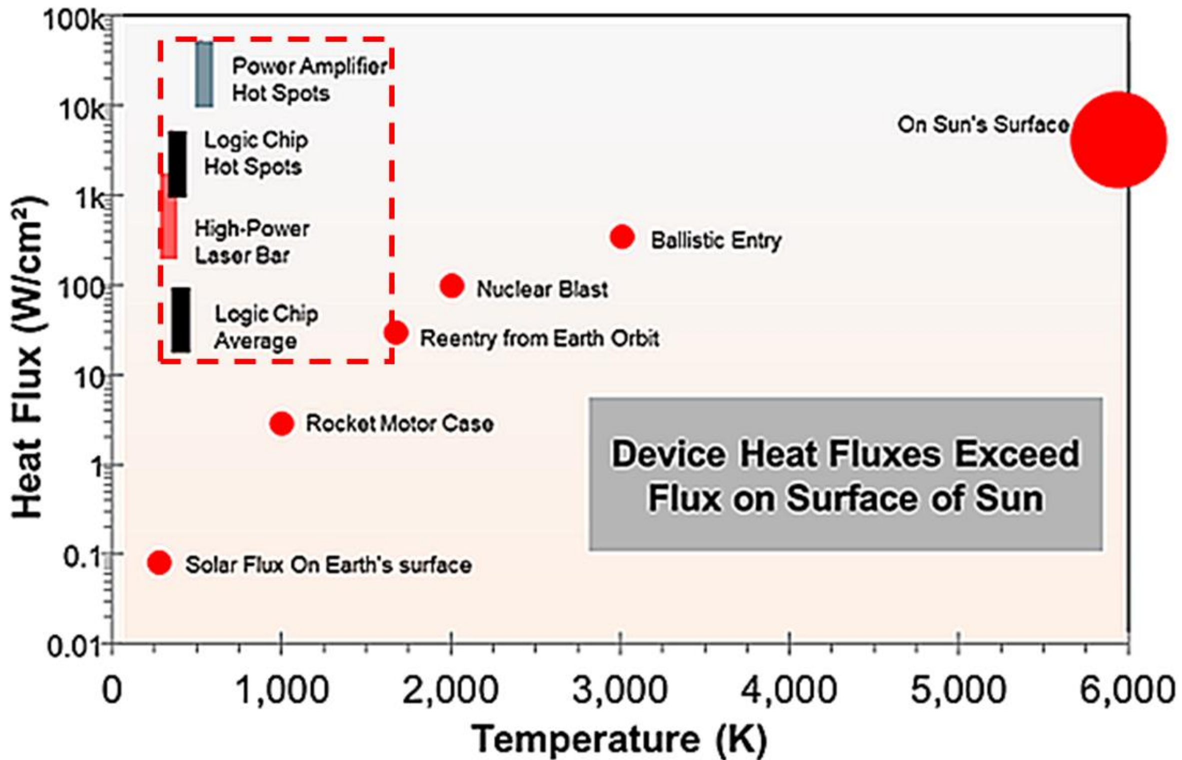

Figure 1-1. Comparison of heat fluxes experienced by high power density electronics with that of other high heat flux events. Adapted from [8].

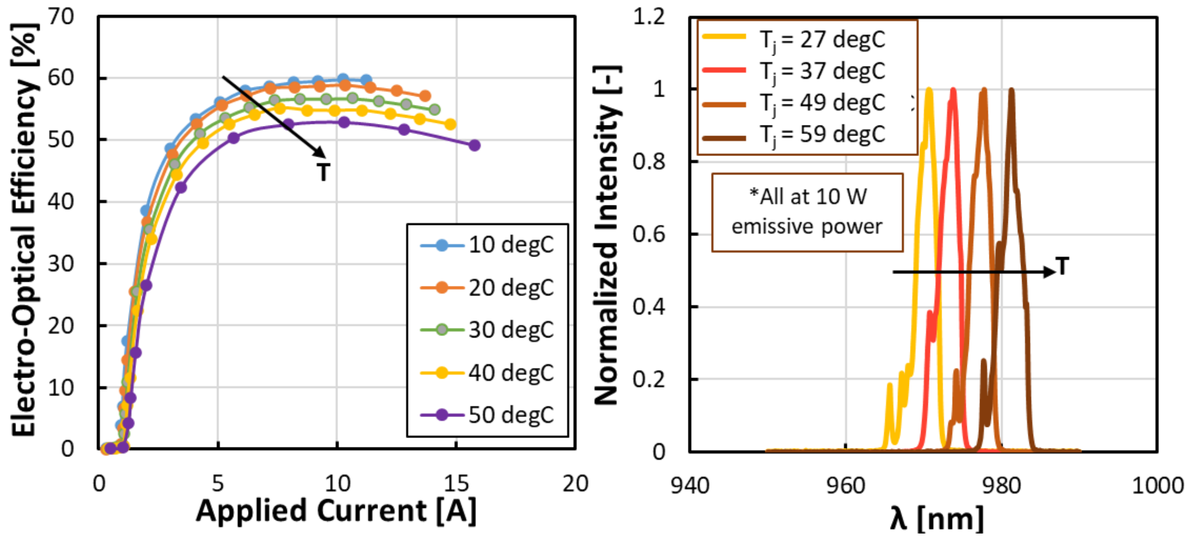

Figure 1-2. Effect of temperature on power conversion efficiency and peak wavelength for an in-house characterized laser diode device.

required operating temperatures of less than 100°C [6–8]. Laser diodes have highly temperature dependent performance metrics, and without sufficient package thermal management, a high heat flux device such as a laser diode will suffer from diminished performance, undesirable drifts in output, lifetime and reliability reduction, and failure in the most extreme cases [2]. An example of this temperature dependent performance is shown in Figure 1-2, where an in-house laser diode was characterized, and its power conversion efficiency was found to decrease while the peak wavelength was found to increase (at ~0.34 nm/°C) when the device temperature was increased.

Embedded or integrated cooling in microchannels utilizes advanced micromachining techniques such as Deep Reactive Ion Etching (DRIE) and laser etching to fabricate large aspect ratio microchannels directly into semiconductor device substrates [9–11]. As shown in the schematic in Figure 1-3, embedded cooling techniques allow for removal of heat spreaders, thermal interface materials, and multiple layers in a device stack up, and provides the utility for custom fluid routing, channel geometries, and smaller channel hydraulic diameters. These features translate into large surface area-to-volume ratios and low thermal resistance packages with greater flexibility in design. Combining embedded microchannel heat sinks with flow boiling heat transfer

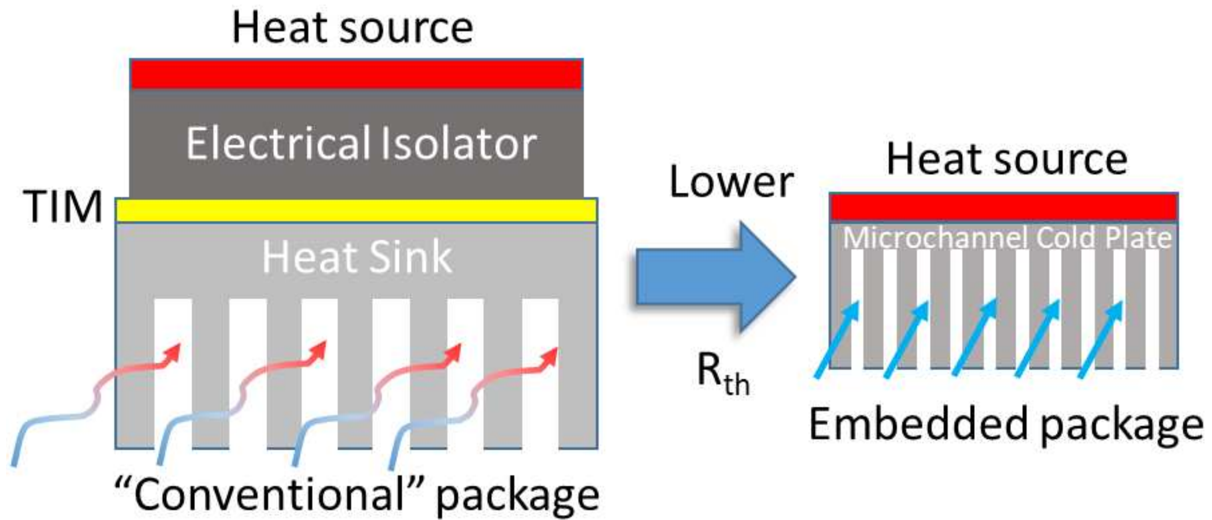

Figure 1-3. Comparison of a typical "conventional" cooling package with a more embedded package, where most layers have been removed, and the cooling channels are packaged directly into the device substrate.

further improves performance due to large heat transfer coefficients which can exceed 100 kW/m^{2}K, greater device temperature uniformity due to nearly isothermal phase change, and smaller required pumping power due to large latent heats of vaporization compared with single-phase cooling [12–15].

These high-performance features are particularly advantageous for cooling high heat flux microelectronics and translate into smaller required component cooling systems due to reduced pumping power requirements and lower required temperature lift by vapor compression systems. Surrogate laser diode devices cooled with microchannel flow boiling with refrigerants have reached 1.5 kW/cm^2 under steady state testing with previous lab studies (see Figure 1-4) [16,17]. Microchannel flow boiling has been studied extensively under steady state operating conditions. Many comprehensive correlations have been developed to predict the heat transfer coefficient and pressure drop under a variety of fluid properties, flow rates, and heat fluxes [14,15,18]. While microchannel flow boiling offers attractive thermal management properties, due to small characteristic length scales, molecular forces such as surface tension and capillary effects interact more strongly with the flow dynamics and result in flow instabilities. Flow boiling heat transfer is

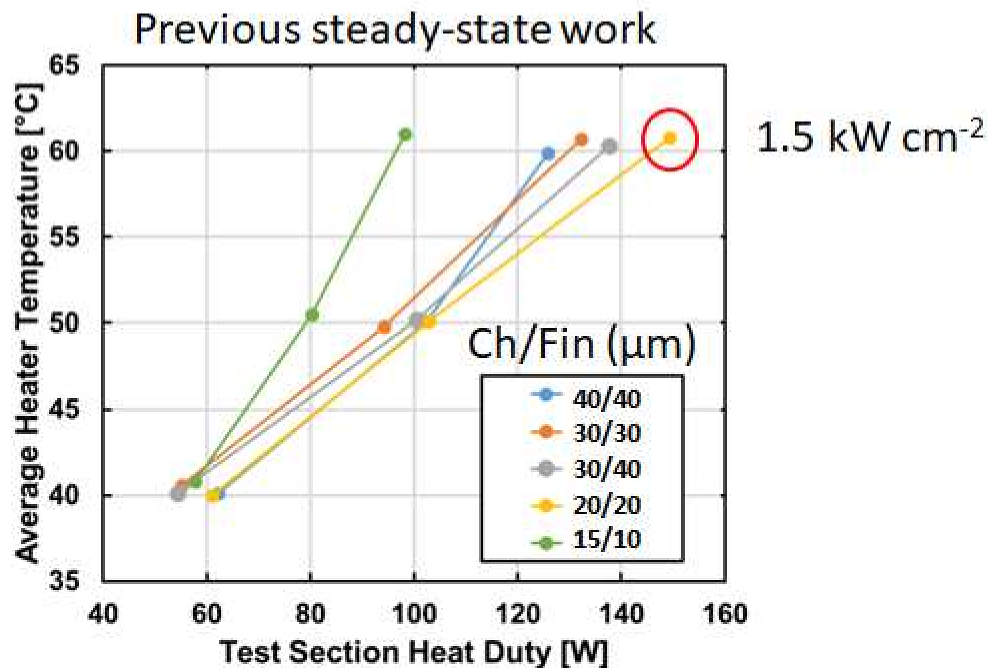

Figure 1-4. Performance achieved in-lab for previous steady state microchannel flow boiling work across a range of channel and fin geometries.

heat flux dependent; therefore, as the heat flux is changed, so are the heat transfer characteristics. The onset of nucleate boiling (ONB) causes rapid changes in flow and heat transfer characteristics as the system responds to the generation of vapor.

Pressure drop and temperature oscillations, parallel channel instability, rapid bubble growth/vapor backflow instability, and critical heat flux are prominent flow instabilities which can seriously degrade microchannel two-phase cooling performance [19–22]. Techniques have been developed to mitigate these challenges and include channel pressure drop elements or inlet restrictions [23–26], reentrant cavities [20], diverging channels [27], and surface enhancements such as nanotubes or nanowires [28]. While these stabilization techniques can successfully mitigate instabilities at steady state, many high heat flux electronics operate under highly unsteady and transient heating conditions which may introduce additional instabilities and complexities.

1.2. Challenges for Microchannel Flow Boiling Under Transient Heating

Many high heat flux devices such as laser diodes and power electronics operate under transient heat loads and cold start-ups which can result in rapid device temperature fluctuations. Figure 1-5 depicts a representative transient temperature response of a high-power pulsed laser diode array, where large temperature swings can be seen at the diode emitter face [29]. Furthermore, utilizing microchannel embedded cooling exacerbates the transient thermal response of the device. While microchannel embedded cooling seeks to minimize thermal resistance, concurrent reductions in package thermal resistance also often result from the reduction in the mass and volume of the cooling architecture [30]. Since the thermal time constant (τ_{th}) is the product of thermal resistance (R_{th}) and thermal capacitance (C_{th}), reductions in both reduce the time to steady state but also increase the potential severity of temperature spikes and fluctuations when exposed to transient heating modes. Figure 1-6 compares the impact of increasingly

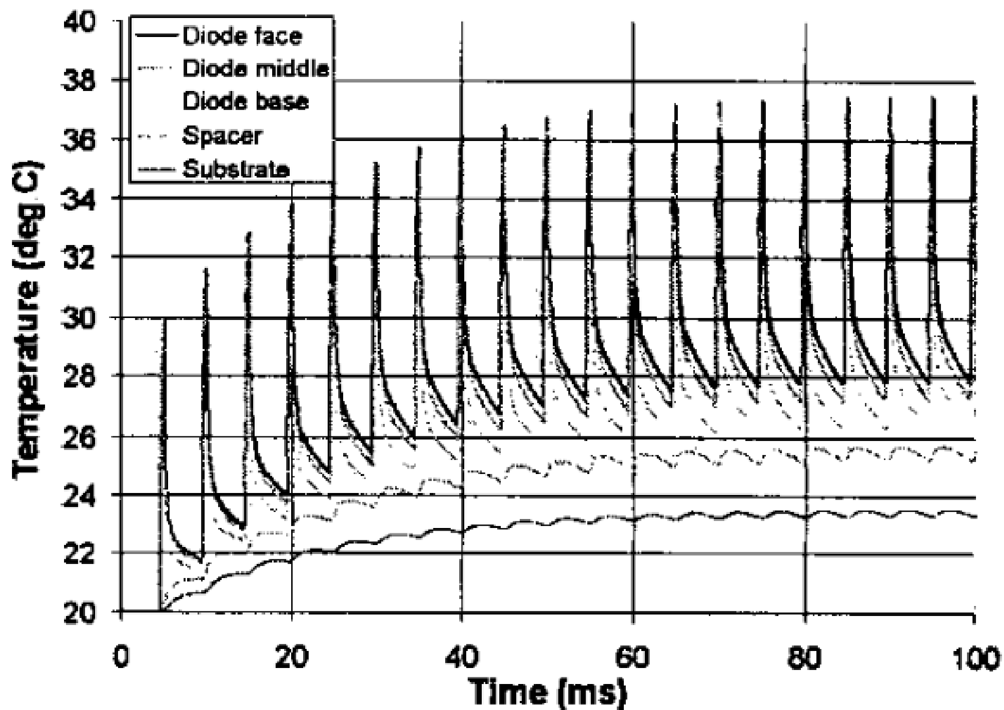

Figure 1-5. Transient temperature profiles across regions in a high-power laser diode bar under 200 Hz pulses, from [29].

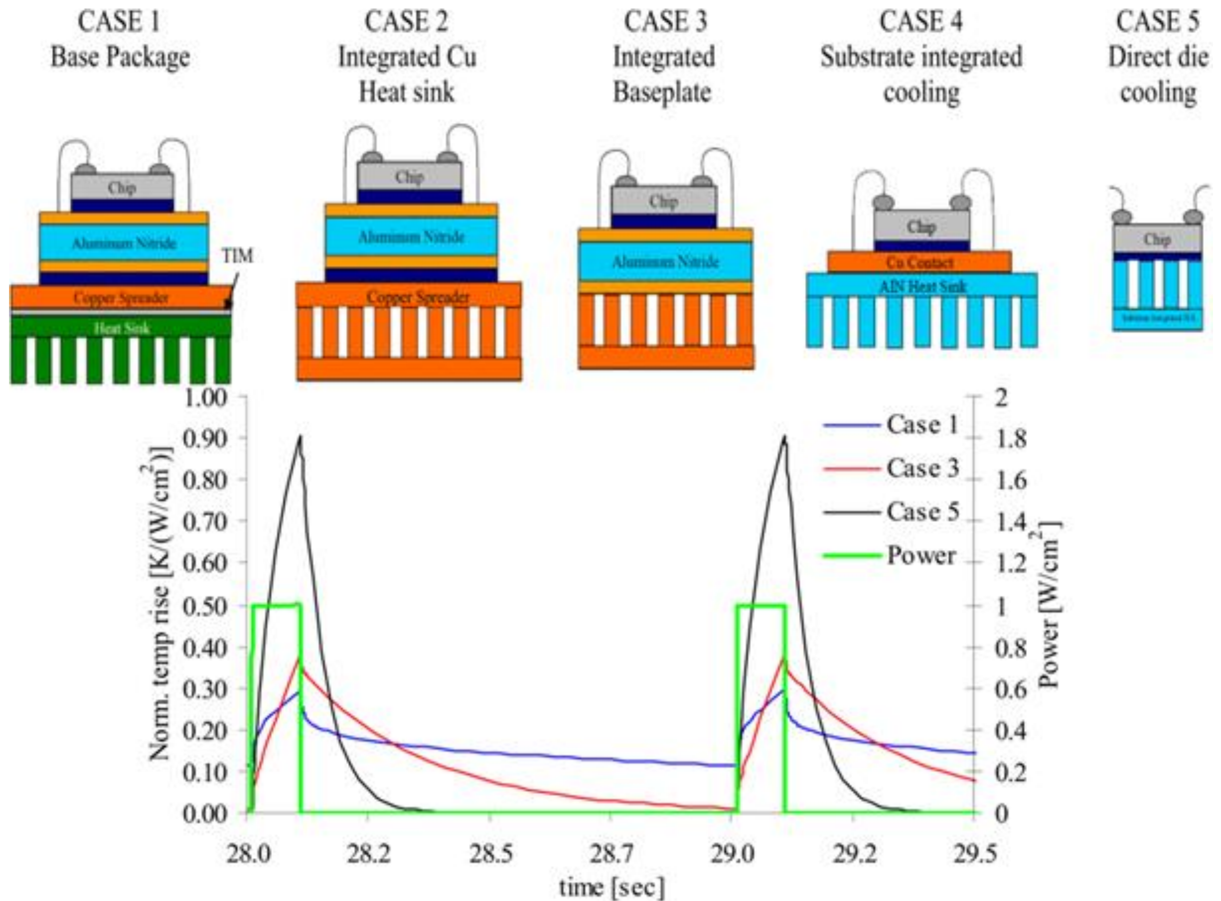

Figure 1-6. Chip cooling architectures with increasing levels of integrated or embedded cooling, with their corresponding impact on transient temperature response [30].

embedded packages on the transient temperature of a representative power electronics chip to a 1 second period pulse at a 10% duty cycle [30]. The packages with additional thermal capacitance effectively buffer the temperature response, while the most embedded package experiences large temperature spikes of up to three times the least embedded due to its small time constant. Low thermal capacitance in microchannel evaporators under transient heating is expected to exacerbate flow instabilities and temperature swings, and result in unexpected behavior compared with steady heating conditions due to the change in vapor generation rates associated with increased heat fluxes. Insight into the impact of transient heating on low thermal resistance microchannel evaporators is paramount to implementation into real devices.

1.3. Transient Thermal Buffering with Phase Change Materials

One possible solution for improving the embedded cooling transient thermal response is to increase thermal capacitance in a way which does not hinder the low thermal resistance pathway to the cooling fluid. Solid-solid and solid-liquid phase change materials (PCMs) are materials which are used in transient thermal storage applications by utilizing the nearly isothermal phase change process to store and retrieve energy. While PCMs have traditionally been considered as a thermal energy storage unit when added to the coolant loop (such as a an additional PCM-heat exchanger component), PCMs which are added directly to the cooling package in a parallel configuration with the cooling fluid can achieve a device-level transient thermal buffering effect without sacrificing the low thermal resistance.

While there are many categories of PCMs, important metrics are melting temperature similar to desired maximum device temperature, high thermal conductivity (k) to effectively spread

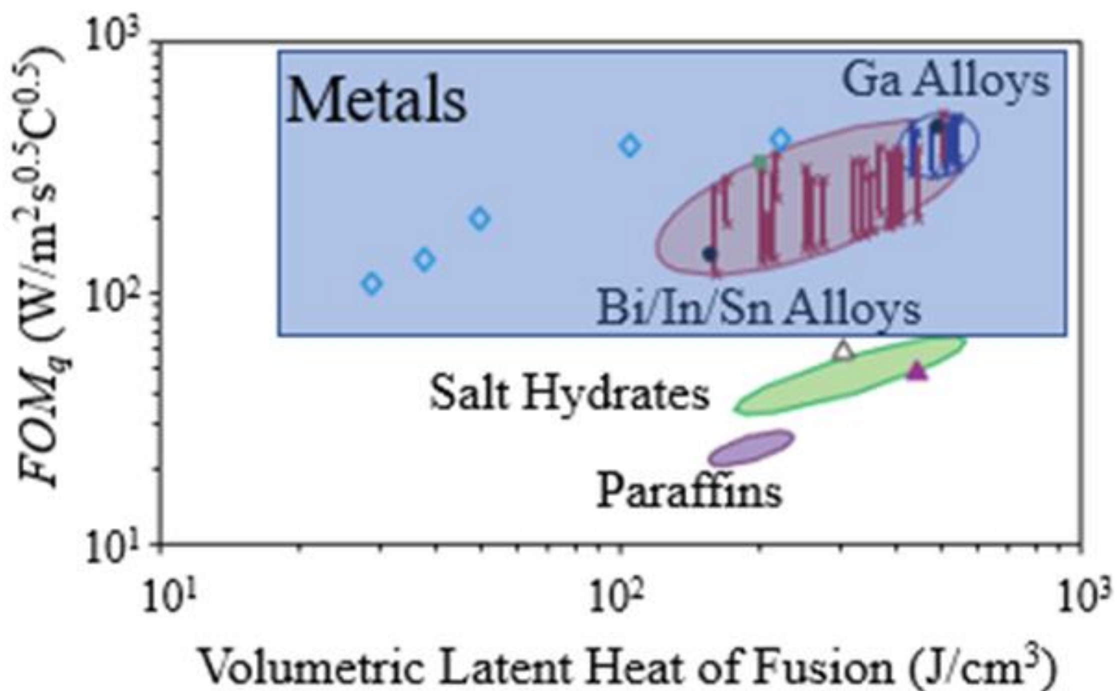

Figure 1-7. Comparison of cooling FOM versus latent heat for various material types. Adapted from [32].

heat into the PCM, and high latent heat of fusion (i_{sl}) to promote large heat absorption at constant temperature [31]. A key metric in the literature which combines the effect of both these properties is the cooling capacity Figure of Merit, defined as $OM_q = \sqrt{k_f i_{sl}}$. Metallic PCMs consistently have FOMs which are at least an order of magnitude higher than non-metals, and within that category, gallium- or Bi/In/Sn-based alloys have particularly advantageous properties (see Figure 1-7) [32]. Advanced PCM packaging techniques allow for creating composite PCM structures which allow higher thermal conductivity metal foams to be impregnated with PCMs of desirable melting temperature and volumetric latent heat. McAfee et al. [33] and Yang et al. [34] reported on two metal PCM/metal foam composite structures: one with gallium/nickel foam; the other, Field's metal/copper foam. This composite metal/metal foam structure further enhanced the viability of these low melting temperature metal PCMs by distributing them inside a much higher conductivity metal foam matrix.

Metallic and composite foam PCMs have demonstrated strong thermal buffering effects to highly transient thermal loads in several studies. Figure 1-8 examines two investigations on the impact of added PCM on transient thermal responses of high heat flux pulsed devices. The top plot compares the effect of several types of PCM, both non-metallic (PureTemp29 and PureTemp58) and metallic (Bi/Pb/Sn/In and Fields Metal), on the thermal response of a surrogate power electronic package exposed to a stepped heat pulse [35]. The arrow and inset text shows an 80°C reduced device temperature with Fields Metal compared with the dielectric gel, demonstrating the superior thermal buffering capability of the metallic PCMs for dampening temperature spikes due to a stepped heat load. The bottom plot in Figure 4 presents results adapted from a previous REACH CoLab study on power electronics packaging with a composite metal foam PCM and shows marked reductions in temperature fluctuations in electric vehicle power electronics under

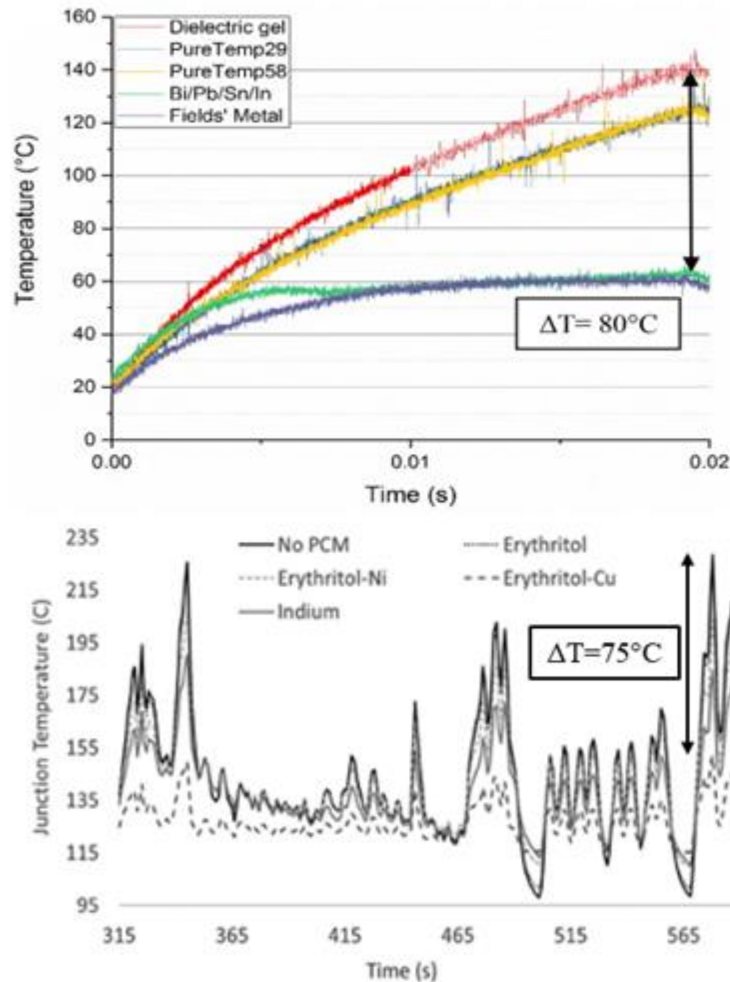

Figure 1-8. Previous studies demonstrating the impact of adding PCMs to high heat flux cooling packages. (Top) Comparison of various PCMs to buffering the thermal response of a surrogate device to a stepped heat load [35]. (Bottom) A study on a vehicular power electronics module with PCM experiencing lessened temperature excursions under an aggressive drive cycle [36].

an aggressive driving profile [36]. As shown in this figure, the addition of the composite metal foam PCM reduced peak temperatures by up to 75°C. Choosing the appropriate metallic or metallic composite PCM greatly improves the transient thermal response of a high heat flux device.

Evidently, metallic composite PCMs may improve the transient thermal performance of low capacitance electronic devices; however, the impact of such a PCM has not been investigated with flow boiling in microchannels. Incorporating PCM into a low thermal resistance, low thermal capacitance microchannel evaporator could improve the transient thermal response of the

evaporator while simultaneously mitigating the impact of flow instabilities which may be exacerbated relative to steady state operating conditions. However, the impact of adding a PCM to such an evaporator is poorly understood and warrants investigation for the potential thermal buffering effects and possible performance enhancements.

1.4. Research Objectives

Microchannel flow boiling represents an effective thermal management strategy for high heat flux microelectronics. While steady state behaviors are well-characterized, the impact of transient heating has only been studied relatively recently. The goal of this work is to investigate the transient thermal behavior of two different microdevices exposed to transient heating modes and develop techniques to predict and mitigate any undesirable behavior. In doing so, this research will add to the growing body of research investigating the performance of microchannel flow boiling while also adding a practical element towards real device implementation which considers the impacts of transient heating on device behaviors.

In summary, this research study will:

- Design and fabricate a testing facility for examining microchannel flow boiling behavior under transient heating modes.
- Characterize the transient thermal response of two different low thermal resistance microchannel evaporators under a range of heating conditions and flow conditions.
- Establish predictive models which are embedded in a computational design tool for understanding tradeoffs in device behavior with system-level performance.
- Investigate the impact of integrating metallic phase change materials (PCMs) into the microdevice for a potential transient thermal buffering effect on the transient flow boiling behaviors.

1.5. Thesis Organization

The following chapters detail the study of flow boiling in microchannels under transient heating and the development of predictive models and mitigation strategies for the observed behavior. Chapter 2 of the document will provide a synthesis of the relevant literature of boiling under transient heating. The literature review will specifically detail both pool boiling and flow boiling, which is further broken into non-microchannel and microchannel-specific studies. Chapter 3 will detail the testing setup, experimental study design, and computational approach, including both the initial testing facility along with the redesigned and rebuilt transient-specific testing rig. Chapter 4 will present the results of testing the first silicon microchannel geometry along with chronicling the development of a computational model for predicting the transient device behavior. Chapter 5 will present the results of the second silicon microchannel device with transient testing under a more extensive range of conditions. The development of an additional model will also be detailed which incorporates the effects of the transient boiling behavior on this second device. Chapter 6 will describe the impact of phase change materials on the device behavior using both semi-empirical and simulation approaches incorporating the model developed in Chapter 5. Chapter 7 will provide closing remarks and offer recommendations for future work.

CHAPTER 2. Literature Review

As electronic device packaging has progressed, component size and scale have decreased with the development of more compact, higher performance devices. To meet the demands of improved performance, device power levels have also been increased to improve operability, particularly in the defense and medical sectors where spatially constrained systems are common. Concurrent reductions in packaging volume with increased power result in commensurately increased heat density dissipation requirements which have necessitated the development of advanced thermal management strategies and architectures to keep these devices operable and below the upper threshold limits for temperature.

While single-phase liquid cooling has been a traditional cooling method of choice which can be improved further by employing microchannels with large surface area-to-volume ratios, to maintain the device temperatures below the cutoff thresholds, large flow rates are required to prevent the fluid temperatures from increasing too much. Larger flow rates translate to increased pressure drop and subsequently required pumping power, and practical constraints on thermal management system size or pumping power limit the effectiveness of such single-phase cooling systems. Microchannel flow boiling has emerged as a promising technology for rejecting the large heat densities of these devices which can easily exceed 1 kW/cm^2 due to its use of latent heat phase change as opposed to sensible heating [8]. Additional benefits of flow boiling compared with single-phase liquid cooling include increased heat transfer rates, lower flow rates, reduced pumping power requirements, smaller fluid inventories, and more isothermal devices with reduced spatial temperature gradients [12–15].

While much work has been dedicated to understanding the fundamental mechanisms of microchannel flow boiling and optimizing its performance at steady state, real devices operate under highly unsteady heating conditions such as pulses or cold-startups. The large change in heating conditions and resulting vapor generation rates may result in unanticipated behaviors which vary from those observed under steady heating conditions. In addition, flow instabilities which were well-controlled at steady state may be exacerbated under transient heating conditions due to the change in vapor generation rates. The following sections provide a survey of important studies in the literature related to transient boiling. Selected studies on transient pool and flow boiling, in both microchannels and macrochannels, will be synthesized in detail, with key gaps identified. Finally, the objectives of the current work will be expanded in relation to these gaps.

2.1. Transient Pool Boiling

While pool boiling lacks the forced convective component of flow boiling, the nucleation mechanisms are still useful in understanding how transient heating affects the boiling process. Many early studies were concerned with the impact of a sudden increase in heat flux which initiated boiling in a liquid-cooled nuclear reactor module [37]. These studies examined the transient response of thin film ribbon heaters immersed in quiescent water tanks under a variety of transient heating conditions. Many of these studies also used exponentially-increasing heat loads due to their ease of solving with analytical models and of their practical element which reasonably represented a thermal runaway condition in a nuclear reactor. Due to the thinness of the ribbons used, there was little thermal lag time in the response, and the transient behaviors observed were quite rapid in nature.

Rosenthal was one of the earliest studies to investigate such a transient boiling response in atmospheric pressure water and looked at the effects of initial subcooling, exponential period, and

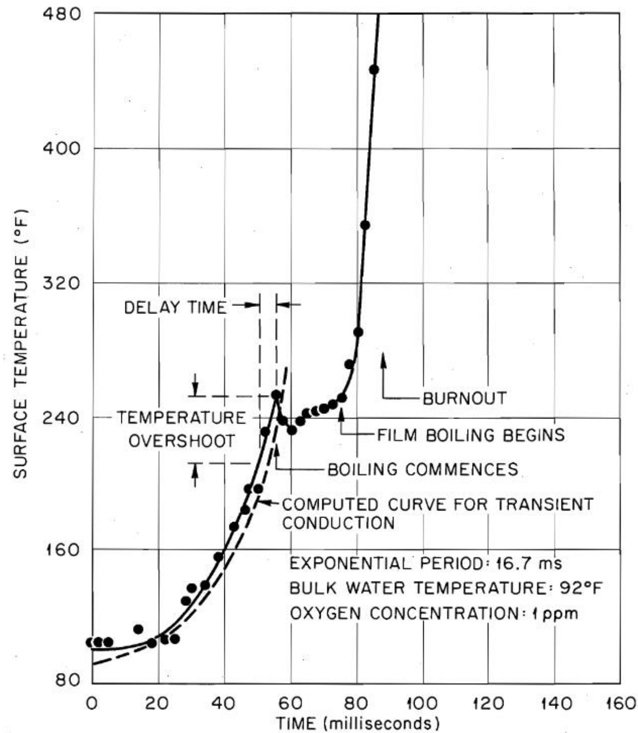

Figure 2-1. Typical temperature response for a ribbon heater experiencing an exponential heat input in time, from [38].

dissolved oxygen concentration [38]. A typical transient temperature contour is shown in Figure 2-1 , where the heater temperature rapidly increased past the saturation temperature of the water and resulted in a temperature overshoot prior to the onset of boiling, which occurred with an explosive growth of bubbles along with a concurrent decrease in temperature. They found that this overshoot was a decreasing function of exponential period and initial subcooling due to changes in required energy supplied to the fluid or differences in necessary superheat prior to boiling. The overshoot was nearly zero with saturated initial conditions. Differences in dissolved oxygen content did not markedly impact the overshoot. These results were confirmed in a similar study by Su et al. [39], who also noted that the larger superheat associated with the increased subcooling resulted in more explosive boiling, and that the more rapid heating rates activated many nucleation sites which rapidly coalesced to form a vapor layer that quickly established dryout/burnout conditions in the device. Yan et al. also performed a similar study with a ribbon heater immersed

in quiescent water and also found a temperature overshoot which increased as liquid subcooling increased but that vanished at saturated initial conditions [40]. However, they found that a surface degassing procedure virtually eliminated the temperature overshoot and thus concluded that the overshoot was a direct result of a delay in boiling associated with the departure of non-condensable trapped gas bubbles prior to boiling inception. It is possible that Rosenthal's dissolved gas content was not low enough to noticeably impact the nucleation conditions.

While these studies looked at ribbon heaters immersed in water and under exponential heating conditions, others have looked at highly wetting fluids with stepped heat loads. Because stepped heat loads are not continuously increasing but are a pointwise increase in heating, the behavior may be different than with exponential heating. Giventer and Smith examined transient pool boiling on a thin wire immersed in liquid nitrogen under stepped heating and observed a temperature overshoot above the steady state which increased with peak heat load [41]. They posited that the temperature overshoot may have been due to the activation of additional nucleation sites which were necessary to sustain nucleate boiling at a higher heat flux. Duluc et al. also investigated pool boiling under stepped heating in liquid nitrogen, but for both a very thin wire [42]. The ONB temperatures increased with peak heat flux and were higher than for steady heating conditions. The low thermal inertia resulted in extremely rapid heating rates in the fluid, and bubble growth appeared to be impeded by an underdeveloped thermal boundary layer. It was concluded the kinetics of the liquid-vapor meniscus inside nucleation cavities likely play a key role in mediating the nucleation process.

Larger thermal inertia samples with flat surfaces were also investigated and impacted the transient thermal behavior observed. Duluc et al. also studied the transient thermal response of a ~30 mm diameter x 150 mm deep copper block and found that large superheats of up to 50°C were

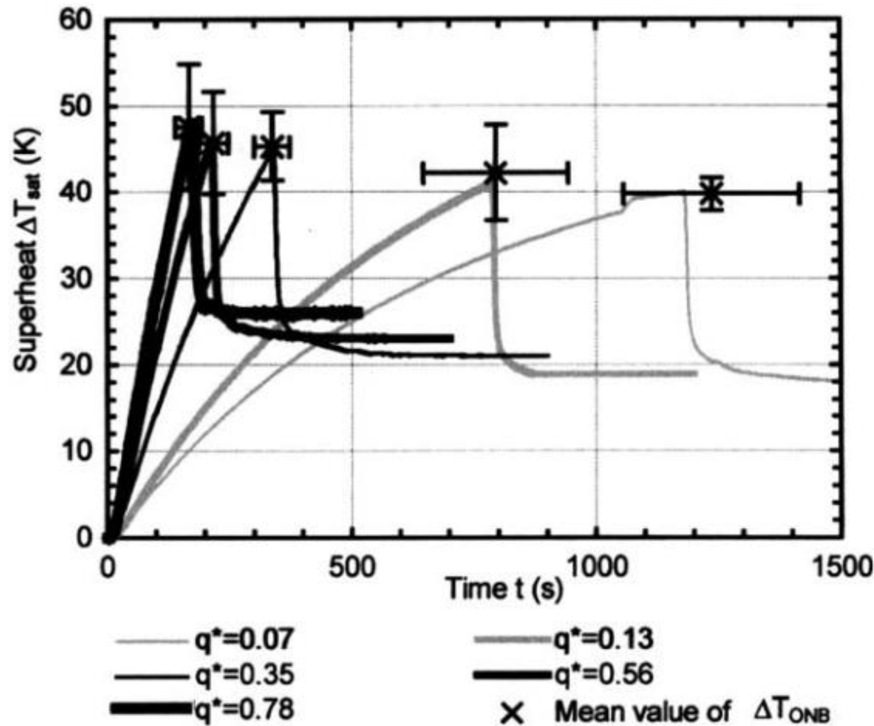

Figure 2-2. Transient superheat curves showing large superheat and temperature overshoot at ONB, with stochasticity and temperatures dependent on peak heat flux [42].

required to initiate boiling, but that due to the large thermal inertia, these superheats were weakly dependent on the peak heat flux [42]. The time and temperature at ONB exhibited stochasticity which was dependent on peak heat flux as well, as shown in Figure 2-2. The temperature then decreased dramatically as the efficient nucleate boiling mechanism dominated. The ONB was thought to be due to pre-existing gas nuclei trapped in cavities as opposed to homogeneous or heterogeneous nucleation due to the smoothness of the surface and a nucleation temperature below the homogeneous nucleation temperature. Heas also studied transient pool boiling with a similar large thermal inertia test fixture but with pentane [43]. They used a preliminary surface priming technique to activate nucleation cavities and articulated that a large stochasticity can result without this technique. Nevertheless, like in Duluc, a large wall superheat of ~54°C at the ONB and a temperature overshoot above the saturation temperature were observed as boiling initiated explosively due to the large superheat. The transient ONB superheat was found to be higher than

at steady state heating conditions and was attributed to a decreased thermal boundary layer thickness during the transient heating events. It was again postulated here that boiling was triggered by gas trapped in cavities, and a long waiting period between priming and testing resulted in an asymptotic increase in superheat from ~43°C to ~50°C.

Overall, for pool boiling, the nature of the transient heating mode and the thermal inertia of the heating device affected the thermal behavior of the onset of boiling and following boiling conditions. In general, large wall superheats and temperature overshoots above the steady state temperature were observed. It appears the presence of trapped gases greatly affects the onset of boiling conditions, and that a pre-boiling surface priming procedure can reduce ONB temperature stochasticity or mitigate the temperature overshoot. In addition, the thermal inertia of the device appears to play a role, with lower thermal mass devices resulting in rapid increases in superheat which were generally higher than at steady heating conditions. This was surmised to be the result of a mismatch in time between thermal boundary layer development and the kinetics of the nucleation process, which then impeded boiling until higher superheats were met. Larger thermal inertia resulted in ONB conditions which were not as strongly dependent on peak heating rate.

2.2. Transient Flow Boiling

While pool boiling provides clues to nucleation mechanisms under transient heating modes, it lacks the forced convective element. Furthermore, most of the studies on pool boiling were in large vessels where the convection was not constrained spatially. In flow boiling, the fluid is constrained to flow within an enclosed passage, and the dimensions of that passage can greatly affect the observed behavior due to the interactions between the fundamental surface tension, gravitational, viscous, and inertial forces. Furthermore, the presence of flow affects the thermal boundary layer development depending on laminar or turbulent flow conditions and may affect the

local boiling behaviors. When the transition between the so-called macroscale and microscale occurs is currently a matter of serious debate within the scientific community, and unfortunately little consensus exists. Some authors proposed specific dimensional criteria [44,45], while others have proposed confinement criteria relating to different nondimensional parameters which determine the relative importance of surface tension, gravity, hydraulic diameter, and channel mass flux [46–48]. What is clear from these studies is that there is a transition below which surface tension and capillary forces become dominant, and that the further the scales reduce, the further confinement is experienced by generated vapor. This section is split into macrochannel and microchannel subsections, where macrochannel studies were chosen if the characteristics were generally far into the conventional size range as discussed in the above studies. The studies were considered microchannel either if so-called by the authors or if they fit most of the criteria in the above listed studies.

2.2.1. Macrochannels

Much of the research at this scale has been regarding liquid-cooled light water reactors, a form of nuclear reactor, where studies of flow boiling in water were conducted to understand if cooling could be reasonably maintained under reactor heating spikes. Much of the focus was on where the critical heat flux threshold was passed where the temperature increased dramatically with further increases in heat flux. Few studies described the conditions surrounding the onset of boiling or boiling under heat load perturbations. Su et al. [49] performed an analogous study to their transient pool boiling study with fully turbulent flow boiling in water in a 30 mm x 10 mm duct and found that, like in the pool boiling study, the temperature at the ONB decreased as the exponential period increased. Furthermore, it was found that wall superheat was higher with higher flow rate and subcooling, and in all cases the wall superheat-heat flux at ONB was higher than

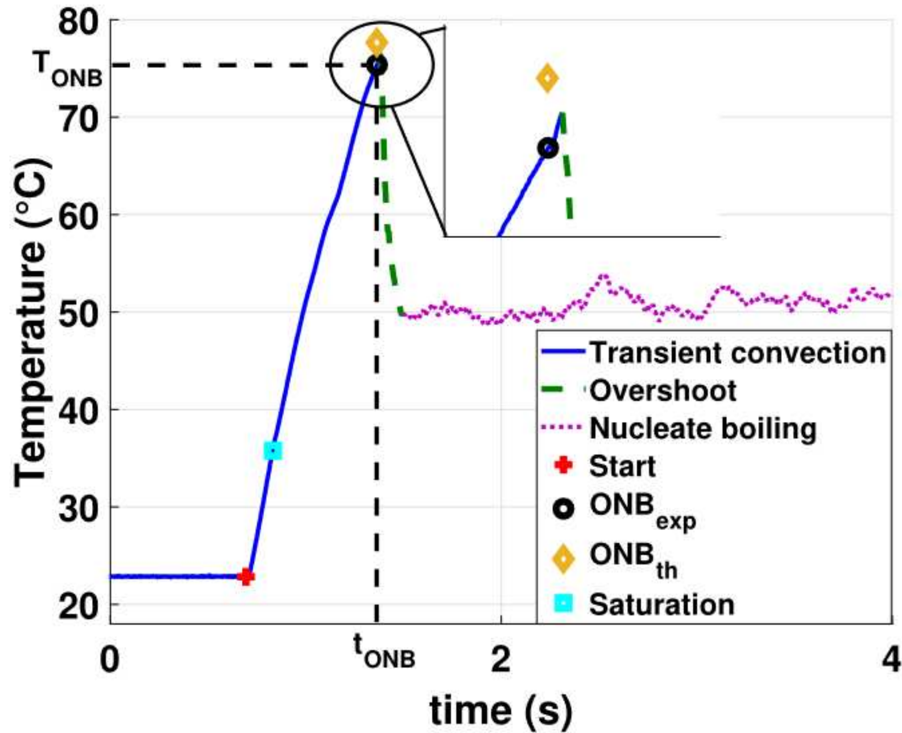

Figure 2-3. Typical transient temperature time series under a transient heat step from [50].

with pool boiling. Temperature overshoots were also observed and followed a similar trend to the ONB superheats; however, at very short periods and low subcoolings, overshoots were not observed due to the rapid increase of heat generation and insufficient increase of the heat transfer coefficient from single-phase to flow boiling.

Scheiff et al. performed a similar study but with HFE7000 (a lower surface tension fluid than water) in a 8.4 mm diameter pipe with a thin film heater subjected to stepped heating [50]. Large wall superheats (~40°C) and temperature overshoots (~26°C) above the steady temperature at the ONB were again observed, as shown in Figure 2-3. The wall superheat at ONB increased with peak heat flux, subcooling, and flow rate like in Su. However, the temperature overshoot and time constant of the decay to steady state flow boiling showed no noticeable dependence on flow rate, heat flux, or subcooling, contrary to the findings in Su. It is possible that these findings may be due to differences in fluid properties and operating conditions across these two studies. Visentini supplanted this study by investigating the effects of square or triangle wave pulses on

the same device under the same flow conditions [51]. Again, superheats of up to 40°C at the ONB were observed, with temperature overshoots above the steady state temperature of up to 33°C. However, they also found that the temperature rise rate during single-phase cooling resulted in an asymptotic increase in the ONB superheat, and that there was a minimum amount of energy needed to initiate boiling, above which the superheat plateaued around 20°C. In particular, the triangle wave pulses at lower linear ramp rates resulted in lower ONB temperatures due to lower temperature rise times compared with the square wave stepped heat loads. Thus, it appears that the conditions surrounding the ONB temperature are dependent not only on fluid conditions and peak heat flux but the rate at which the heat load is increased and possibly indicating rate-limited growth of vapor bubbles.

While the previous three studies were interested in nuclear reactor applications from cold start-ups, Van den Bergh et al., motivated by irradiation flareups for concentrated solar power applications, instead investigated transient heating perturbations to the flow boiling process on flow boiling with R-245fa in a 8.31 mm diameter tube [52]. It was found that during a heat load perturbation, the change in heat transfer coefficient did not mirror the change in vapor quality, and the heat transfer coefficient dropped significantly upon increasing the heat flux. While flow instabilities did not surface during these transients, the reduction of the flow boiling heat transfer coefficient with a transient increase in heat load is concerning because it could lead to a rise in device temperature over the safe limit. Thus, temperature overshoots and large wall superheats are present with cold startup conditions, but transient perturbations to previously boiling flows may be detrimental to device performance if the heat transfer coefficient drops dramatically during this heat load perturbation.

In flow boiling at the macroscale, large wall superheats and temperature overshoots above the steady state temperatures were observed like in the pool boiling studies. However, due to the convective effects which increased heat transfer coefficient, the observed superheats were higher. In general, these effects were more significant with higher flow rates and subcooling, though the temperature overshoot was inconsistently affected by flow conditions. This may have been due to differences in fluid properties used across these studies or the presence of highly turbulent flow conditions. The rate at how quickly the heat flux to the fluid is increased played an important role, with higher rates tending to impede the nucleation process and resulting in larger superheats and temperature overshoots. Finally, transient perturbations in the heat rate after steady boiling was already established appeared to impact the heat transfer coefficient in a way not predictable by changes in vapor production rates alone. These results suggest that for devices cooled with flow boiling and which experience power transients, large temperature swings could result under cold startups or for heat load perturbations and may in turn reduce device longevity or performance.

2.2.2. Microchannels

As mentioned above, microchannels tend to experience higher capillary and surface tension forces compared with macrochannels. In addition, unlike with the large-scale channels observed above, the small scales of microchannels usually result in laminar flow conditions, which increase the thermal boundary layer thickness. Because of this, depending on the channel dimensions, the boundary layers may penetrate more deeply into the fluid bulk compared with larger channels in which often turbulent flow constrains the boundary layers to nearer the channel walls. This leads to relatively larger vapor bubbles which may be confined by the small length scales of the microchannel and thus potentially expand both upstream and downstream in the channel, leading to flow reversal [46,53]. Finally, many microchannels are typically arrayed parallel to each other

Table 2-1. Studies on microchannel flow boiling under transient heating

Study	Microchannel Evaporator Parameters					Testing Conditions			Working Fluid(s)
	Material	Number of Channels	Inlet Orifice	D_h [μm]	th_{base} [μm]	q''_{max} [W/cm^2]	G_{max} [kg/m^{2}s^2]	T_{sat} [°C]	
Basu et al. [55]	Silicon	1	No	343	0	675	3800	34	HFE-7000
Chen & Cheng [56]	Silicon	1	No	214	0	7200	267	100	Water
Kingston et al. [57]	Pyrex	1	No	500	100	15	400	65	HFE-7100
Zhuang et al. [58]	Copper	1	No	400	19600	62	720	100	Water
Huang et al. [59]	Silicon	67	Yes	100	280	30	2000	31.5, 35, 40	R236fa, R245fa
Markal & Evcimen [60]	Copper	11	No	333	1800	31.25	200	100	Water

in devices to maximize surface area enhancement with connecting plenums at their inlets and outlets. This leads to additional interactions between channels not typically seen with single large macrochannels or tubes and which may be dependent on the number of channels, plenum design, and thickness and specific heat capacity of channel walls (or fins) [19,23,54]. Therefore, due to bubble confinement and cross-channel interactions, microchannels tend to be susceptible to intensified flow instabilities compared to larger scale channels. Furthermore, as microchannels are typically used in embedded cooling strategies, as mentioned in Chapter 1, the thermal capacitance is typically low. Transient heating may thus worsen flow instabilities while resulting in rapid temperature fluctuations that would not be observed during steady state operating conditions.

There are limited published studies on the transient impact of microchannel evaporators subjected to transient heat loads. Previous studies investigating microchannel flow boiling under transient heating are divided between single microchannel and multi-microchannel evaporators. Table 2-1 lists relevant experimental studies and their testing conditions to date. Basu et al. [55], Chen and Cheng [56], and Kingston et al. [57] studied flow boiling under stepped or pulsed heat loads in single microchannel devices without inlet restrictions. Basu et al. noted very large

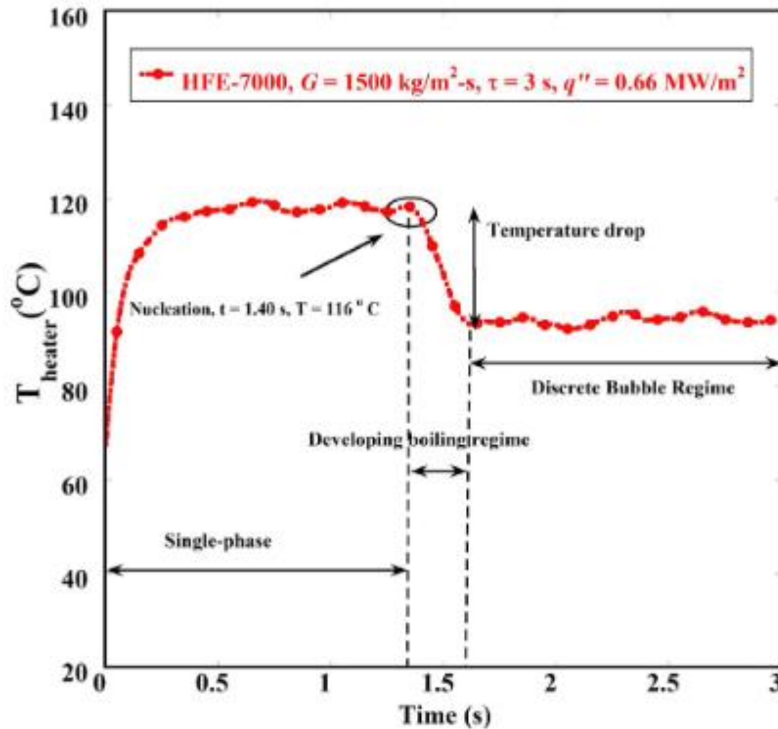

Figure 2-4. Typical transient temperature response under a transient heat step from [54].

superheats of up to 110°C and temperature overshoots above the steady state boiling temperature of ~20°C at the ONB followed by a drop to steady-state boiling at lower heat fluxes, with a representative transient thermal response shown in Figure 2-4. The large superheat and overshoot were attributed to the low surface tension HFE-7000 and the smooth surface of the heater with an average roughness of less than 30 nm. The wall superheat increased linearly with heat flux until it plateaued at ~110°C for heat fluxes greater than 375 W/cm^2. Kington et al. also observed a ~20°C temperature overshoot and a ~50°C wall superheat at the ONB [57]. In addition, vapor backflow occurred into the inlet plenum due to rapid bubble growth at the ONB and mass flow/pressure drop oscillations after the ONB, characteristic of microchannel evaporators without inlet orifices. Chen and Chen did not observe a temperature overshoot at the onset of boiling, though wall superheats did increase with heat flux but were much lower overall (<30°C) [56]. While they also used a thin film heater which likely also had a very smooth surface, the use of a higher surface tension fluid, water, may have been responsible for these differences.

At higher heat fluxes, Basu et al. and Chen and Cheng commented on a near immediate transition to film boiling with a continuously increasing heater temperature even after the ONB as the vapor fraction increased and insulated the wall from the liquid [55,56]. The time to boiling inception (defined as the growth and detachment of a vapor bubble) also decreased as heat flux increased due to more active nucleation sites which increased the rate of bubble growth and departure. It was suggested that at the higher heat fluxes and heating rates, the surface temperature may have risen quicker than boiling could initiate, and thus boiling was delayed until higher superheats were met. Contrary to the results observed in Kingston, flow instabilities due to the transient heating were not observed (or were simply not reported). Nevertheless, the immediate shift to film boiling at the onset of boiling for these higher heat fluxes due to the vigorous generation of rapidly coalescing vapor bubbles could lead to catastrophic effects on a device such as thermal runaway or dryout, given that the temperatures of the devices in these studies did not reach a steady state after film boiling was initiated.

While the single channel studies examined the effect of stepped changes in heat load that initiated boiling had on the microchannel behavior, Zhuang et al. examined perturbations in heat load after boiling had already been initiated and the influence of subcooling and flow rate on the following transient flow behaviors [58]. Because boiling had already been initiated, upon a sudden additional increase in heat flux, no overshoot was observed. However, the increase in vapor production resulted in a temporarily unsteady boiling regime where the pressure drop and flow within the channel experienced large oscillations. Due to the large thermal mass of the device, the temperature did not fluctuate more than 0.5°C. Increasing the inlet subcooling or increasing the mass flux reduced the transient spike in pressure drop as well as the intensity of pressure drop oscillations due to a reduced vapor quality. The results of this study are similar to the results of

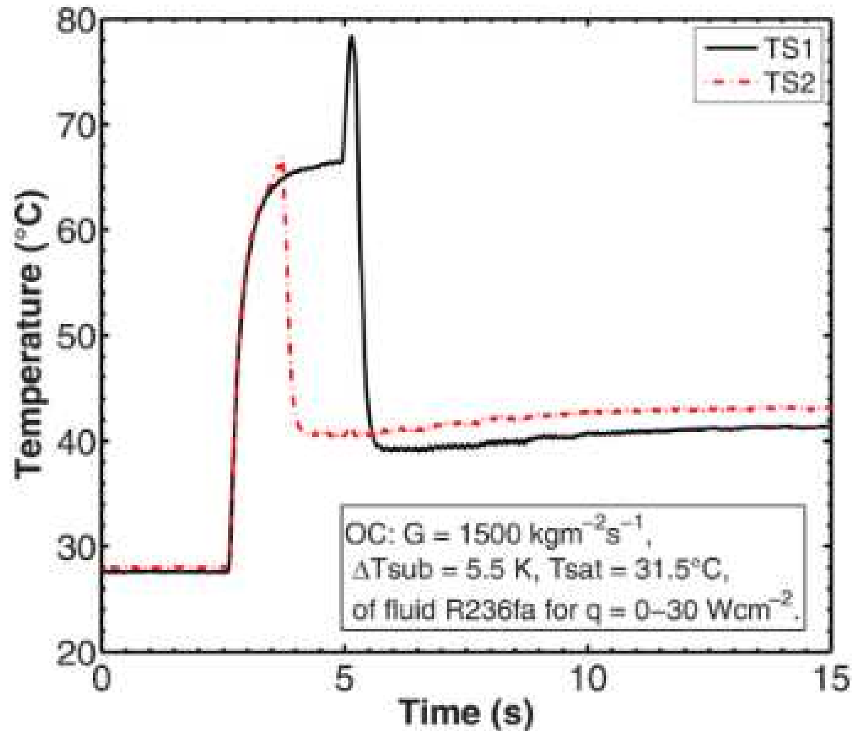

Figure 2-5. Transient flow boiling temperature response compared across test sections with 2:1 and 4:1 inlet restriction ratios from [59].

Van den Bergh [52] discussed earlier despite differences in channel dimensions and show that even once boiling has occurred, transient heat fluxes may result in flow instabilities.

These previous observations for single channel evaporators indicate the presence of flow instabilities and temperature excursions at the ONB under transient heating or upon increasing the heat flux after a steady boiling regime had already been attained, particularly at higher heat fluxes and in channels without inlet restrictions. Multi-channel devices have additional considerations due to cross-channel interactions such as the parallel channel instability mentioned earlier. Huang et al. studied a silicon, multi-microchannel evaporator with two different sizes of channel inlet restriction ratios of 2:1 and 4:1 subjected to stepped heat loads [59]. As shown in Figure 2-5, large wall superheats of up to 34°C and temperature overshoots above the steady state temperature of up to 36°C were seen before a sharp drop to steady state occurred after the ONB. Like in Kingston et al., vapor backflow out of the channel was seen at the ONB but was significantly reduced with

the increased 4:1 inlet restriction ratio. In addition, reductions in heat flux, inlet restriction dimensions, subcooling, saturation temperature, and increasing mass flux all reduced peak temperatures, while nucleation time was inversely proportional to heat flux as observed by the single channel studies. Markal and Evcimen also investigated stepped heating but on a copper multi-microchannel evaporator with water [60]. At the highest heat fluxes, again large wall superheats of up to 52°C and temperature overshoots of up to 44°C were observed prior to the ONB, which then rapidly reduced the heater temperature. Oscillating flow reversal was also observed, though this device did not have inlet orifices. In both of these studies, the high superheats were attributed to either a smooth surface which reduced nucleation site density, fluid surface tension, or a delayed start of nucleation due to the transient heating and quenching of bubbles.

2.3. Specific Aims of this Study

It is clear from these previous studies that boiling under transient heating can result in large wall superheats and temperature overshoots prior to the onset of boiling [42,43,50,59–61]. Fluid properties, peak heat loads and heating rates, flow conditions, and surface finish generally influenced the resulting peak temperatures or temperature overshoot conditions observed. Furthermore, the transient superheats required for boiling initiation were found to be higher than at the equivalent conditions under steady state heating [41–43]. At least one study found that thermal mass impacted the superheat necessary for boiling initiation and the overshoot above the steady state temperature [42]. Pre-priming nucleation sites also played a major role in the observed behavior in many of these studies [40,42,43]. In some cases, due to the high heating rates, film boiling was quickly reached after ONB, and a quasi-thermal runaway condition followed [56,61]. In several of the microchannel studies, due to bubble confinement and the large wall superheats at

the ONB, vapor backflow and flow reversal were observed along with other flow instabilities [57,59,60].

In the microchannel studies, vapor backflow, flow reversal, and other flow instabilities also resulted from step changes in heat load [55,57–60]. The low thermal mass of most microchannel evaporators exacerbates the transient thermal response from high wall superheats and temperature overshoots [30]. The resulting flow instabilities alongside the rapidly fluctuating device temperatures could quickly result in device damage or failure. However, only a step or pulsating function in heat load was investigated. Only one study used an inlet restriction which partially mitigated peak temperatures and reduced the occurrence of flow instabilities [59]. No study investigated hydraulic diameters smaller than 100 μm, which would further improve device compactness and steady state performance due to the additional surface area and heat transfer coefficient enhancement but may result in even more intensified transient behavior. Furthermore, no study investigated measures such as modulating how quickly heat flux is applied to the fluid, to mitigate the peak temperature before the ONB or the transient vapor backflow with a given set of fluid conditions. A more gradually applied transient heat load could act similar to additional thermal mass which would buffer the rate in which heat is added to the fluid and potentially improve the transient response as was seen in at least one study [51].

While steady state performance of microchannel evaporators may result in optimal thermal management conditions, the transient response may result in unexpected behaviors which could quickly damage or destroy the device due to reaching a dryout-like condition under a transient power or heating spike. Holistic design approaches should incorporate both transient and steady state performance to most accurately access the usefulness of a given cooling strategy. Predicting and mitigating the impact of transient operation on low thermal resistance microchannel

evaporators is paramount to practical implementation into such embedded cooling thermal management techniques. No study to date has attempted to create a model for the transient temperature response of a microchannel evaporator under transient heat loads. Predictive methods must be developed to understand the tradeoffs of incorporating microchannel evaporators into the thermal management systems of pulsed high heat flux devices since the transient response of microchannel evaporators can produce unexpected behavior such as temperature overshoots and flow instabilities [57–59,61]. In addition, given the desirable thermal buffering effects of improved thermal capacity and the inclusion of a PCM as mentioned in Refs [30,35,36], understanding the potential impact of incorporating PCM into the evaporator to improve the device-level thermal capacitance is key to potentially buffering the transient thermal response and reducing the observed flow instabilities and temperature spikes. To date, no study has investigated the impact of including PCM despite the potential for buffering the transient response of a microchannel evaporator.

This work seeks to address these literature gaps by contributing additional experimental microchannel evaporator device studies with transient heating on sub-100 µm hydraulic diameter devices. In addition, a predictive computational model for microchannel evaporators under transient heat loads will be developed and embedded within a thermal management system design suite. The model will provide a useful tool for tradeoff and design studies for thermal management systems which incorporate microchannel embedded two-phase cooling techniques. In addition, the impact of incorporating a metallic PCM into a microchannel evaporator will be studied and quantified to understand any potential benefits for inclusion into future transient thermal management strategies.

CHAPTER 3. Experimental and Computational Methods

This chapter will detail the experimental and computational methods which were used to collect the data and develop the models discussed in this dissertation work. Two different test sections were used with distinct geometries. Two testing facilities were also used to collect data. The first test facility was designed for steady state testing but with several modifications for transient testing on the initial device, though it still proved difficult to control the system responses. Therefore, another test facility was designed and built to accommodate an improved transient response and was used for testing the second test section. The testing plan for each test piece is also included in this section. Finally, the NavyHHF-ParaPower software used in developing the computational models will also be discussed, and the PCM properties used to develop the semi-empirical PCM model in Chapter 6 will also be detailed.

3.1. Experimental Setup

The experimental test sections, testing facilities, and testing approaches used in this effort will be described in this section.

3.1.1. Test Sections

The testing was conducted on custom microchannel evaporator etched from a 300 µm thick silicon wafer with a Deep Reactive Ion Etching (DRIE) fabrication process by Lawrence Livermore National Lab (LLNL) which is discussed in detail in Bevis [12]. Extensive steady-state testing of similar evaporators with different channel geometries operating under different mass fluxes and saturation pressures was performed in this previous study and influenced the choice of

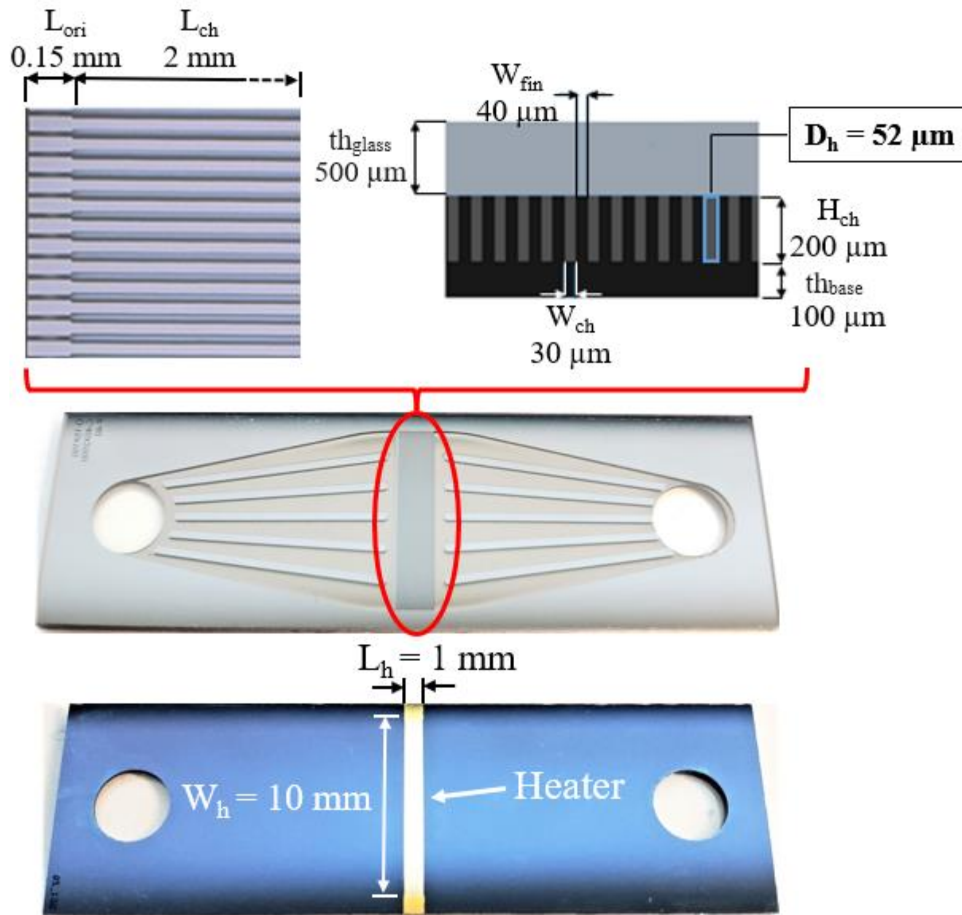

Figure 3-1. Detailed dimensions of 52 µm hydraulic diameter, silicon, microchannel evaporator investigated in this work.

test conditions and test section geometry in this effort. R134a refrigerant was used as the working fluid since this was the fluid tested in the steady state studies and has well-characterized thermophysical properties.

3.1.1.1. 52 µm Hydraulic Diameter Microchannel Evaporator

Figure 3-1 shows the first test section used in this work. The refrigerant enters the device and is distributed throughout an inlet plenum by supporting silicon features. Prior to entering the channels, the refrigerant flows through restrictions etched at the inlet of each channel which stabilized the flow at steady state. The inlet orifices are nominally 15 µm wide and 150 µm long. The orifice to channel restriction ratio is ~2:1. Upon exiting the inlet restrictions, the fluid flows

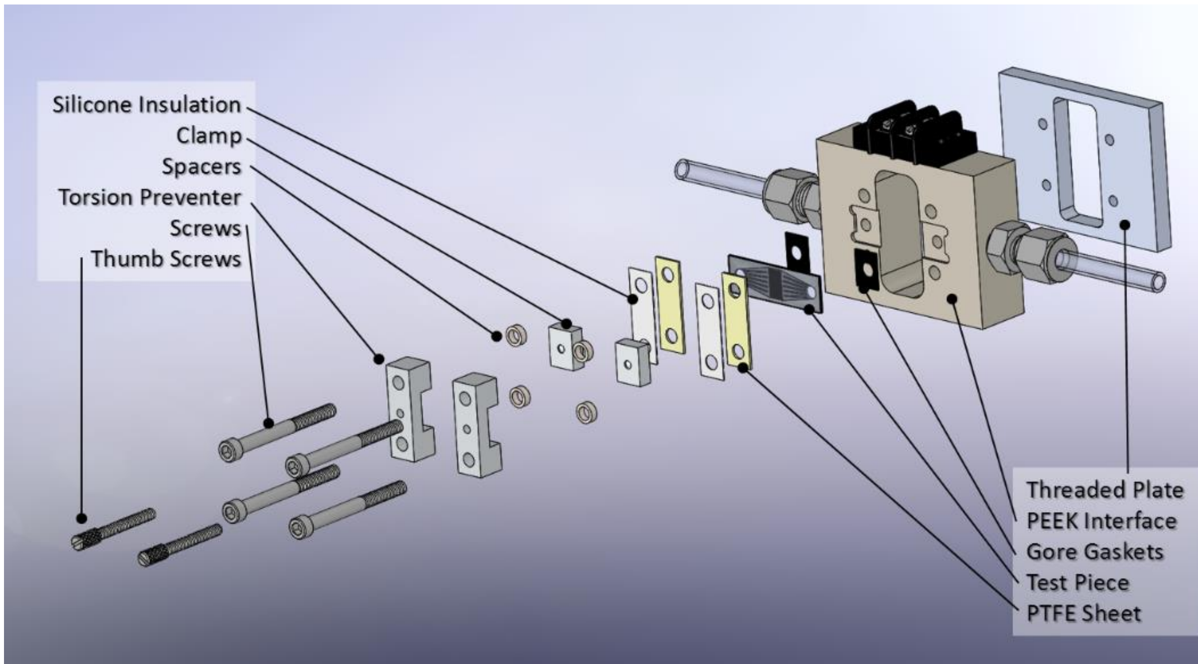

Figure 3-2. Fluidic manifold for 52 μm hydraulic diameter microchannel test section which interfaces to two-phase pumped loop [12].

through the 142 channels which are 2 mm long, 30 μm wide, and 200 μm deep. The channel hydraulic diameter is 52 μm. The fins separating the channels are 40 μm wide. A 500 μm-thick sheet of borosilicate glass was anodically bonded to the top of the silicon channels to provide a hermetic fluid seal. A 10 mm-by-1 mm thin film platinum resistive heater was deposited over the center of the channels on the backside of the test section to act as a surrogate laser diode bar. Current is passed through the heater to produce Joule heating. The base thickness between the heater and the bottom of the channels is 100 μm. Since the heater only spans half the length of the channels, axial conduction, or heat spreading, is expected to play a larger role than previous transient boiling studies with uniform heat distributions. The test section interfaced with the fluidic test facility with a low thermal conductivity (~0.25 W/m-K) poly-ether-ether-ketone (PEEK) plastic manifold structure shown in exploded view in Figure 3-2 [12].

3.1.1.2. 38 μm Hydraulic Diameter Microchannel Evaporator

Figure 3-3 shows the salient details of the second test section investigated. The heater element and plenum regions are the same, but the channel geometry is different. In particular, the channels are 22 μm wide x 141 μm deep, with 250 channels as opposed to 142 in the other test section. The fins are 18 μm wide with the same depth. The inlet orifices are ~17.5 μm wide, which provides a 1.26:1 restriction ratio that is noticeably smaller than for the larger channel test section. For this test section, an improved manifold was designed and fabricated to bring the pressure and temperature measurements closer to the inlet and outlet of the test section. This manifold is shown in an exploded view in Figure 3-4. For both evaporators and manifolds, the test section was

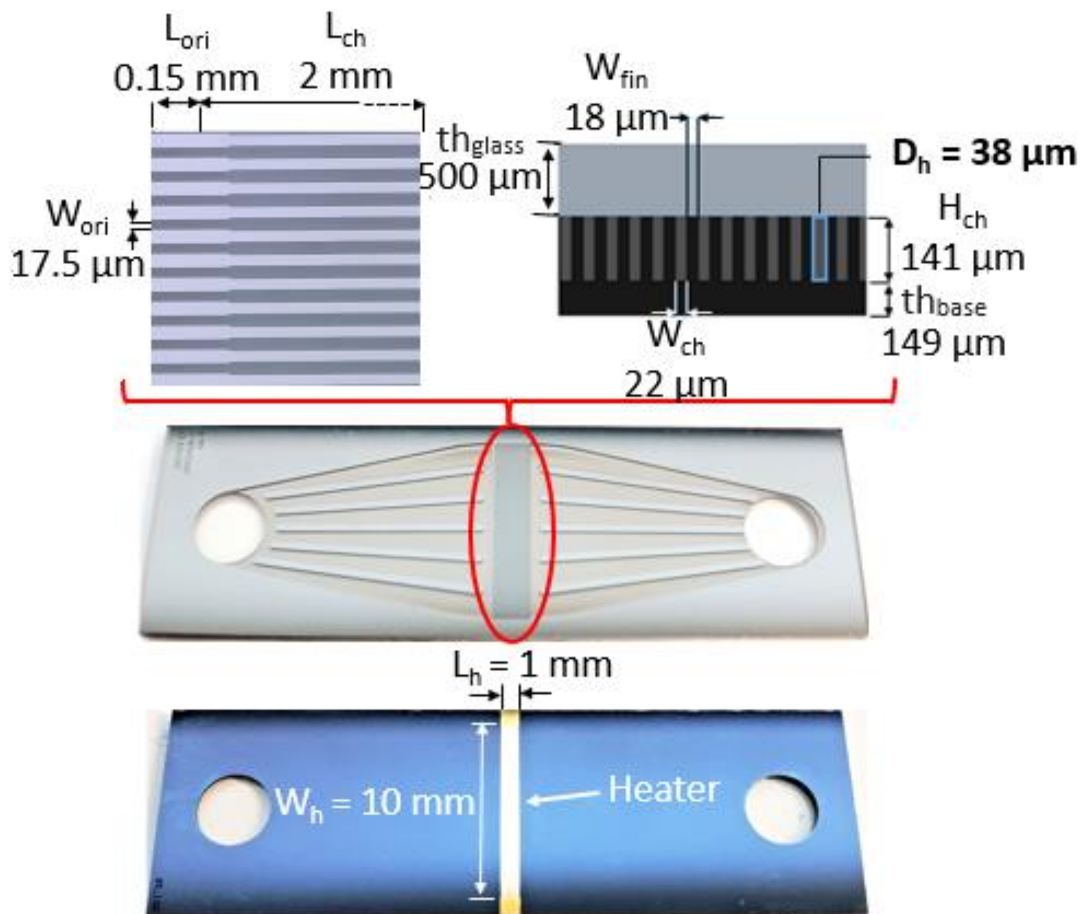

Figure 3-3. Detailed dimensions of 38 μm hydraulic diameter, silicon, microchannel evaporator investigated in this effort.

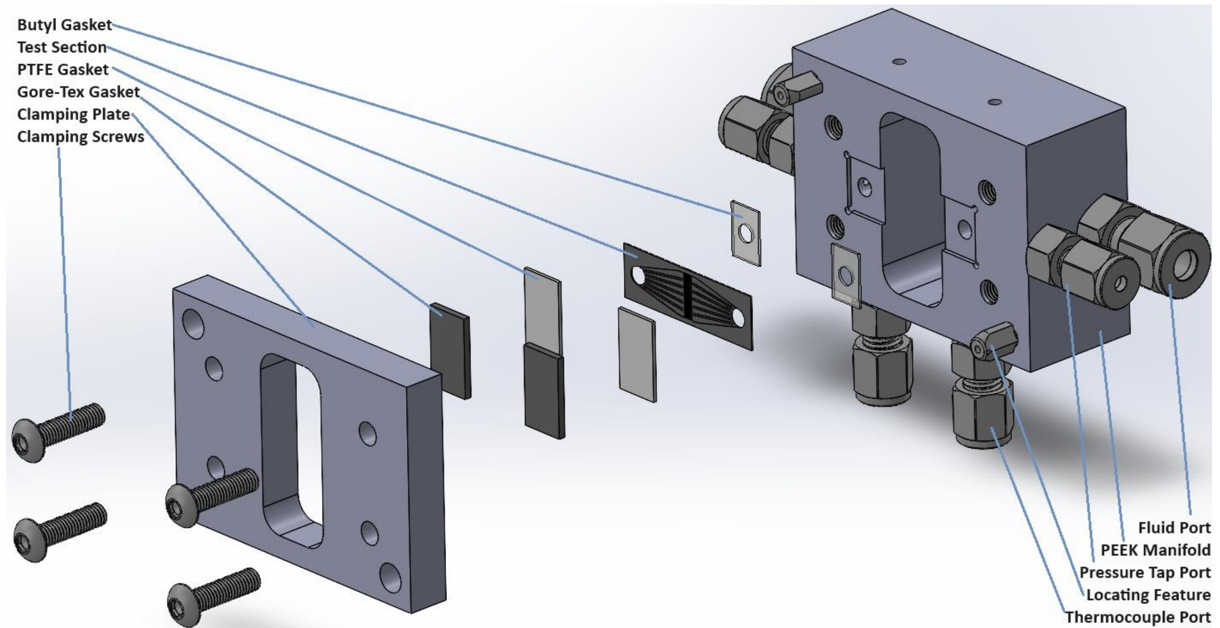

Figure 3-4. Exploded schematic of fluidic interface manifold for 38 µm test section.

electrically interfaced using the same electrical harness designed and fabricated by Bevis [12]. This electrical harness made it simple to determine the electrical resistance-temperature relationship of the second test section heater which was used to measure the temperature of that device. The details of that method will be discussed later in this chapter.

3.1.2. Testing Facilities

Two test facilities were used in this work. The first one was the legacy two-phase pumped loop facility built in Bevis [12] and updated in Richey [17] to accommodate transient testing on the 52 µm microchannel test section. However, based off the observed transient behaviors, a new test facility was designed and built to better accommodate the transient perturbations to the system, streamline the data collection process, and improve the overall operability of the system. Both testing facilities will be discussed here.

3.1.2.1. Legacy Two-Phase Pumped Loop Test Facility

The testing facility used for the 52 µm microchannel test section was based on the work of Bevis [12], with updates for transient testing provided by Richey [17]. A detailed schematic along

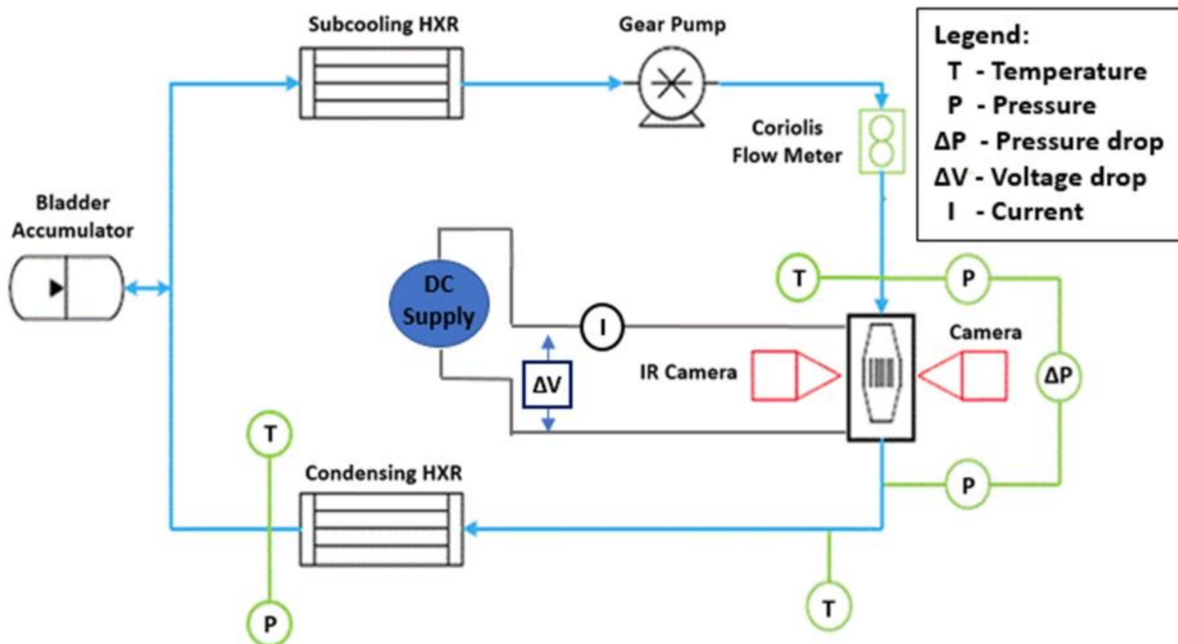

Figure 3-5. Simplified schematic of legacy testing facility from [62].

with the equipment is contained within Bevis, but a simplified schematic which was published in Anderson et al. [62] with the important updates and is shown in Figure 3-5 will be described here to highlight the changes made. Prior to testing, the facility was evacuated to remove air bubbles and then was filled with liquid R134a. A positive displacement pump (GA-T23, Micropump Inc, WA) circulated the fluid while the mass flow rate was monitored by a Coriolis flow meter (RHM015L, Rheonik, Germany) just upstream of the test section. The refrigerant was condensed and subcooled below the inlet saturation temperature to the appropriate degree using two plate heat exchangers (HXP-193 Rev. 2, Koolance, WA) and monitored using a calibrated K-type thermocouple. The test section inlet pressure (and subsequently saturation temperature) was set using a bladder accumulator (A1QT3100B, Accumulators Inc, TX) by adjusting the compressed nitrogen side and was monitored by an upstream pressure transducer, while pressure drop through the test section was measured using a differential pressure transmitter (all pressure transmitters: PX409 series, Omegadyne Inc, OH). The heat load was applied by varying the electrical voltage

with a programmable power supply (N8735A, Keysight, CO). The test section temperature was measured at a frame rate of 120 Hz using a calibrated infrared (IR) camera (TIM160, Micro-Epsilon, Germany). To monitor flow conditions, a microscopic camera (AF7915MZT, Dino-Lite, CA) synchronized to start simultaneously with the IR camera, was used to view the channels through the borosilicate glass at a rate of 20 Hz and a resolution of 640 x 480 pixels with an on-axis LED ring light. Temperature, pressure, mass flow rate, and power measurements were obtained using a cDAQ-9174 with appropriate measurement modules (National Instruments Inc, TX). A custom LABVIEW program collected data from the DAQ at a frequency of 5 Hz.

3.1.2.2. Transient Two-Phase Pumped Loop Test Facility

As mentioned above, because the first test facility was difficult to maintain at the desired testing conditions and had a sluggish response, an updated facility was designed and built with

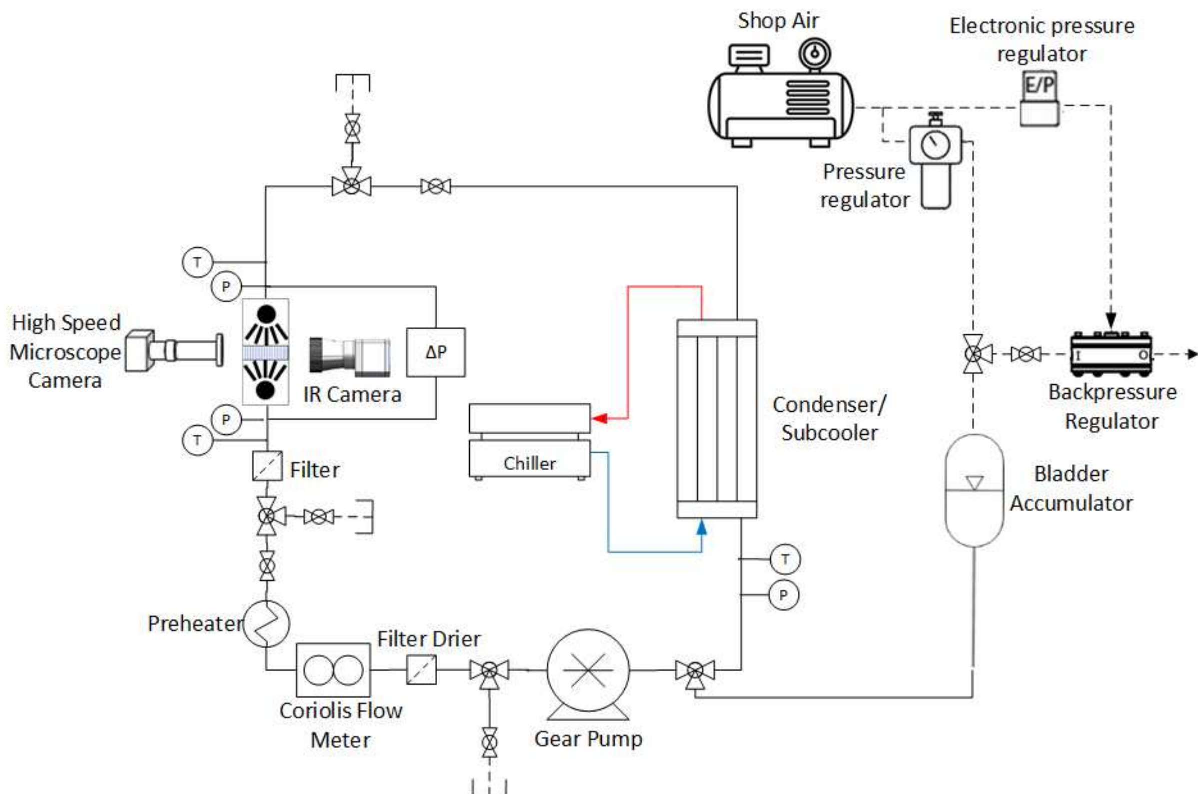

Figure 3-6. Schematic of updated transient two-phase pumped loop testing facility.

active feedback control to improve transient performance and workflow. Active control was achieved using the tuning approach described in Shamssuzzoha [63]. The test facility is shown schematically in Figure 3-6 and as-built in Figure 3-7. A gear pump (GA-V21, Micropump, WA)

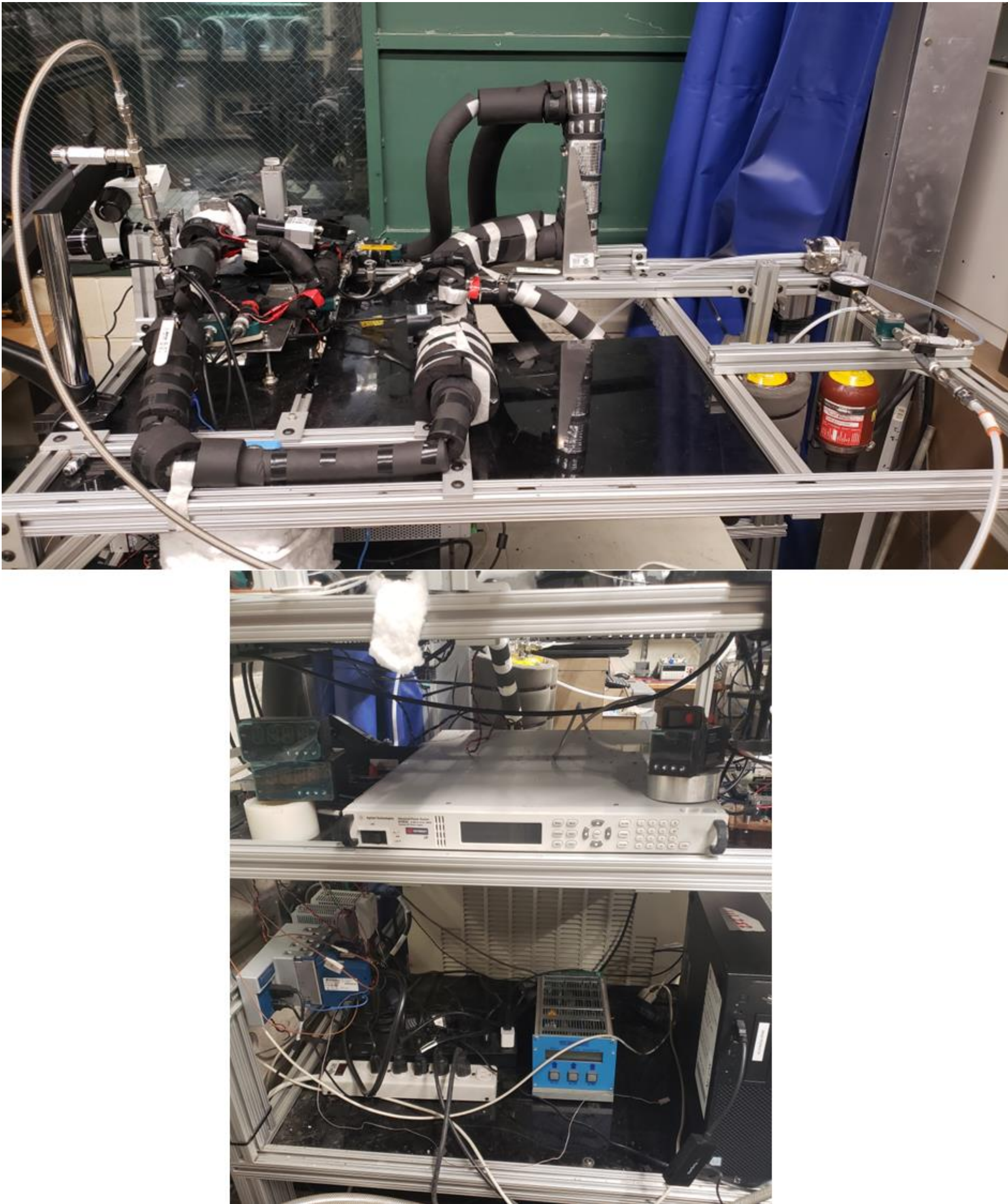

Figure 3-7. Updated transient two-phase pumped loop testing facility and associated controls.

with an EagleDrive motor (DEMSE, Micropump, WA) was used to circulate the refrigerant. A Coriolis flow meter (RHM015L, Rheonik, Germany) measured the mass flow rate and provided feedback to an Omega Platinum controller (CN32PT-305, Omegadyne, OH) which controlled the pump speed to maintain the mass flow rate at the desired setpoint. The degree of refrigerant subcooling below the saturation temperature was controlled with an inline fluid preheater (FLUENT FLC-2, WATLOW, MO) and another Omega Platinum controller using feedback from a T-type thermocouple probe installed at the inlet of the test section.

A refrigerant filter-drier and a 2 μm stainless steel mesh filter were installed upstream of the test section to remove contaminants and moisture from the fluid. There were upstream and downstream T- and K-type temperature and pressure sensors as well as a differential pressure transmitter at the inlet and outlet of the test section (all sensors same models as used in legacy facility). A video camera (PL-D753, Pixelink, NY) with a Navitar modular microscope lens and a thermal camera (PI640i, Optris, Germany) with microscope optics were used to simultaneously record test section temperature and observe the fluid dynamics in the channel at a rate of 125 Hz (the maximum frame rate of the thermal camera). Synchronicity between the cameras and power supply was achieved using an Arduino-based switch with an N-channel MOSFET and is detailed in APPENDIX A. The boiling fluid was then condensed and subcooled via a single, large, plate heat exchanger (GBS400H-10, Kelvion, KY).

The system pressure was maintained using a bladder accumulator (A1QT3100B, Accumulators Inc, TX). The air-side pressure of the accumulator was set at a baseline using regulated shop air. Then, an Equilibar backpressure regulator (LF2, Equilibar, NC) loaded via an electronic pressure regulator (QPV2, Equilibar, NC) was teed in at the inlet of the accumulator air-side. The QPV2 was controlled by another Omega Platinum controller with feedback from the test

section inlet pressure transducer and exhausted air from the regulated shop air line using the backpressure regulator as necessary to control the inlet pressure to the test section. Power to the test section heater was delivered via a high-accuracy (<0.1%), programmable DC power supply (N7953A, Keysight, CO). A National Instruments cDAQ-9174 was used to collect measurements from the system sensors. The system was controlled and monitored with a custom LabVIEW program running at 125 Hz, the same frequency as the thermal camera and the microscope camera.

3.1.3. Experimental Testing Procedure and Test Matrix

3.1.3.1. Testing Procedure and Test Matrix for 52 µm Test Section

For the legacy test facility, the system chiller was first turned on to allow fluid to condense. Once enough fluid was condensed to liquid as indicated by the sight glass between the subcooler and pump suction line, the pump was powered on, and the potentiometer dial on the motor was adjusted until the flow rate met the nominal value. The relative proportion of flow through both heat exchangers was adjusted using a fine needle valve along with the chiller temperature to set

Table 3-1. Transient heat load test matrix for 52 µm microchannel evaporator

Condition	Value
P_{in} [kPa]	572
$T_{sat,in}$ [°C]	20
$T_{f,in}$ [°C]	15
$\Delta T_{sub,in}$ [°C]	5
$\dot{m}$ [g/min]	50
q [W]	15 25 36 39 43
Ramp rate [W/s]	4 9.5 29 50

the inlet fluid temperature to the test section. Then, the system pressure was set by adjusting the shop air-line pressure to the accumulator using the wall pressure regulator. The fluid conditions were considered to have reached steady state when they varied by no more than their uncertainty estimate over a one-minute period. Once steady state conditions were reached, transient testing commenced. Heat was applied in two ways: in a stepped heat load from 0 to the max value, and in a linearly ramped profile with different ramping rates applied as a sequence of small steps. The test matrix is shown in Table 3-1.

3.1.3.2. Testing Procedure and Test Matrix for 38 µm Test Section

The 38 µm microchannel evaporator was tested in the new transient test facility. The chiller was first powered up to condense and subcool liquid upstream of the pump suction. Once the entirety of the fluid in this line was liquid, the flow rate setpoint was set, and the pump was turned on. After the flow rate stabilized, the accumulator control was initiated by opening the shop air line and then setting the inlet pressure setpoint to the desired value. Once stabilization was reached with the pressure control, the preheater temperature was set, and the preheater control was initiated to hit the target inlet subcooling. Then, once the system was stabilized and reached a steady state,

Table 3-2. Stepped heat load test matrix for 38 µm microchannel evaporator

Condition	**Value**
$P_{in.ch}$ **[kPa]**	572
$T_{sat,in}$ **[°C]**	20
$T_{f,in}$ **[°C]**	10,15,17.5
$\Delta T_{sub,in}$ **[°C]**	2.5,5,10
$\dot{m}$ **[g/min]**	50,75,100
q **[W]**	24,26,29,31,33,35, 40,45,50,55,60,65,70

once again defined as values changing less than their uncertainty estimates (or within the margin of error of the system controllers), the transient testing was initiated. Heat loads were initiated as a step function from 0 to maximum heat duty by varying the voltage of the power supply. The test matrix shown in Table 3-2 was run based on heating conditions which resulted in two-phase conditions for the given subcooling and flow rate, so not all combinations of conditions were tested. For testing variations in flow rate, a subcooling of 5°C was maintained, while for testing variations in inlet subcooling, a flow rate of 50 g/min was used.

3.1.3.3. Inlet Pressure Correction for 38 μm Test Section

Because flow rate and subcooling were parametrized for this device, there was a change in pressure drop from the inlet pressure measurement spot and the actual inlet of the channel due to the orifice and complex fluid routing through the inlet plenums. Therefore, to keep inlet conditions to the channel consistent, the pressure drop was estimated through this inlet region, and the actual inlet pressure was set by adding the pressure drop to the 572 kPa which resulted in a 20°C saturation temperature at the inlet of the channel:

$$P_{in} = \Delta P_{upstr} + P_{in,ch}(T_{sat} = 20°C). \tag{3-1}$$

To calculate the pressure drop in the complex plenum and inlet restrictor region, the following approach was used. There is a short section of the inlet tube from the inlet pressure transducer to the inlet hole of the test section. The fluid makes a 90-degree bend and is contracted from 4 mm to ~190 μm. Then, the fluid is split into 5 channels due to the silicon rib features. Finally, fluid is recombined in a ~191 μm deep by 10 mm wide region before entering the channels. This entire plenum and tube region was modeled in COMSOL MultiPhysics v5.6 using computational fluid dynamics (CFD) to determine the pressure drop at the range of flow rates and inlet temperatures used experimentally, and a representative SolidWorks model of this region is shown in Figure 3-8.

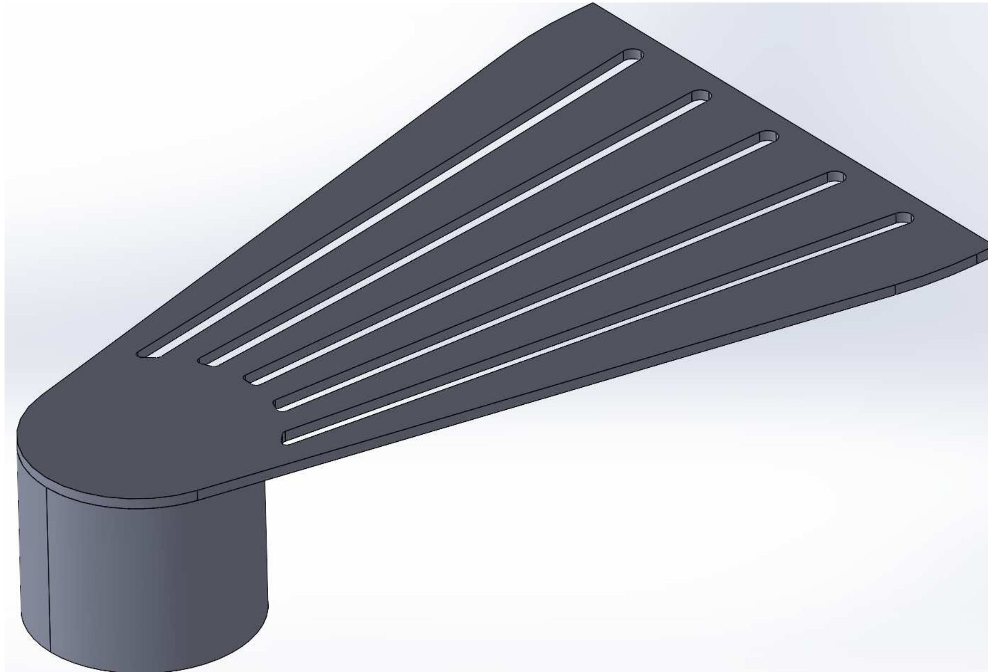

Figure 3-8. SolidWorks model used to calculate inlet plenum pressure drop.

In addition, there is pressure drop in the inlet restrictor due to contraction into the restrictor, frictional losses, and then further expansion into the channel. However, the inlet restriction has a complex depth profile due to gas dynamics behaviors experienced in etching different width features and is discussed in Ref [12]. The only way to measure this depth profile was to destroy the device, so a similar device with the same nominal dimensions was cut down the length of a channel, and the restrictor profile was characterized. The profile as seen by optical microscopy is shown in Figure 3-9. Then, another separate model was created in COMSOL consisting of the restrictor and the channel, and the combined pressure drop through the inlet restrictor was

Table 3-3. Inlet pressure transducer setpoints (in kPa) to maintain 20°C channel inlet saturation temperature (572 kPa).

Mass Flow Rate [g/min]	**Inlet Temperature [°C]**		
	10	**15**	**17.5**
50	576.1	576	575.97
75	579.7	N/A	N/A
100	584.4	N/A	N/A

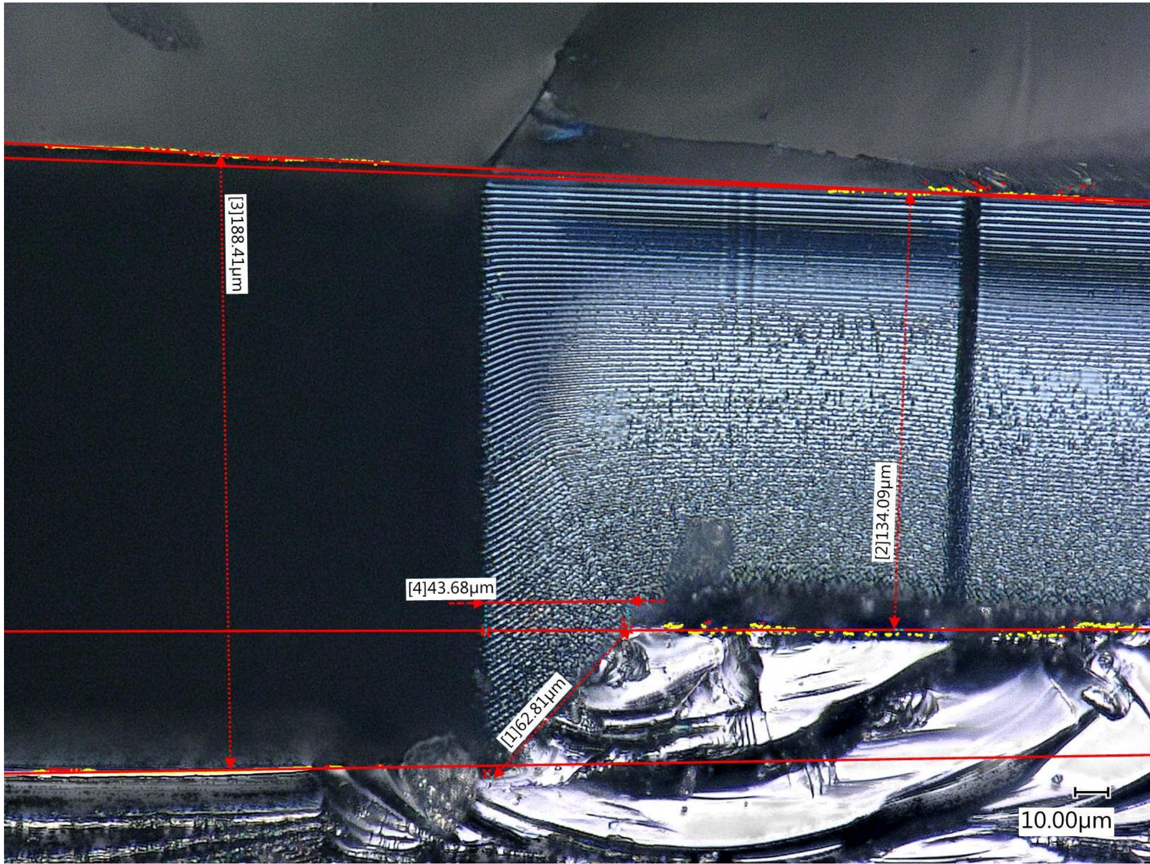

Figure 3-9. Magnified optical microscopy image of inlet restrictor complex depth profile.

calculated for the same inlet flow and temperature conditions. The plenum and inlet restrictor pressure drop were then summed to determine the necessary inlet pressure transducer pressure setpoint for the channel inlet to result in a 20°C saturation temperature. The details of the models, including the CFD approach, the mesh sensitivity study, and representative profiles are found in Appendix C. The calculated inlet pressures for the given flow and inlet temperature conditions are given in Table 3-3. When uncertainties are propagated, a 20% uncertainty was enforced on these pressure drop corrections due to the potential for geometric uncertainty.

3.1.4. Uncertainties and Calibrations

Uncertainties are inherent in any experimental setup and are quantified here. In addition, calibration procedures used for the heater temperature measurements are also discussed. Experimental uncertainties generally consisted of measurement uncertainties, and when multiple

measurements were made, also included statistical uncertainties, which were summed together using the root-sum-square method for an average measurement $\bar{X}$:

$$\delta_{\bar{X}} = \sqrt{\delta_{meas}^2 + \delta_{stat}^2}. \quad (3\text{-}2)$$

Measurement errors included device uncertainties given by either the manufacturer or from a calibration procedure. When functional relationships between variables were used, the error is propagated according to the root-sum-square truncated Taylor series approach [64]

$$\delta_{\bar{X}} = \sqrt{\sum_i \left(\frac{\partial \bar{X}}{\partial x_i}\delta_{x_i}\right)^2}. \quad (3\text{-}3)$$

When statistical uncertainties were appropriate, the statistical uncertainty was calculated according to

$$\delta_{stat} = \frac{t_{stat}S}{\sqrt{N_{samples}}}, \quad (3\text{-}4)$$

where $t_{0.005}$ corresponds to a two-tailed t-statistic for a 99% confidence interval and S is the sample standard deviation. The sample standard deviation is normalized by the number of samples and is also known as the standard error.

3.1.4.1. Uncertainties for 52 µm Test Section and Legacy Test Facility

For the legacy test facility and the 52 µm test section, equipment was calibrated and uncertainties in the equipment were detailed in Ref [12]. The infrared camera, which was the upgraded measurement device for the heater temperature, was calibrated in the range of 15-80°C on an area averaged basis against a high-accuracy (±0.012°C), reference resistive temperature detector (RTD) and had a calibrated full-scale temperature accuracy of ±0.3°C [17]. The calculated uncertainties for both measured and derived quantities under the testing conditions in this study are shown in Table 3-4.

Table 3-4. Experimental uncertainties for 52 µm test section and legacy test facility.

Condition	Uncertainty
P_{in}	±0.6 kPa
ΔP	±0.3 kPa
$T_{sat,in}$	±0.03°C
$T_{f,in}$	±0.5°C
$\Delta T_{sub,in}$	±0.5°C
T_h	±0.3°C
$\dot{m}$	<±0.2%
q	±2.6-4.1%

3.1.4.2. Uncertainties for 38 µm Test Section and Transient Test Facility

The new testing facility used new data acquisition modules and additional or new sensors. Therefore, temperature and pressure sensors were recalibrated against high accuracy reference standards, with temperature sensors against the ±0.012°C platinum RTD and pressure sensors against a ±0.025 psi (±0.17 kPa) pressure gauge. In addition, the test section heater electrical resistance was calibrated against the same high-accuracy RTD in a convection oven from 20-90°C. A linearly increasing resistance with temperature was observed, which resulted in the following curve fit

$$T_h\ (°C) = 49.544 R_h(\Omega) - 404.090, \quad (3\text{-}5)$$

with a highly linear relationship defined by a correlation coefficient of 0.99992. A linearly increasing electrical resistance with temperature is consistent with the behavior of commercial platinum RTDs [65]. The resulting temperature uncertainty using a 99% confidence interval of the curve fit root-mean-square error was ±0.34°C. While an infrared camera was also available, measurements with the resistance method were more convenient due to ease of processing and data analysis. The resistance-temperature approach was thus the method of choice for measuring

Table 3-5. Experimental uncertainties for 38 μm test section and transient test facility.

Condition	Uncertainty
$P_{in,ch}$	±0.9-2.5 kPa
ΔP	±0.2 kPa
$T_{sat,in}$	±0.05-0.14°C
$T_{f,in}$	±0.2°C
$\Delta T_{sub,in}$	±0.2-0.25°C
T_h	±0.3°C
$\dot{m}$	<±0.2%
q	±0.1-0.2%

the heater temperature for this test section, as the electrical resistance could be easily calculated from the test section voltage and current using Ohm's Law during testing. Thus, this curve fit was programmed into the LabVIEW code to directly calculate and log the test section temperature. The resulting uncertainties for the 38 μm test section and transient test facility are given in Table 3-5.

3.1.5. Heat Losses

Heat exchange with the ambient is unavoidable in any experimental setting, though attempts may be made to minimize its effect. Due to the small scale of the test device and its containment in a highly-insulating, plastic manifold, heat losses were expected to be small. Nevertheless, the heat losses will be estimated based off the geometry and literature correlations for convective and radiative heat loss to fully encompass the experimental approach. Due to differences in peak temperatures and the test section geometries across the two different devices, heat losses will be calculated separately for each device.

Convective and radiative heat losses were calculated for both the heater side as well as the exposed fluid side of the device and then summed to get a net heat transfer to the ambient for each device. The heater was treated as an isothermal, vertical plate for literature correlation purposes. On the fluid side, the area used was the exposed fluid area in the channels, with the fins assumed

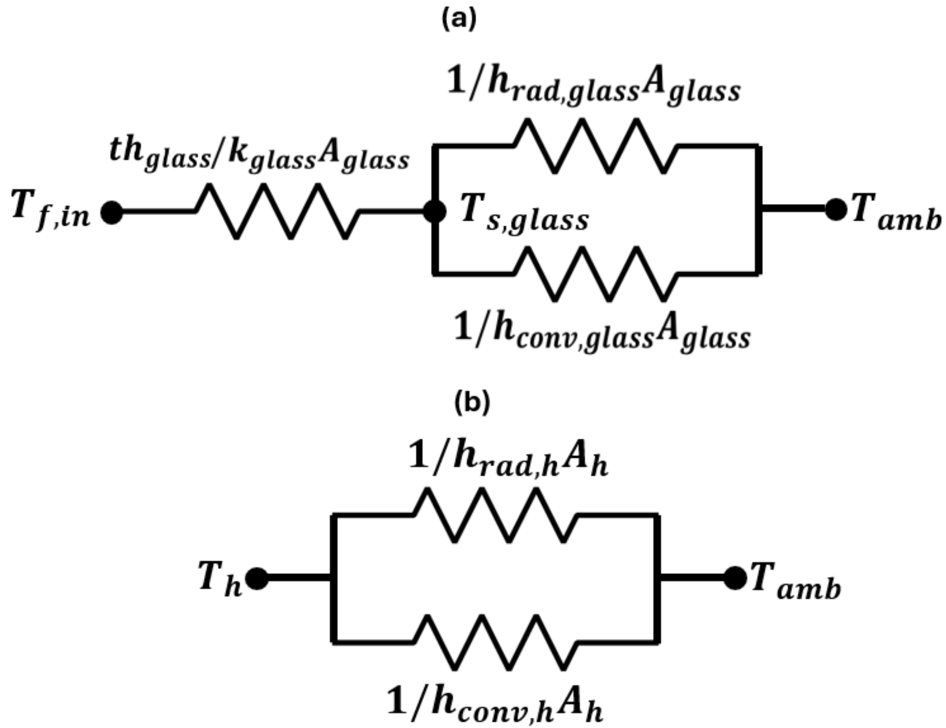

Figure 3-10. 1D thermal resistance loss networks from (a) the fluid side and (b) the heater side.

insulated. There was a 500 µm thick borosilicate glass cap on this side, so conductive heat transfer was also considered. A quasi-steady 1D thermal resistance network as shown in Figure 3-10(a) and (b) was used to estimate the losses. Due to the small channel geometries and large area enhancement, the inner fluid convective thermal resistance was neglected. The glass outer surface temperature was unknown, so an additional thermal resistance energy balance was used to solve for it. The peak temperature measured for each device was used to provide an upper bound for the losses, which from the above thermal resistance networks were calculated according to the following equations, defining heat flow to be away from the test section

$$q_{loss,glass} = \frac{T_{f,in} - T_{amb}}{\frac{th_{glass}}{k_{glass}A_{glass}} + \frac{1}{(h_{conv,glass} + h_{rad,glass})A_{glass}}} \tag{3-6}$$

$$\frac{T_{f,in} - T_{glass}}{\frac{th_{glass}}{k_{glass}A_{glass}}} = \frac{T_{glass} - T_{amb}}{\frac{1}{(h_{conv,glass} + h_{rad,glass})A_{glass}}} \tag{3-7}$$

$$q_{loss,h} = (h_{conv,h} + h_{rad,h})A_h(T_h - T_{amb}) \quad (3\text{-}8)$$

$$q_{loss,net} = q_{loss,glass} + q_{loss,h}. \quad (3\text{-}9)$$

The convective and radiative heat transfer coefficients were calculated according to [66]

$$h_{conv,x} = \left[0.68 + \frac{0.67Ra_x^{1/4}}{(1 + (0.492/Pr_x)^{9/16})^{4/9}}\right]\frac{k_{air,x}}{L_h} \quad (3\text{-}10)$$

$$h_{rad,i} = \varepsilon\sigma(T_x^2 + T_{amb}^2)(T_x + T_{amb}), \quad (3\text{-}11)$$

where *Ra* is the Raleigh number, *Pr* is the fluid Prandtl number, ε is the surface emissivity (set to 1 to overestimate losses), and σ is the Stefan-Boltzmann constant. All fluid properties of the air were evaluated at the film temperature $T_{film} = (T_x + T_{amb})/2$, where *x* corresponds to either the glass or heater surface temperature. Table 3-6 lists the values for the inputs and resulting outputs. The negative heat loss values reflect heat gain from the ambient due to the convention in which

Table 3-6. Heat loss parameters for both test sections.

Parameter	38 µm	52 µm
$T_{f,in}$ [K]	283	288
T_{amb} [K]	294	294
T_h [K]	391	344
T_{glass} [K]	289	288
th_{glass} [m]	$5.00\text{x}10^{-4}$	$5.00\text{x}10^{-4}$
k_{glass} [W/m-K]	1.20	1.20
A_{glass} [m^2]	$1.10\text{x}10^{-5}$	$8.52\text{x}10^{-6}$
A_h [m^2]	$1.00\text{x}10^{-5}$	$1.00\text{x}10^{-5}$
$h_{conv,glass}$ [W/m^2-K]	4.00	3.53
$h_{conv,h}$ [W/m^2-K]	6.71	5.83
$h_{rad,glass}$ [W/m^2-K]	5.46	5.60
$h_{rad,h}$ [W/m^2-K]	9.31	7.42
$q_{loss,h}$ [W]	$1.56\text{x}10^{-2}$	$6.61\text{x}10^{-3}$
$q_{loss,glass}$ [W]	$-1.15\text{x}10^{-3}$	$-4.74\text{x}10^{-4}$
$q_{loss,net}$ [W]	$1.44\text{x}10^{-2}$	$6.14\text{x}10^{-3}$

heat flow was defined. The net heat loss from the test sections was smaller than or comparable to the uncertainty of the measurement equipment and was thus neglected in this study. In addition, the small heat gain from the ambient on the fluid side due to the glass cap justified the insulated tip fin assumption.

3.2. Computational Methods and Setup

This section details the computational tools used in the current investigation to develop the transient, microchannel, flow boiling models in Chapters 5 and 6. In addition, the PCM model setup and semi-empirical approach used to apply the simulated PCM heating effect will also be discussed.

3.2.1. ParaPower-NavyHHF Computational Design Tool

Two separate computational design tools were developed and combined to take advantage of the specific features of each. ParaPower is a 3D centered finite difference software, shown in

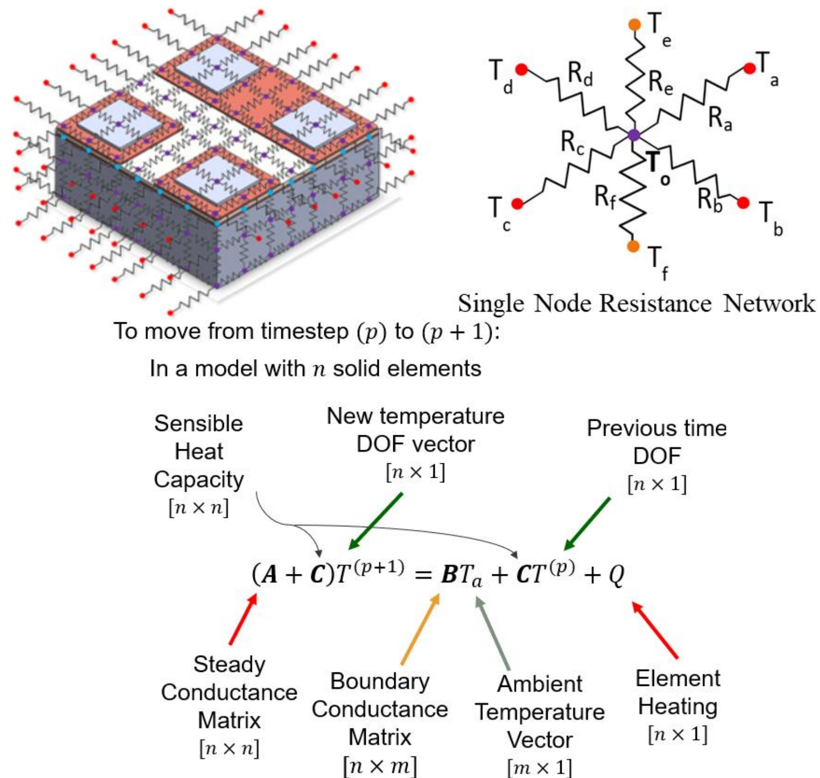

Figure 3-11. ParaPower thermal resistance network in matrix form from [66–68].

Figure 3-11, developed in a collaboration by the DEVCOM Army Research Lab and Texas A&M University for rapid parametric analysis of heat transfer in power electronics packages [67–69]. ParaPower includes a validated phase change material (PCM) modeling component to evaluate the impact of including such materials into power electronics packaging architectures. The tool offers the flexibility of defining geometry, materials, and custom boundary conditions from either a graphical user interface or at the script level and was built in MATLAB.

The second computational tool used was NavyHHF which was originally a subcomponent library in a broader system analysis tool called ATTMOsphere, developed by PC Krause and Associates for dynamic system-level Size, Weight, and Power (SWaP) analysis studies [70]. The software was built in a Simulink-MATLAB interface to take advantage of the block-based programming architecture along with MATLAB's built-in ordinary differential equations solvers. NavyHHF offered component level thermal analysis using a 1D, finite volume-based, reduced-order, fluid solver to calculate fluid state points such as temperature, pressure, and heat transfer over a wide range of possible fluids and conditions. While full systems could be modeled, for the purposes of this work, only the two-phase cold plate was modeled with appropriate flow boundary conditions (inlet temperature, mass flow rate, outlet pressure) imported from the experiments to

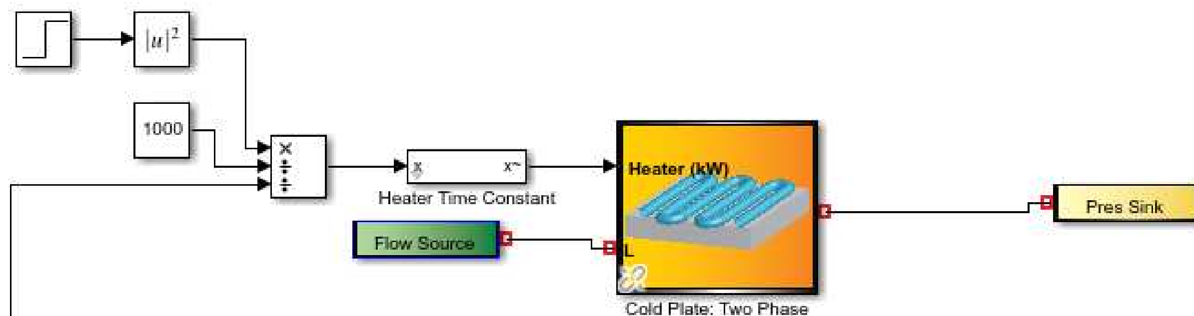

Figure 3-12. Sample simplified block diagram for NavyHHF-ParaPower two-phase cold plate and boundary conditions.

simplify the computational effort. Figure 3-12 displays a sample block-system of the modeled two-phase cold plate.

Because ParaPower provides in-depth solid heat transfer and PCM modeling, and NavyHHF provides in-depth fluid state modeling, both softwares were combined to create the ParaPower-NavyHHF tool which was utilized in this work. The computational approach for these models is described in detail below for a discretized network in the flow direction and shown schematically in Figure 3-13. The reduced order mass, momentum, and enthalpy balances were given for each discrete control volume *N* as

$$\frac{d\dot{m}}{dt} = \frac{\dot{m}_{in}v_{in} - \dot{m}_{out}v_{out}}{\Delta N} + \frac{A_c(P_{in} - P_{out})}{\Delta N} - \frac{f_f\dot{m}_{out}v_{out}}{2D_h} \tag{3-12}$$

$$\forall\left[\frac{\partial\rho}{\partial P}\frac{dP}{dt} + \frac{\partial\rho}{\partial i}\frac{di}{dt}\right] = \dot{m}_{in} - \dot{m}_{out} \tag{3-13}$$

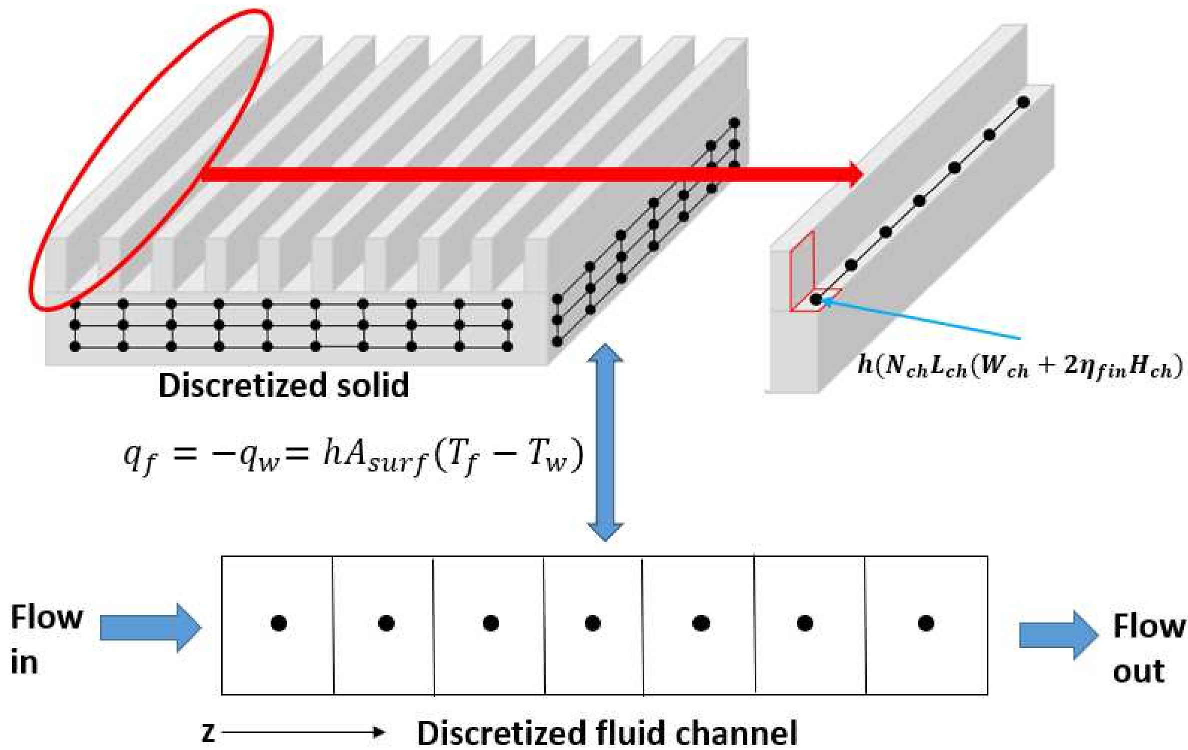

Figure 3-13. Schematic for discretized solid and fluid with energy balance at interface and fin efficiency approach.

$$\forall\left[\left(i\frac{\partial\rho}{\partial P}-1\right)\frac{dP}{dt}+\ \left(i\frac{\partial\rho}{\partial i}+\rho\right)\frac{di}{dt}\right]=\ \dot{m}_{in}i_{in}-\dot{m}_{out}i_{out}-q_f, \tag{3-14}$$

where the heat transfer to the fluid q_f was calculated according to an energy balance at the solid-fluid interface at each volume N as

$$q_f=-q_w=hA_{surf}(T_f-T_w) \tag{3-15}$$

This energy balance was also used as the boundary condition for the solid heat transfer on the ParaPower side of the model to determine the equivalent wall temperature at the given boundary. Fins were modeled implicitly using a fin efficiency approach with insulated tip fin which was justified in Section 3.1.5:

$$A_{surf}=N_{ch}L_{ch}(W_{ch}+2\eta_{fin}H_{ch}) \tag{3-16}$$

$$\eta_{fin}=\frac{\tanh\left(m_{fin}H_{ch}\right)}{m_{fin}H_{ch}} \tag{3-17}$$

$$m_{fin}=\sqrt{\frac{2h}{k_{fin}th_{fin}}}. \tag{3-18}$$

The heat transfer coefficient was calculated using literature correlations for fully-developed, laminar flow in rectangular ducts [71]

$$h_{sp}=8.235(1-1.833\beta+3.767\beta^2-5.814\beta^3+5.361\beta^4-2\beta^5)\frac{k_f}{D_h} \tag{3-19}$$

The two-phase heat transfer coefficient is calculated using the Kim and Mudawar correlation [14]

$$h_{tp,km}=(h_{nb}^2+h_{cb}^2)^{0.5} \tag{3-20}$$

$$h_{nb}=\left[2345\left(Bo\frac{PH}{PW}\right)^{0.7}\left(\frac{P}{P_{crit}}\right)^{0.38}(1-\chi)^{-0.51}\right]h_{DB,l} \tag{3-21}$$

$$h_{cb}=\left[5.2\left(Bo\frac{PH}{PW}\right)^{0.08}We_{lo}^{-0.54}+3.5\left(\frac{1}{X_{tt}}\right)^{0.94}\left(\frac{\rho_l}{\rho_v}\right)^{0.25}\right]h_{DB,l} \tag{3-22}$$

Table 3-7. Material properties of solids used in NavyHHF models.

Material	k [W/m-K]	c_p [J/kg-K]	ρ [kg/m^3]
Silicon	$0.00141T^2$-$0.676T+160$	$9.38E$-$5T^3$-$0.0188T^2+1.96T+669$	2329
Silica (SiO2)	1.3	680	2170
Platinum	72.7	134	21424

$$h_{DB,l} = 0.023 Re_l^{0.8} Pr_l^{0.4} \frac{k_l}{D_h} \tag{3-23}$$

$$Bo = \frac{q''_w}{G_{ch} i_{lv}}, Re_l = \frac{(1-\chi) G_{ch} D_h}{\mu_l}, We_{lo} = \frac{G_{ch}^2 D_h}{\rho_l \sigma}, X_{tt} = \left(\frac{\mu_l}{\mu_v}\right)^{0.1} \left(\frac{1-\chi}{\chi}\right)^{0.9} \left(\frac{\rho_v}{\rho_l}\right)^{0.5}. \tag{3-24}$$

Because this correlation is dependent on the local wall heat flux which is in turn dependent on the heat transfer coefficient, an iterative approach is needed to determine the final heat transfer coefficient. A modified bisection method was used in the software to guarantee iterative convergence.

3.2.2. Model Setup and Configuration

The model domain was created using the silicon substrate base with fluid domain and embedded fins, a 1 µm thick layer of silicon dioxide electrically passivating the silicon surface, and the ~0.2 µm thick heater. An example of the computational domain is shown in Figure 3-14. The fluid domain is shown in blue while the silicon is shown in purple, and the heater is shown in red. Solid properties for these materials are shown in Table 3-7, where the thermal conductivity of silicon was obtained from Ref [72] and other properties were obtained from Engineering Equation Solver [73].

Boundary conditions were needed for each model and were determined from the experimental operating conditions. The heat load from the experiment for the nominal testing conditions was applied to the test section heater as a step heat load. To correct for the finite power supply switch-on time and differences in how Simulink applies a step function, a low pass filter

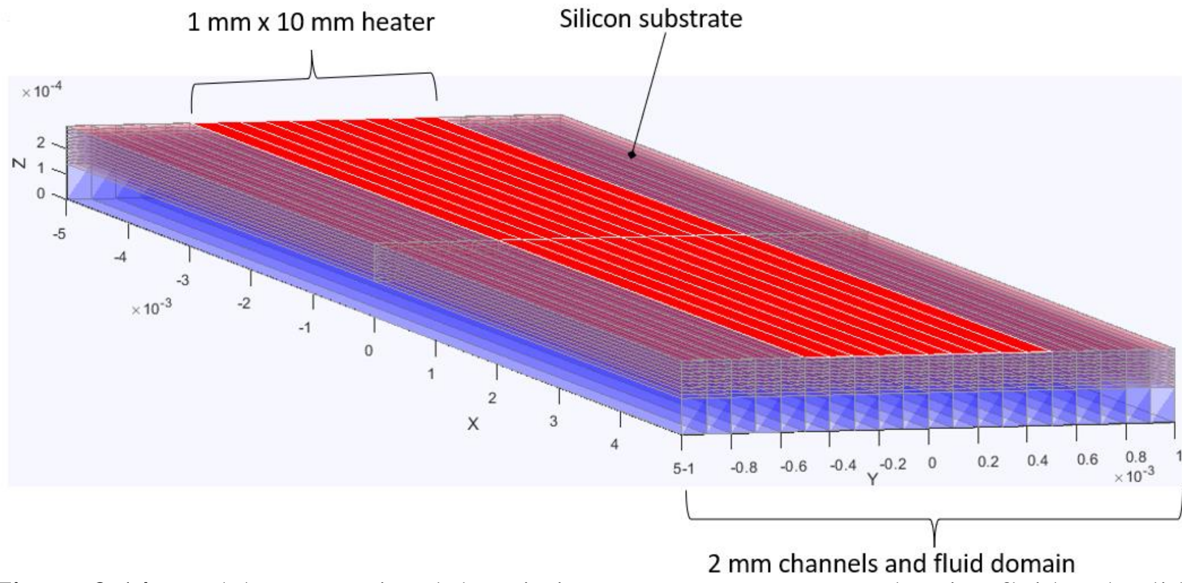

Figure 3-14. Model computational domain in NavyHHF-ParaPower showing fluid and solid regions and select dimensions.

time constant was applied to the heat load and was adjusted as needed based on the power supply used and heat load level. Heater time constants ranged from about 1/(4π) to 1/(22π) but would need to be adjusted manually for a given test section, power supply, and power level. For the 38 μm test section, because the temperature-resistance relationship had been characterized, the stepped heat load to that test section was applied using Ohm's Law with the experimental measured voltage to the test section and with the calculated electrical resistance from the average heater temperature for that time step. A mass flow inlet and pressure outlet were provided to the model using built-in blocks as shown in Figure 3-15. The inlet temperature was also set here. For the 38 μm test section, like with the inlet pressure, due to the downstream plenum region between the channel outlet and the pressure transducer, a pressure drop correction was calculated using another similar plenum model in COMSOL and a literature correlation for expansion pressure drop out of microchannels into a plenum [74]. This is also detailed in APPENDIX B. Finally, MATLAB's built-in, adaptive time step, differential equation solver `ode23tb` was used to integrate all equations in time due to its guaranteed convergence for computationally stiff problems where the solution

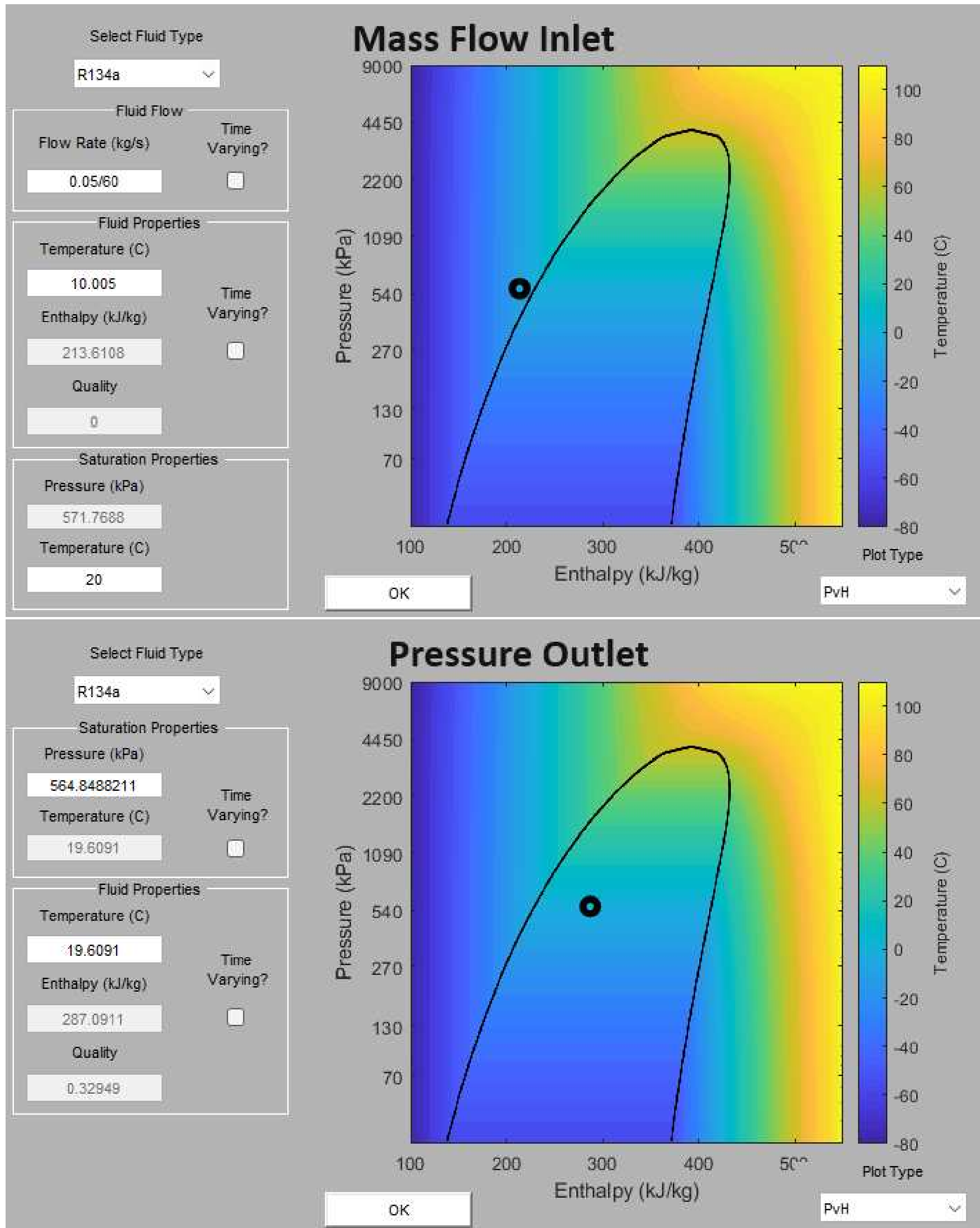

Figure 3-15. Inlet and outlet boundary condition block dialog boxes for model fluid domain.

changes quickly and would otherwise force the time step to tiny values with other solvers. Mesh Sensitivity Study

Mesh sensitivity studies were necessary to determine the effect of discretization error on the solution temperatures. A separate sensitivity study was conducted for each test section.

Table 3-8. Mesh sensitivity study for 52 μm evaporator at 43 W.

Nz	Nx	Ny (flow CVs)	$T_{h,ss}$	% Diff from Finest
3	1	20	33.38	1.213
6	1	20	33.57	0.651
9	1	20	33.64	0.444
6	**2**	**20**	**33.58**	**0.621**
9	2	20	33.65	0.414
6	3	20	33.58	0.621
6	2	12	33.25	1.598
6	2	30	33.72	0.207
9	3	30	33.79	--

3.2.2.1. Mesh Sensitivity for 52 μm Test Section

The mesh sensitivity study for this device was determined using the steady state two-phase flow boiling heater temperature for the highest heat load tested which was 43 W. The mesh study was conducted by modifying the number of nodes in the x, y, and z-directions. As seen in Figure 3-14, the y-direction corresponded to number of flow control volumes (CVs), while in the x- and z-directions corresponded to number of in-plane lateral and vertical nodes in the silicon substrate The bolded numbers in Table 3-8 were the final values used due to balance between computational

Table 3-9. Mesh sensitivity study for 38 μm evaporator at 55 W.

Nz	Nx	Ny (flow CVs)	$T_{h,ss}$	% Diff from Finest
5	1	20	36.62	1.427
10	1	20	36.85	0.808
15	1	20	36.93	0.592
10	**2**	**20**	**36.86**	**0.781**
15	2	20	36.94	0.565
10	3	20	36.86	0.781
10	2	12	36.78	0.996
10	2	30	37.07	0.215
15	3	30	37.15	--

accuracy and solution time. The temperature difference from the most refined mesh is still less than the uncertainty of the heater temperature.

3.2.2.2. Mesh Sensitivity for 38 µm Test Section

Just like with the other test section, a mesh sensitivity study was also conducted for this device but at 55 W using the steady state, flow boiling heater temperature. The bold data in Table 3-9 are the values used balancing the computational time and the device temperature accuracy, which was still within 0.3°C of the densest mesh and was within the uncertainty of the experimental heater temperature measurement.

3.2.3. PCM Model Configuration and Setup

PCM was modeled in NavyHHF-ParaPower by placing it directly on top of the test section heater and modifying both the material and the geometry. Because the heater was 10 mm wide transverse to the flow direction, the PCM was kept 10 mm wide in this direction. An example PCM with dimensions highlighted is shown in Figure 3-16. In the naming convention for the PCM geometry, the first number represents the thickness of the PCM in the z-direction (in Z mm), the second number represents the length of the PCM in the flow direction (the y-axis) centered on the heater (in Y mm), and the transverse x-direction was not included because this was kept at the

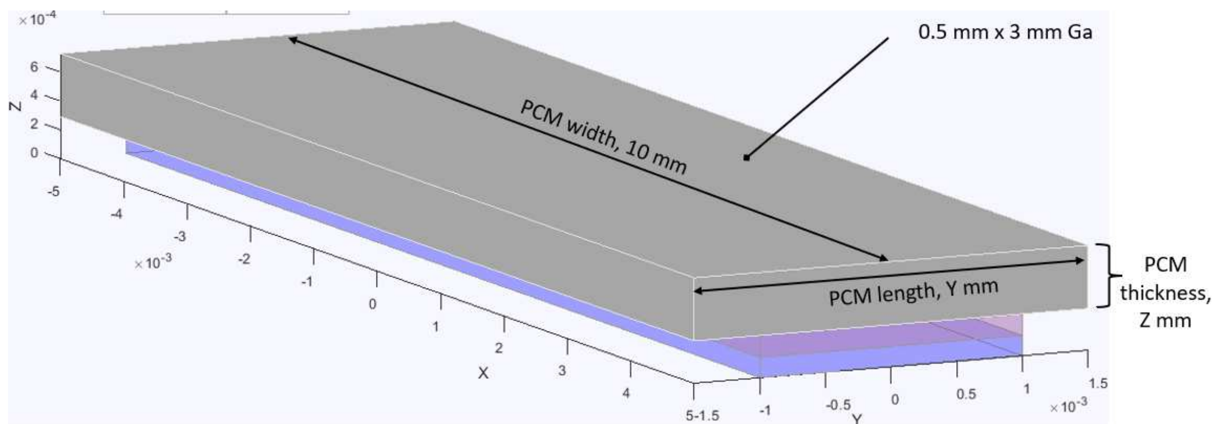

Figure 3-16. Example computational domain and naming convention for PCM study.

constant 10 mm. The PCM Z and Y dimensions were parametrized from 0.4 to 3 mm and from 1 to 3 mm, respectively.

The PCMs used were gallium-based due to gallium's desirably low melting temperature, high latent heat, and relatively high thermal conductivity for a phase change material. Pure gallium (Ga) was compared with selected composite metal foam structures filled with Ga for boosting the thermal conductivity of the material. Copper (Cu) and nickel (Ni) were both considered since copper has a high thermal conductivity (~400 W/m-K), and nickel has been experimentally proven as a practical foam material [33]. Properties of the composite foam structures were calculated using rule of mixture laws or pulled directly from the experimentally measured values, in the case of the Ga/Ni-based foams. Effective density, specific heat, and latent heat of fusion were calculated as follows

$$\rho_{eff} = \phi\rho_{Ga} + (1-\phi)\rho_{foam} \tag{3-25}$$

$$c_{p,eff} = \phi\frac{\rho_{Ga}}{\rho_{eff}}c_{p,Ga} + (1-\phi)\frac{\rho_{foam}}{\rho_{eff}}c_{p,foam} \tag{3-26}$$

$$i_{sl,eff} = \phi\,\frac{\rho_{Ga}}{\rho_{eff}}i_{sl,Ga}. \tag{3-27}$$

where for the latent heat equation the term associated with the metal foam was zero since the metal foam did not reach its melting temperature in these simulations. While the above properties can be easily calculated with a parallel configuration, thermal conductivity is less straightforward since the materials used and the porous structure may uniquely influence the heat flow behavior and may not result in entirely series or parallel configurations. Theoretically, a series configuration will result in the lowest conductivity, while a parallel configuration will result in the highest, for high porosity foams with much higher thermal conductivity than the filling material. To address this, selected formulations for effective porous media thermal conductivity were taken from the

literature, and an average value was calculated. The three general mixture rules are parallel, series, and geometric

$$k_{par} = \phi k_{Ga} + (1-\phi)k_{foam} \tag{3-28}$$

$$k_{ser} = \left(\frac{\phi}{k_{Ga}} + \frac{(1-\phi)}{k_{foam}}\right)^{-1} \tag{3-29}$$

$$k_{geo} = k_{Ga}^{\phi} k_{foam}^{1-\phi}. \tag{3-30}$$

The following four methods have also been proposed in the literature, the Maxwell-Eucken model [75], effective medium theory (EMT) [76], biphasic model [77], and a high porosity, metal foam-specific model weighting parallel and series formulations [78]

$$k_{ME} = k_{foam}\left[\frac{k_{Ga} + 2k_{foam} + 2\phi\left(k_{Ga} - k_{foam}\right)}{k_{Ga} + 2k_{foam} - \phi\left(k_{Ga} - k_{foam}\right)}\right] \tag{3-31}$$

$$(1-\phi)\left(\frac{k_{foam} - k_{EMT}}{k_{foam} + 2k_{EMT}}\right) + \phi\left(\frac{k_{Ga} - k_{EMT}}{k_{Ga} + 2k_{EMT}}\right) = 0 \tag{3-32}$$

$$\left(\frac{k_{bp} - k_{Ga}}{k_{foam} - k_{Ga}}\right)\left(\frac{k_{foam}}{k_{bp}}\right)^{\frac{1}{3}} = 1 - \phi \tag{3-33}$$

$$k_{weight} = 0.35\left(\varepsilon k_{Ga} + (1-\varepsilon)k_{foam}\right) + (1-0.35)\left(\frac{\varepsilon}{k_{Ga}} + \frac{(1-\varepsilon)}{k_{foam}}\right)^{-1}. \tag{3-34}$$

Because there are variations in effective thermal conductivity and latent heat as the porosity of the foam is changed, several different porosities from 60% to 95% were used to explore potential tradeoffs in buffering effect. The effective properties for the simulations are given in Table 3-10, where the naming convention for composite PCMs uses the material name followed by its percentage of the composition.

Table 3-10. Properties of PCM materials investigated in this work.

Property	Ga	Ga80/Cu20	Ga60/Cu40	Ga95/Ni5
k_s (W/m-K)	33.7	70.6	119.7	37.4
k_l (W/m-K)	29.4	65.8	114.7	39.1
$c_{p,s}$ (J/kg-K)	370	375	379.5	371
$c_{p,l}$ (J/kg-K)	397	394	392.5	440
ρ_s (kg/m^3)	5910	6519	7128	6059
ρ_l (kg/m^3)	6095	6638	7239	6233
T_{melt} (°C)	30.2	30.2	30.2	30.2
i_{sl} (J/kg)	80000	58200	39797	72460

3.2.4. PCM Model Mesh Sensitivity

For the initial PCM simulations, a 35.4 W peak heat load was applied using single phase heat transfer in the fluid. The number of layers used in the vertical Z-dimension of the PCM will influence the transient melting behavior. Due to the adaptive time step solver used, the PCM transient effect was not strongly sensitive to the number of Z-nodes used. Nevertheless, a mesh

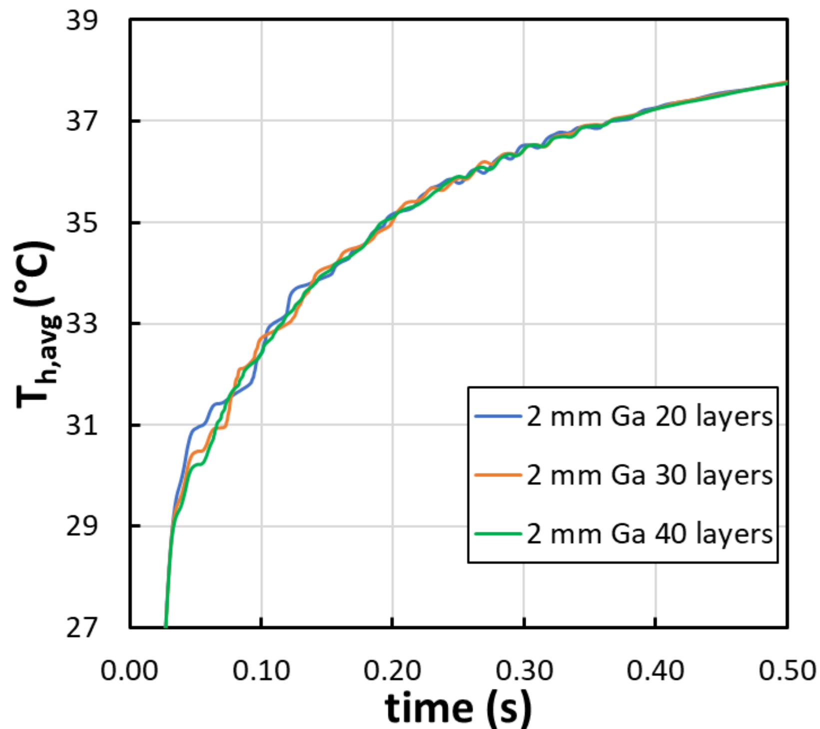

Figure 3-17. Sensitivity effect of number of vertical nodes on 35.4 W heat load and 2 mm thick gallium PCM during initial fast transient temperature rise.

Table 3-11. Mesh sensitivity for number of PCM vertical nodes by thickness.

PCM Thickness [mm]	Number of Vertical Nodes Nz
0.4	6
0.6	8
0.8	10
1	15
2	30
3	40

sensitivity was thus undertaken for each PCM thickness to determine the optimal number of nodes which changed the solution insignificantly relative to the computational demand of the simulation. This study was undertaken for each PCM thickness, and an example is shown here in Figure 3-17 for the 2 mm thick Ga PCM. This figure is magnified to the point where the PCM starts melting. During this transient, the largest differences of ~0.5°C are seen between the 20 and 30 node simulations. Therefore, 30 nodes were used for this thickness. Table 3-11 presents the number of vertical nodes (Nz) for each of the different PCM thicknesses studied here. The number sufficient nodes did not vary significantly with PCM area, so only the thickness was considered here.

3.2.5. Semi-Empirical Parametric PCM Study at 35.4 W

After the mesh sensitivity study was completed, simulations were run for all the considered PCMs at the 35.4 W peak heat load. The predicted transient heat rate to the fluid was extracted from NavyHHF-ParaPower for all the PCM cases and then applied experimentally to the microchannel evaporator as an arbitrary voltage waveform, with resulting transient heat rates shown in Figure 3-18. The black dashed line in Fig. 2 shows the baseline step heat load profile. Since the thermal capacitance of the silicon substrate is extremely low, without a PCM, heat transfer to the fluid is nearly immediate. Thus, using the predicted transient heat rates as the experimentally applied heat load simulates the heating rate experienced by the fluid with the additional thermal capacitance added by a PCM. It should be noted that because the simulations

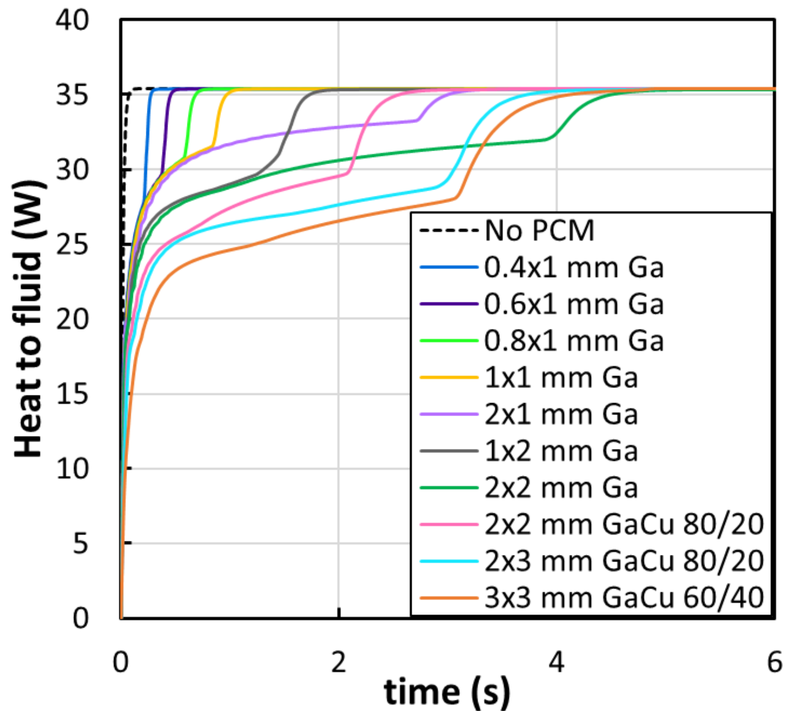

Figure 3-18. Effect of different PCM material and volumes on the effective heat load to the fluid in the 35.4 W peak heat load simulations.

were conducted for single phase only, the heat rate will only be valid prior to boiling. However, any effect the PCM has on the time and temperature for which boiling occurs will be captured and will give insights into possible benefits the PCM may offer at the onset of boiling conditions. It is also apparent that the two cases with the 3 mm long PCM result in strongest amount of thermal buffering. Therefore, it is expected that these two cases will offer the strongest thermal buffering effect.

CHAPTER 4. Preliminary Work Investigating a 52 µm Hydraulic Diameter Silicon Microchannel Evaporator

This chapter details the preliminary work which investigated transient heating and developed a transient boiling model for a 52 µm hydraulic diameter, low thermal resistance, silicon microchannel evaporator. This work was conducted using a testing facility which was originally developed for steady state testing but was modified slightly to accommodate transient heat load testing. Stepped heating and ramped heating results at different power levels will be discussed alongside flow visualization and proposed hypotheses on the observed boiling behavior. The experimental portion of this chapter was published in the ASME Journal of Electronic Packaging in Anderson et al. [62] and most of the images are from that paper. A model using the NavyHHF-ParaPower tool was developed to predict the observed transient behavior for stepped heat loads under the current testing conditions.

4.1. Stepped Heating Results

Stepped heat load experiments were conducted to represent a cold start up on an electronic device. This section describes the transient temperature response along with synchronized flow visualization to a variety of stepped heat loads.

4.1.1. Transient Thermal Response with Flow Visualization

A typical time series of the transient heater temperature exposed to a stepped heat load is shown in Figure 4-1. The heat load was applied as a step function at 0.5 s from 0 to a maximum value of 43 W. The heater temperature rose rapidly due to the step as the liquid R134a underwent sensible heating and reached a maximum of 70.6°C approximately 117 ms later. At this peak, there is a point of inflection, represented by the Onset of Nucleate Boiling (ONB), where the temperature

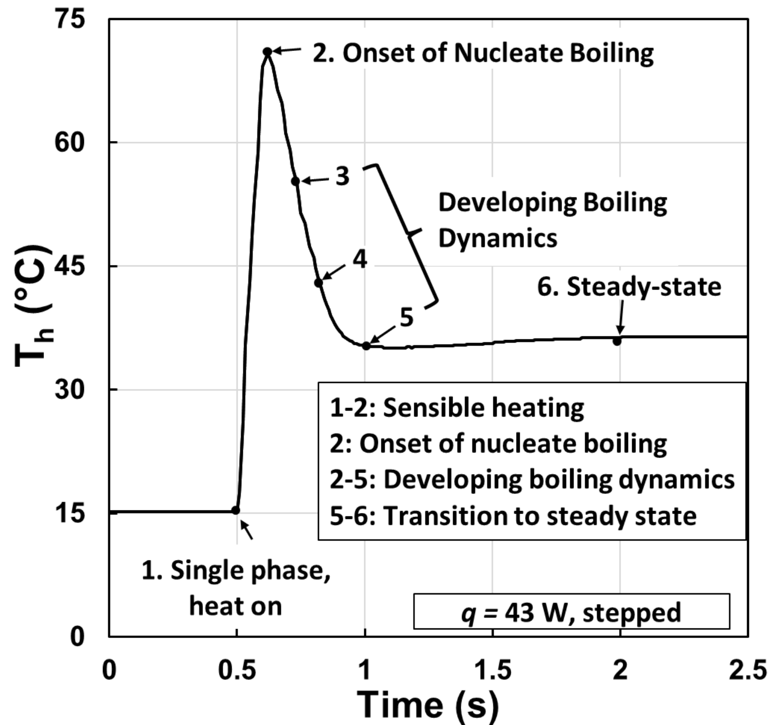

Figure 4-1. Transient heater temperature response to a stepped heat load, where numbers correspond to different flow visualization states.

decreased sharply as the heat transfer coefficient increased drastically due to boiling heat transfer in a developing boiling dynamics region. Finally, a steady state boiling temperature was reached at 36.4°C and at ~1.5 seconds after heat was applied.

Flow visualization in the channels was employed to understand the two-phase flow dynamics and is chronicled at the states of interest marked in Figure 4-2. For reference, adiabatic single-phase steady state flow is shown prior to a heat load (state 1). At the ONB (state 2), rapid generation of vapor resulted in vapor expansion both downstream and upstream. Vaporization in the inlet plenum, marked by the white dotted lines in Figure 4-2, was unexpected considering the inlet restrictions. The large superheat temperature (~50°C) before the ONB provoked extremely rapid vapor generation at the ONB, producing a large, localized pressure in the channels which

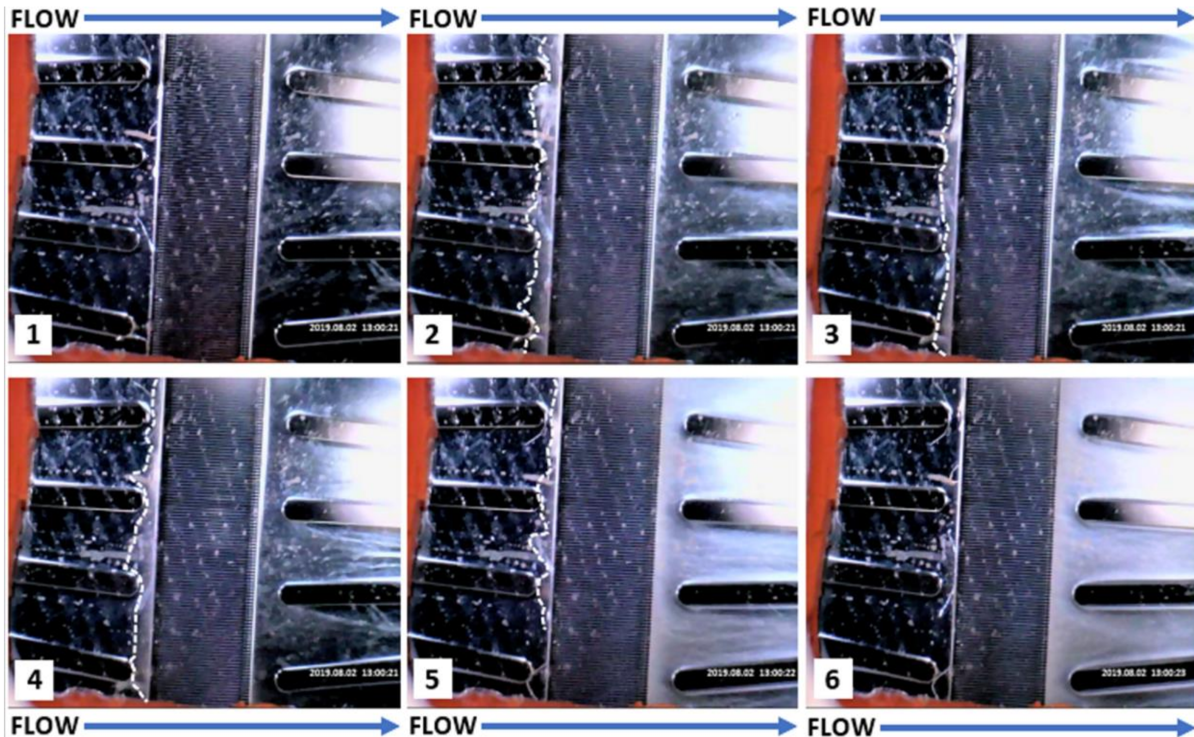

Figure 4-2. Images from a 43 W stepped heat load. Flow is from left to right, and the white dotted line denotes the two-phase mixture/liquid interface in the upstream manifold: (1) Steady state single-phase. (2) Onset of boiling. (3) 0.1 seconds after ONB. (4) 0.2 seconds after ONB. (5) 0.4 seconds after ONB. (6) Steady state flow boiling.

overcame both the pressure drop due to the inlet orifice and the upstream flow inertia. From states 3-4, the inlet flow began to overcome the large pressure gradient from the ONB and vapor was pushed downstream through the channels which precipitated a gradual reduction in test section temperature. At state 5, the majority of vapor was pushed downstream, and more two-phase flow was entering the outlet. At this point, the flow approached steady state boiling, and the rate of change in temperature decreased. Finally, at point 6, no more vapor was present at the inlet, and steady state boiling was reached.

The large temperature overshoot (34.2°C) and subsequent vapor backflow are supposed to be attributed to two factors. Steady state correlations specify the minimum wall superheat required to sustain nucleation given a specified heat flux [79]. However, there may be a limit on the rate under which nucleation conditions occur due to the growth rate of the thermal boundary layer.

Hsu's work showed that an underdeveloped thermal boundary layer impeded nucleation site activation due to the suppression of bubble growth by the subcooled bulk liquid [79]. In addition, as discussed in Steiner et al. [80], even within the thermal boundary layer, there is only a small region where the liquid is superheated enough to facilitate bubble growth, and bubbles may be quenched if this region is too thin since the bulk liquid temperature would be too high. During a stepped heat load, the heat is applied rapidly to the fluid in a manner which may exceed the conduction rate of growth of this superheated liquid layer for a given amount of time. Therefore, though bubbles may nucleate, their growth may be quenched and condensed by the small thickness of this layer, leading to increased wall superheats at the ONB relative to steady state flow boiling. As the superheat increases, the bulk fluid temperature increases, and nucleation sites begin to activate.

It is also possible that the microchannel evaporator surface is smooth enough that the range of cavities available to initiate boiling is small and thus delays boiling to a higher temperature. DRIE fabrication techniques often result in smooth sidewalls, and a smoother surface finish was posited as a nucleation delaying mechanism in both Huang [59] and Basu [61]. With the high wall superheat, liquid near the wall is likely superheated, leading to rapid vapor generation at the ONB, which, combined with small channel dimensions, results in pressure gradients that cause vapor backflow into the inlet plenum. It should also be noted that while the inlet orifices stabilize flow at steady state, their dimensions are clearly not enough to prevent transient backflow. Additional design constraints may be necessary to prevent this backflow given the large superheats and small channel dimensions.

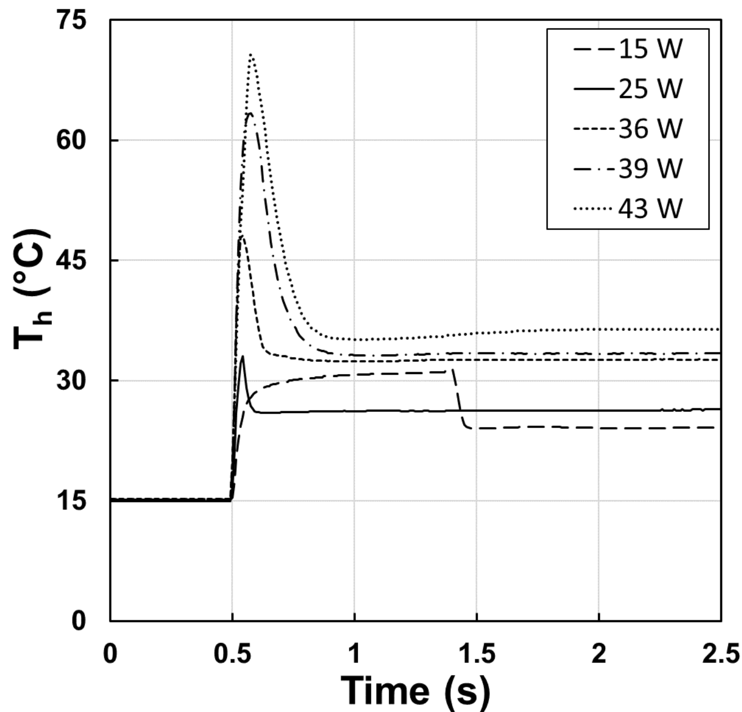

Figure 4-3. Comparison of the transient temperatures of different peak stepped heat fluxes, where heat loads are applied at 0.5 s for ease in visualizing the rapid temperature response.

4.1.2. Effect of Peak Heat Load Magnitude

Figure 4-3 shows the effect of increasing the peak heat load on the experimentally measured heater temperature. As the applied peak heat load increases, the peak temperature at the ONB also rises. However, the increase in temperature overshoot is not equal to the shift in steady state temperature. It is possible that these discrepancies stem from differences in maximum single-phase and two-phase temperature for that particular heat load. Single-phase heat transfer coefficients in microchannels are insensitive to heat flux, while two-phase heat transfer coefficients are highly heat flux dependent [14]. The required superheat for boiling generally increases with heat load; however, the superheat prior to boiling increased with peak heat flux despite significantly exceeding the temperature where boiling had initiated earlier. There appears to be a delay or a time constant on which the onset of boiling is dependent, and the rate of

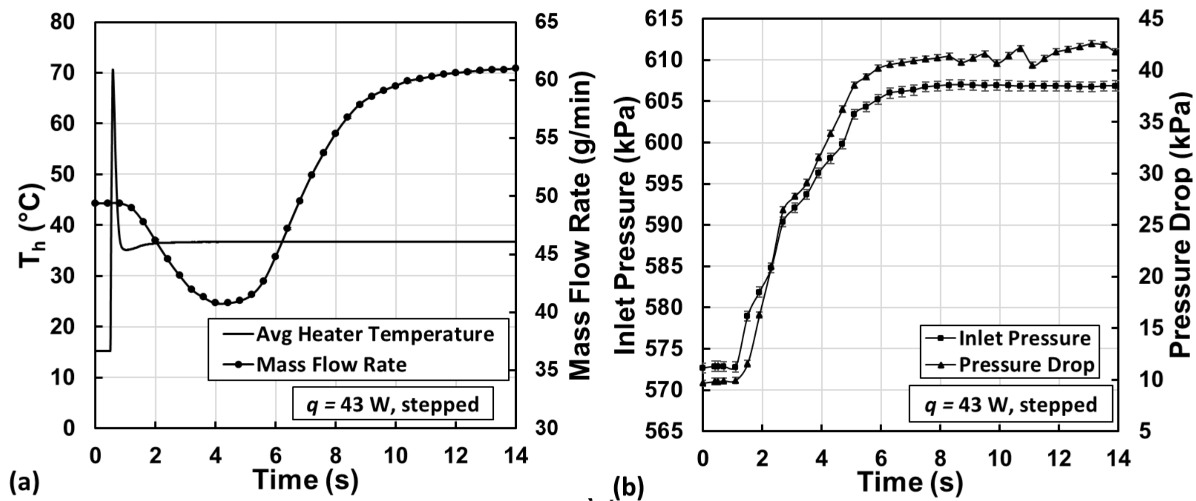

Figure 4-4. **(a)** Transient temperature and mass flux response to a pulsed heat load, applied at 0.5 s. **(b)** Test section inlet pressure and pressure drop response to same heat load.

temperature rise is quicker than this for the higher heat loads. These non-commensurate shifts between transient and steady operating temperatures require extra attention because knowledge of the steady state temperature difference between two different applied heat flux levels on a similar evaporator is insufficient to predict the difference in peak transient temperatures. This could have drastic consequences if a similar microchannel evaporator operating under a high heat flux maintains an adequate steady state temperature but results in thermal runaway or a device-damaging peak temperature under a transient heat pulse.

4.1.3. System Perturbations in Response to a Stepped Heat Load

In addition to transient temperature changes, system flow conditions also experienced transients after the ONB. The ONB generated a pressure wave which opposed the flow and caused compressibility effects upstream of the test section. After the initial ONB pressure wave subsided and the evaporator reached steady state, the mass flow rate increased to a higher value, as shown in Figure 4-4 (a). Figure 4-4 (b) details the transient inlet pressure and pressure drop measurements for this test, where sharp increases in both pressure drop and inlet pressure were observed

following the ONB. The increase in pressure drop was due to an increase in frictional and accelerational losses that are inherent with two-phase flow. This changed the system demand pressure requirement and thus changed the system flow rate due to a shift on the pump supply curve. The increase in inlet pressure was initiated by the increased low-density vapor which was unable to expand fully in the nearly constant volume loop (accumulator absorbs some of the vapor volume). The change in inlet pressure changed the inlet saturation temperature to 22°C and thus increased the inlet subcooling from 5 to 7°C. While the steady state temperature did not change appreciably (reflecting a weak nucleate boiling dependence on saturation properties and flow rate with these evaporators), larger changes in inlet pressure and flow rate at higher heat fluxes may induce longer lasting flow instabilities. System control along with a larger accumulator and more efficient pump would improve system performance following the generation of vapor.

4.2. Ramped Heating Results

This section discusses the results obtained by slowing down the transient heating rate via programmed ramp rates. Ramping represents an additional way that a device could be started or may represent additional heat capacity on the device. The overall effect of ramping as well as flow visualization is also presented for a selected heat load.

4.2.1. Effect of Ramping Compared with Stepped Heating

Ramping heat loads were investigated to mimic possible addition of additional heat capacitance which buffers the heating rate to the fluid by absorbing part of a stepped heat load. The transient peak temperatures, vapor backflow, and system dynamics seen in stepped heat load testing may be harmful to a device and result in damage or failure. The large temperature overshoots and vapor generation rates were attributed to large wall superheats possibly from the combination of a smooth surface finish and bubble quenching due to the rapid heat application

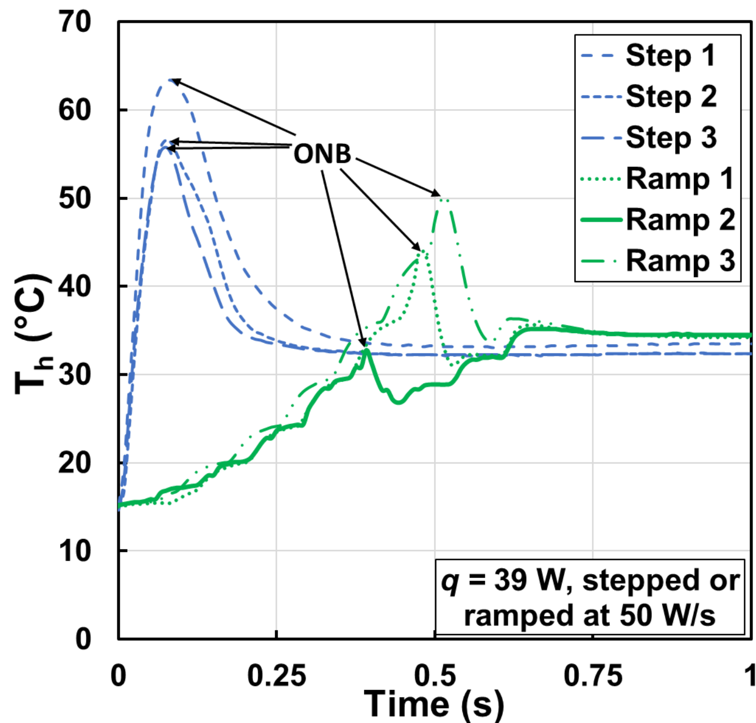

Figure 4-5. Stepped heat load compared to ramped heat load at 50 W/s. Stochasticity in the ONB is observed but ramping results in a lower peak temperature in all cases.

which is faster than the kinetics of boundary layer growth can occur. If ramping can reduce the transient heating rate to the fluid, it may potentially reduce temperature overshoots and vapor backflow and thus prolong device longevity or keep performance consistent.

Figure 4-5 compares the transient temperature profiles of stepped and ramped (at 50 W/s) heat loads at the same peak magnitude of 39 W. All ramped heat loads at this ramping rate reduced peak ONB temperature relative to a stepped heat load, up to 32°C in the most extreme case. In addition, unlike under stepped heating, with ramped heating, boiling commences prior to reaching the maximum heat load but still results in a similar sharp drop in temperature as the stepped case due to the increase in heat transfer coefficient. The temperature continues to increase as the heat load reaches the maximum value for the test; however, the rate of temperature increase is slower than prior to the ONB consistent with improved heat transfer due to boiling conditions. Slight

differences in final steady state temperature are likely due to changes in saturation properties and flow rate which occurred after the transient perturbation to the system.

Stochasticity in ONB time and peak temperature were observed in both stepped and ramped heat loads; however, in ramped heating cases, the differences were much larger (up to 17°C). Randomness between trials are suspected to be the result of local differences in trapped vapor pockets within nucleation cavities. More entrapped vapor enhances the boiling process by facilitating nucleation quicker and at lower wall superheats [43]. As the amount of vapor within cavities is inherently a random phenomenon, stochasticity in peak temperatures should be expected. Trapped vapor could act to prime nucleation sites for activation and thus influence the temperature at the ONB. Another possible explanation is that there are local variations in fluid conditions across the large number of channels since the heater temperature represents a superimposed average of the effects of all the channels. Individual channels may nucleate at different times and locations and thus affect the average temperature measured. Further investigation into the impact of ramping on peak temperature reduction is discussed in the next section.

4.2.2. Effect of Ramping Rate

The effect of ramping rate is shown in Figure 4-6 for one heat load compared to a step at the same peak heat load. In all cases, the heat load was initiated at 0 seconds and the test section allowed to reach steady state. For ramp rates of 4, 9.5, and 29 W/s, similar peak temperatures are reached at different times. The ONB temperature appears to have a superheat-heat flux threshold that is met by each of these ramp rates but which is lower than for either the stepped heat load or the 50 W/s ramped case. Therefore, an optimal ramping rate likely exists which minimizes the peak temperature but which gets the device to steady flow boiling as quickly as possible. The

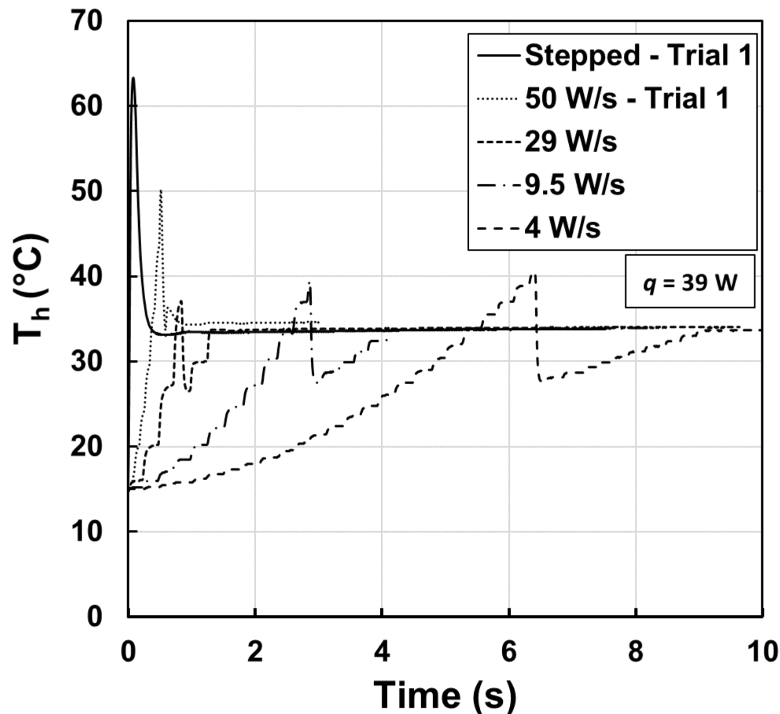

Figure 4-6. Test section temperature compared across different heating rates with a peak heat load of 39 W.

stochasticity seen in Figure 4-5 for the stepped and 50 W/s ramped cases was not observed in the slower ramp rate cases. The slower heating rate may facilitate growth of the superheated liquid layer which facilitates higher nucleation site density in a more regular manner compared to the more stochastic response with the underdeveloped boundary layer where local variations in temperature and fluid properties likely induce boiling in a small number of sites. It is possible that the priming effect mentioned before does not play as large of a role with the much slower ramped rates.

All the tested ramped heat loads reduced peak temperatures relative to a stepped heat load at the same nominal peak heat load magnitude. It is posited that more slowly applying the heat load facilitates enough growth of the superheated liquid layer both spatially and temporally. As this layer grows and penetrates more of the bulk liquid, the bulk temperature will increase, more of the fluid will attain saturation conditions, and the bubbles can nucleate more readily without

being condensed by the subcooled bulk liquid. Thus, boiling initiates at a lower superheat than with the faster heating rates. Therefore, from these results, one approach for preventing high peak temperatures prior to ONB is to keep the heating rate below the threshold imposed by the kinetics of the superheated liquid boundary layer development.

4.2.3. Effect of Ramping on Fluid Flow Behavior

Ramped heating was shown to reduce the peak temperature in all cases. Because the wall superheat at the ONB was greatly lowered, it is expected that the vapor backflow would also be mitigated. Therefore, flow visualization for the slowest ramping rate (4 W/s) was compared to stepped heating at the same times at and following the ONB in Figure 4-7. Images R1 – R3 were recorded during the ramped test, while images P1 – P3 were recorded at the times during the

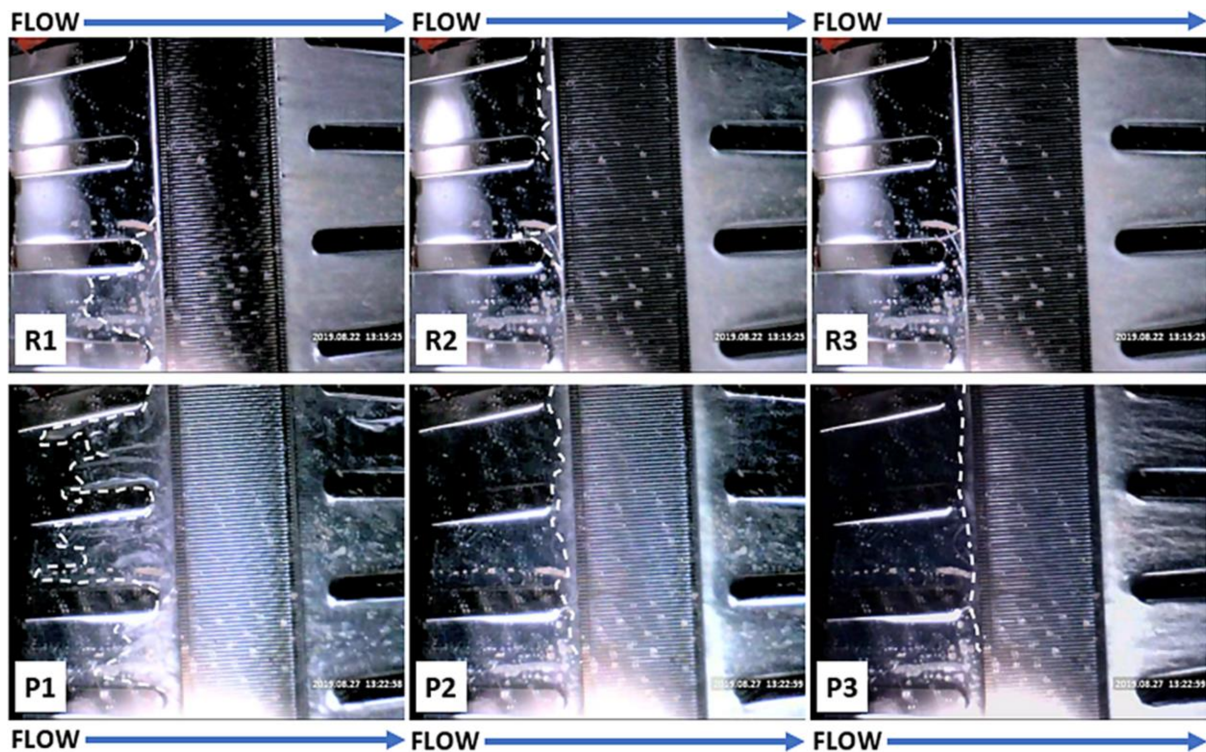

Figure 4-7. Images for ramped heat load at 4 W/s (R1 – R3) and stepped heat load (P1 – P3), for a peak heat load of 39 W. (R1) and (P1) are at the ONB. (R2) and (P2) are 0.05 s (1 frame) after the ONB. Vapor backflow for the stepped test is much greater. (R3) coincides with the steady boiling time 0.15 s (3 frames) after the ONB for the ramped case. (P3) occurs at same time after the ONB for the stepped test and still shows vapor backflow and developing boiling dynamics.

stepped test. The white trace highlights vapor backflow, as detailed earlier. Images R2 and P2 are one frame (0.05 s) after the ONB. In the ramped heat test (image R2) most of the vapor has moved into the channels. In contrast, a significant amount of vapor is still present in the inlet plenum in the stepped load test. In image R3 the ramped test reaches steady state two-phase boiling, while the stepped heat test in image P3 still has vapor present at the inlet and has not reached steady state boiling. In the ramped heat load, vapor backflow is greatly suppressed and steady state boiling is reached more quickly relative to the stepped heating condition. As explained above, the reduced vapor backflow is likely due to the decreased wall superheat (~20.5°C vs. ~43.3°C) and subsequently less rapid vapor generation rate in the ramped heat load test due to a more developed thermal boundary layer. In addition to the decreased backflow, the ramped tests allowed the system to reach steady state two-phase boiling after ONB quicker than a pulsed heat load. Clearly, a microchannel evaporator such as this would greatly benefit from added thermal capacity which does not impede the low thermal resistance pathway.

4.2.4. System Perturbations in Response to a Ramped Heat Load

Like with the stepped heat load, the ramped heat load also impacted the system dynamics and the test section inlet conditions due to the generation of vapor. Figure 4-8 details the corresponding test section flow dynamics with respect to the heater temperature response. For this case, the heat is initiated at 0 s. As in the stepped heat load, the inlet pressure and pressure drop remain roughly constant until the ONB, where both rapidly rose to a new steady state around 10 s due to the same reasons of reduced fluid density at nearly constant volume and increased pressure drop due to accelerational and frictional components of two-phase flow. This approximately coincides with the time the evaporator temperature reaches a steady state. However, the flow rate continued to gradually drop to a new steady state of ~28 g/min. Despite the flow rate decreasing

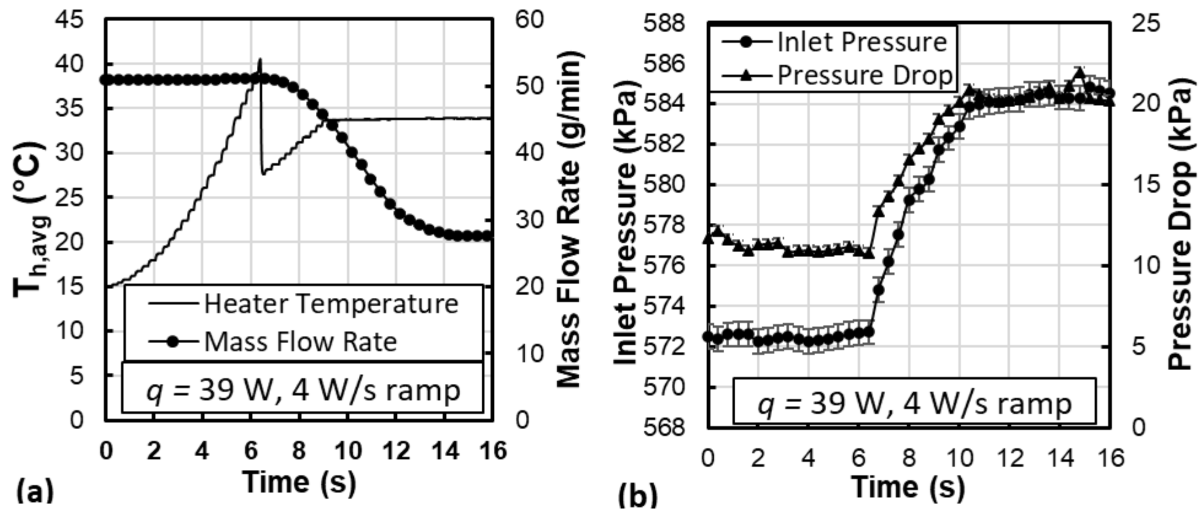

Figure 4-8. **(a)** Inlet pressure and pressure drop time series, with pressure spikes coinciding with ONB. **(b)** Transient test section temperature and mass flux. Mass flux drop coincides with pressure drop spike and ONB.

by nearly half of the initial value, the test section temperature remained nearly constant, reflecting a weak flow rate dependence on the steady state two-phase heat transfer coefficient.

4.3. Computational Modeling Approach and Results

Based on the data collected on the stepped heating in the above sections, a computational model was developed using the ParaPower-NavyHHF tool for rapid simulations of transient heating in microchannel evaporators. The results from this section extend the results of Richey's model [17] in an improved version of that software to handle the transient heating behaviors observed with this test section under a variety of transient heat loads. The modeling effort integrates two approaches to addressing the temperature overshoot and decay to steady state, which were heat flux dependent, and outlines a pathway towards development of a correlation for future efforts.

4.3.1. Onset of Nucleate Boiling – Default Model Behavior

In the model, the default approach was to switch from a single-phase to a fully developed two-phase heat transfer coefficient when the bulk temperature of the fluid reached the local

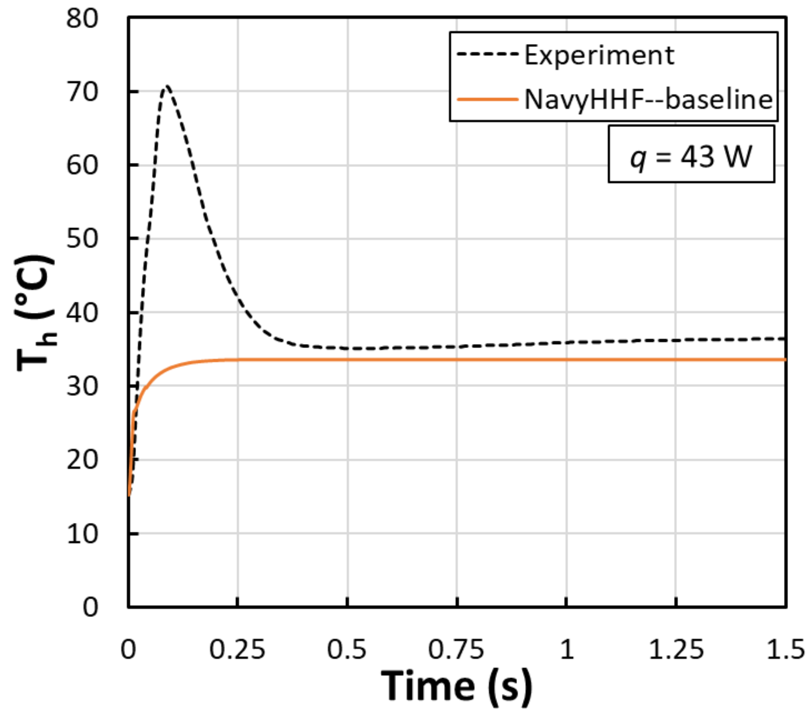

Figure 4-9. Comparison of the default simulation behavior with the experimental data to a transient heat load that transitions to subcooled flow boiling, where the simulation fails to capture the overshoot.

saturation temperature calculated via an energy balance for each volume node *N* and time step *t* according to the following equation:

$$h(N,t) = \begin{cases} h_{sp,l}, & if\ T_f < T_{sat} \\ h_{tp}, & if\ T_f = T_{sat} \end{cases} \quad (4\text{-}1)$$

However, this approach neglected the impact of a wall superheat which must be present for boiling to occur. For these test pieces and this fluid in particular, the wall superheat at the ONB was high, up to ~50°C for the highest heat load. Therefore, as shown in Figure 4-9, the model did not capture the temperature overshoot behavior, and instead clipped the temperature at roughly the steady state flow boiling temperature. Therefore, an improved approach was needed to capture the delayed onset of boiling.

4.3.2. Onset of Nucleate Boiling – Preliminary Correlative Approach

To fit the experimental data better, Richey [17] used a series of delays in NavyHHF until the proper superheat was reached. This was determined iteratively by forcing the software to maintain a liquid heat transfer coefficient until a specific time was met where the heater temperature in the model roughly coincided with that from the experiment. Then, a switch to a two-phase heat transfer coefficient was allowed to occur if the vapor quality in that specific volume was between 0 and 1. In this work, an improved approach was developed in the updated software combining the NavyHHF and ParaPower tools, an improved approach was used. First, unlike in Richey, the pressure drop was incorporated into the updated model. Next, instead of manually setting the time for the fluid to remain liquid for each heat load case, the wall superheat was determined iteratively for each heat load by matching the peak heater temperatures across the experiment and model. A correlation was created using the wall superheats and wall heat fluxes at

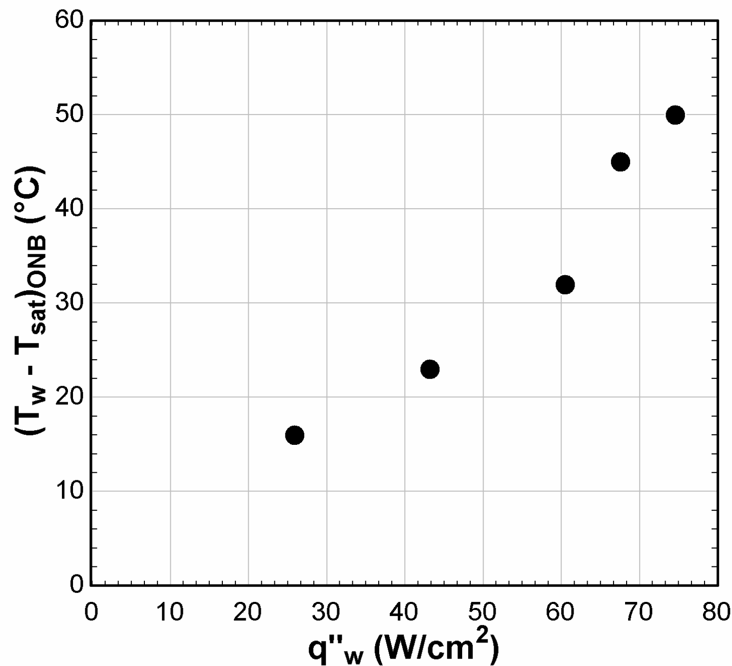

Figure 4-10. Superheat-peak wall heat flux at ONB model embedded as interpolation table in NavyHHF-ParaPower tool.

ONB calculated in the model for each heat load, which was then embedded into the software in the form of an interpolation look-up table. The correlation is shown in Figure 4-10, where the superheat needed to initiate boiling appears to increase quadratically with peak wall heat flux. To prevent spurious oscillations, all volumes downstream of the first which met the ONB criteria were immediately transitioned to using two-phase heat transfer coefficients, and a flag was thrown to signal that boiling was initiated. This prevented boiling from extinguishing once the wall superheat dropped to the much lower steady state value. Boiling would only stop in the model if the vapor quality dropped below zero.

The correlation approach resulted in the model behavior shown in Figure 4-11, with the ONB model capturing the proper time and temperature for which boiling was triggered. However, notably, this abrupt transition to a two-phase heat transfer coefficient drastically overpredicted the decay rate to steady state. Instead, the model predicted an instantaneous transition to steady flow

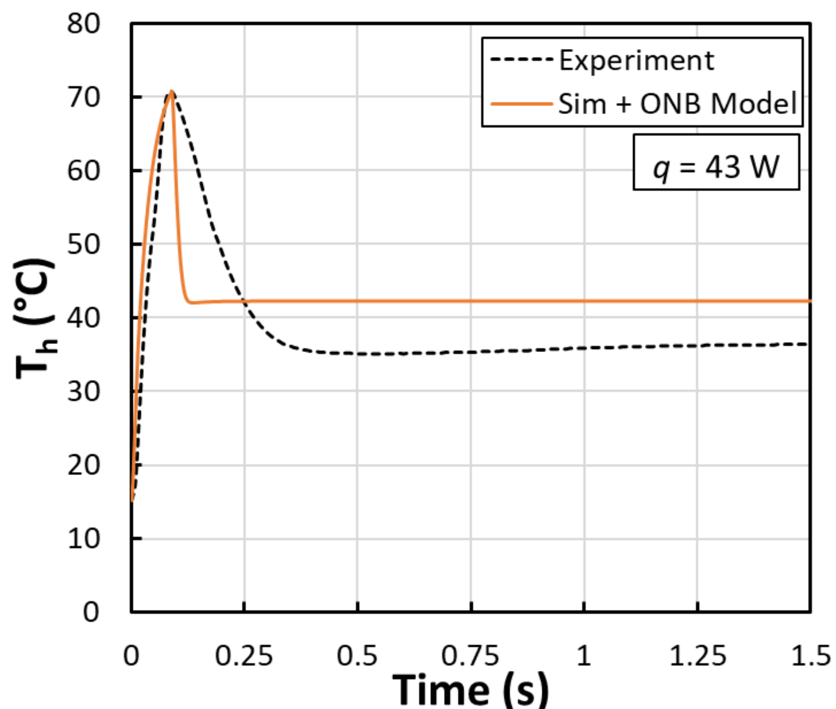

Figure 4-11. Improved ONB model embedded in NavyHHF-ParaPower software, where ONB temperature matches experiment; however, the decay to steady state is too abrupt.

boiling. Physically, however, there is a lag time associated with developing boiling dynamics due to the vapor backflow in the device and the resulting perturbations which follow. Therefore, an additional approach was needed to predict this behavior.

4.3.3. Population Growth Model for Developing Boiling Heat Transfer Coefficient

As an abrupt transition to fully developed subcooled flow boiling proved to be too quick, an additional approach considering the physics of the situation was developed to capture the transition to steady state. The flow visualization results revealed that ONB greatly perturbed the flow due to the large wall superheats, and the resulting violent vapor generation resulted in temporary vapor backflow. This backflow was gradually pushed downstream, coinciding with the development of steady state, fully developed flow boiling. To capture this behavior a population growth model, which is a special form of a logistic curve, was utilized to transition the heat transfer coefficient between the single-phase and fully developed two-phase values. Richey manually embedded the particular solution of the equation into the Simulink interface and used delays to start it [17]. In this work, an ordinary differential equation which describes this behavior was integrated into the software to utilize MATLAB's built-in differential equation solvers.

Assuming a quasi-steady state value for $h_{sp,l}$ and h_{tp} at each finite volume and each time step, the ordinary, nonlinear, differential equation for the population growth curve model reaching a maximum value h_{tp} with growth rate κ_{tp} can be expressed as the following

$$\frac{dh}{dt} = \kappa_{tp} h \left(1 - \frac{h}{h_{tp}}\right) \tag{4-2a}$$

$$h(t \leq t_{ONB}) = h_{sp,l}, \tag{4-2b}$$

where t_{ONB} is the time when the onset of nucleate boiling occurs. The resulting solution used in Richey's thesis can be obtained using separation of variables, applying some integration techniques, and by simplifying as

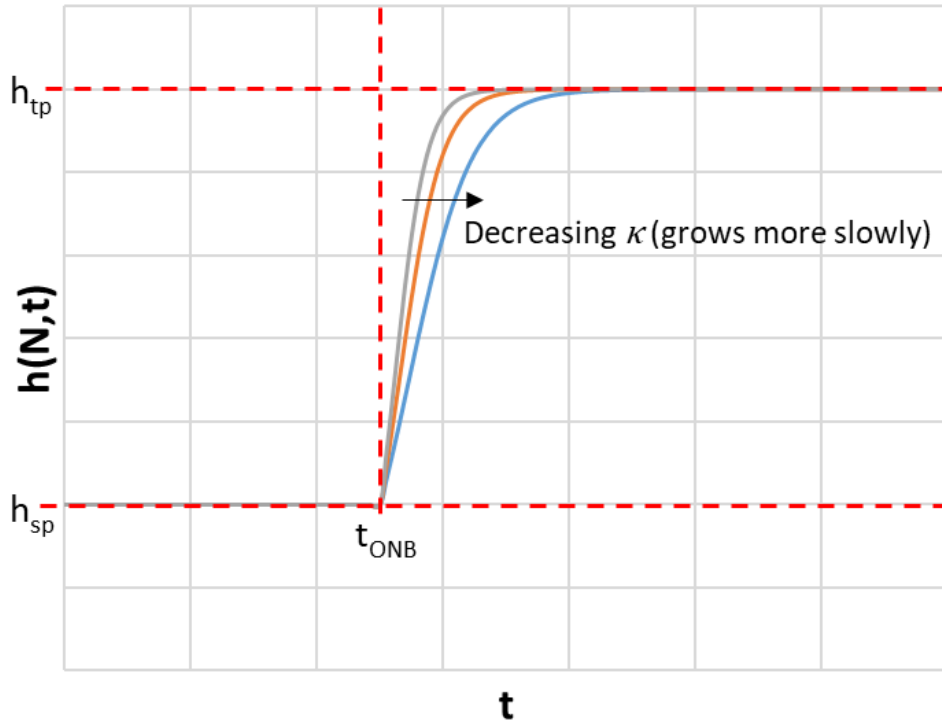

Figure 4-12. Plot depicting the exponential growth model equation bounded between the single-phase and two-phase heat transfer coefficients, with growth rate controlled by κ.

$$h(N,t) = \frac{h_{tp}}{1 + \left(\frac{h_{tp}}{h_{sp,l}} - 1\right) e^{-\kappa_{tp}(t - t_{ONB})}}. \tag{4-3}$$

The derivation of this equation is described in detail in APPENDIX C. This equation is shown graphically in Figure 4-12 where the heat transfer coefficient is bounded between the single-phase and two-phase values, and the growth constant affects how quickly the vapor backflow is extinguished as the flow moves towards steady state flow boiling. Figure 4-13 shows that incorporating the heat flux-superheat correlation with the exponential growth model results in satisfactory predictions for the transient heater temperature. For this set of testing conditions, by using trial and error, a growth factor of 15/s satisfactorily predicted the temperature decay rate to steady state. While the transient temperature closely corresponds to the experimental results, there is some deviation in the steady state temperature (~6°C). The choice of two-phase correlation strongly impacts the performance, but no literature correlation fully covers the conditions or

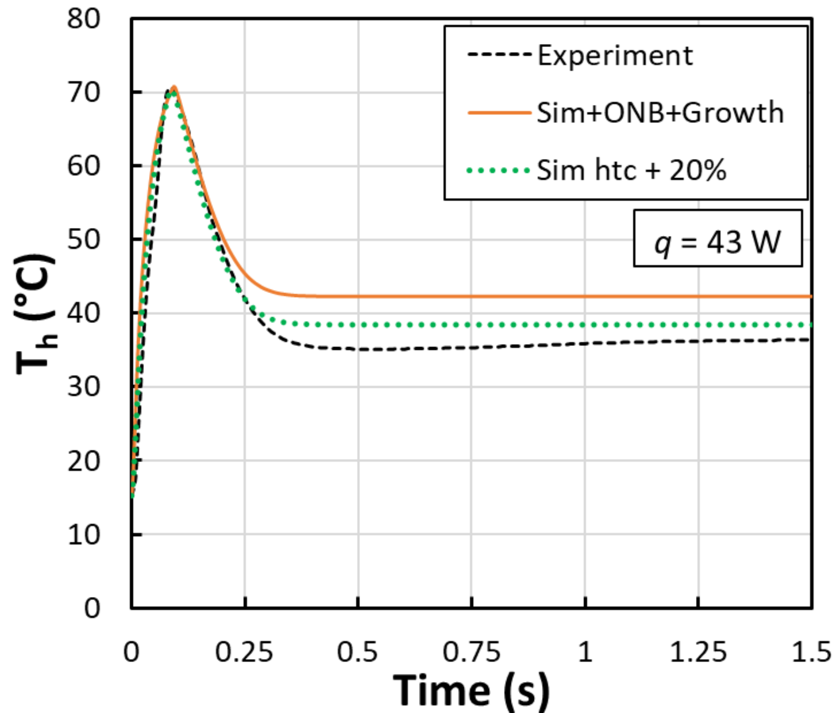

Figure 4-13. Resulting model combining exponential growth model with wall superheat correlation, showing adequate agreement with the experiment, especially during the transient.

geometry of this setup. Here the Mudawar correlation was found to best predict the results despite previous lab investigations showing stronger agreement with the Agostini correlation [81]. It should be noted that the channels used here are smaller than those used in Burke (30 vs 45 µm wide), and that in either case the channel hydraulic diameter (52 µm) is significantly smaller than the 190 µm lower bound in the correlation [14]. Uncertainty in channel dimensions, silicon thermophysical properties, and single-phase heat transfer correlation error could also play a role. A 20% increase in two-phase heat transfer coefficient was applied, and the resulting temperature is also shown in Figure 4-13. This improves the match with the steady state experimental results, but clearly improved correlations are needed to better predict the steady state performance of this small hydraulic diameter device. With reasonable confidence in the transient boiling model, the ONB correlation determined here was then compared to representative correlations from the literature.

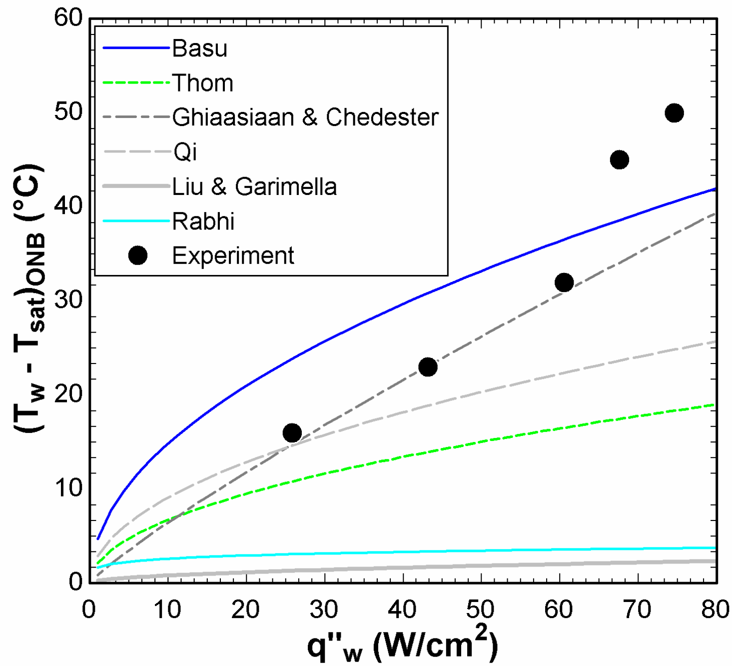

Figure 4-14. Comparison of current ONB superheat results compared with selected correlations from the literature.

4.3.4. Comparison with ONB Superheat Correlations from the Literature

The experimental data was used to create a simulation model to extract the ONB superheat-heat flux criteria for this set of testing conditions on this evaporator. This correlation was compared to others selected from the literature to assess trends and differences in the ONB behaviors. The wall heat flux from the model was used as the heat flux in these literature correlations to determine the resulting wall superheat at the onset of boiling. These correlations were developed for microchannels; however, their resulting predictions vary greatly, likely due to the difference in assumptions, testing conditions, and fluids used. The experimental data were compared with these correlations in Figure 4-14. The Ghiaasiaan & Chedester model [82], which incorporated the thermocapillary effect, predicts the data best below 60 W/cm^2 followed closely by Qi [83] and then Basu [84]. Qi's model was developed for liquid nitrogen and was a modified form of Thom's model [85]. The use of nitrogen, which is more like R134a than water, might explain why Qi's

model predicts results better than Thom's water-based model. Rabhi [86] and Liu [87] predict very low superheats and greatly underestimate the experimental behaviors, but this could be due to development with water and with much larger channels. Basu's correlation is heavily dependent on an accurate value of the surface contact angle, but this value likely varies with temperature and surface condition. The value used here for Basu's correlation was 2.2° and was found in a study on the contact angle of refrigerants on stainless steel [88]. R134a on silicon would be expected to exhibit a different contact angle but it has not been measured for this combination of materials. The observed increase in superheat at the higher heat fluxes is not intrinsically explained by the current model but as described earlier, could be due to a delay in thermal boundary layer growth rate due to a large transient heating rate which suppressed bubble formation. This behavior may not be properly captured by the ONB correlations which were developed under steady heating conditions, or due to a small range of nucleation cavity sizes that result in larger changes in superheat above a certain heating rate. Further investigation and inclusion of these mechanisms in the model are recommended for future efforts.

4.4. Summary and Challenges with the Preliminary Approach

The preliminary findings of this chapter found large temperature overshoots at the onset of boiling in a 52 μm hydraulic diameter microchannel evaporator when exposed to a stepped heat load. The ONB temperatures increased with heat load in a nonlinear manner compared with the steady state flow boiling temperatures, which were less affected by peak heat flux. In addition, the large superheats at the onset of boiling resulted in vapor backflow into the inlet plenum of the device. Ramping the heat load at a lower rate to simulate the presence of additional heat capacity resulted in lower peak temperatures and reduced vapor backflow. It was hypothesized that slowly adding heat facilitates growth of the superheated liquid layer where bubbles may grow and detach

without quenching from the subcooled bulk liquid, and that the large transient heating rate in a step may happen quicker than this layer can grow, thus impeding bubble growth and resulting in higher temperatures at the ONB. Further increases in ramping rate resulted in a nearly asymptotic reduction of the peak temperature, suggesting an optimal ramping rate, though this was not studied in detail. In addition, system dynamics were strongly coupled with the evaporator response and likely affected results. Improved system control and design will be needed for enhanced study into device behaviors and to isolate the evaporator transient response more effectively.

A computational model was developed in the NavyHHF software to predict the transient thermal response of this evaporator under a stepped heat load. The initial model failed to capture the large temperature overshoot, and while the ONB could be manually delayed in the model, it still overpredicted the temperature decay rate due to the presence of vapor backflow. A wall superheat-peak heat flux correlation was developed iteratively by attempting to match the temperature in the experiment with the model where the ONB occurred. Then, a logistic growth model was employed to transition the flow from single phase cooling to fully developed two-phase flow boiling at steady state. The growth constant was determined iteratively by fitting to the experimental data, and values between 15 and 100/s were used, reflecting a large variation in backflow intensity across the different heat loads. While this model was useful in the context of this device under these conditions, a larger range of data encompassing more conditions must be studied to make a more predictive model.

Finally, while ramped heat loads resulted in a desirable thermal response from a safety and stability standpoint, this type of slow heating is impractical for many devices which must be quickly cycled or are exposed to rapid start-ups. In addition, ramping does not represent the physical effect of additional heat capacitance which typically results in an exponentially decaying

thermal response. Incorporating and quantifying the impact of including additional thermal capacity such as a phase change material into the evaporator may be valuable if the PCM could offset the peak temperatures by buffering the transient and resulting in ONB temperatures more similar to the ramping heat load. The coupling of a PCM with the evaporator thermal response must be better understood to evaluate these potential impacts on the device behavior.

CHAPTER 5. Results, Discussion, and Model Development for 38 μm Hydraulic Diameter Silicon Microchannel Evaporator

This chapter details the results of testing the second silicon microchannel evaporator under a more extensive range of testing conditions than the first evaporator. In addition, the effect of adding PCM to the device was also studied semi-empirically. A model was developed in NavyHHF to predict the transient device behavior under the range of conditions tested herein. This model was then used to predict the performance of the device with the addition of various metallic-composite PCMs.

5.1. Steady State Boiling Curve

Before transient testing was conducted, steady state test data was first collected as a baseline under low heating conditions to determine where ONB would occur. The steady performance can be considered the optimal cooling behavior of the device in the absence of

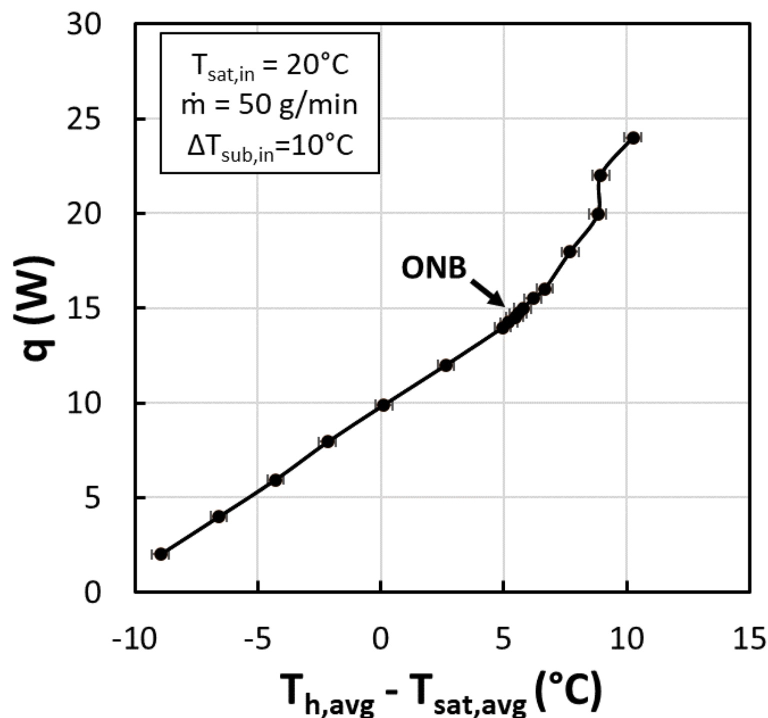

Figure 5-1. Steady state boiling curve at baseline flow conditions; ONB occurred at ~14.75 W.

transient heat load fluctuations which may affect the performance due to possible flow instabilities and temperature overshoots. Figure 5-1 details the resulting device performance. For these testing conditions, the onset of nucleate boiling (ONB) was first observed around 14.75 W, with a superheat of ~5.6°C (at the heater level), characterized by a change in slope of the superheat curve. Prior to this heat load, the superheat increased linearly with heat load due to the nearly constant heat transfer coefficient associated with laminar single-phase heat transfer in microchannels. The slope increased after the ONB because the heat transfer coefficient associated with the latent heat phase change process is much greater than in single-phase cooling.

5.2. Stepped Heating Results

Having established a baseline for ONB conditions under steady state heating, this section describes the behaviors observed in the micro-evaporator under the application of stepped heat loads. The generalized behavior observed for a given set of flow conditions and different heat loads is discussed first with additional accompanying flow visualization included to assist in explaining observations. Then, the results of testing under a larger set of flow conditions are compared with the baseline flow conditions to determine additional dependencies.

5.2.1. Transient Thermal Response with Flow Visualization

The baseline testing scenario with $T_{sat,in}$ = 20°C, $\Delta T_{sub,in}$ = 10°C, and $\dot{m}$ = 50 g/min was first considered across the range of peak stepped heat loads ranging from ~24 W – 55 W. Figure 5-2 shows a typical transient temperature time series (at ~35.4 W) with notable points marked for corresponding synchronized fluid flow visualization from a high-speed microscope camera in

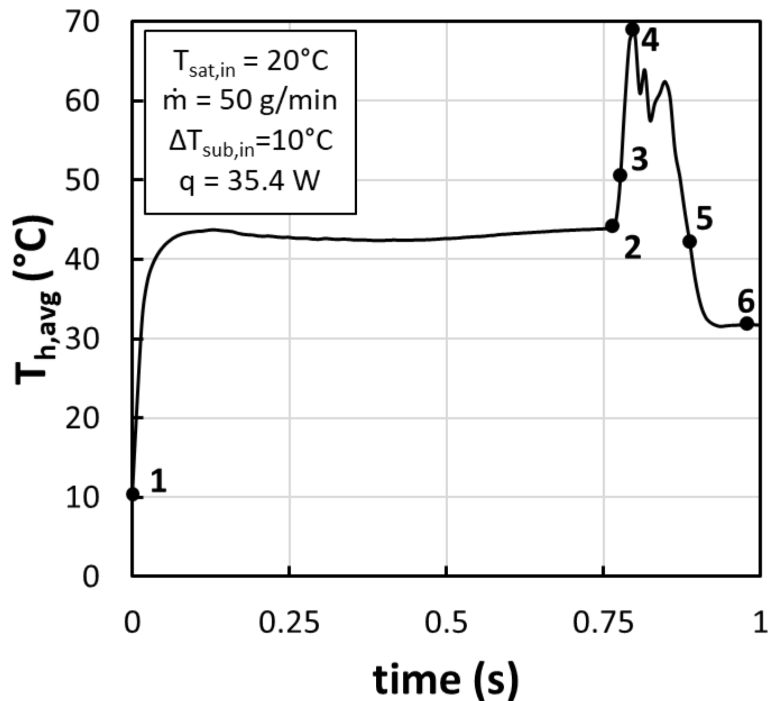

Figure 5-2. Typical transient temperature profile with important points in time marked for accompanying flow visualization, with a peak stepped heat load of 35.4 W.

Figure 5-3. The liquid-only cooling condition at the start of heating is shown in the first image of Figure 5-3 as a baseline reference. Similar to the results described in Chapter 4 for the 52 μm hydraulic diameter evaporator, as heat was applied, the heater temperature increased due to sensible heating while the fluid reached a steady state under single-phase liquid cooling. Then, boiling initiates at point 2. The large superheat (~23°C) combined with the narrow channels resulted in rapid bubble growth and vapor backflow out of the channel, as seen in the image corresponding to point 3. Due to this vapor backflow, the liquid was expelled from the channel, and conduction to vapor temporarily ensued, resulting in a transient dryout condition as the heater temperature rapidly increased to ~70°C. However, a point of inflection at point 4 resulted as incoming liquid gradually overcame the vapor backflow and drove the device toward steady boiling. By point 5, most of the inlet vapor had been expelled downstream. Finally, steady state

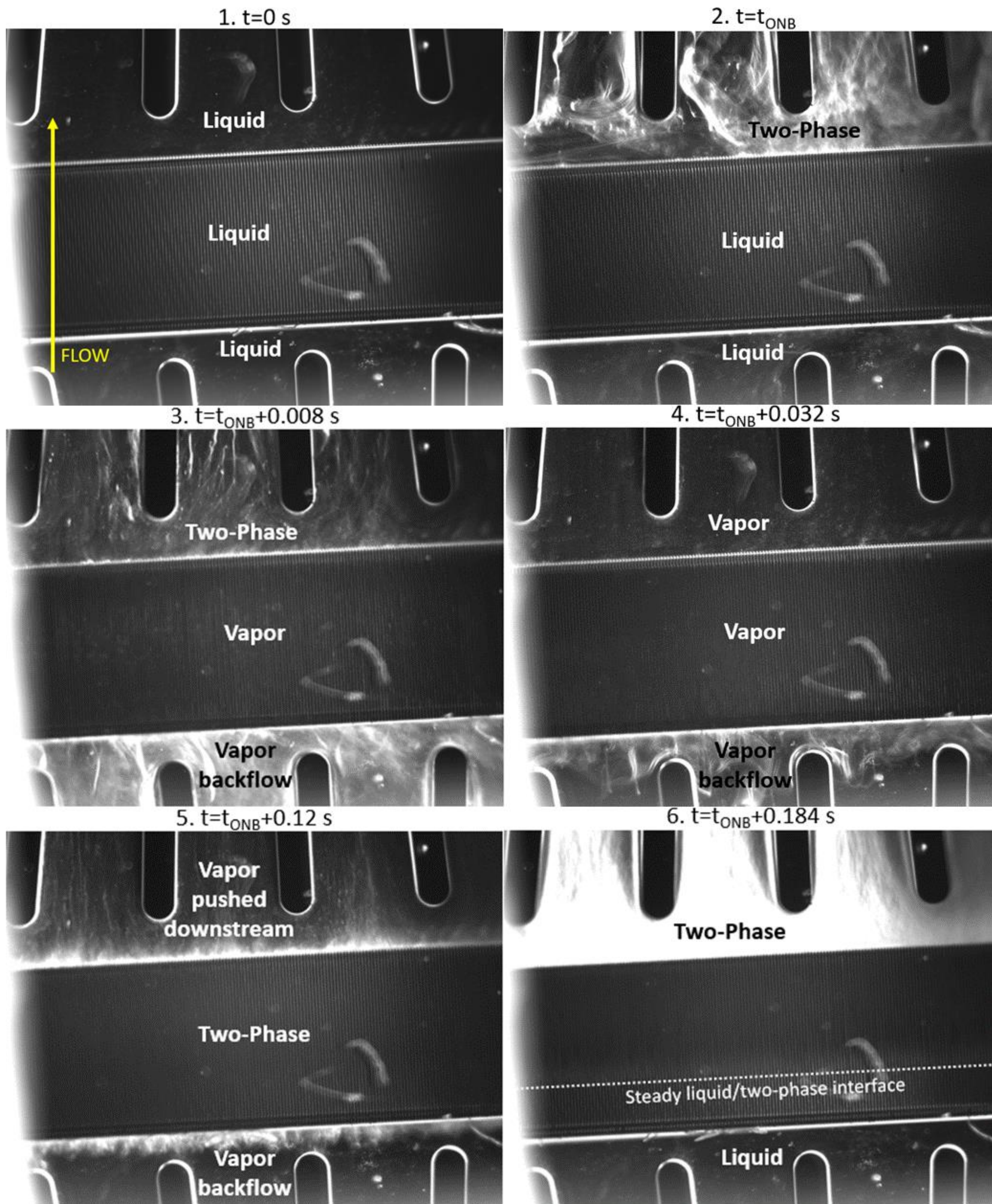

Figure 5-3. Flow visualization in the channels, with 1. Liquid only, 2. ONB, 3. Severe vapor backflow into inlet plenum, 4. Backflow lingers but is slowly pushed downstream, 5. Nearing steady state, 6. Steady state flow boiling with no vapor present in the inlet plenum.

boiling was reached at a much lower temperature due to the heat transfer enhancement associated with latent heat phase change. Notably, the vapor backflow had been completely extinguished.

Recalling the behavior seen in the 52 µm hydraulic diameter evaporator and referring back to Figures 4-1, 4-2, and 4-3, it is clear that the transient thermal response in the 38 µm hydraulic diameter evaporator exhibited significantly different behavior. These figures are not completely comparable because of the difference in inlet subcooling between the two devices, but there are still comparable observations which can be made. Only at a low heat load of 15 W did the other evaporator reach a transient steady state in liquid cooling. The difference in inlet subcooling could partially explain these different results since a higher subcooling would increase the time to boiling, reduce the vapor quality, and possibly delay nucleation due to quenching. However, the 52 µm evaporator did not experience a large temperature spike after ONB like with the 38 µm evaporator. With the 52 µm evaporator, the temperature immediately dropped after ONB occurred. Furthermore, the 38 µm device should have significantly superior performance due to the much larger quantity of smaller channels. However, even at a heat load ~8 W less, the peak temperature for the 38 µm device is comparable to the 52 µm device. This different observed behavior alongside the flow visualization comparisons between Figure 4-2 and Figure 5-3 show that the backflow was much more severe with the 38 µm device than with the 52 µm device.

5.2.2. Effect of Peak Heat Load Magnitude

Figure 5-4 shows the resulting representative temperature time series across the range of tested stepped heat loads overlaid on the same plot. It should be noted that below a peak heat load of 24 W, boiling was not observed, though theoretical vapor quality calculations suggest two-phase conditions may be possible down to ~12.5 W. Boiling occurred only when the wall superheat-heat flux threshold was met, which in this case appears to have occurred around a 24 W heat load. Notably, during the steady testing of the device under these same conditions, boiling commenced around 14.75 W of applied heat, suggesting a delay in the onset of nucleate boiling (ONB) caused

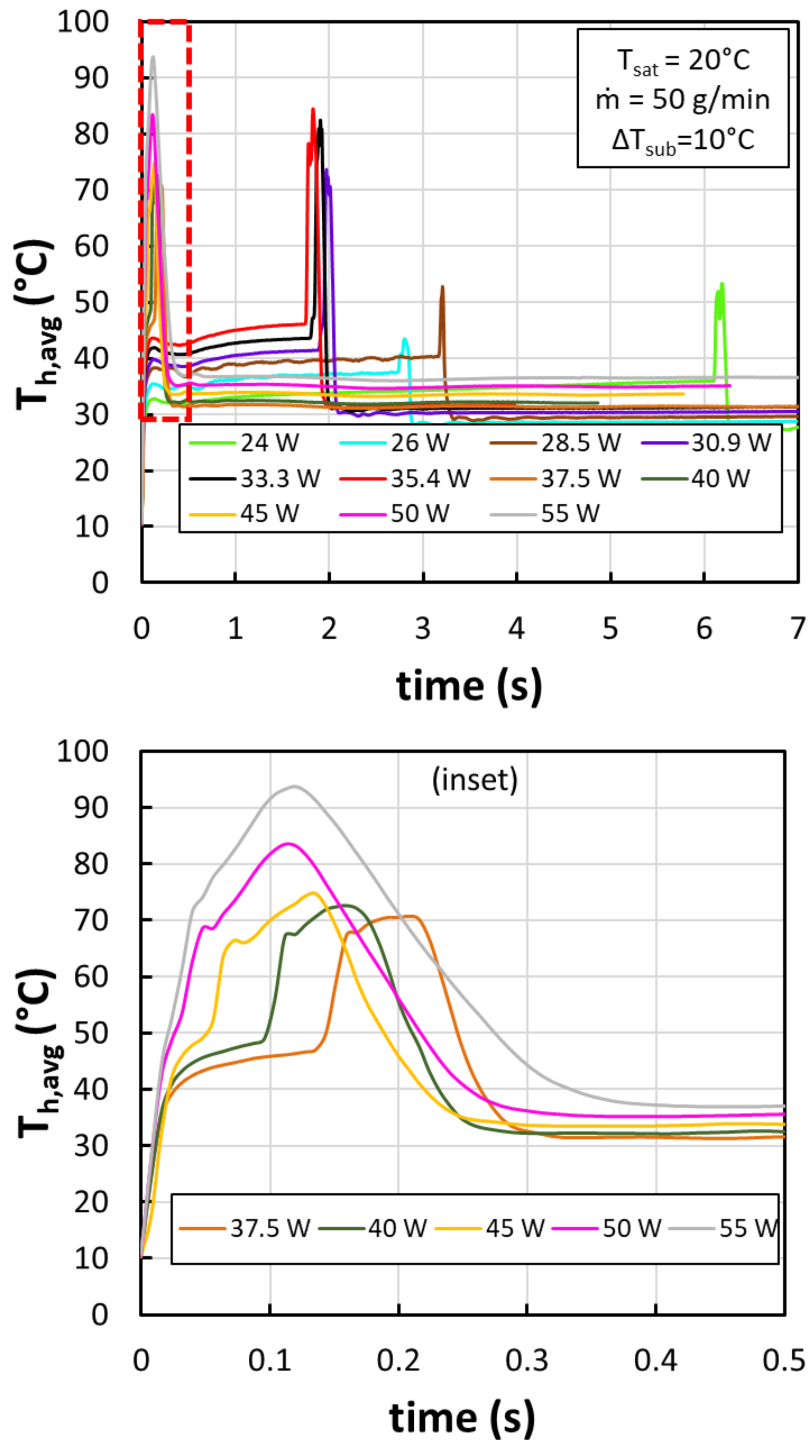

Figure 5-4. Representative transient temperature responses across range of peak heat loads for given baseline flow conditions. Inset plot shows zoomed-in perspective for >35 W cases.

by the transient heating mode. For heat loads >35 W, the steady liquid-cooled state diminished in duration as boiling was initiated earlier. Conversely, the duration of time spent in the developing

transient boiling regime from the onset of boiling to steady state increased with heat load, while peak temperatures generally also increased with peak heat load. This increase in peak temperature is due to the increased vapor generation rate and the resulting longer duration of time spent in vapor-only heat transfer (or dryout conditions) at a higher heat load. For example, the outlet vapor quality in the 24 W case was ~8.5%, while for the 55 W case was 33.5%. In addition, based on these figures, while the peak, ONB, and steady state temperatures generally increased with heat load, they did not shift commensurately.

Comparing the results across all trials and heat loads allows for more in-depth understanding of the observed behaviors in Figure 5-4. First, Figure 5-5 confirms the observations from Figure 5-4 that the time to ONB generally decreases inversely with peak heat load from about 4 s to 0.016 s, with error bars representing 99% confidence intervals for the trials. This is to be expected since the rate of thermal energy supplied to the fluid increases as the peak heat load

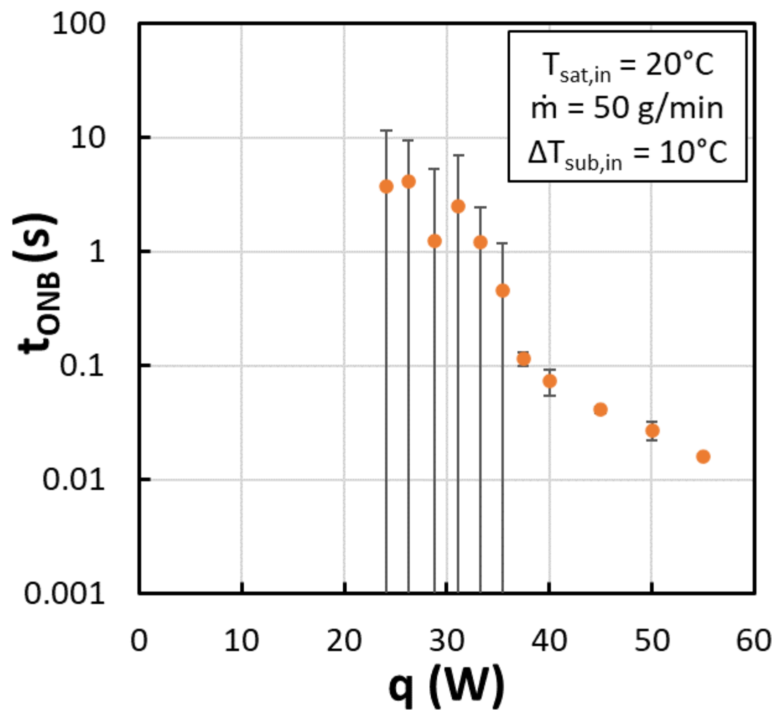

Figure 5-5. Time to onset of boiling for baseline fluid conditions across all heat loads and trials, where variability decreases greatly as q increases.

increases and promotes boiling more promptly. The variability for the time to ONB is much larger for heat loads <35 W and decreases rapidly above 35 W. This is possibly due to proximity to the wall superheat threshold and the steady liquid state which exists in this region is likely destabilized by small local variations in pressure or temperature which then trigger boiling. With the smoother channel sidewalls due to the etching process, which results in characteristic scalloping features that were ~3 μm wide and can be seen in Figure 5-6. The distribution of nucleation sites is likely small due to this narrow range of feature sizes, and the lower range of nucleation sites which has enough energy to nucleate at lower heat loads leads to a wider scatter in the results. With higher heat fluxes than 35 W (where the wall superheat is higher), more energy is available to allow nucleation to occur from a wider range of these potential sites, which facilitates boiling sooner and less stochastically.

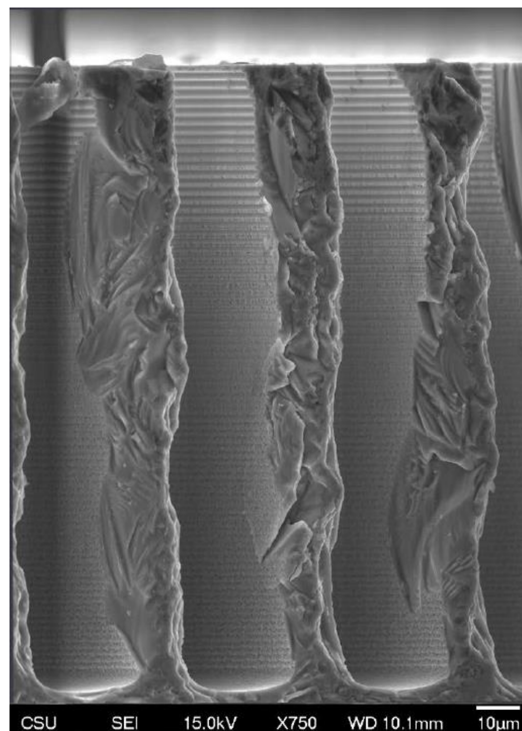

Figure 5-6. Characteristic sidewall scalloping associated with the DRIE etching process used to fabricate the microchannels.

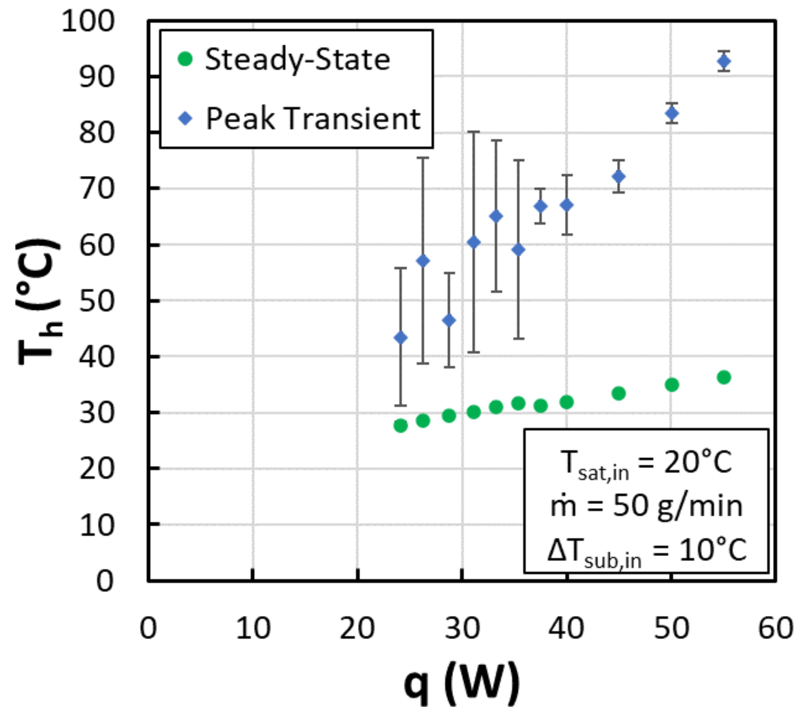

Figure 5-7. Comparison of the steady state and peak temperatures for the baseline fluid conditions across all heat loads, with error bars reflecting 99% confidence intervals across multiple trials.

The peak device temperatures also reflect the trends in time to boiling but are significantly higher than the steady state flow boiling temperatures. Figure 5-7 compares the peak device temperatures with the steady state temperatures, with error bars again reflecting the variability observed across subsequent trials using 99% statistical confidence intervals. The steady state performance of this device is excellent, as steady state temperatures are <40°C for heat loads up to at least 55 W (or 550 W/cm^2), with a thermal resistance at this heat load (using the average saturation temperature from inlet to outlet) of ~0.3 K/W. In addition, due to the passive improvement of the flow boiling heat transfer coefficient with increases in heat load ($h_{tp} \propto q^m$), the steady temperatures vary by <10°C over a span of ~30 W, demonstrating efficient cooling. On the contrary, the peak temperatures exhibit a much steeper rise with applied heat load, with values which are significantly higher than the steady temperatures. This is likely due to the combination

of the longer backflow duration due to the higher vapor quality at higher heat loads combined with the temporary dryout conditions during the vapor backflow period as mentioned earlier.

The heat loads ≤35 W exhibit large peak temperature variability, but this generally decreases with heat load. In addition, some of the cases have higher peak temperatures than the higher heat loads. Kandlikar [53] suggested that due to the high single-phase heat transfer coefficients and wall superheats often observed within microchannels, the local liquid subcooling at the nucleation site, given by

$$\Delta T_{sub,ONB} = \frac{q''_w}{h_{sp,l}} - \Delta T_{w,ONB} \tag{5-1}$$

can be negative, meaning that bubble nucleation occurs under superheated liquid conditions. Under these superheated liquid conditions where the fluid remains liquid above the saturation temperature, the bubble growth will be explosive. The lower heat load cases reached steady state in this likely superheated liquid state which can also be described as form of metastable state where the liquid exists temporarily at a temperature above the saturation temperature [89]. It should be noted that such a metastable superheated liquid state may be readily destabilized by the activation of any nucleation sites due to local fluctuations in temperature or pressure. Given the large number of channels, this is a likely scenario.

Estimating the wall heat flux using Equations (3-15)-(3-16), heat transfer coefficient using Equation (3-19), and wall superheat from the heater temperature and saturation temperature as 250 kW/m^2, 15 kW/m^{2}K, and 22°C, respectively, for the exemplary 35.4 W case, gives a local liquid subcooling of -6°C, which is a superheated liquid at 26°C. For several of the cases, the fluid outlet temperature was measured at ~24-25°C, which agrees well with these calculations and confirms the superheated liquid condition. Also given the large variability for the time to ONB and the general increase in peak temperature with increase in time to ONB for these lower heat loads, it is

plausible that remaining in the metastable liquid state for longer results in more explosive boiling due to the largely superheated conditions of the surrounding liquid. As mentioned above in explaining the variability in ONB time, the likely proximity of the conditions to the ONB threshold superheat, and the differing durations spent developing this superheated liquid state due to destabilization by small, local temperature or pressure fluctuations across many channels may explain the variability in peak temperatures since vapor generation is more explosive with higher liquid superheating [53].

In addition to the increase in peak temperature with heat load seen in Figure 5-7, the ONB temperatures also increased with heat load, as indicated in Figure 5-8. The increase appears to level off at the higher heat loads and follows a sub-linear relationship, similar to the trends observed with wall superheat and heat flux in literature correlations, where $\Delta T_{w,ONB} \propto q''_{w,ONB}{}^{1/m}$, and m is usually ~2 [90]. The heater temperature trend observed here is proportional to $q^{0.46}$, which

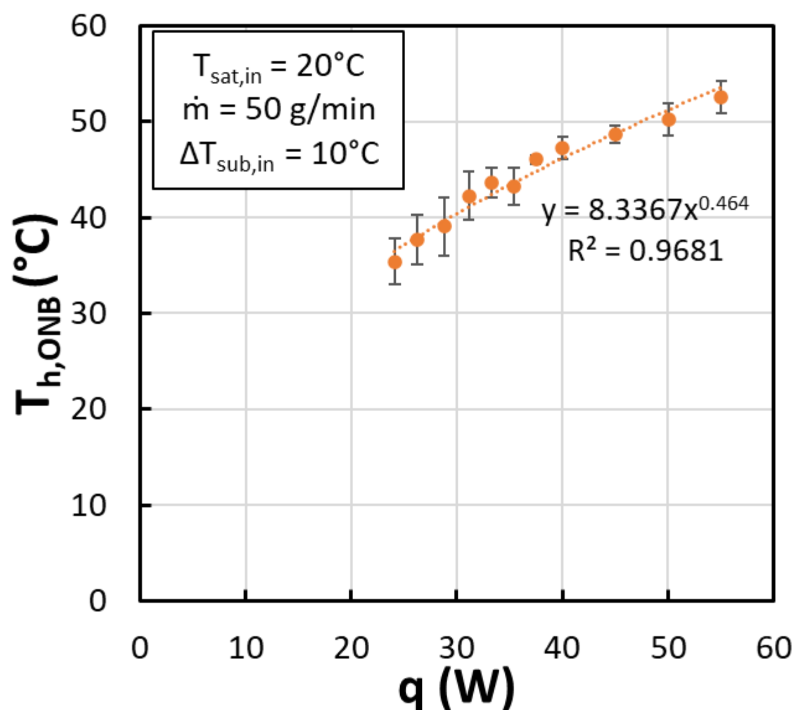

Figure 5-8. Comparison of the ONB temperature versus peak heat load for baseline flow conditions across all trials.

results in a similar m of ~2.17, though the wall superheat and wall heat flux will be different due to the heat spreading in the silicon substrate. The large superheat and the increase in the temperature overshoot at the ONB temperature with peak stepped heat load was also observed previously in the preliminary work with the 52 μm hydraulic diameter evaporator and in Refs [61,91]. However, the increase in superheat with heat load observed in those scenarios followed a different type of trend, as shown in Figure 4-10 which could be due to differences in surface characteristic/roughness, microchannel dimensions, fluid conditions, or too few data points to establish a reasonable trend.

Given that the inlet saturation temperature was ~20°C, the observed superheats are between ~15 and 32°C, which are quite large. One possible explanation for the delay in onset of boiling conditions relative to steady state conditions is that cavities that might normally have initiated nucleation at lower temperatures may have been flooded due to the subcooled liquid since the thermal boundary layer may not have fully developed spatio-temporally yet as described in Chapter 4 [53,79], and due to the rapidly increasing heat load may not have nucleated until a higher temperature was reached. At this higher superheat, a larger range of cavities was therefore activated and increased the chance that boiling would occur. Another possible explanation relates to the channel fabrication technique and the test fluid. The etching process used to fabricate the microchannels results in smoother sidewalls with a reduced range of possible nucleation cavities. In addition, R134a is considered a low surface tension fluid compared with water, and Refs. [90,92] suggest that a highly wetting refrigerant like R134a combined with the smooth channel sidewalls results in a narrower range of nucleation cavities which are easily flooded until higher superheats are met.

5.2.3. Effect of Subcooling on Stepped Heat Loads

The baseline tests resulted in high wall superheats and peak temperatures during flow boiling under stepped heating. Changing the fluid parameters may impact the observed results due to changes in nucleation behaviors associated with different fluid properties and flow conditions. Subcooling directly affects the amount of thermal energy needed to reach saturation conditions in the fluid, so it follows that changing subcooling degree may plausibly impact transient performance. Inlet subcooling was decreased from 10°C down to 2.5°C while holding the inlet saturation temperature at 20°C and the mass flow rate at 50 g/min.

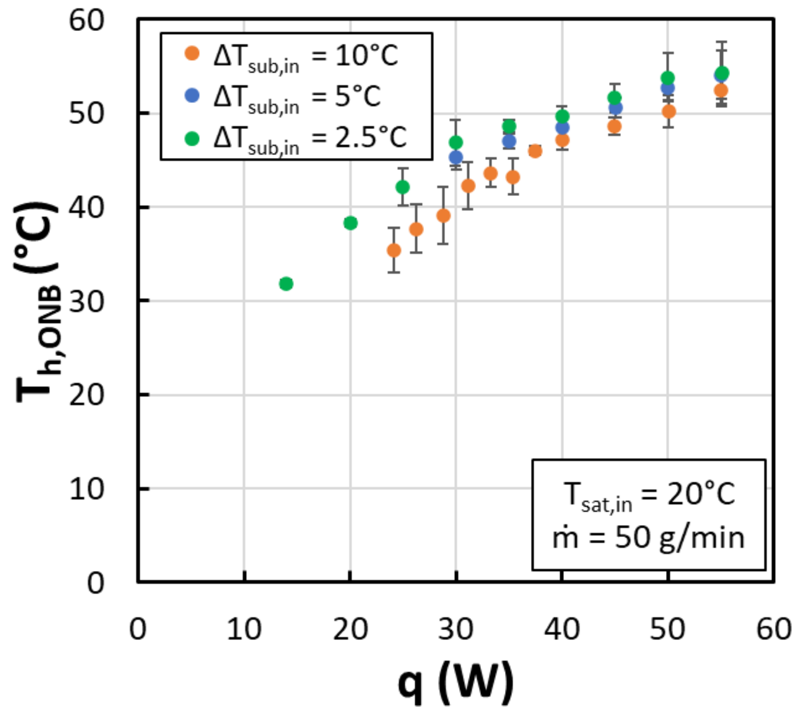

Figure 5-9. Comparison of the ONB temperature versus peak heat load across different inlet subcooling conditions.

Figure 5-9 compares the ONB heater temperature as a function of heat load and subcooling, where it is apparent that heater temperatures were lower at the ONB under higher inlet subcooling. The overall trend of ONB temperature with heat load appears similar across subcooling conditions, though the curves are shifted vertically with respect to each other. These results may seem

counterintuitive since increased subcooling increases the amount of thermal energy required for reaching saturated conditions and may also delay nucleation site activation to higher superheats, as was observed in Ref [93]. However, it is important to note that this is the average heater temperature, not localized wall temperatures. The fluid entered at a lower temperature with higher subcooling, so it is reasonable to believe that since the average fluid temperature was, the average heater temperature was also reduced. In addition, the heat transfer coefficient, which is directly dependent on the liquid thermal conductivity, decreases about 2% from the 10°C to 2.5°C subcooling scenario, and will also contribute slightly to an increased heater temperature at ONB.

The maximum difference between the 10°C and 2.5°C subcooled cases was about 6.8°C near 25 W peak heat load, which is close to the 7.5°C difference in subcooling. This difference decreased as heat load increased, down to ~1.8°C, reflecting the increased rate at which the fluid temperature hit saturation and the diminishing effect of the subcooling on contributing to heater temperature. It is still possible that subcooling affected nucleation conditions, but this effect is not directly observable here due to the measurement of the average heater temperature. In addition, the subcooling range studied here might also not be large enough to observe a measurable effect of quenching, as was observed in a steady state study by Cheng et al. [93]. In that study, where water was used with subcooling levels ranging from 20 to 70°C, the higher degrees of subcooling resulted in a larger wall superheat at ONB (30°C versus less than 10°C at the lowest level of subcooling), a larger temperature overshoot over the fully developed boiling temperature (~15°C vs 0°C for the lowest level of subcooling), and a much more violent boiling inception relative to the reduced degrees of inlet subcooling. Furthermore, vapor backflow was improved at higher degrees of subcooling.

While subcooling did not greatly affect ONB conditions at the average heater temperature level, marked differences in peak temperature were observed across the subcooling range that extend beyond simply the difference in inlet subcooling temperature. Figure 5-10 details the peak temperature trends with heat load and inlet subcooling. For heat loads below ~40 W, differences in peak temperature were insignificant. However, at and above 40 W, the peak temperatures observed with 10°C subcooling were significantly lower (by up to 22°C across this range of heat loads) than with the other subcooling levels, which were not appreciably different from each other. This observed trend is likely due to the difference in generated vapor since higher subcooling will reduce the outlet vapor quality of the fluid. For example, for the 55 W heat loads, the steady state outlet vapor quality with 10°C of subcooling was ~33.5%, while for 2.5°C and 5°C of subcooling was ~41% and 39%, respectively. Due to this reduction in generated vapor, the backflow effect was less intense, and the peak temperature due to this backflow was partially mitigated. Therefore,

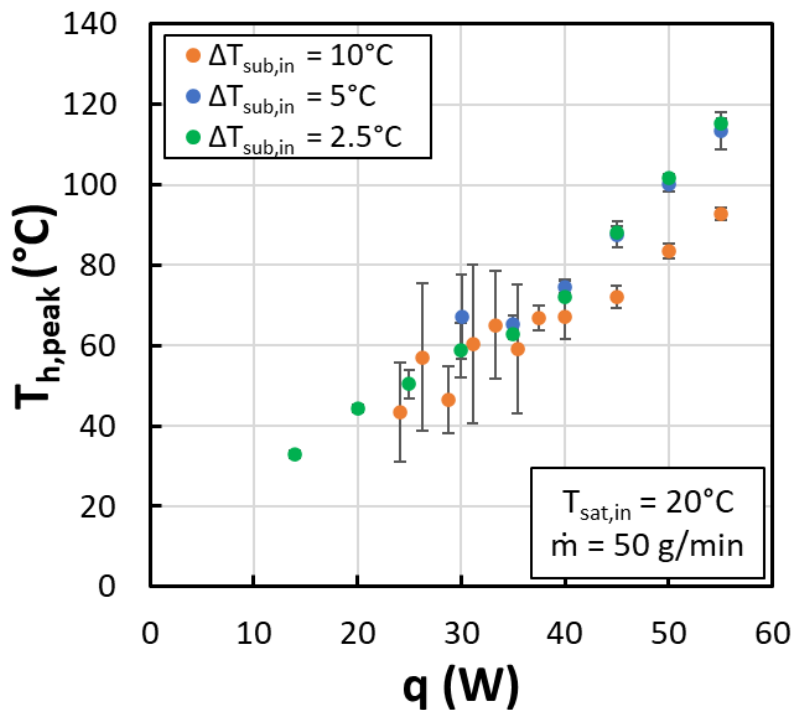

Figure 5-10. Peak heater temperature comparison across heat loads and different inlet subcooling degrees.

increased subcooling may be used to reduce the transient peak temperatures in this microchannel evaporator at heat loads above ~35 W.

While peak temperatures and ONB heater temperatures were reduced overall with higher amounts of inlet subcooling, the variability across different trials at a given peak heat load was inversely affected, particularly at heat loads <37.5 W. This variability was discussed in the context of the 10°C subcooling conditions above; however, it is interesting to note the reduction in variability in peak temperature with respect to reduced subcooling. To discuss this variability in peak temperature, it is also instructive to consider the time to boiling initiation in this context, which is shown in Figure 5-11. As heat load increases and inlet subcooling decreases, average time to boiling initiation decreases nearly monotonically. This follows logically from less thermal energy needed to reach saturation conditions at higher heating rates or reduced inlet subcooling.

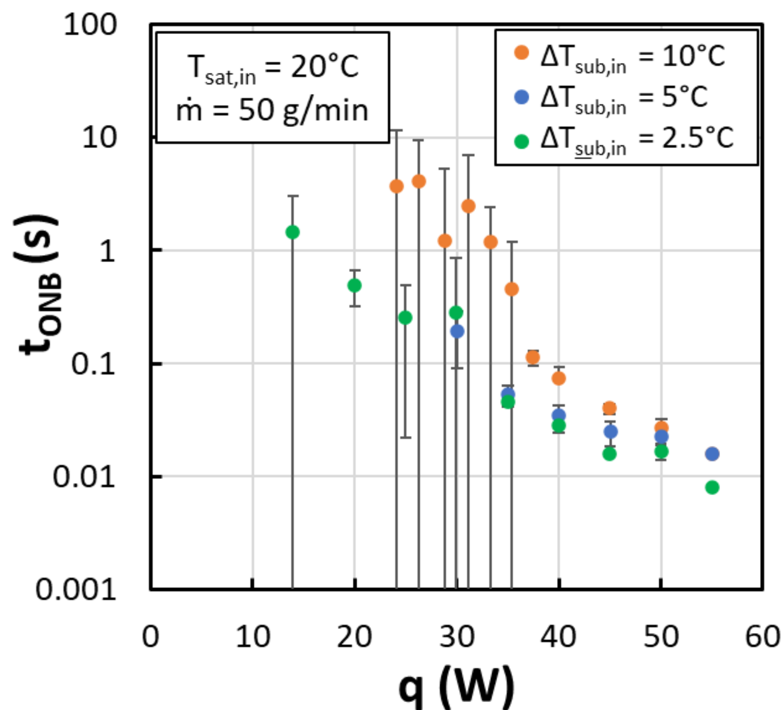

Figure 5-11. Time to boiling incipience conditions across multiple trials compared by heat load and inlet subcooling.

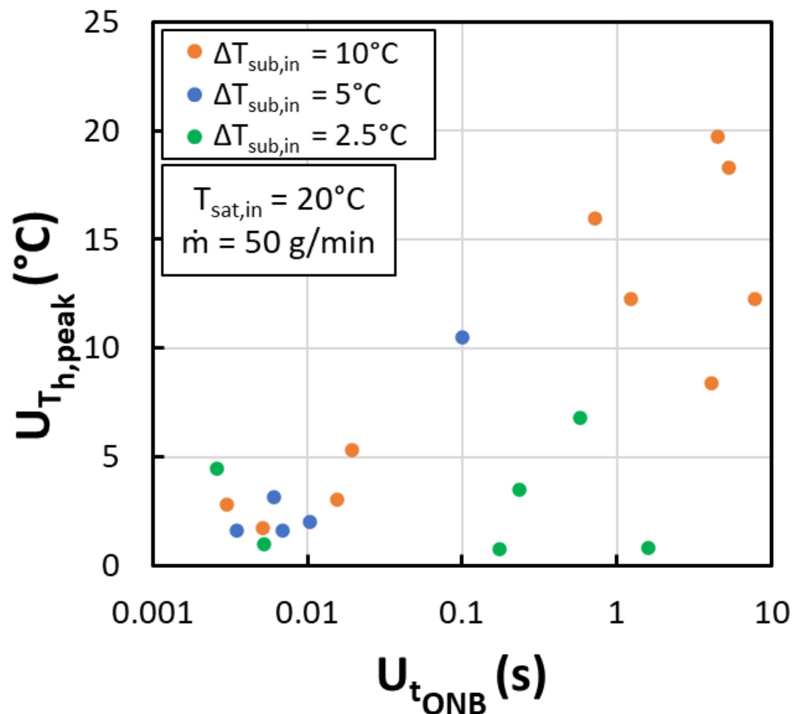

Figure 5-12. Variability across trials, heat loads, and inlet subcooling scenarios in peak temperature as a function of the variability in time to ONB at the same conditions.

However, the variability in ONB time is reduced at higher heat loads and at lower subcooling degrees.

Both peak transient temperature and time to ONB exhibited large variability at lower heat loads and increased subcooling, the trends of which are plotted versus each other in Figure 5-12. In general, the variability in peak temperature decreases as the variability in time to ONB decreases. The peak temperature and time to ONB variability were significantly higher with the 10°C inlet subcooling scenario, at up to 20°C at ~32.5 W, while the 5°C and 2.5°C scenarios had roughly 10.5°C and 7°C of variability, respectively, at a similar heat load. Furthermore, looking back to Figure 5-10, peak temperatures were not reduced for the lower heat loads with the increased subcooling, and considering the variability, were occasionally significantly higher than with the reduced subcooling scenarios.

The reduced vapor generation for the cases under the higher subcooling scenarios should result in less intense vapor backflow behavior, but this was not observed at the lower heat loads, as evidenced by the larger peak temperatures. It is possible that because decreasing the subcooling reduced the time to boiling, there was less time spent in the metastable superheated liquid state mentioned earlier, and backflow may have been lessened because of this. This agrees well with the variability plot, since variability in peak temperature generally decreased with variability in time to boiling incipience, and increased time to boiling generally correlated with increased peak temperature for the heat loads <37.5 W.

It is also possible that nucleation did happen at a lower temperature with lower levels of subcooling. However, this may not be reflected in the average heater temperature measurement, where differences in fluid temperature across the different subcooling levels will influence the average heater temperature. In this case, the higher inlet subcooling scenarios may have quenched nucleation site activation for a longer duration of time as mentioned in Chapter 4 with the other evaporator. A final point to highlight is that the higher vapor generation rate at a given heat load for the reduced subcooling scenarios resulted in similar behavior seen in the 10°C subcooling case but shifted to lower overall heat loads and with reduced variability. What this implies is that the nucleation process may have happened more consistently across conditions as heat load increased or as inlet subcooling decreased, though higher levels of inlet subcooling still generally resulted in decreased peak temperatures despite more observed variability at lower heat loads.

5.2.4. Effect of Mass Flow Rate on Stepped Heat Loads

As mass flow rate represents the convective and inertial impact of fluid flow on the boiling behavior, its impact was also studied parametrically. In this case, three different flow rates were studied while the other flow conditions (inlet saturation temperature and inlet subcooling) were held constant. Figure 5-13 presents the average heater temperature at the onset of boiling across the heat loads and mass flow rates investigated here. Increased flow rate slightly reduced average heater temperature at the onset of boiling, but again, it is difficult to draw conclusions on potential differences in nucleation dynamics since the average heater temperature was measured here. Cheng et al. [93] also found that increased mass flux generally suppressed nucleation site activation and resulted in up to a 10° increase in ONB superheat when doubling flow rate by decreasing the thermal boundary layer thickness and exposing the nucleation sites to increasing amounts of subcooled liquid. Cheng studied an appreciably wider channel in water with a

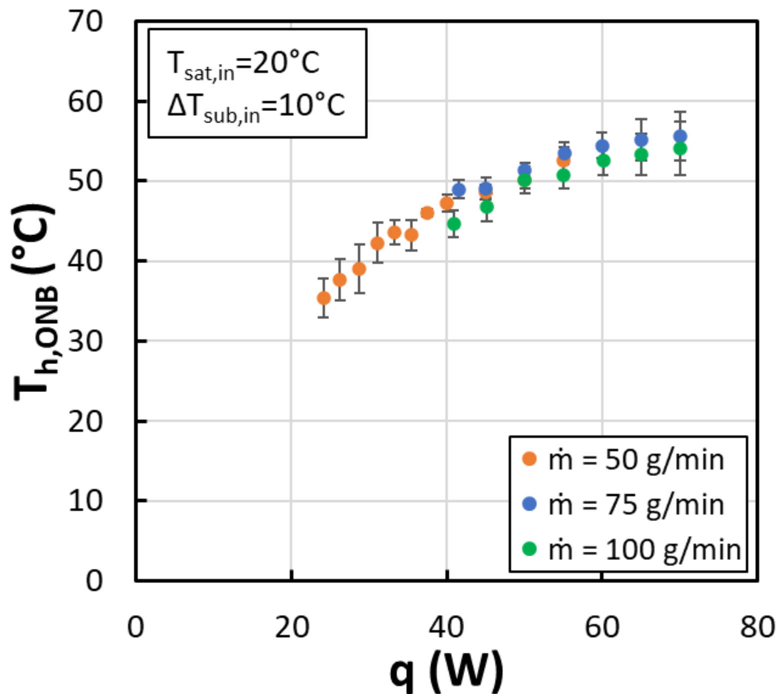

Figure 5-13. Effect of mass flow rate on average heater temperature at the ONB across heat loads.

subcooling level which was already significantly higher than this study, while the maximum mass flux studied (963 kg/m^{2}s) was lower than the lowest (1067 kg/m^{2}s) studied here. These could all contribute to the different results observed here.

The increased flow rate decreased the rate that the fluid heated up in the axial direction y according to an energy balance

$$T_f(y) = \frac{q(y)}{\dot{m}c_p} + T_{f,in}, \quad (5\text{-}2)$$

reducing the average fluid temperature similar to increased subcooling. Increased flow inertia will increase the length thermal boundary layer developing region and slightly increase the average heat transfer coefficient according to $y_{dev} \sim RePrD_{ch}$ and

$$h_{sp,avg} = \frac{1}{L_{ch}} \int_0^{L_{ch}} h(y, y_{dev}) dy. \quad (5\text{-}3)$$

The combined effect reduced the average heater temperature with higher flow rate, but there was a small reduction of several degrees at most. In addition, the increase in average heat transfer coefficient will increase the possible liquid superheat by more efficiently removing heat from the wall and possibly quenching the nucleation process.

Based on Hsu's work [79], the range of possible nucleation cavities is directly related to the thermal boundary layer thickness and the wall superheat, and as this boundary layer thickness decreases with higher flow rate due to increased flow inertial effects, the range of possible nucleation cavities which activate should also be reduced slightly and may be shifted to higher superheats. In addition, as discussed earlier, if the thermal boundary layer is reduced in size, so also will the superheated liquid sublayer. If this superheated liquid layer is thinner, nucleating bubbles may be condensed by the bulk liquid and require a larger wall superheat to effectively grow and detach [80]. In addition, boiling was not observed at the higher flow rates until 40 W,

despite the theoretical outlet vapor quality of >1-3% at down to 25-30 W, suggesting at least some form of delayed nucleation at least at lower heat loads. Therefore, it is possible that nucleation did indeed occur at a higher wall superheat overall with increased flow rate, but the effect may have been overshadowed in the average heater temperature measurement by the contribution from the enhanced single-phase cooling region.

While heater temperatures were not significantly affected by flow rate at the onset of boiling, peak transient heater temperatures were greatly impacted by flow rate in a highly non-linear manner. Figure 5-13 displays the comparison of peak transient heater temperature with flow rate and heat load, across multiple trials. First off, it should be noted that boiling was not observed during the interval under which a trial was conducted (~20 seconds) for heat loads below 40 W for the higher flow rate cases than 50 g/min. Next, perhaps the most interesting observation is that increasing the mass flow rate affects the peak temperature in a nearly parabolic manner, where a

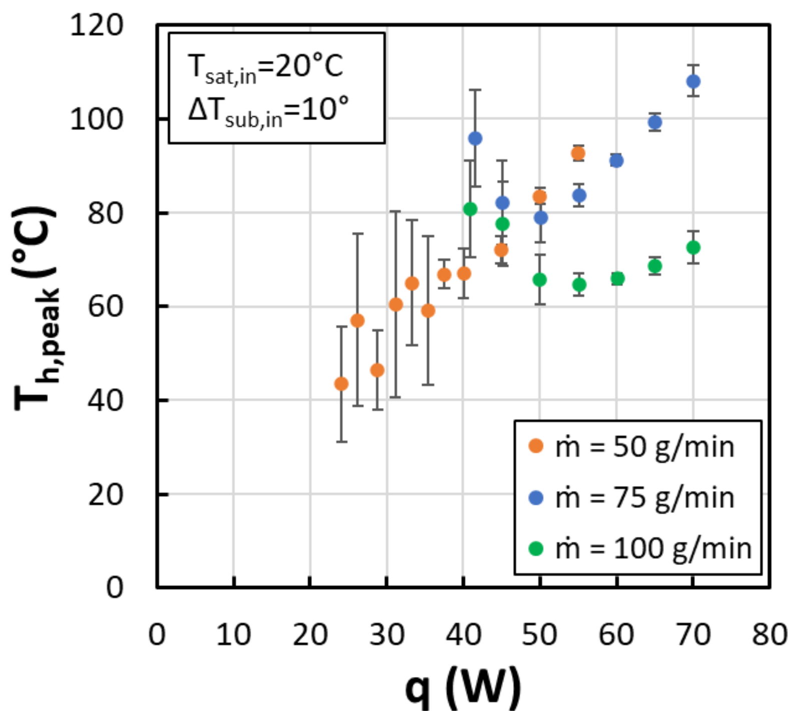

Figure 5-14. Effect of mass flow rate on peak transient heater temperature across heat loads and trials.

minimum peak temperature is observed. This behavior was not observed with the 50 g/min scenario, where a nearly monotonic increase in the average peak temperature occurred; however, certain trials did indeed reach temperatures which crested even those at much higher heat loads. This minimum peak temperature shifted to higher heat loads with increased mass flow rate. For example, at 75 g/min, the minimum occurred at 50 W, while for 100 g/min, the minimum occurred at 55 W. Furthermore, the peak temperatures at 40-45 W were significantly higher than that for many higher heat loads even beyond the minimum, for both the 75 and 100 g/min scenarios, while the rate that the peak increased was reduced as flow rate increased. At the highest heat load where all three flow rates were tested, 55 W, there was nearly a 30°C reduction between the 50 and 100 g/min peak temperatures. At 70 W, the difference between the 75 g/min and 100 g/min peak temperatures was ~36°C, or up to a massive 33% reduction in peak temperature.

This large reduction in peak temperature translates to significantly improved transient thermal performance of the device at higher flow rates and heat loads. However, the tradeoff is that higher peak temperatures must be accepted at lower heat loads. Increased flow rate reduced the amount of vapor production, and as with increased subcooling, decreased vapor production generally resulted in less intense vapor backflow and therefore diminished peak temperatures at higher heat loads. However, vapor generation rates do not fully capture the trends. For example, going from 50 to 75 to 100 g/min at 55 W decreased the steady outlet vapor quality from 33.5 to 20 to ~13% due to concomitant changes in flow rate, pressure, and outlet pressure drop dictated by the test facility response to the rapid generation of vapor. Interestingly, while the change in vapor quality was higher between the 50 and 75 g/min scenarios, the peak temperature dropped significantly more between 75 and 100 g/min. Furthermore, at 40-41 W, the vapor quality decreased from 21 to 11 to 7.5% when moving from 50 to 75 to 100 g/min, but in this case the

peak temperature trends were different, where now the 50 g/min scenario had the lowest peak temperature at 67°C and the 75 g/min scenario had the highest at ~96°C.

This complex behavior between peak temperature, vapor quality, and heat load suggests competing effects or different dominant mechanisms between heat loads at a transition of around 40-45 W, and at vapor qualities close to or below 10%. The time to boiling incipience may also help interpret the results, particularly for these lower heat load cases. Figure 5-15 shows the ONB time across the different flow rates and peak heat loads tested. Despite boiling triggering earlier and at lower heat loads for the 50 g/min scenario, with the 75 and 100 g/min scenarios, boiling was not observed below 40 W. In addition, boiling incipience times increased with flow rate, reflecting a reduced sensible heating rate in the fluid. The time to boiling again also exhibited significant variability at the higher flow rates on the lower end of the heating range <50 W, and

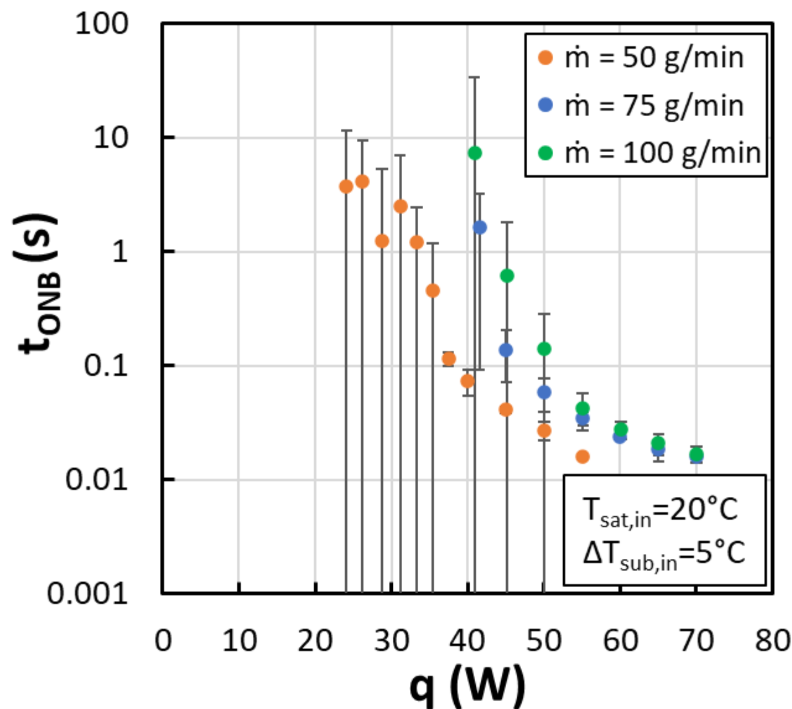

Figure 5-15. Time to boiling inception across multiple trials compared at different peak heat loads and flow rates.

these cases again remained in the metastable superheated liquid state for longer durations

according to flow visualization. A longer duration in this state could explain why the average peak temperatures for the 75 and 100 g/min scenarios were significantly higher than the 50 g/min scenario around 40-45 W. The steady state vapor quality underestimate the vapor generated in these scenarios due to the existence of a transient non-equilibrium state, since, if the fluid temperature is in a superheated liquid state, an additional amount of sensible energy stored in the superheated liquid will be released on top of the energy coming from the heater at boiling incipience.

The inversion in peak temperatures with flow rate between 40 W and 55 W suggests a transition in dominant mechanism. Despite the lower steady vapor quality but higher time to ONB for the 100 g/min scenario compared with the 75 g/min scenario at ~40 W, the average peak temperature of the 100 g/min scenario is about 15°C lower. Furthermore, both temperatures are higher than the 50 g/min case at the same heat load, which should have a higher steady vapor quality. The 75 g/min case might reasonably be expected to have a lower peak temperature than the 100 g/min scenario, since it would spend less time in the metastable liquid state and therefore generate less additional vapor. The lower peak temperature for the 100 g/min scenario suggests an inertially-dominant mechanism partially mitigates vapor backflow and subsequently reduces peak temperature while simultaneously also potentially delaying the onset of boiling and increasing time spent in the metastable liquid state. However, as superheats increase, nucleation site activity also increases, and the possible quenching effects of the increased flow rate may have diminishing effects while the backflow mitigation effect becomes dominant especially as flow rate increases.

Lee [21] developed a stability parameter R_{stab} based on an analysis of the static forces experienced in a microchannel during bubble generation. Lee described a forward force due to upstream incoming liquid and the presence of an inlet restriction, while a backward force was due

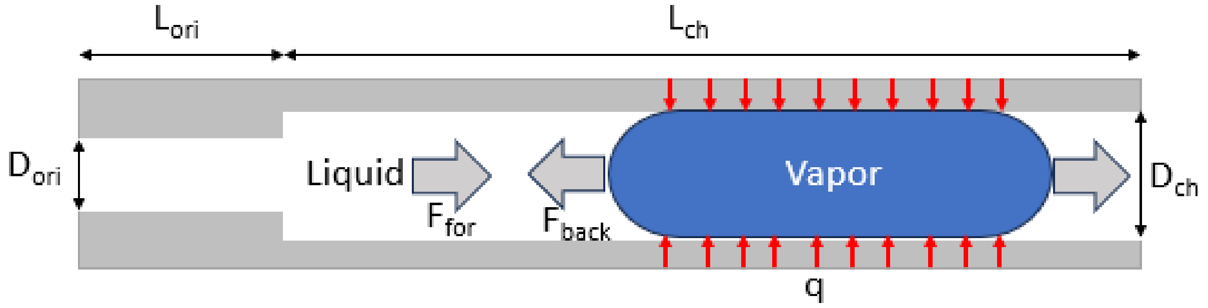

Figure 5-16. Schematic depicting various forces acting on fluid in a microchannel during the flow boiling process.

to the evaporation momentum flux from rapidly generated vapor. Figure 5-16 schematically depicts these forces. Theoretically, if the ratio of these forces is less than 1, then the vapor backflow will not occur, and the flow will be stable. Stability with $R_{stab}<1$ was experimentally validated in Lee's paper. This relationship was developed in the context of steady heating; however, the principle should still apply during the transient, though additional dynamic forces due to the bubble expansion and additional vapor generation due to the liquid superheating may need to be considered. In addition, there will be additional forward frictional forces due to the frictional losses in the channel depending on where the bubble first forms. This channel frictional force, which would serve to increase the forward force, was neglected in the analysis to provide an upper bound on the stability ratio and not require knowledge of the first bubble location. The stability ratio R_{stab} was defined as

$$R_{stab} = \sqrt{\frac{F_{back}}{F_{for}}} \tag{5-4}$$

$$F_{back} = \frac{1}{4\rho_v A_{c,ch}} \left(\frac{q}{N_{ch} h_{lv}}\right)^2 \tag{5-5}$$

$$F_{for} = \frac{G^2 A_{c,ch}}{\rho_l} + F_{ori} \tag{5-6}$$

$$F_{ori} = \frac{1}{2\rho_l}\left(\frac{GA_{c,ch}}{A_{c,ori}}\right)^2 A_{c,ch}\left[\frac{1}{2}\left(1-\frac{N_{ch}A_{c,ori}}{A_{c,plen}}\right)+\frac{f_{ori}L_{ori}}{D_{ori}}+\left(1-\frac{A_{c,ori}}{A_{c,ch}}\right)^2\right]. \quad (5\text{-}7)$$

Based on flow visualization where residual vapor was not observed in the inlet plenum for all flow rates at steady state, R_{stab} should be close to or less than 1 at steady state. Calculating the values for R_{stab} at 55 W gives between 1.2 and 0.6 for 50 and 100 g/min, respectively. In this case, $R_{stab}>1$ for 55 W at 50 g/min, but given the stability at steady state, there is likely some additional forward force provided from the frictional losses in the channel that assists in stabilizing the flow. However, during the transient, the forward forces are insufficient to prevent the backflow from the temporarily increased rate of vapor generation due to the initially high wall superheat. The forward force relationships in this ratio depend on the channel mass flux, G, which is simply the mass flow rate normalized by the total channel cross-sectional area. Therefore, based on the above equations, increasing the mass flow rate from 50 to 100 g/min while holding every other parameter constant will quadruple the forward inertial force and subsequently half R_{stab}.

Another justification of this improved flow inertial effect at higher heat loads relates to the vapor backflow flushing rate, or the decay rate from the peak temperature to steady state. A simple logistic growth curve model can be employed to understand how these values vary across the different flow rates. The following equation represents the non-dimensionalized heater temperature as a function of time between the peak and steady state temperatures as a fit to a logistic growth curve.

$$\frac{T_h - T_{h,ss}}{T_{h,peak} - T_{h,ss}} = \frac{1}{1+\exp\left(\kappa\left(t-t_{mp}\right)\right)}, \quad (5\text{-}8)$$

Table 5-1. Vapor backflow decay rate as a function of flow rate.

Mass Flow Rate (g/min)	50	75	100
κ (1/s)	25.6	69.7	121.6

where κ is the growth/decay rate coefficient, and t_{mp} is the midpoint of the curve. This logistic model is a simplified version of the exponential growth model used in Chapter 4. In this case, a larger value of κ represents a faster decay rate and therefore a stronger vapor backflow flushing rate since the device reaches steady state quicker. This above equation was fit to the non-dimensionalized temperature data for 55 W, which is the maximum heat load for which there was data across all three flow rates. The resulting decay rate factors are shown in Table 5-1. As is clear from the table, the decay rate from peak temperature to steady state is much steeper as the flow rate is increased, indicative of an improved vapor backflow flushing rate. This further justifies the increased flow inertial mechanism as a peak temperature reduction behavior at the higher flow rates. As mentioned above, increasing mass flow rate likely does not increase the forward force independently of the backward momentum force (and additional dynamic forces not considered in the force balance), especially at lower heat loads where few nucleation sites may be activated. The relative strengths of these forces then greatly influence the peak temperature as heat load is increased, resulting in the highly non-linear relationship observed. Nevertheless, increasing mass flow rate presents an effective strategy for reducing transient peak temperature spikes in this evaporator.

5.2.5. Effect of Inlet Restriction on Device Behaviors

The vapor backflow and subsequent spikes in device temperature observed here shed insight on the effects of channel and inlet restriction ratios on performance. Figure 5-17 compares the transient temperature responses of both evaporators. For the 38 μm hydraulic diameter device, the observed wall superheats at ONB were large at up to 33°C while for the 52 μm hydraulic

diameter device, wall superheats reached up to 50°C. The inlet orifices promote flow stability and uniformity at steady state, as clearly observed in Figures 4-3 and 5-2; however, during the transient, they are clearly not sufficient, as both devices suffered from vapor backflow. The combination of the small channel dimensions along with the large superheat may result in intensified vapor backflow due to the bubble confinement under rapid vapor generation rates. However, while the ONB temperature was higher with the 52 μm device, the peak temperature was overall significantly lower than the 38 μm device by ~20°C. The inlet restriction ratio with the 38 μm device, ~1.3:1, is much smaller ~2:1 ratio for 52 μm device or the 4:1 ratio which was seen to limit vapor backflow during transient flow boiling in Huang et al. [59]. In addition, the channel dimensions are much smaller for the 38 μm device than either of those other mentioned devices. These channel and orifice dimensional differences likely contributed to the differential responses observed across these devices in Figure 5-17. Although smaller channels are attractive from a

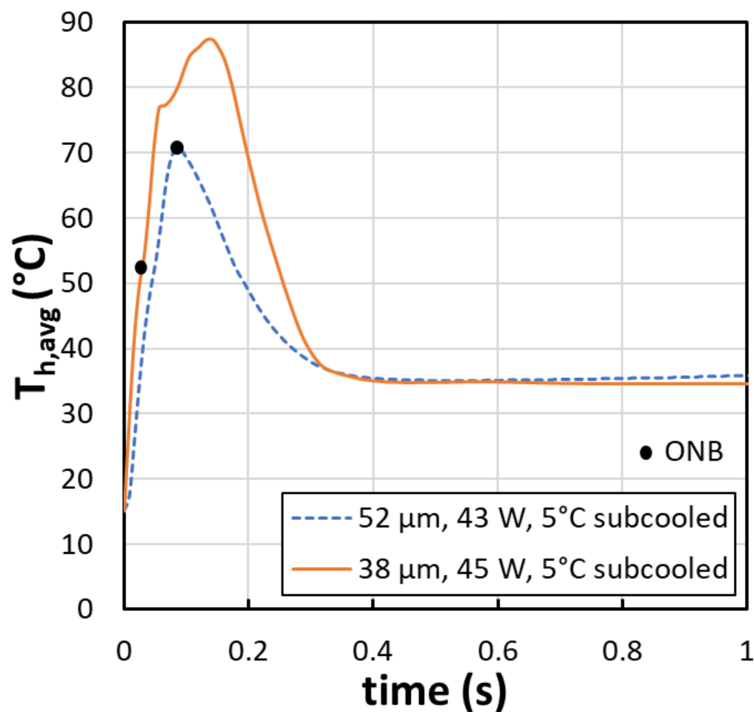

Figure 5-17. Comparison of transient behavior between both test devices at similar tested conditions.

steady state performance standpoint due to an increase the heat transfer area and improvement in heat transfer coefficient, as is clearly noticeable here where the steady state temperature of the 38 μm device is slightly lower than the 52 μm device even at a slightly higher power, their effects on transient boiling are evidently important, and additional constraints on design may be required to achieve both high effectiveness and minimal overshoot during device transients. In addition, a more critical approach to designing the channel inlet orifices may be required to reduce vapor backflow during the transients as well as during steady state .

5.3. Flow Boiling Model for Stepped Heat Loads

The onset of nucleate boiling for this microevaporator subjected to stepped heat loads resulted in large peak temperatures due to high superheats and subsequently intense vapor backflow which led to temporary dryout conditions within the channels. The peak temperatures were strong functions of heat load, flow rate, and subcooling, while the ONB temperatures were strong functions of heat load and to a lesser extent subcooling and flow rate. These high peak temperatures and vapor backflow would be seriously detrimental to the longevity and performance of a real high-heat flux device cooled with such a microevaporator. Continued pulses or cold-startups would drastically accelerate the thermal fatigue and failure of the device due to large temperature fluctuations experienced during every ONB condition. Therefore, a model framework was developed within the NavyHHF tool for use as a design tool in predicting future performance and for understanding the potential role a phase change material may have on device behavior.

5.3.1. Development of Model Framework within NavyHHF

As mentioned in Chapter 4 for the preliminary work, the NavyHHF default model required adaptation to capture the observed transient behavior. However, the vapor backflow experienced by the 52 μm evaporator did not lead to an extended peak temperature; rather, the ONB commenced and resulted in an immediate decrease in temperature. Therefore, a new framework which was adapted from the work in Chapter 4 was developed to capture the current device behavior under a selection of heat loads at the baseline fluid flow conditions. The proposed approach breaks the transient behavior into three distinct regions that are highlighted for a representative test case in Figure 5-18: (1) the subcooled liquid-only cooling region, (2) the vapor backflow region immediately following the ONB, and (3) the transitional region from the peak temperature reached to the steady state subcooled flow boiling state. To determine the behavior in each regime, a semi-empirical iterative method was used where transient values, which will be

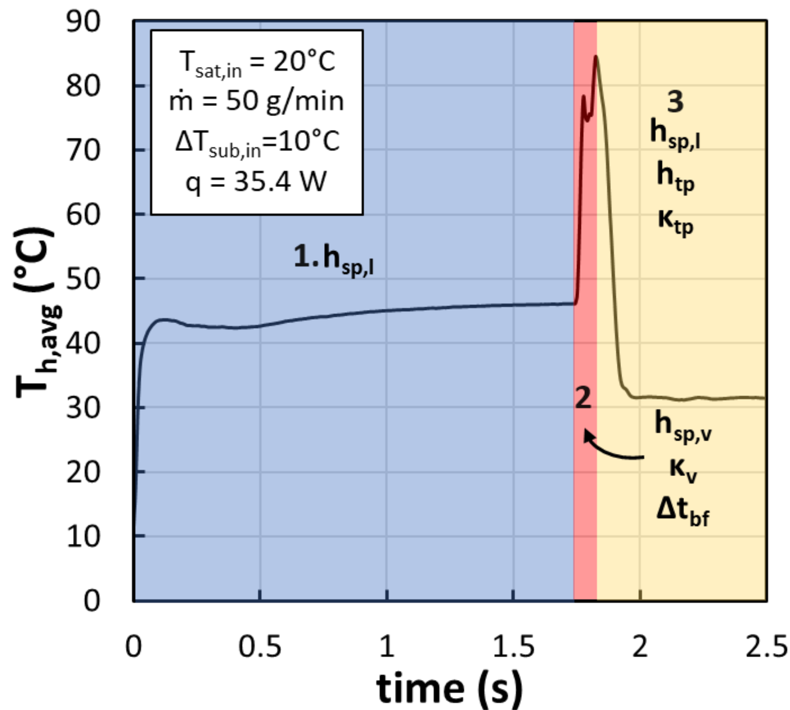

Figure 5-18. Representative regime map for transient flow boiling model created in NavyHHF.

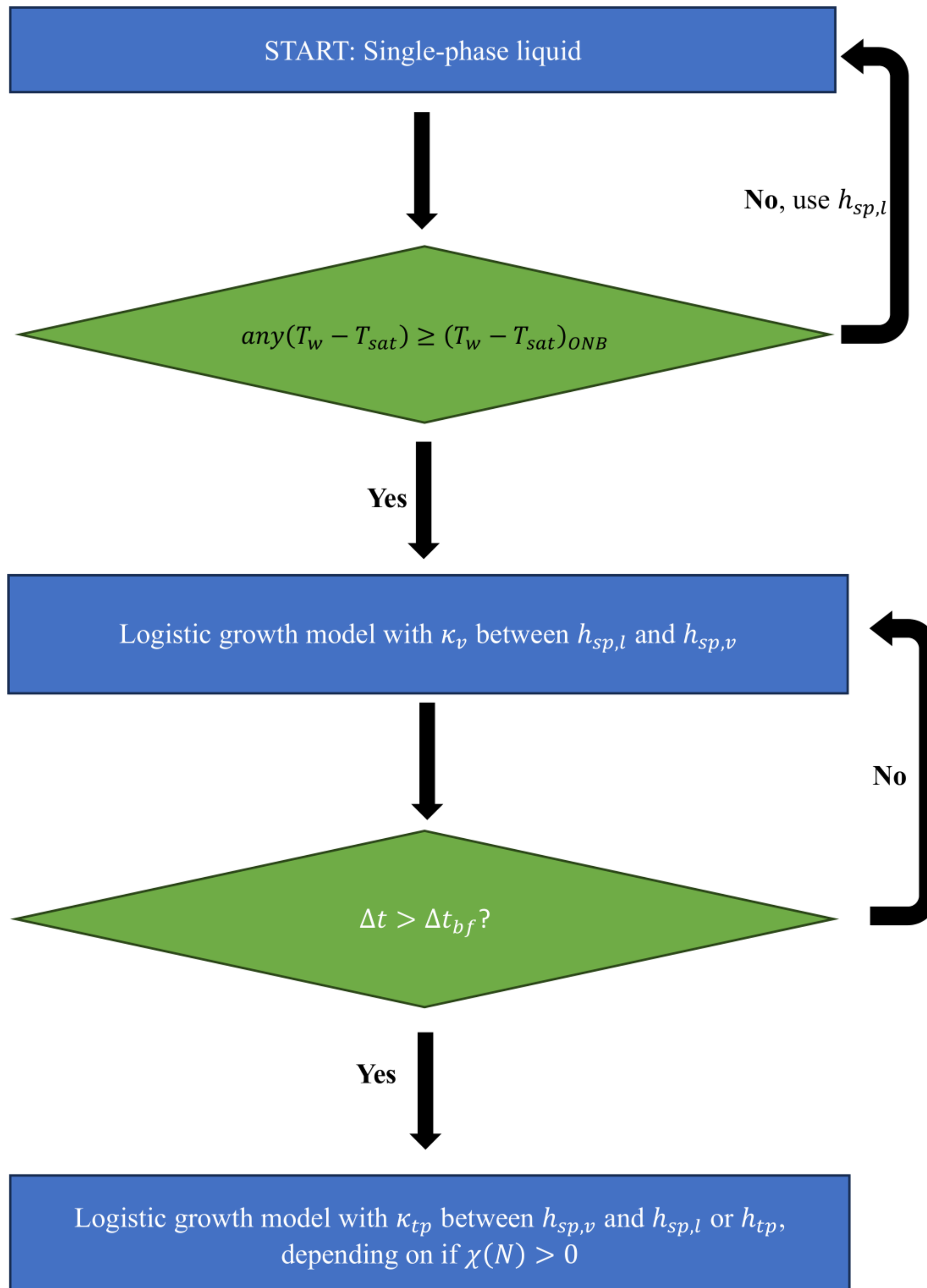

Figure 5-19. Process flow schematic for transient flow boiling model approach in NavyHHF.

detailed shortly, were modified until the average heater temperature in the model closely matched that in the experiment.

The exponential growth model approach from Chapter 4 was again adapted here but with a regime-dependent growth factor. A process flow schematic of the model approach is shown in

Figure 5-19. First the wall superheat which resulted in the closest heater temperature match at ONB between the model and experiment was determined iteratively. Then, the heat transfer coefficient was transitioned to a vapor-only heat transfer coefficient for the backflow regime. During the vapor backflow regime, the backflow intensity and duration is represented by κ_v, which affects the rate of transition from the single-phase liquid heat transfer coefficient to the single-phase vapor heat transfer coefficient. The total duration of this backflow regime was obtained by matching the time at which the model and experiment reached their peak temperatures, then κ_v was modified until the rise time and peak temperatures roughly coincided between model and experiment. Finally, the growth factor κ_{tp} used for the transition between the single-phase vapor heat transfer coefficient and single-phase liquid/two-phase fluid heat transfer coefficients sets the transition from the peak temperature to the steady state subcooled flow boiling regime. The method which is normally used in NavyHHF to differentiate which nodes are single-phase or two-phase, which is dependent on vapor quality, χ, was then again used for this regime:

$$h_{reg}(N,t) = \begin{cases} h_{sp,l}, & \chi \leq 0 \\ h_{tp}, & 0 < \chi < 1 \\ h_{sp,v}, & \chi \geq 1 \end{cases} \tag{5-9}$$

In the model, the exponential growth model is

$$\frac{dh}{dt} = \kappa_x h \left(1 - \frac{h}{h_x}\right) \tag{5-10}$$

where

$$\kappa_x = \begin{cases} 1 & (T_w - T_{sat}) < (T_w - T_{sat})_{ONB} \\ \kappa_v & (T_w - T_{sat}) \geq (T_w - T_{sat})_{ONB} \ \&\ \Delta t \leq \Delta t_{bf} \\ \kappa_{tp} & \Delta t > \Delta t_{bf} \end{cases} \tag{5-11}$$

and

$$h_{tb} = \begin{cases} h_{sp,l} & (T_w - T_{sat}) < (T_w - T_{sat})_{ONB} \\ h_{sp,v} & (T_w - T_{sat}) \geq (T_w - T_{sat})_{ONB} \ \& \ \Delta t \leq \Delta t_{bf}. \\ h_{reg} & \Delta t > \Delta t_{bf} \end{cases} \qquad (5\text{-}12)$$

This approach was used to build a model in NavyHHF for three representative heat load cases, all at the baseline flow conditions ($\dot{m}$ = 50 g/min, $\Delta T_{sub,in}$ = 10°C, $T_{sat,in}$ = 20°C): 35.4 W, 37.5 W, and 55 W. These cases were chosen for the following reasons. First, between the 35.4 and 37.5 W heat loads represented a transition in observed transient boiling behavior. Those cases ≤35.4 W peak heat load reached a steady state in liquid-cooling prior to the ONB and reached severe peak temperatures in some cases, though variability was large. The 37.5 W and 55 W cases represented the effective bounds for the range of additional heat loads tested with more predictable behavior between these. Therefore, it was deemed sufficient to model these cases, considering the remaining cases could easily be added with more time in future efforts if needed.

5.3.2. NavyHHF Model for 35.4 W Case

The first test case modeled was the 35.4 W case with the highest peak temperature across the trials. This case reached a metastable steady state in liquid cooling prior to ONB, and because of this, the model required an additional factor where boiling was delayed until the time and temperature matched the experiment. The results of this model compared with the experiment are shown in Figure 5-20. The steady state liquid temperature matches closely between the experiment and model, though there is some slight oscillation in the experimental profile due to pressure and flow rate response. The transient rise time and peak temperature match the experimental profile well, though there is an additional dynamic which was not captured but will be discussed later. The predicted decay time to steady state and steady state temperature also match the experimental results well. Thus, this model gives a reliable prediction into the transient device behavior and

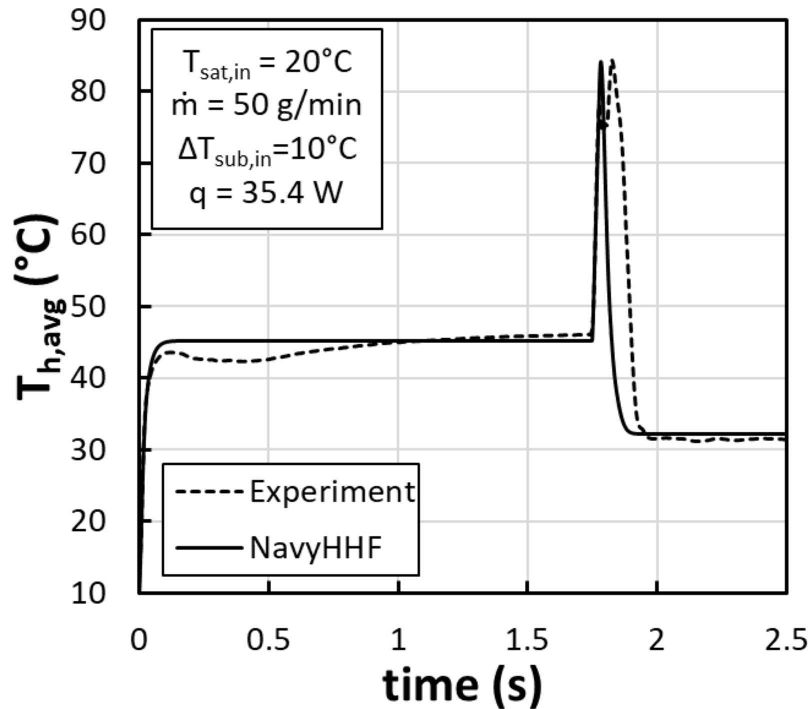

Figure 5-20. Experimental results compared with transient boiling model in NavyHHF at 35.4 W peak heat load.

peak temperature reached, though additional optimization is needed to account for this additional dynamic during the backflow phase.

Figure 5-21 details the backflow region in more detail, where an additional dynamic, which is not captured with this model, resulted in a delayed decay to steady state. This dynamic was difficult to interpret since flow visualization during this stage revealed nearly entirely vapor within the channel. However, there are several possible explanations for this behavior. One is that in the model, each channel is assumed to have the same behavior due to the large computational complexity and demand which would be needed to model every channel independently. In the real device, there are 250 channels which have complex and dynamic interactions, and the heater temperature is an average of the superimposed contributions of these different channels. It is therefore possible that the multitude of channels are contributing to a different dynamic backflow behavior in this region which is not captured by the simple identical channel behavior within the

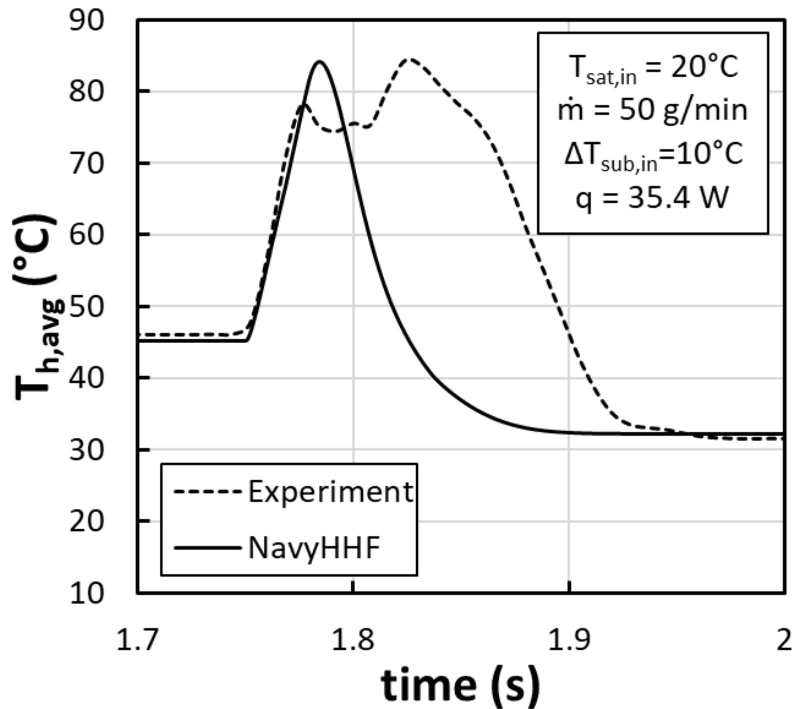

Figure 5-21. Zoomed-in view of Figure 5-20 to show comparison of backflow region, which experiences an additional dynamic that delays the temperature decay.

model. It is also possible that the perturbations to the system resulted in coupled behavior which is not captured in a model of just the evaporator. The vapor backflow phase may therefore include several different stages of behavior dependent on local pressure and mass flow rate, and either transient flow conditions or another backflow growth rate would be required to capture this more accurately. NavyHHF includes the possibility of modeling additional system components such as pumps, heat exchangers, and reservoirs; however, a detailed characterization of these components would be required for accurate performance expectations but was beyond the scope of this work.

The synchronized heater temperature and exponential growth model heat transfer coefficient are shown in Figure 5-22. While each node has its own associated heat transfer coefficient (and some of which are two-phase or single-phase at steady state), an average value was used for demonstrating the behavior. The initial heat transfer coefficient is liquid-only and does not change much during the single-phase heating phase, with a value of ~14 kW/m^2-K. At

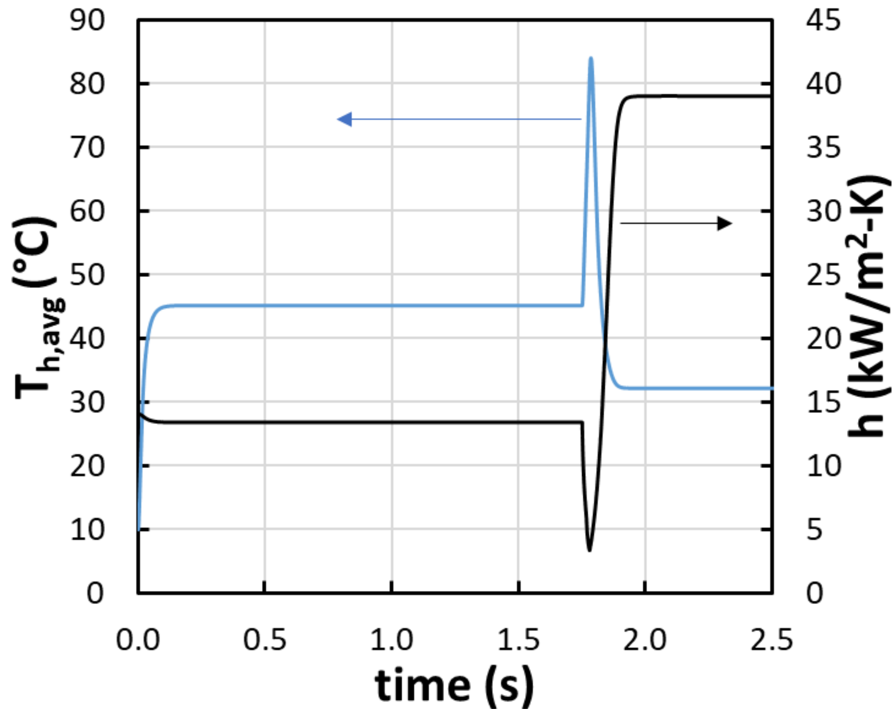

Figure 5-22. Model heater temperature synchronized with heat transfer coefficient following the exponential growth model for 35.4 W heat load.

the ONB, the backflow model transitions the heat transfer coefficient to a vapor heat transfer coefficient with a rate which depends on the vapor growth constant value, which here was 42/s, and diminishes to an average minimum of ~3.4 kW/m^2-K. Then, at the peak temperature, as the vapor backflow is slowly overcome, the model transitions again to a steady state subcooled flow boiling phase at a much lower temperature according to the two-phase growth constant at 35/s. The average steady state heat transfer coefficient (which includes both nodes of single-phase and two-phase) was ~39 kW/m^2-K, reflecting the large increase in heat transfer performance characteristic of flow boiling.

5.3.3. NavyHHF Model for 37.5 W Case

The next case modeled was the 37.5 W case since a transition in behavior was observed at this heat load. For 37.5 W and all subsequent higher heat loads, the liquid-only state diminished in duration while the vapor backflow phase lasted longer and resulted in higher peak temperatures

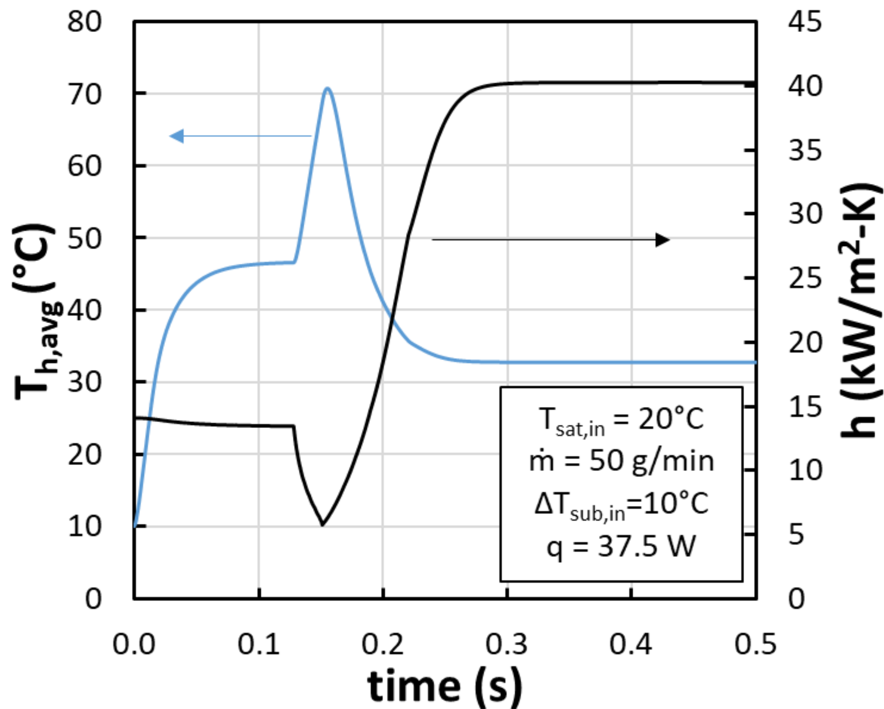

Figure 5-23. Model heater temperature synchronized with heat transfer coefficient following the exponential growth model for 37.5 W heat load.

with heat load. Figure 5-23 compares the NavyHHF model and experiment for this heat load. The single-phase only duration is only about 0.14 seconds here, reflecting the much quicker activation of nucleation sites. Again, the model captures this liquid-cooling region, the ONB temperature, and the temperature rise rate during backflow exceptionally well. The ONB temperature happens slightly earlier in the model, but this difference is negligible. However, while the peak temperature is well-predicted, there is again a second backflow phase with nearly stagnant behavior where the temperature does not change much but then reached the point of rapid decay as the backflow is quickly swept downstream of the channel. In this phase, the decay rate is well predicted by the same 35/s decay rate, and the steady state temperatures agree well again. It is possible that in this case this dynamic could be captured with an additional, reduced growth rate factor; however, the overall trend in transient temperature as well as the ONB and peak temperatures is well-captured.

The heat transfer coefficient for this 37.5 W case is shown alongside the corresponding heater temperature in Figure 5-23. During the transient liquid cooling phase, the heat transfer coefficient is nearly constant but decreases slightly due to the increase in fluid temperature, with an average value of around 13.8 kW/m^2-K. At the ONB, the vapor backflow model drives the average heat transfer coefficient down due to vapor heat transfer, with an average value declining to about 5 kW/m^2-K before the peak temperature is reached, and the heat transfer rate begins to increase again. At this point, the average heat transfer coefficient increases monotonically until about 0.3 seconds and attains the steady state value of ~42 kW/m^2-K, a slightly higher value than the 35.4 W heat load due to the heat flux dependency of the two-phase heat transfer coefficient. The remaining heat load cases have similar behavior, with the ONB time decreasing while wall temperature at ONB increases. In addition, the vapor backflow and two-phase growth rates vary by case as well due to different prevailing strengths of the dynamics in these phases. For comparison to the low heat load case, 35.4 W, and the transitional case, 37.5 W, the 55 W case was also chosen for modeling since it was the maximum peak heat load tested under this set of inlet fluid conditions.

5.3.4. NavyHHF Model for 55 W Case

The 55 W heat load case was the last modeled case and is shown in Figure 5-24 across both model and experiment. In this case, the secondary backflow dynamic resulted in a much steeper slope than the lower heat loads and capturing the overall temperature rise matched more closely to the experiment with the single backflow growth rate. The vapor growth rate was much slower here to match this overall temperature rise time, at about 5/s. However, the temperature decay rate to steady state was also much lower, with a two-phase growth rate of 10/s, reflecting the much longer prevalence of the transient boiling dynamics due to the much higher vapor generation rate and

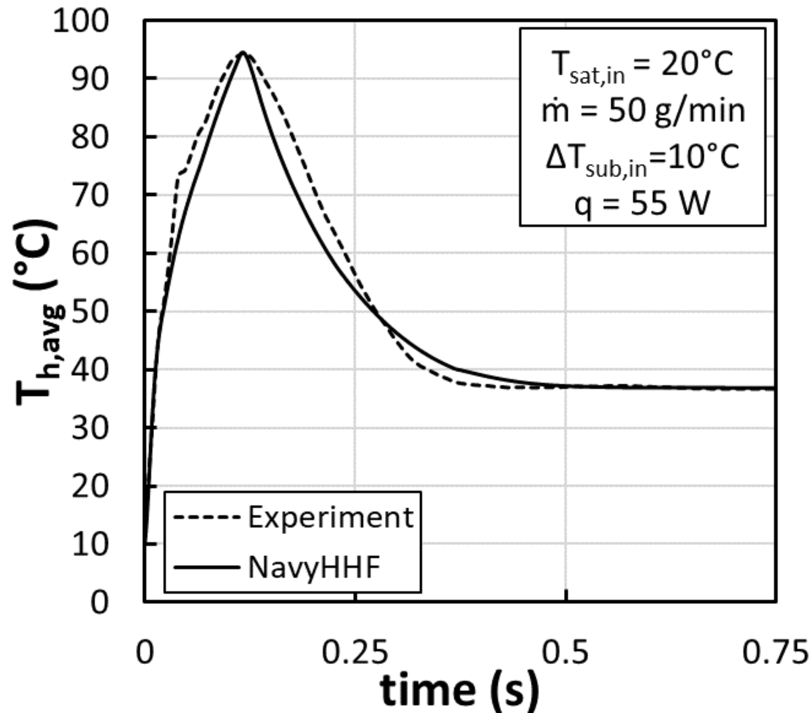

Figure 5-24. NavyHHF and experimental heater temperatures synchronized for 55 W heat load case.

higher heat load. Finally, the temperature decays to the steady flow boiling phase, where again the steady temperature is exceptionally well-predicted by the heat transfer correlations.

The transient heat transfer coefficient for this final heat load case is shown in Figure 5-25. Again, the heat transfer coefficient starts out in the liquid-only phase at 14 kW/m^2-K and stays roughly constant until the ONB occurs a short time later, then decaying to a minimum average value of ~5.4 kW/m^2-K as the peak temperature is reached at 93.4°C. Then, the much slower temperature decay to steady state with the growth factor of 10/s results in a steady, average heat transfer coefficient of ~52.5 kW/m^2-K. This is about 30% higher than the two lower tested heat loads again due to the heat flux dependence of the two-phase heat transfer coefficient which boosts cooling performance at higher heat loads. This transient heat transfer coefficient behavior captures the transient temperature profile of the device well and thus demonstrates the large shift in heat transfer which occurs during the transition from liquid cooling to steady state flow boiling when

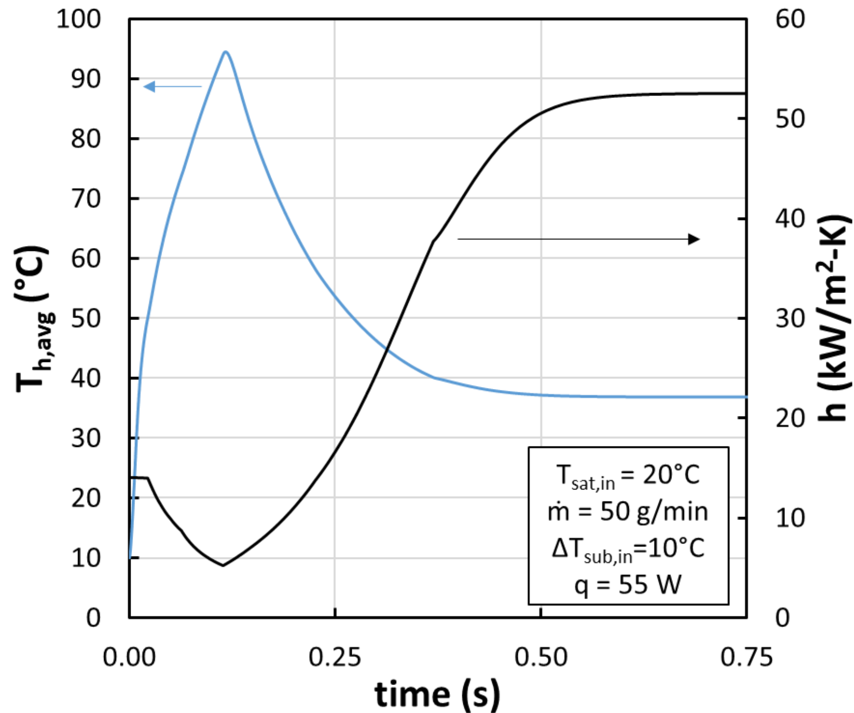

Figure 5-25. Model heater temperature synchronized with heat transfer coefficient following the exponential growth model for 55 W heat load.

vapor backflow dynamics are prevalent in the device, demonstrating the need for methods to reduce this peak temperature, such as increased subcooling or mass flow rate.

5.4. Chapter Summary

In this chapter, stepped heat loads on a 38 μm hydraulic diameter, 250 microchannel evaporator with a small time constant were investigated across a range flow rates, inlet subcooling levels, and peak heat loads. Large superheats prior to the onset of nucleate boiling (ONB) of up to 35°C were observed and were dependent on peak heat load, similar to the 52 μm hydraulic diameter evaporator, and to a less extent possibly subcooling and flow rate, though the latter two were difficult to confirm due to the use of the average heater temperature in measurements. The large superheats were likely due to a combination of smooth channel surface, low surface tension fluid, and a delay in nucleation conditions associated with delayed thermal boundary layer growth

or bubble quenching from the transient heating conditions and large liquid heat transfer coefficients.

Notably, due to the small channel dimensions and the large superheats, vapor generation at the ONB was explosive and resulted in severe vapor backflow despite the presence of inlet orifices. The intense vapor backflow resulted in temporary dryout conditions within the channel, rapidly driving up the device temperature. This contrasts with the response of the 52 µm hydraulic diameter evaporator where the temperature dropped immediately after the ONB despite the presence of vapor backflow. Eventually, incoming subcooled liquid overcame this backflow and precipitated a decay to a steady state flow boiling condition at a much lower temperature characteristic of the efficient phase change heat transfer process, with notably no backflow observed in the inlet plenum at steady state. The transient differences observed between the two test sections suggest that additional design constraints are needed on channel and inlet restriction design to optimize both the transient and steady state performance rather than using an inlet restriction dimension which is agnostic to the channel dimensions.

The peak temperature generally increased with peak heat load; however, for heat loads with lower vapor qualities, a metastable liquid cooled state with a stochastic duration was reached prior to boiling. In this state, it was hypothesized that due to the large wall superheat and liquid heat transfer coefficient, a superheated liquid state existed and further increased the intensity of vapor generation at the ONB. In some cases, due to this state, the peak temperatures were highly stochastic and occasionally higher at the lower heat loads than for the higher ones. Increasing the subcooling reduced the time to ONB conditions but also greatly reduced the peak temperatures, particularly at higher heat loads, likely due to the reduced amount of vapor production. Increasing the mass flow rate resulted in significantly reduced peak temperatures at the higher heat load

ranges of up to 33%. However, a complex peak temperature relationship, characterized by a parabolic shape with a minimum which shifted by flow rate, was observed. It was hypothesized that this behavior was due to competing effects by dominant mechanisms which varied with heat load and thus resulted in an optimal peak heat load condition.

The large transient temperature spikes experienced by this evaporator may be detrimental to device performance and long-term reliability. Increasing mass flow rate and subcooling significantly improved transient performance; however, predicting the device behavior for a given set of conditions is important to designing effective thermal management solutions under encompassing both transient and steady state behaviors. To that end, a model was developed in the computational design tool NavyHHF to predict the transient flow boiling performance of this evaporator under a selection of testing conditions. The model was developed semi-empirically and by considering the different physics to determine phases of behavior. An exponential growth model was employed to define the rate of transition between liquid-cooling, vapor backflow, and steady state flow boiling regimes to match experimental observations. After tuning, the model captured the experimental temperature trends adequately, though further optimization and an understanding of the dynamic behavior experienced during the backflow phase are necessary to fully capture the dynamics during this state. Notably, the development of this model can then be used to understand the potential role of incorporating phase change materials into the device.

CHAPTER 6. Impact of Phase Change Material on Microchannel Flow Boiling Under Stepped Heating

Phase Change Materials (PCMs) were found to mitigate the transient temperature response in several earlier studies, as was mentioned in Chapter 1. In addition, in Chapter 4, ramped heating, which mimicked additional heat capacity, was found to greatly reduce the peak temperatures and mitigate vapor backflow at the onset of nucleate boiling (ONB). Therefore, the impact of PCM on microchannel flow boiling under transient heat loads was investigated semi-empirically for its potential transient thermal buffering impacts and to determine trade-offs in PCM choice with observed behaviors.

6.1. General PCM Buffering Effects at 35.4 W

The impact of including a PCM was investigated comprehensively at 35.4 W of peak heating for gallium and gallium-metal foam composite structures, which had the most desirable properties for buffering these microchannel devices as mentioned in Chapter 1. The PCM area and thickness as well as effective PCM latent heat and thermal conductivity were parametrized to identify trends in behavior and possible thermal buffering capabilities. In Chapter 3, the heat to the fluid was extracted and plotted versus the baseline case without PCM. In Figure 6-1, (a) the average heater temperature in the model corresponding to different PCM thicknesses and areas was plotted alongside (b) the amount of heat flowing into the PCMs for insights into the device behavior. There is initially a large spike in heat absorbed by all the PCMs due to sensible heating which then rapidly decays off and reaches a primary buffering state for a duration and level which is influenced by the PCM material and volume. From these figures, it is evident that increasing the thickness for a specific PCM area delays the temperature rise to steady state due to the increase in

latent heat. For example, the 0.4 x 1 mm Ga PCM melts in about 0.25 s while the 2 x 1 mm Ga PCM melts in about 2.75 s, as evidenced by the rapid drop in heat flowing into the PCMs at these

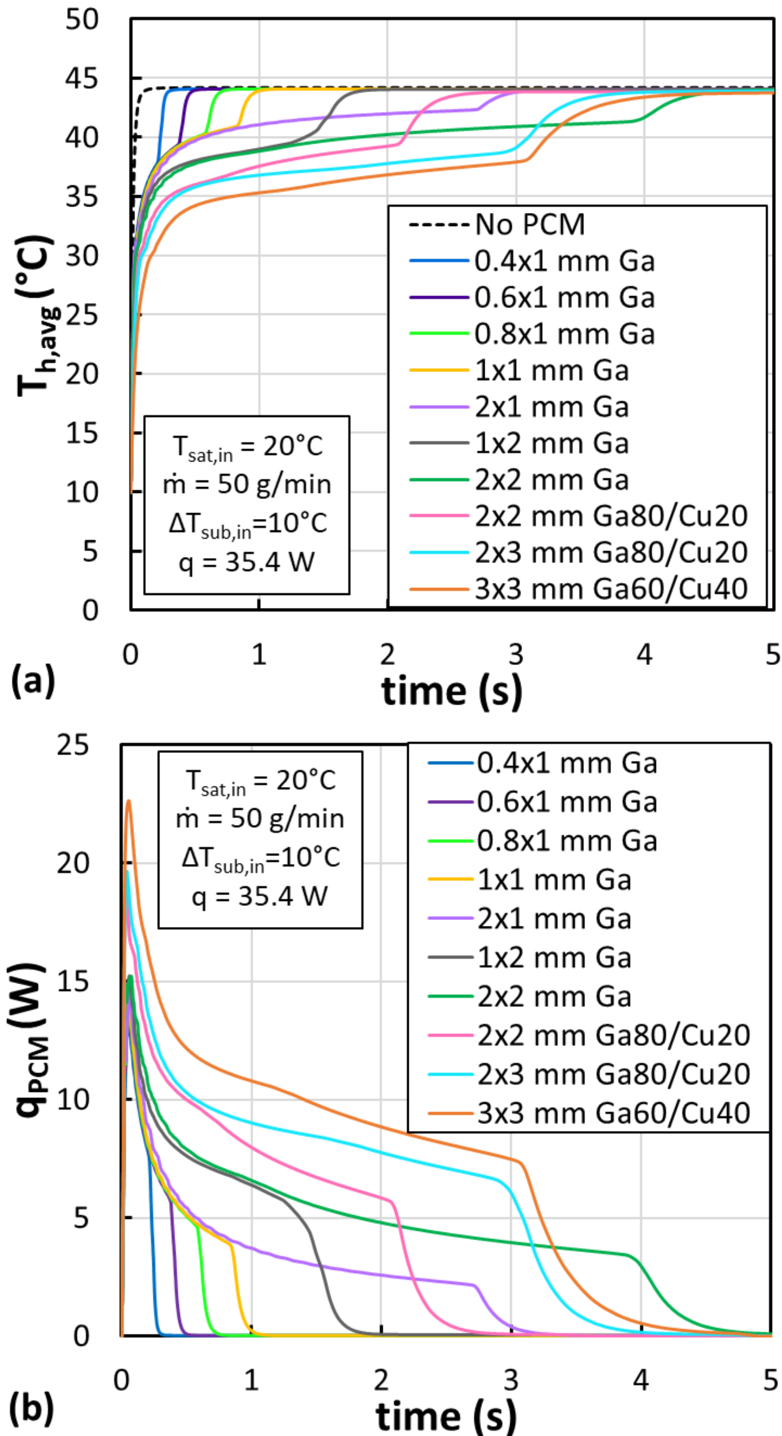

Figure 6-1. PCM cases studied under a 35.4 W heat step. **(a)** Average heater temperature versus time in simulation with different PCMs compared with baseline step response with black dashed line. **(b)** Amount of heat absorbed by PCMs versus time.

times. As the PCM melts, the lower PCM liquid phase thermal conductivity reduces the amount of heat that flows into the solid above and reduces the effective PCM utilization. Increasing the area reduces not only the rate of temperature rise but also shifts the overall transient temperature curve downward for longer during the PCM melting due to the increased amount of heat driven into the PCM. This can be seen by comparing, for example, the 2 x 1 and 2 x 2 mm Ga cases, where melting occurs up to ~2.75 s for the 2 x 1 mm case and up to ~4 s for the 2 x 2 mm case. The improvement is also due to the lateral conduction in the PCM where the larger area allows for more solid PCM utility prior to conducting through the melted liquid PCM. The benefit of the enhanced thermal conductivity of the gallium-copper foam composites is also clear. During the initial transient, up to 65% of the heat is absorbed by the PCM, with the amount absorbed here directly dependent on the thermal conductivity more so than latent heat. While the reduction in latent heat, relative to pure gallium, for a given volume results in shorter durations of PCM thermal buffering effects, the increased thermal conductivity drives more heat into the PCM and greatly reduces the temperature rise time overall before the PCM finishes melting.

Furthermore, increasing the PCM thickness (which increases the volume vertically) of the composites relative to the gallium results in similar durations of transient thermal dampening but retains the improved buffering effect due to the increased thermal conductivity. These effects are most pronounced when comparing the 2 x 2 mm Ga with the 3 x 3 mm Ga60/Cu40 cases. The melting duration differs by only about a second, but the increased thermal conductivity of the copper foam results in an enhanced buffering effect as more heat, about two times more, on average, is driven into the PCM for the 3 x 3 mm Ga60/Cu40 case. As another comparison, the reduced volumetric latent heat of the 3 x 3 mm Ga60/Cu40 PCM is remedied by the increased volume relative to the 2 x 3 mm Ga80/Cu20 PCM, resulting in nearly identical qualitative transient

temperature behavior and melting duration but with the overall transient temperature shifted downward in the 3 x 3 mm Ga60/Cu40 PCM due to its increased thermal conductivity. This is paralleled by the larger amount of heat, ~20% more, buffering into the PCM during this duration which results in the improved transient temperature response.

These results demonstrate tradeoffs in PCM power and energy density impacts. High power density more effectively dampens fast transients, but high energy density increases the duration of the dampening. The composite structures studied here have lower energy density than pure gallium, but it is easy to increase the PCM total volume to compensate for the lower energy density while retaining the higher power density. A higher volume composite with higher conductivity than pure gallium alone therefore results in an overall improvement in the transient thermal buffering capability. Finally, it should be noted that the heating mode studied here was a single step. While the high-power density PCMs resulted in the most favorable thermal buffering response to a stepped heat load, optimizing PCM volume and material properties for pulse trains of different duty cycles and pulse widths such as those experienced in many high heat flux devices may require additional considerations to achieve an overall improved device thermal response.

6.2. Effect of PCM on Heater Temperature at ONB

As discussed in Chapter 4, reduced ramping rate heat loads resulted in reduced ONB and peak temperatures and vapor backflow for evaporators without PCMs. However, the ramping profiles do not fully capture the damped temperature response characteristic of additional heat capacitance. Therefore, PCMs simulated were experimentally investigated by use of an arbitrary voltage waveform applied to the test section heater. Because the voltage is fixed to the single-phase PCM behavior in the model, after ONB, the heating rate will not accurately capture the PCM interaction. However, any insights on reducing the temperature at ONB should be captured. Figure

6-2 presents the experimental heat load versus heater superheat relative to the average saturation temperature at the ONB. Error bars represent 99% confidence intervals based on averaging at least 9 trials per case. In general, the instantaneous heat load and heater temperature at ONB follow a linear trend, with smaller values of q at ONB resulting in a lower average heater temperature. The exception is the baseline case with no PCM, where the heat load at ONB is higher than the PCM cases but with a heater temperature which occurs roughly in the middle of the PCM cases. Most notably, when considering the variability, most of the PCMs have negligible differences in the superheat needed to initiate boiling compared with each other and the baseline case. However, the 0.4 x 1 mm gallium PCM case does have the highest heater temperature and the most similar

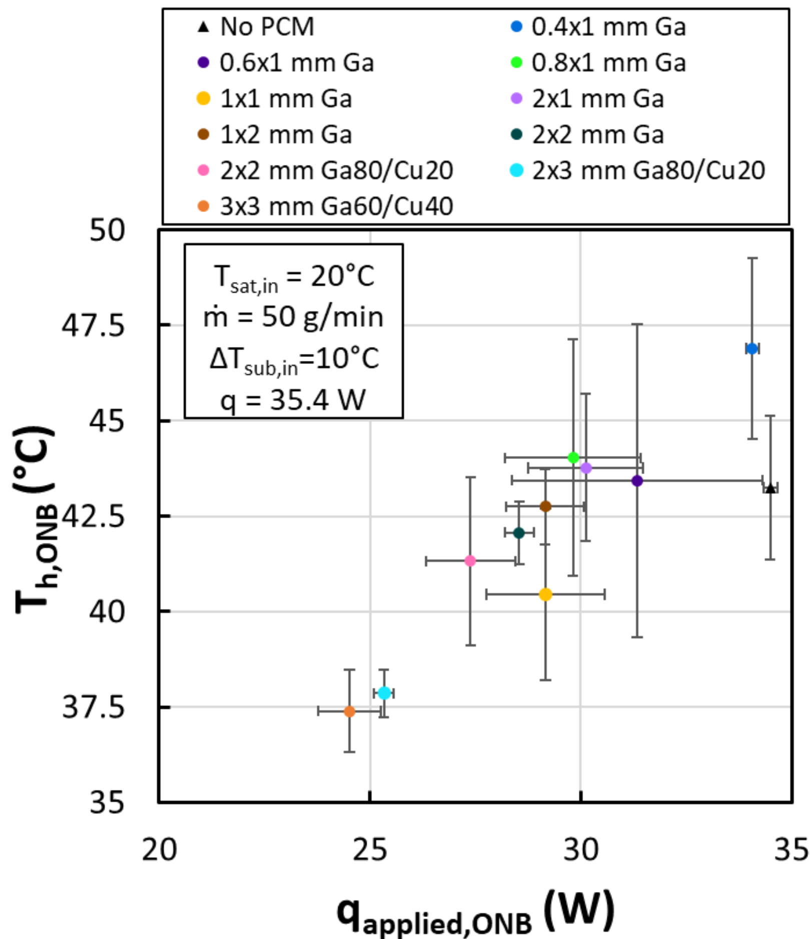

Figure 6-2. Linear trend observed in average ONB heater temperature and instantaneous heat load.

instantaneous heat load compared with the baseline. In addition, the two PCMs with the 3 mm length (again, covering the entire 10 x 2 mm chip and extending 0.5 mm beyond its length on either side), also appear to be outliers with significantly reduced heater temperature and heat load at ONB. Running a statistical Kruskal-Wallis test, since the assumption of normality and sample variances is not held to run an ANOVA test, followed by a Dunning's comparison test against the No PCM case, confirms that these two cases have significantly different means down to a 0.5% significance level.

Again referencing Figure 6-1, it is apparent that the two PCMs with the 3 mm length result in the lowest temperature rise after the initial fast transient. Since the temperature is kept lower while the PCM is "melting" due to the influence of the increased conductivity material, less heat enters the fluid during this time. Thus, nucleation can occur at lower temperatures compared to the gallium-only PCMs where the temperature after the fast transient is higher. With only gallium, the low thermal resistance of the device makes it difficult to drive a large amount of heat into the PCM unless the PCM thermal conductivity is much larger than gallium alone can provide. Therefore, the initial fast transient results in much of the heat entering the fluid and then a slow rise as the PCM melts, resulting in transient temperatures again much closer to the baseline step.

Considering the ramping results from Chapter 4, reducing the temperature rise slowly from the start appeared most beneficial. In this case, there is still an initial rapid temperature rise which results in much of the heat transferring to the fluid before the PCM buffer takes effect. It is possible that the differences in the transient heating rates perturb the thermal boundary layer development enough to affect the nucleation conditions in differing ways. Regardless, with the right combination of thermal conductivity, latent heat, and volume, PCMs can reduce the heater temperature and thus the wall superheat at the ONB. For the current evaporator, the low thermal

resistance to the fluid makes it difficult to drive a large amount of heat into the PCM and thus reduce the fluid heat gain rate unless the PCM thermal conductivity is much larger than gallium alone can provide. A high conductivity PCM with a melting point near the 10°C initial temperature may result in behavior more similar to the ramping results.

6.3. Effect of PCM on Peak Device Temperatures

Reductions in the heater temperature (and wall superheat) at the ONB are helpful because they should also reduce the intensity of vapor backflow and temperature spikes. Therefore, the peak temperatures were also compared for each PCM case against the baseline relative to the heater temperatures observed in Figure 6-3. The error bars again reflect 99% confidence intervals from

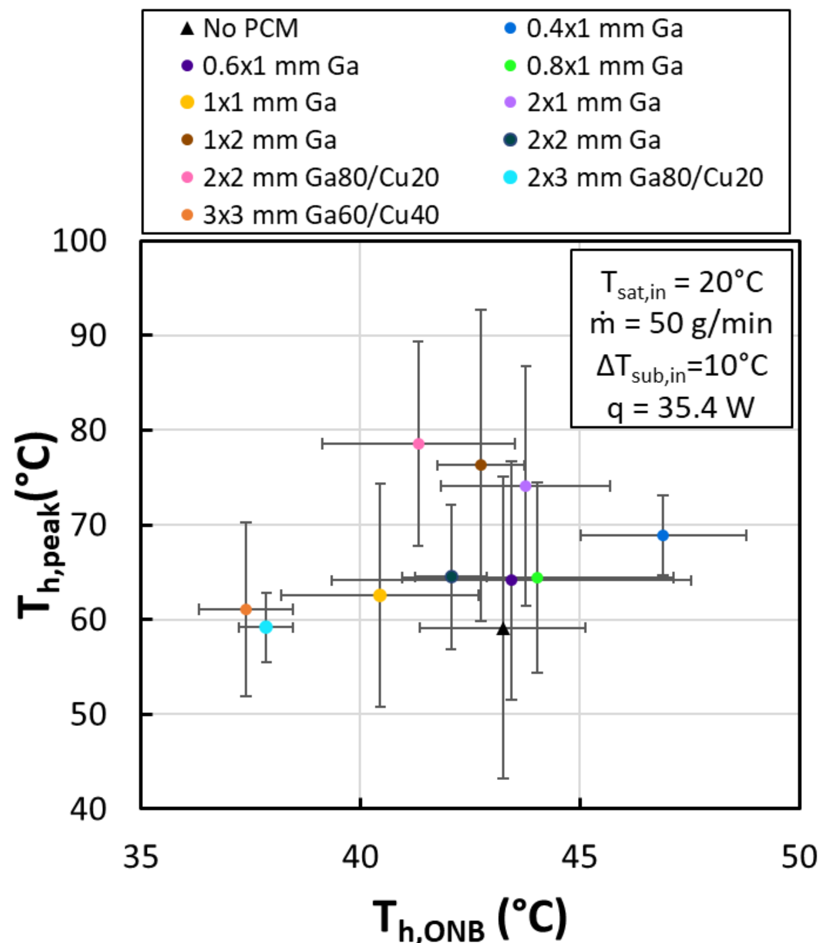

Figure 6-3. Peak temperatures versus ONB temperatures across baseline step and different PCM test cases.

the data based on at least 9 trials per case. The results are shown in. Despite the hypothesis that the lower superheat should result in a lower peak temperature, the results in this figure are mostly the contrary. The n x 3 mm PCM cases along with the 1 x 1 mm gallium-only case do have the lowest average heater temperatures and have the lowest average peak temperatures of the PCM test cases. However, the 0.4 x 1 mm gallium case has the highest average superheat but is average for peak temperature. In fact, the baseline case has the lowest average peak temperature. Another Kruskal-Wallis followed by a Dunning test confirms that there are no significant differences in peak temperature between the baseline and PCM cases.

While the average values of the peak temperatures vary by about 20°C, the variability across each scenario is also large. This reflects the randomness of the nucleation process where differences in entrapped vapor in cavities may exist and make subsequent trials or testing conditions not independent. The large number of channels may also have been partially responsible for this observed behavior since it is possible that local fluctuations or cross-channel interactions occurred more readily. Finally, the large variation in observed peak temperatures reflects the large variation in time to boiling, where for longer durations spent in a quasi-stable state may have reached higher superheated liquid levels as discussed in Chapter 5. The range in average heater temperature at ONB was about 10°C across all scenarios, but the minimum value of superheat at the minimum heater temperature was still large (~17°C), and for this test section at this heat load condition, may still have been high enough that the narrow channels and small orifice-to-channel area ratio still play the most dominant role in producing the severe vapor backflow at this heat load. It should be noted that the PCM performance modeling assumed entirely single-phase heating conditions. During the vapor backflow stage, due to the poor heat transfer to vapor and the large rise in thermal resistance to the fluid, a large amount of heat may possibly be driven into the PCM,

which may in turn reduce the transient peak temperature spike and may beneficially impact the flow dynamics as well. This effect was investigated using the previously developed NavyHHF ONB model with some simplifying assumptions.

6.4. NavyHHF Model with PCM

The NavyHHF model developed in Chapter 5 was used to understand what impact a PCM may have on the peak device temperatures, subject to some limitations and assumptions in the model. Short of testing with a PCM experimentally, the true behavior will not be captured. Nevertheless, the assumptions here should still provide an understanding of the impact a PCM may provide to transient thermal buffering on this microchannel evaporator. The same heat loads used in the NavyHHF model were modeled with selected PCMs here. The first was the Ga60/Cu40 composite with a 3 mm footprint and thicknesses from 0.5 to 2 mm. The second was a Ga95/Ni5 composite foam PCM which was developed by the Army Research Lab [33] and will be integrated into this evaporator in future efforts.

To determine the potential impact of the PCM on the vapor backflow in the model, the following assumptions were used. Given the relative ineffectiveness of the PCMs on average across all those tested to reduce the heater temperatures at the ONB, with only several resulting in slightly lowered ONB temperatures, it was decided that the same ONB temperature as the baseline case for a given heat load without PCM would be retained agnostic of the PCM to compare results equally. In addition, given the absence of any data on how a real PCM impacts the vapor backflow dynamics and the subsequent decay to steady state flow boiling, the same backflow duration along with the same respective growth constants was used as the baseline cases to simplify the model, though these will likely be coupled to the PCM response. However, with these assumptions, the performance of a given PCM can be directly assessed relative to other PCMs based on material

properties and volume and can thus be used as a design tool for understanding tradeoffs in different PCM impacts in the absence of real device data with that PCM.

6.4.1. PCM Model at 35.4 W Peak Heat Load

6.4.1.1. Impact of Ga95/Ni5 Composite Foam PCM at 35.4 W

The experimental and model baseline temperatures without PCM for the worst-case trials are shown alongside the PCM response in Figure 6-4 for different thicknesses of Ga95/Ni5 ranging from 0.5 to 2 mm thick, for the same PCM footprint. While the original model had forced the fluid to remain in liquid cooled steady state until the time and temperature coincided with when boiling began experimentally, this restriction was removed for the PCM cases given the relative stochasticity observed experimentally. Even so, the larger capacity PCMs did not reach the ONB temperature until after that time and therefore a negligible change would be expected. There are clearly diminishing returns as the thickness is increased. Increasing the thickness further beyond

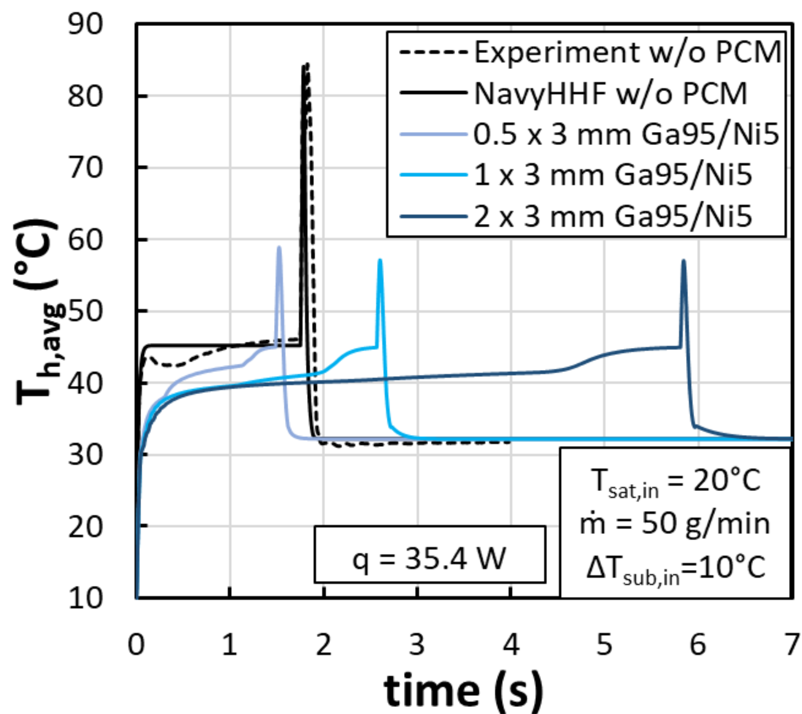

Figure 6-4. Comparison of the GaNi-foam PCM impact on transient device temperatures with baseline case without a PCM at a 35.4 W peak heat load.

1 mm generally just extended the duration of melting but at nearly constant temperature up to ~4.5 seconds. The peak temperature reduction depends on the thickness of PCM but for this case was not strongly impacted. Nevertheless, even with as small as a 0.5 mm thick PCM layer, there wass a significant reduction, ~30%, relative to the peak temperature without PCM, and a ~50% reduction in the temperature overshoot above the steady state flow boiling temperature. The 2 mm thick PCM only offered a ~2.2% further reduction in peak temperature over the 0.5 mm thick PCM.

Examining the heat transfer to the PCM with time elucidates the physical mechanism by which the PCM improves the temperature response during the vapor backflow. Figure 6-5 shows the variation in heat absorbed or extracted from the PCM with time for the three thickness levels. This figure is initially qualitatively like Figure 6-1(a) until the ONB. Up until this point, the amount of heat transferring to the PCM decreased as the utility is reduced by an increasing melt fraction

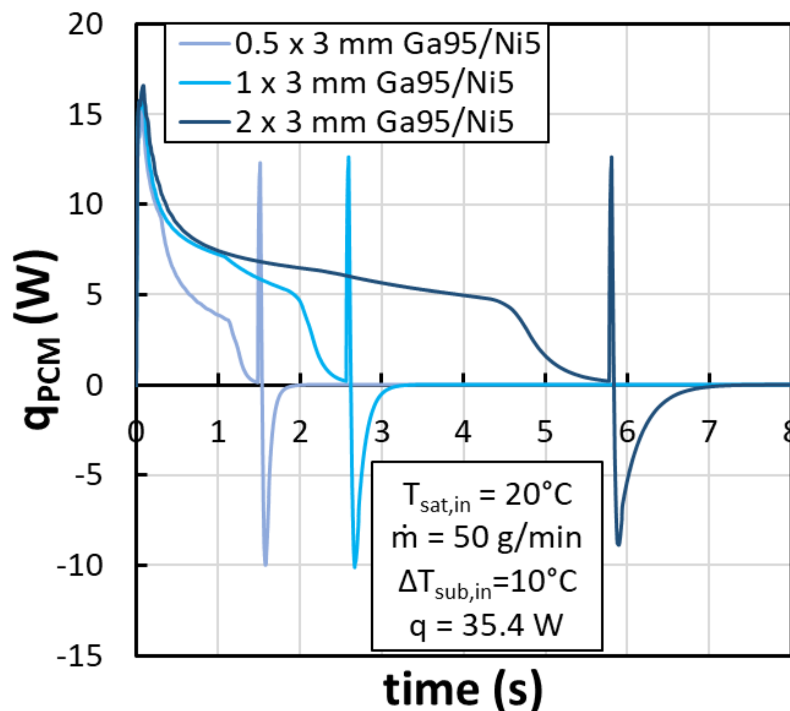

Figure 6-5. Comparison of the heat transfer into or out of the PCM in time across the different PCM thicknesses.

and the increased thermal resistance through the liquid-PCM layer. However, during the vapor backflow phase, the thermal resistance to the coolant fluid increased drastically, driving more heat into the PCM in the form of sensible heating and thus temporarily buffering the device during the vapor backflow event. The maximum increase in additional heat stored in the PCM during the backflow regime was proportional to the thickness, increasing slightly from 12.3 W to 12.6 W as thickness increased from 0.5 to 2 mm. Given that in some cases the temperature at ONB decreased with the simulated PCM addition in the experiments, it should be expected that a PCM could potentially buffer even more heat. In all the cases here, the ONB temperature was held constant, and the PCM was nearly fully melted since boiling was triggered near the steady state liquid-cooled temperature.

After the peak temperature was reached and the device was driven towards steady state flow boiling, the large increase in heat transfer coefficient rapidly removed this additional stored heat out of the PCM and into the coolant fluid. The amount of heat removed from the PCM reached a maximum (in magnitude) before diminishing more slowly and following a classic exponential decay to steady state where the net flow of heat was zero into/out of the PCM. Interestingly, with the 2 mm thick PCM, the maximum rate of heat drawn out of the PCM was less than the thinner PCMs, though the duration of heat removal from the PCM was longer. As the two-phase heat transfer coefficient is a function of heat load, the coupled response here with additional heat transfer to and from the PCM played an additional role in the behavior seen here alongside the differing amounts of heat storage capacity.

6.4.1.2. Impact of Ga60/Cu40 Composite Foam PCM at 35.4 W

The Ga/Ni PCM has a much larger effective latent heat than the Ga/Cu composite modeled earlier due to the higher ratio of gallium in the composite; however, the large fraction of copper in the latter greatly increases thermal conductivity and sensible heat capacity. The increase in conductivity should drive more heat into the PCM during the backflow phase and compensate for the reduced latent heat capacity by increasing the utilization of the PCM volume and thus should reduce peak temperatures more than the Ga/Ni-based composite, particularly with increased thickness. Figure 6-6 contrasts the transient thermal responses of the different Ga/Cu composite thicknesses with the baseline response. As predicted, the Ga60/Cu40 composite more effectively buffered the peak temperatures than the Ga95/Ni5 foam. Furthermore, there was a greater improvement by increasing the PCM thickness compared with the Ga/Ni, though this improvement quickly plateaued. The peak temperature was reduced by ~32.5%, 37.6%, and 38.7%, for the 0.5,

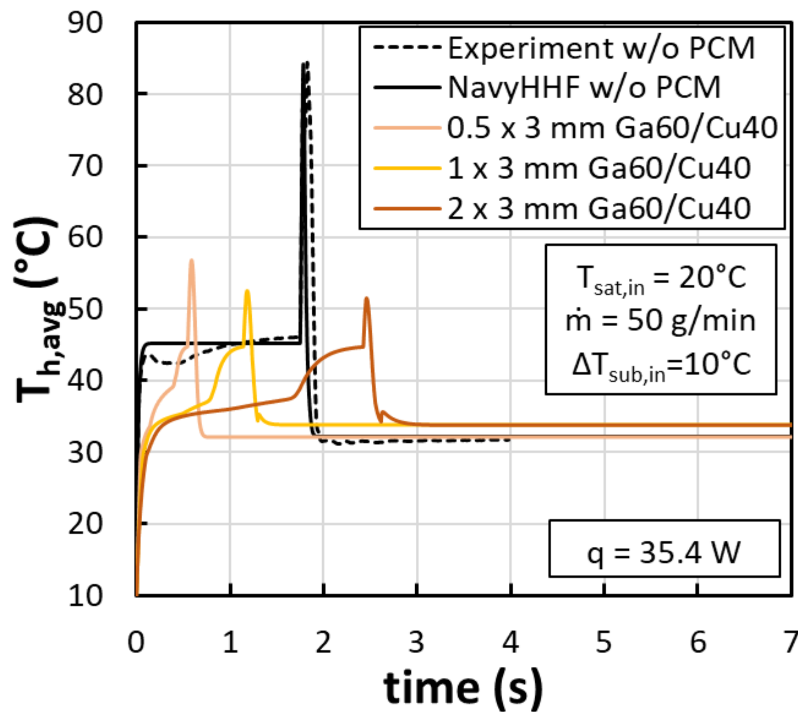

Figure 6-6. Comparison of the Ga60/Cu40 PCM impact on transient device temperatures.

1, and 2 mm thick PCMs, respectively. Despite the lower latent heat, which resulted in an increased rate of PCM melting and a shorter overall duration of buffering prior to the ONB condition, the increased thermal conductivity and larger thermal mass due to the higher fraction of high-density copper allowed more heat to be driven into the PCM during the backflow stage in the form of sensible heating and thus reduced the peak temperatures to a greater extent.

Figure 6-7 compares the heat transfer into the PCM for the Ga/Cu composite across the different thicknesses. Compared with the Ga/Ni foam composite at 12.6 W, a maximum of up to ~14.6 W of additional heat was stored in the PCM after ONB. Even the 0.5 mm thick Ga/Cu PCM stores about 14 W of additional heat at the maximum, proving that the higher power density of this copper foam-based PCM due to its enhanced thermal conductivity is a more important marker for improving the transient thermal performance than the latent heat capacity in this instance. Because the backflow duration is brief, very little PCM volume is needed to provide the energy storage to

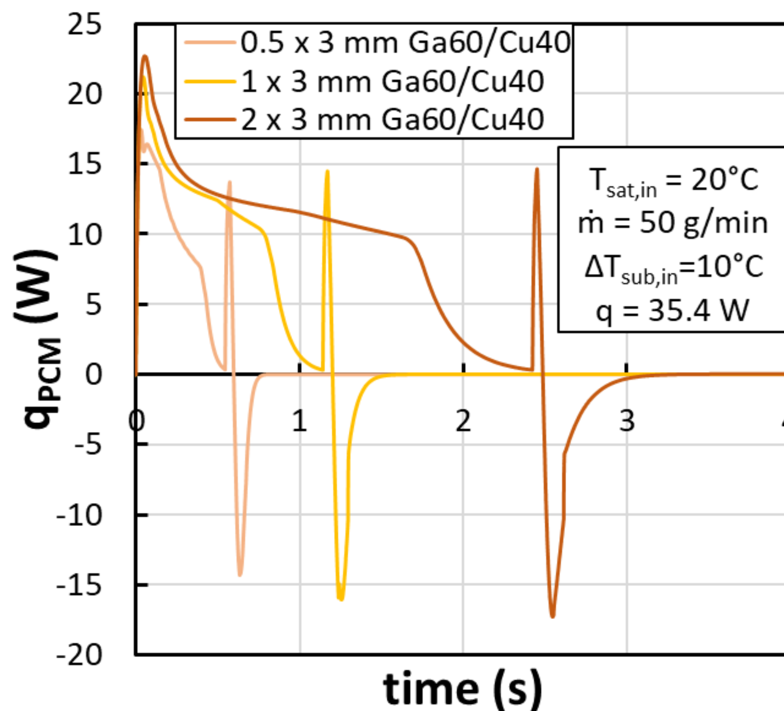

Figure 6-7. Comparison of the heat transfer into or out of the Ga60/Cu40 composite across the different PCM.

offset the reduced heat transfer rate more effectively to the fluid. In addition, after the peak temperature had been reached, the amount of heat removed from the PCM reached about 17.5 W in the thickest PCM case, which was more than that absorbed during the backflow. However, eventually this decays to net zero.

6.4.1.3. Overall Comparison of PCM Impact at 35.4 W

In the preceding sections, the impact of including two different types of PCMs at increasing volumes (by increasing thickness) was investigated with a 35.4 W peak heat load. The effects were studied assuming the worst-case scenario trial as observed in the experiments. Figure 6-8 shows the large observed variability in peak temperatures given the difference in backflow behavior. Given this large variability across peak temperatures, and therefore in device peak temperature, the cases with the least amount of backflow and lowest peak temperature were both modeled, and the corresponding PCM effects elucidated with the same PCMs. The Ga95/Ni5 and Ga60/Cu40 PCMs at the different thicknesses were directly compared to the baseline without PCM, and the resulting ranges in peak temperatures between the worst and lowest backflow trials are shown in

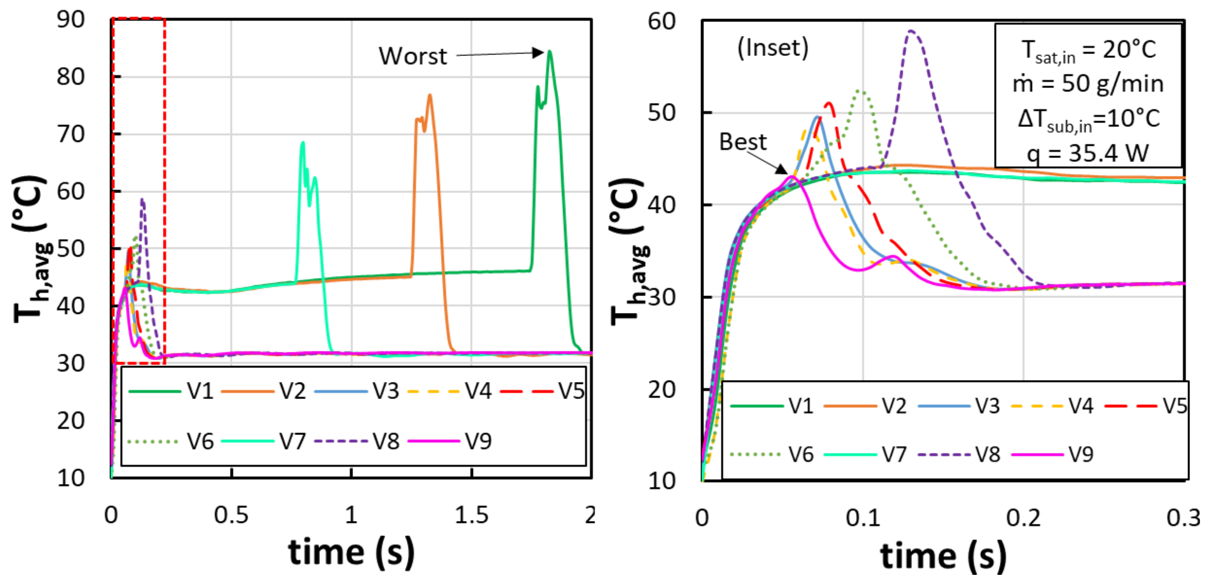

Figure 6-8. Variation in transient temperature response and peak temperature observed across trials, with the worst-case and best-case trials identified.

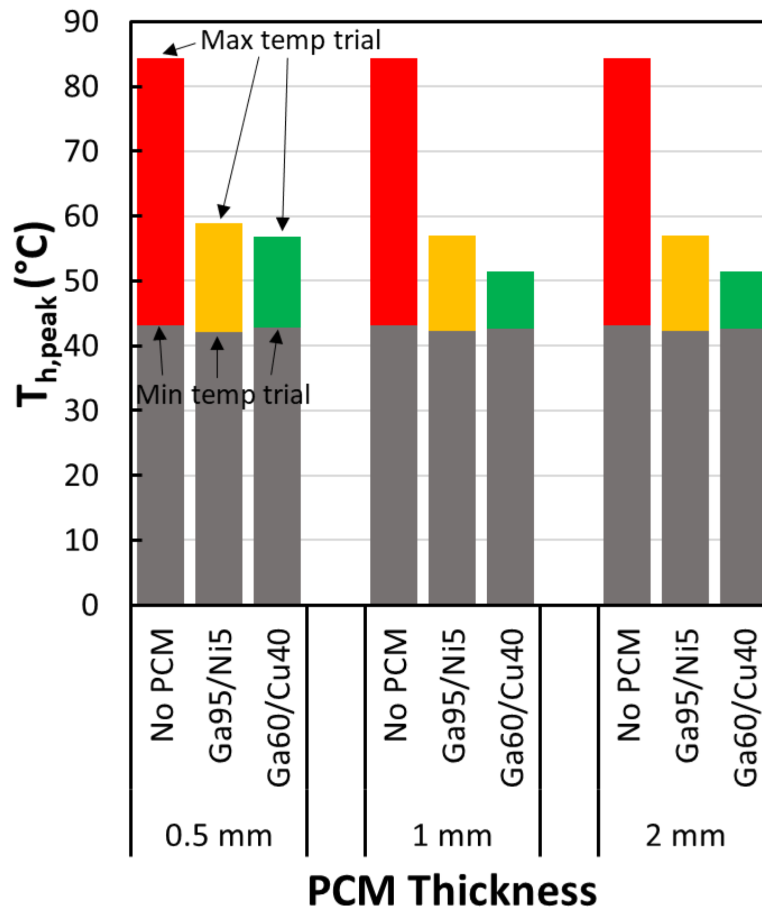

Figure 6-9. Comparison of peak temperature ranges across the baseline and both PCM types at a 35.4 W peak heat load, at different PCM thicknesses, where the PCMs significantly reduce peak temperatures in the worst-case trial.

Figure 6-9. In this figure, the top of the colored bars represent the peak temperature of the trial with the worst-case vapor backflow condition, while the bottom of the colored bars represent the peak temperature of the trial with the least amount of vapor backflow. Thus, Figure 6-9 presents the range of expected PCM thermal buffering across the observed experimental trials. While the time series for the worst-case trial were shown above, demonstrating the large peak temperature reduction, this figure highlights the reduced temperatures even more clearly. Even with a small amount of PCM, the peak temperatures are drastically reduced by up to 30°C. The differences in the copper and nickel foam-based composites are also clearer, with the Ga60/Cu40 attaining a more pronounced effect on the temperature reduction due to its increased thermal conductivity

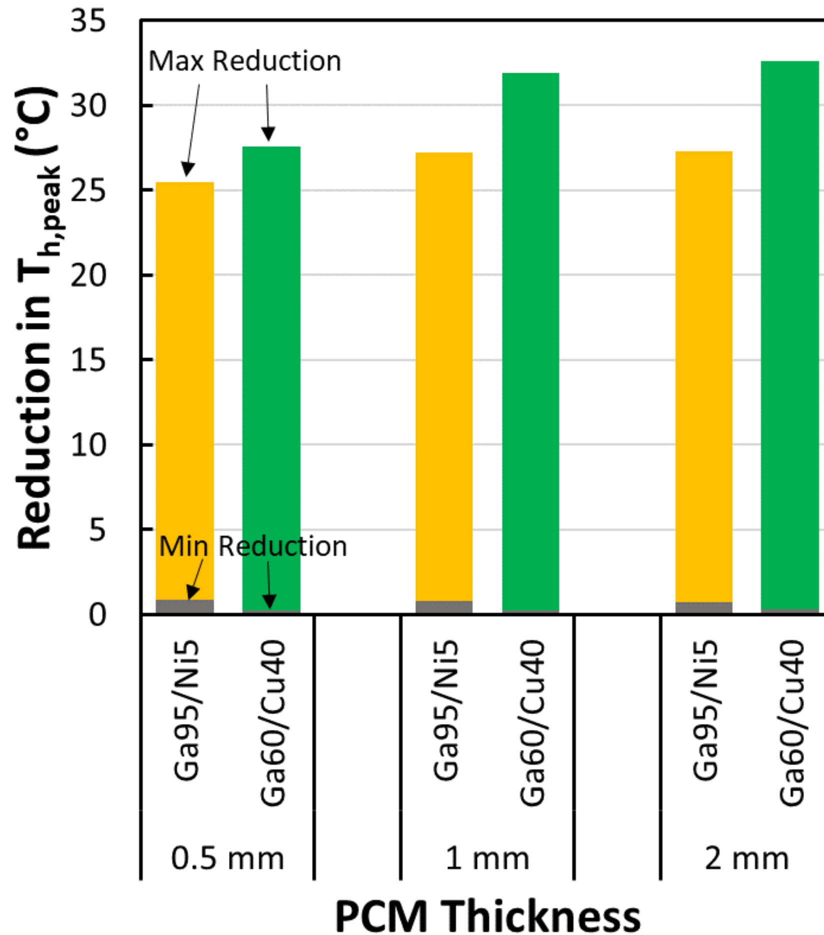

Figure 6-10. Comparison of peak temperature reductions with both PCM types at a 35.4 W peak heat load, at different PCM thicknesses, where the range in peak temperature reduction is large.

which improves power density and increases PCM volume utilization. The differences grow more significant between 0.5 and 1 mm of PCM, where the peak temperature difference between the two PCM types increases from ~3°C to ~5°C. Further increasing thickness to 2 mm appears to result in a plateau, with the difference in peak temperatures changing from 5°C to 6°C between the two PCMs.

Figure 6-10 and Table 6-1 show the range in temperature reduction from the baseline cases across the PCMs investigated. The style of Figure 6-10 is similar to Figure 6-9, where the top of the colored bars corresponds to the peak temperature reduction of the worst case trial, while the bottom of the colored bars represents the peak temperature reduction of the best case trial. While

Table 6-1. Temperature reduction range across PCM types and thicknesses at 35.4 W

		0.5 mm	**1 mm**	**2 mm**
Ga95/Ni5	Min (°C)	0.84	0.77	0.76
	Max (°C)	25.5	27.3	27.3
Ga60/Cu40	Min (°C)	0.21	0.27	0.32
	Max (°C)	27.6	31.9	32.6

the PCMs greatly mitigated the peak temperature for the initially worst-case trial with the highest peak temperature (by up to ~33°C), for the trial with the lowest initial peak temperature, the PCM reduced the peak temperatures by <1° C across all PCMs and thicknesses. This is due to the reduced duration and intensity of backflow, which in turn reduced the duration of vapor heat transfer that would otherwise drive the temperature higher. Given the shorter duration of backflow, the PCM did not buffer as much heat, and therefore the peak temperatures did not change as appreciably because they were already low. Nevertheless, under the assumption that the backflow behavior remains identical to the case without a PCM, this figure and table display the expected range in PCM performance enhancement. A maximum temperature reduction range of 0.21°C to 32.6°C, depending on PCM type and thickness, was observed. Therefore, given the large variability in backflow intensity at this heat load, the inclusion of a PCM will mitigate the effect of any backflow intensity and will thus keep the device temperature lower overall homogenizing the difference in peak temperatures across different heating events. While the copper foam-based composite was clearly superior, it is encouraging that the nickel foam-based composite still effectively improved the transient response, especially since a high-quality foam composite has already been practically demonstrated and produced.

6.4.2. PCM Model at 37.5 W Peak Heat Load

The next heat load investigated with the inclusion of PCM was the 37.5 W case. Here, variability between trials was much less significant than with the 35.4 W scenario, with about 10°C of difference between the "worst" and "best" case trials. Thus, the detailed transient behavior will

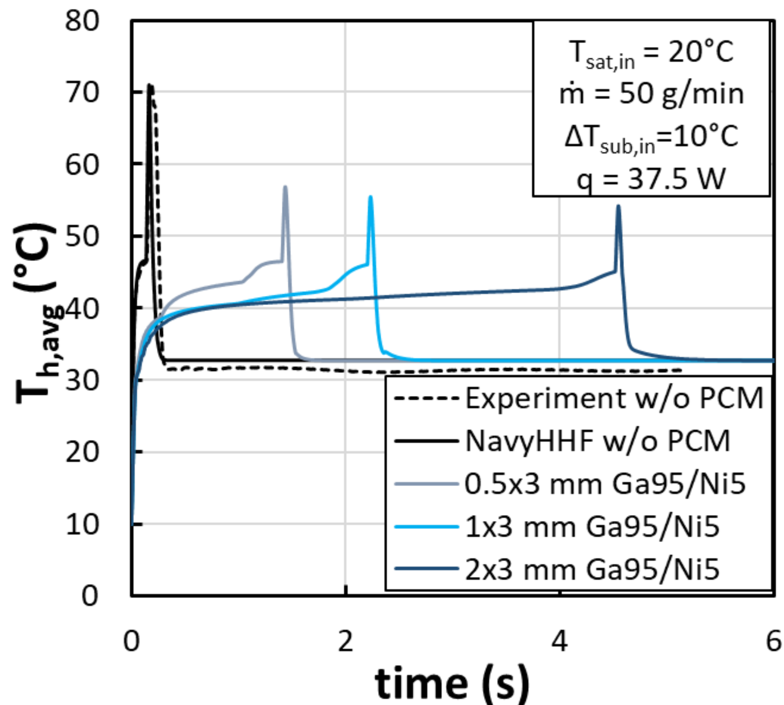

Figure 6-11. Comparison of transient temperatures across baseline case without PCM and with different Ga95/Ni5 PCM thicknesses, where the peak temperature drops sharply upon addition of PCM but with a lessened effect with further increases PCM thickness.

be illustrated for the worst-case trial as in the 35.4 W case, and the overall differences between PCM, thickness, and best/worst trials will be compared at the end.

6.4.2.1. Impact of Ga95/Ni5 Composite Foam PCM at 37.5 W

The transient temperature time series for the baseline experiment and model are compared against the three PCM thicknesses for the Ga/Ni composite in Figure 6-11. As in the 35.4 W case, the addition of PCM results in a stark reduction of the peak temperature regardless of PCM thickness. However, in this case, the reduction in peak temperature is about 20% up to ~24% for the 0.5 mm to 2 mm thick PCMs, respectively. While the performance does level off slightly with increases in PCM, there is still about a further ~2% reduction in peak temperature relative to baseline for each increase in thickness, which shows a greater impact of PCM thickness at this heat load. However, the increased volume of PCM does result in a much more gradual increase in the device temperature and may keep it higher longer despite a corresponding reduction in peak.

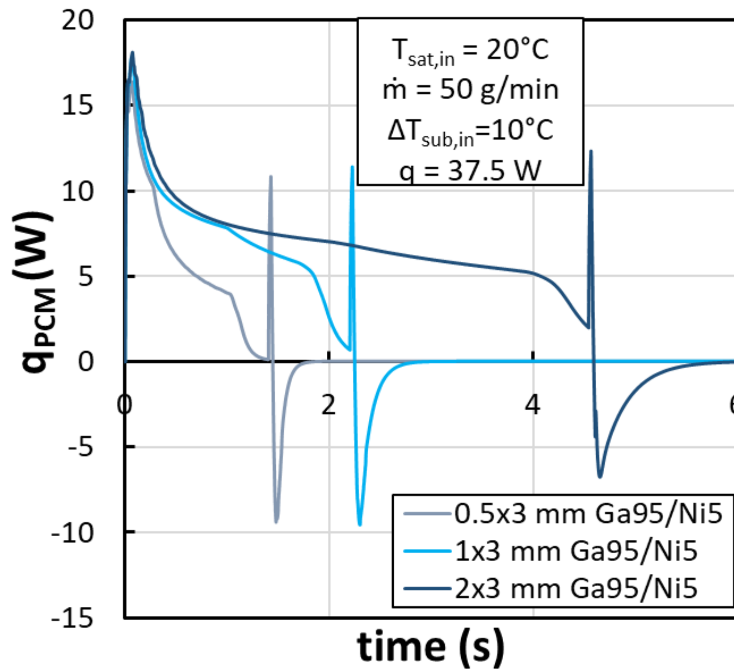

Figure 6-12. Transient heat rate into the PCM for a peak heat load of 37.5 W, showing the large amount of heat stored and then subsequently removed in the PCM during the vapor backflow regime.

This tradeoff should be evaluated in terms of device longevity given the large reduction in temperature under steady state boiling.

To gain further insight into the physical nature of why the temperatures are reduced, the transient heat rates into the PCM were again plotted across the PCM thicknesses. Figure 6-12 contrasts this heat transfer behavior across the different PCM thicknesses and shows that, with increasing volume of PCM, more heat is initially stored in the PCM and declines slowly over time as more PCM melts. While the thinnest PCM melted nearly entirely under liquid cooling conditions, the thicker PCMs did not prior to the ONB conditions. Regardless, the heightened thermal resistance to the coolant fluid during the backflow regime drove more heat into the PCM and increased effective volume utilization since the thermal resistance through the liquid PCM to the remaining solid fraction was suddenly a reduced barrier to heat transfer relative to the other pathways in the device. The large amount of heat stored in the PCM during this backflow regime

therefore precludes the large reduction in peak temperature, as mentioned in the 35.4 W section. There is a slight increase in heat stored from ~11 to ~12.5 W during this backflow regime commensurate with an increase in thickness which is reflected in the further reductions in peak temperature moving from 0.5 mm to 2 mm thick PCMs. As the peak temperature was reached and two-phase heat transfer became dominant, the large increase in heat transfer coefficient precipitated a rapid decrease in device temperature while the extra sensible heat stored in the PCM was quickly rejected to the coolant as evidenced by the negative heating rate. An absolute negative amount of heat at up to 10 W was removed from the PCM in the 0.5 mm case; however, the total energy stored was likely greater in the 2 mm thick PCM, as this heat was removed and then reached a net zero at steady state far more slowly given the additional thermal capacitance.

6.4.2.2. Impact of Ga60/Cu40 Composite Foam PCM at 37.5 W

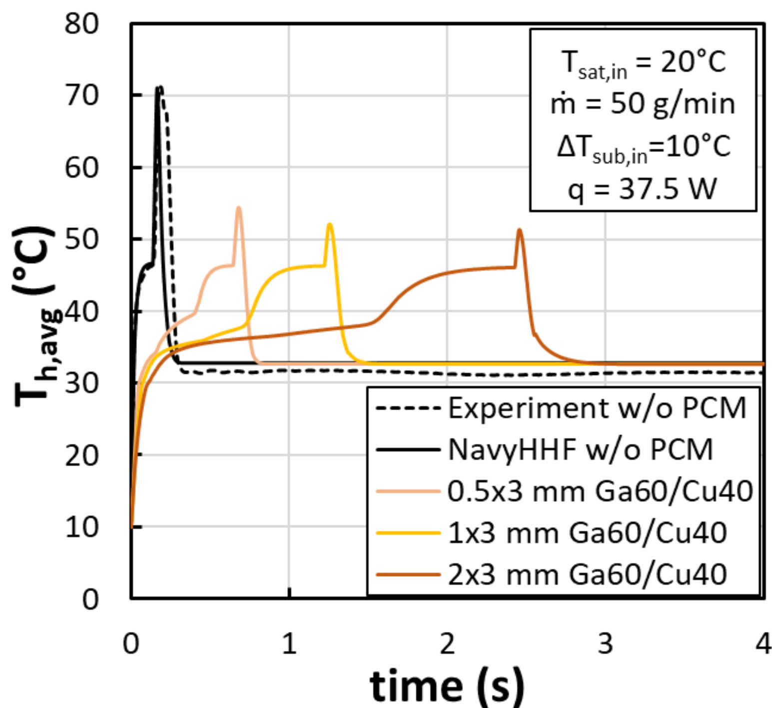

Figure 6-13. Transient temperature comparison across baseline and Ga60/Cu40 PCMs at 37.5 W, showing the large reduction in peak temperatures.

The Ga60/Cu40 composite results are shown alongside the baseline without PCM temperatures in Figure 6-13. Like with the Ga95/Ni5, there is a large reduction in peak temperature, in this case by at least 17°C. This is again due to the increased thermal conductivity of the copper foam which enhances the heat transfer into the PCM and promotes increased PCM volume utilization during the backflow regime. The peak temperature is reduced by at least 23% and up to ~28% in the thickest PCM case. The incremental reduction in peak temperature between PCM thicknesses diminished as the thickness of the PCM increased further, with further reductions in peak temperature of about 3% between 0.5 to 1 mm and ~1.1% between 1 to 2 mm.

The temporal heat transfer to the PCM for the Ga60/Cu40 PCMs is shown in Figure 6-14. In this case, due to the overall decreased amount of latent heat capacity for this PCM, the heating rates into the PCM decline rather quickly; however, there is again another uptick in thermal energy storage during the backflow phase. In this case, the peak amount of heat stored reached ~12.3 W

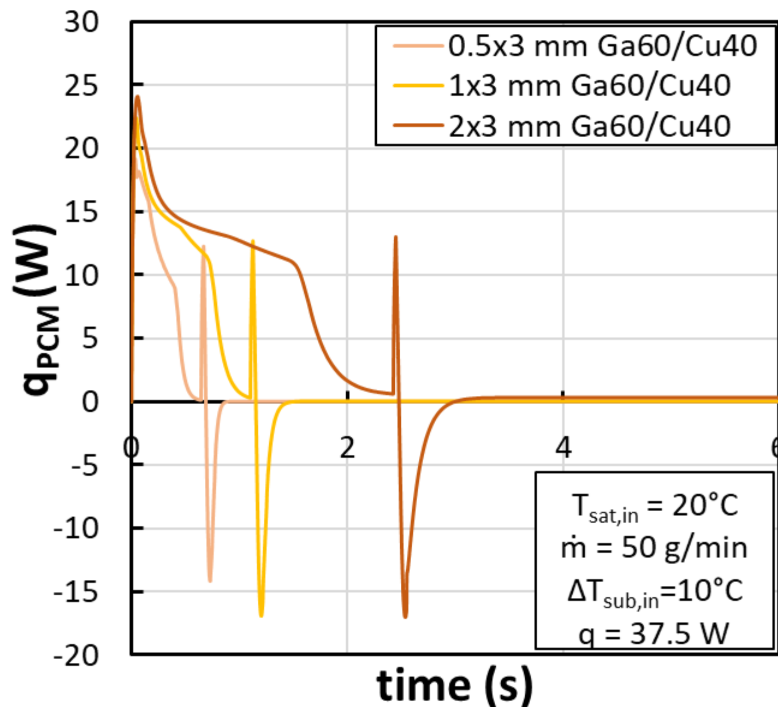

Figure 6-14. Temporal heating rate to the PCM at 37.5 W of peak heating across the three different Ga60/Cu40 PCM cases, showing the rapid transfer of energy to and from the PCM during the backflow phase.

at the 0.5 mm thickness up to 13 W with the 2 mm thickness. As the two-phase heat transfer takes over, the amount of heat drawn from the PCM reached ~17 W maximum before declining back to a net zero at steady state. The relative maximum rate that heat is removed from the PCM is dependent on the coupling between how quickly heat can be drawn from the PCM and the associated increase in two-phase heat transfer coefficient. Unlike in the Ga95/Ni5 case where the peak heat drawn from the PCM generally decreased with thickness, here the peak heat drawn from the PCM increased slightly due to the higher thermal conductivity which facilitated more sensible heating in the PCM during the backflow regime.

6.4.2.3. Overall Comparison of PCM Impact at 37.5 W

Again, the two trials with the lowest and highest peak temperatures were run through the model to determine bounds on the PCM thermal buffering effect assuming backflow conditions would be identical to their respective trials without PCM. The resulting range of peak temperatures for both types of PCM investigated across the three thicknesses was compared against the range of peak temperatures observed without the PCM in Figure 6-15. As mentioned in the above sections with the transient temperature profiles, a significant reduction in peak temperature is observed due to the presence of a PCM since the PCM absorbs part of the heat during the vapor backflow phase.

Unlike in the 35.4 W scenario, at the 37.5 W peak heat load, the variability in peak temperature is much lower (<10°C), and thus even in the trial with the least amount of backflow and lowest peak temperature, there is still a significant reduction in peak temperature. The peak temperatures in all PCM cases are still much lower than the minimum peak observed experimentally in the absence of PCM, suggesting a compelling benefit to including PCM at this heat load regardless of backflow intensity. The addition of PCM also reduced the maximum

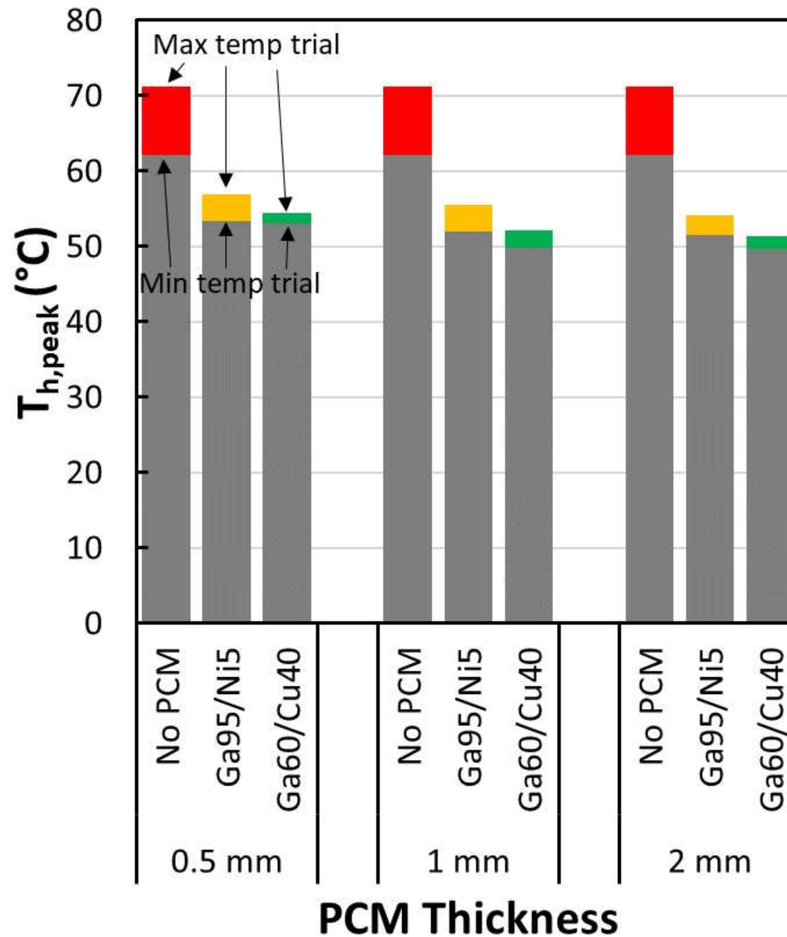

Figure 6-15. Comparison of peak temperature ranges obtained with a peak heat load of 37.5 W with best- and worst-case trials using both PCM types and across the thickness range, with significant reduction in peak temperature observed for all PCM cases.

temperature range from just under a 10°C range to about a 2°C range. Once again the copper foam composite outperformed the nickel foam composite at all thicknesses and across the range of trials due to its increased thermal conductivity which improved its ability to absorb heat during the backflow duration. Again, the PCMs effectively homogenize the spread in peak temperatures across different backflow conditions and thus provide more uniform device temperature behavior over different testing trials.

Figure 6-16 and Table 6-2 present the resulting range in the reduction of the peak temperatures from the respective baseline cases with the inclusion of PCM. There are reductions in peak temperature of 8.6°C at a minimum up to 19.7°C. The maximum peak temperature

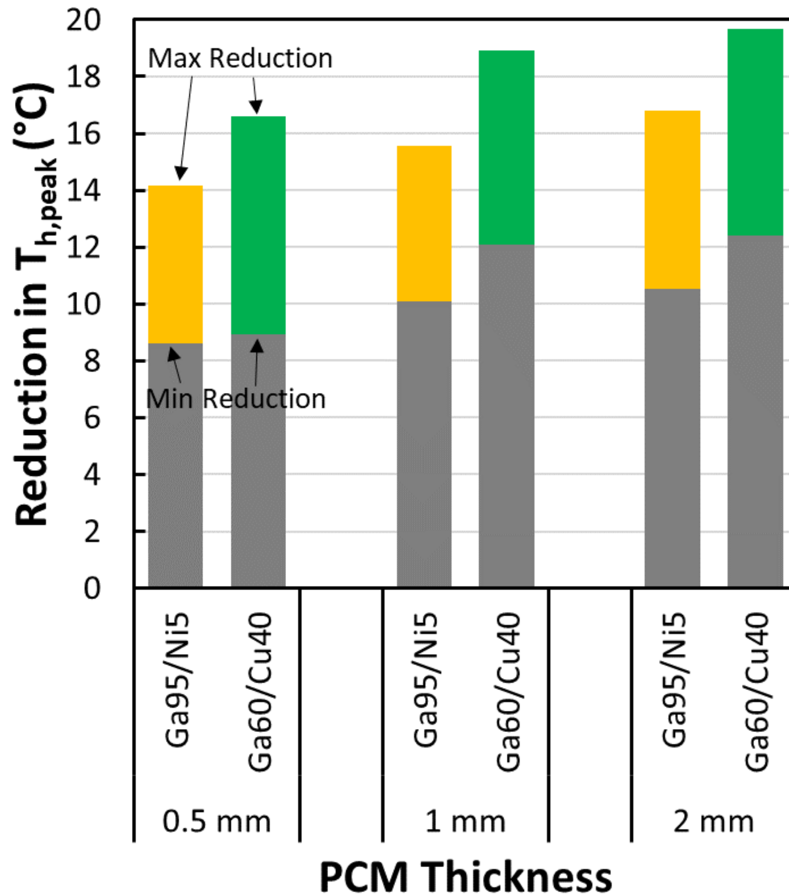

Figure 6-16. Range of peak temperature reductions from baseline obtained with a peak heat load of 37.5 W with best- and worst-case trials using both PCM types and across the thickness range.

reduction for the Ga/Cu composite was ~19.7°C versus the 16.8°C with the nickel foam-based PCM. As clearly shown in Figure 6-16, thicker PCMs play a larger role at this heat load in mitigating the peak temperature but provide diminishing returns as thickness increases at this heat load, regardless of PCM type or initial backflow intensity. For example, the peak temperature reduction of the worst-case trial using the Ga/Cu PCM increases from ~2.3°C between 0.5 and 1

Table 6-2. Temperature reduction range across PCM types and thicknesses at 37.5 W.

		0.5 mm	**1 mm**	**2 mm**
Ga95/Ni5	Min (°C)	8.61	10.08	10.53
	Max (°C)	14.15	15.55	16.81
Ga60/Cu40	Min (°C)	8.95	12.10	12.39
	Max (°C)	16.62	18.93	19.69

mm but only increases by <1°C between 1 and 2 mm. With the best-case trial, the temperature reduction between 0.5 and 1 mm is similar but between 1 and 2 mm decreases to ~0.3°C.

6.4.3. PCM Model at 55 W Peak Heat Load

The final heat load modeled was 55 W, which represents a much higher amount of necessary heat buffering in a PCM to reduce the vapor backflow detriment to the peak temperature. In addition, because the ONB occurs before reaching a near steady state temperature in liquid cooling, there will be more PCM available which has not yet melted. Therefore, this case was investigated since it is relevant to heat loads where steady state is reached in liquid cooling prior to the ONB.

6.4.3.1. Impact of Ga95/Ni5 Composite Foam PCM at 55 W

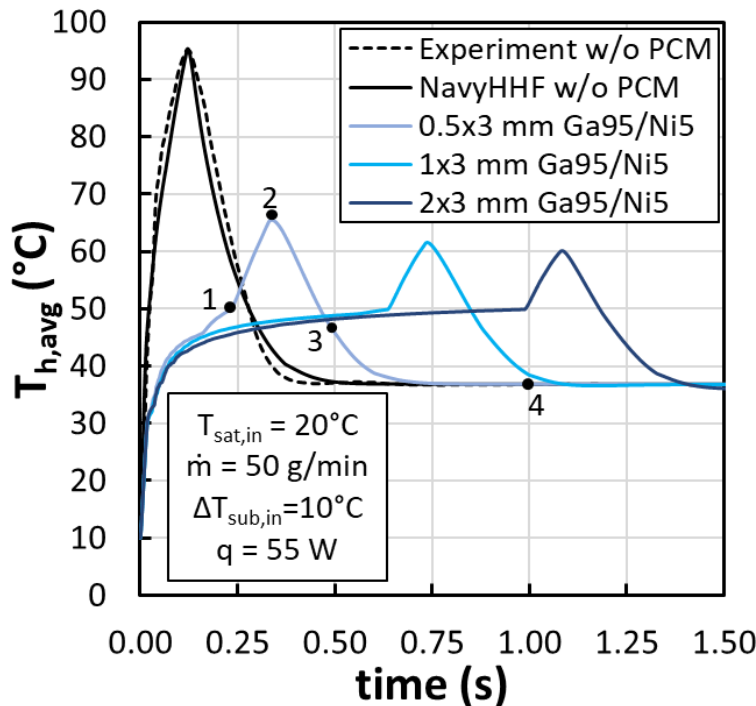

Figure 6-17. Transient heater temperatures at 55 W peak heat load across the baseline and Ga95/Ni5 PCMs with different thicknesses, showcasing the large peak temperature reduction effect due to incorporating a PCM. Numbers 1-4 correspond to specific states in time in Figure 6-19.

The transient thermal buffering effect on the device temperature for the worst-case trial with the highest peak temperature is shown in Figure 6-17 for the Ga95/Ni5 PCM at 55 W of peak heating. The peak temperature was greatly improved immediately in the presence of a PCM, even in a small thickness of 0.5 mm, where the peak temperature decreased from 95°C to 65°C. Further increases in PCM thickness provided diminishing returns, as shown before, with up to a further reduction in peak temperature of ~5°C, while also slowing the temperature rise time during the liquid-only cooling state and delaying the peak temperature time by up to ~0.75 s. The ONB temperature was kept constant in the models, so any changes in this temperature due to the presence of a PCM which slows down the temperature rise time would modify the PCM effect observed here.

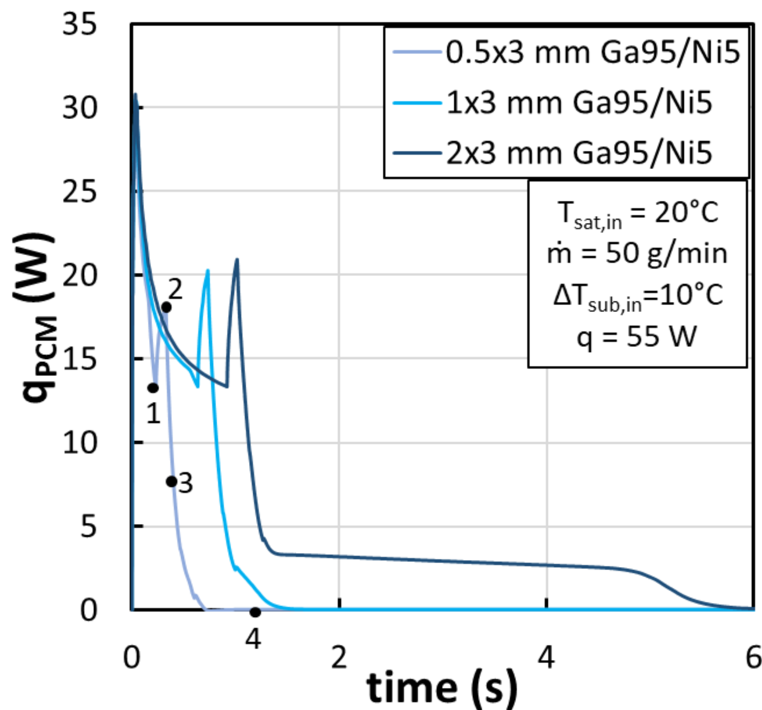

Figure 6-18. Transient heating rates into the PCM compared across the three PCM thicknesses for the Ga95/Ni5 PCM at a 55 W peak heating rate, where numbers 1-4 correspond to specific states with highlighted in Figure 6-19**.**

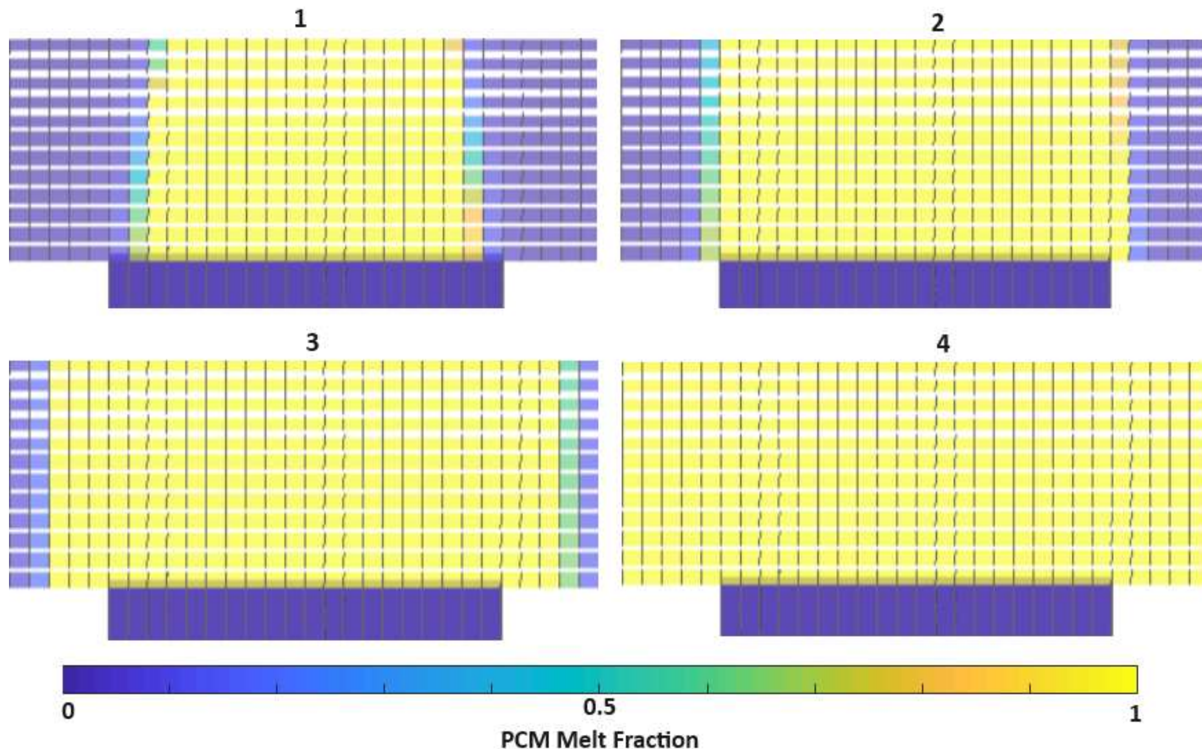

Figure 6-19. PCM melt fraction at selected instants in time from Figure 6-18. (1) ONB, PCM not fully melted, (2) peak temperature reached and PCM is still not fully melted, (3) intermediate state between peak temperature and fully developed two-phase state, (4) steady state flow boiling, PCM is fully melted.

The transient heating rates into the Ga95/Ni5 PCM help explain the transient temperature behavior and are plotted for the three thicknesses in Figure 6-18. Given the much quicker temperature rise time and occurrence of ONB prior to reaching a liquid steady state, the heating behavior into the PCM is different than for the lower heat loads. To understand this behavior, the PCM melt fraction is plotted in Figure 6-19 for selected points in time highlighted by the 0.5 mm PCM case heater temperature and PCM heat load traces in Figures 6-17 and 6-18. The heat absorbed by the PCM dropped exponentially over time until it reached roughly 13 W, with a time constant directly dependent on the thickness. As seen in Figure 6-19 and referencing Figure 6-18, at state (1), the ONB, the PCM was not fully melted and thus had a significant amount of latent heat available to store additional heat. Once ONB occurred and the vapor backflow phase enforced vapor convection as the dominant heat transfer mode, the heat driven into the PCM increased

sharply, up to between 17 and 21 W, depending on the PCM thickness. This additional heat absorbed into the PCM offered a tremendous thermal buffering capability to the device which coincided with the stark reduction in peak temperatures. However, even after this point, which marks the peak temperature and state (2), the PCM was not fully melted, as is evidenced by Figure 6-19. Once the vapor backflow was eventually overcome and two-phase flow boiling heat transfer became the dominant mode, the amount of heat absorbed by the PCM fell quickly as more of the PCM melted as shown in state (3), and eventually at state (4) a steady state is reached with no net heat into or out of the PCM when all the PCM had been melted.

6.4.3.2. Impact of Ga60/Cu40 Composite Foam PCM at 55 W

Given the superior transient buffering effect of the Ga60/Cu40 composite over the Ga95/Ni5 composite for the previous heat loads, it may be assumed that this would hold for the higher powers. Figure 6-20 shows that the results are to the contrary. The 0.5 mm thick PCM

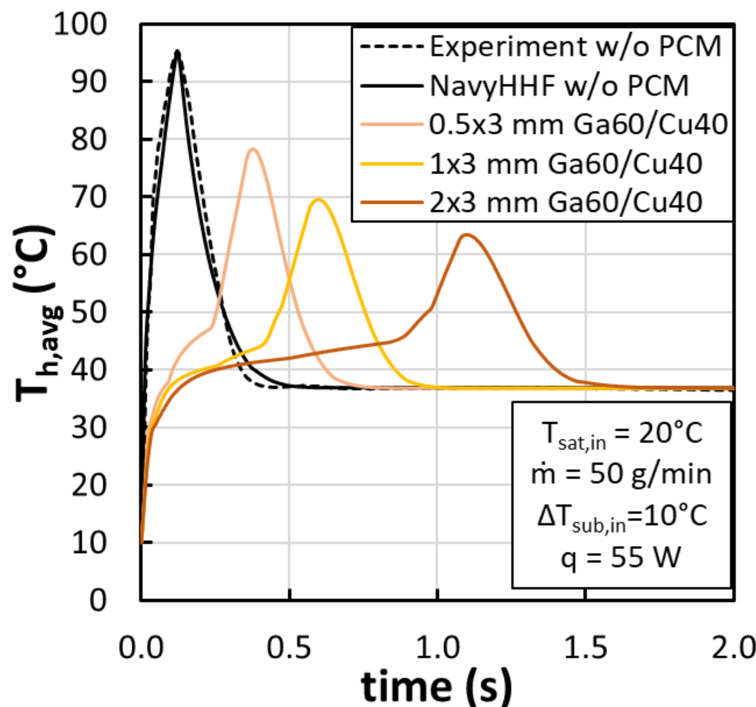

Figure 6-20. Transient heater temperatures compared across the baseline and three different thicknesses of Ga60/Cu40 PCM at a peak heat load of 55 W.

reduces the temperature from 95°C to ~78°C, and the 2 mm thick PCM reduces the peak temperature even further to 64°C, which is close to the Ga95/Ni5 PCM. However, the overall duration of buffering is reduced due to the lower amount of latent heat capacity available for this volume of PCM, since the volume fraction of gallium was reduced from 95 to 60%. Thus, the amount of available thermal buffering was lessened with the copper foam PCM compared with the nickel foam PCM. This effect was not as pronounced earlier since boiling was initiated at near liquid steady state where the PCM heating rate had nearly reached zero and thus the PCM had nearly fully melted in all cases. The difference in thickness had a greater effect here than on the Ga95/Ni5 composite since the additional latent heat available was more effectively utilized with the higher conductivity foam.

The transient heating rates to the PCM shown in Figure 6-21 assist in explaining this apparently contradictory effect, with reference to Figure 6-22 to understand the melt fractions and temperatures in the PCM at selected states in time. Heat was driven more rapidly into the PCM and thus resulted in more melting sooner than with the Ga95/Ni5 PCM. The highlighted times on the 0.5 mm trace are shown with corresponding detailed nodal temperatures and melt fractions within the PCM in Figure 6-22. At state (1), the PCM was already fully melted at the ONB time unlike with the Ga95/Ni5 PCM in Figure 6-19. As time progresses, the melt fraction images look identical, while the PCM temperatures change dramatically, indicative of sensible heating in the PCM during the transient backflow regime. State (2) represents when the peak temperature has been reached, and the PCM temperature is large due to sensible heat absorption. However, at state (3), which is nearing steady state, the PCM temperature has clearly decreased from ~70-80°C to ~50°C. Therefore, the negative heating or heat removal from the PCM represents the removal of the additional transient sensible heat which was stored in the PCM during the vapor backflow

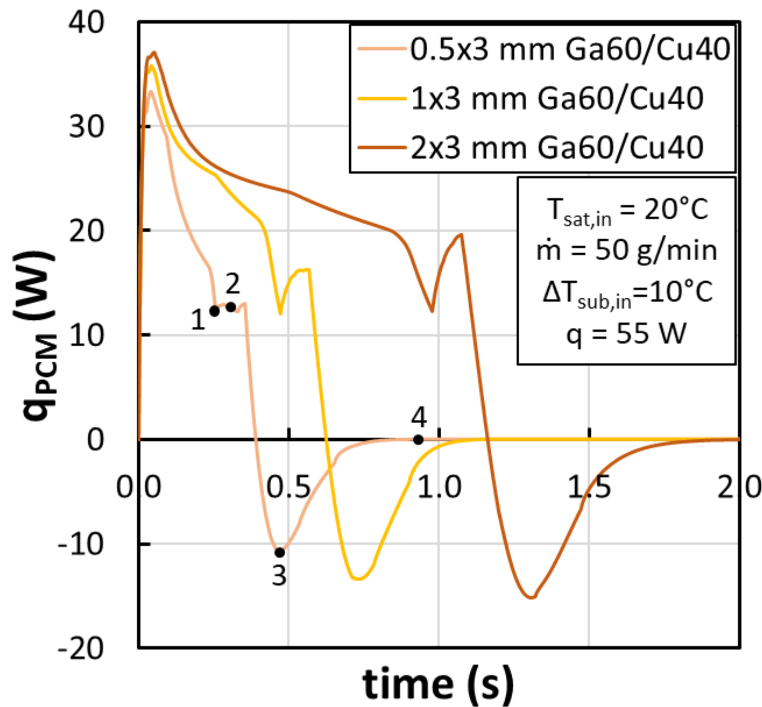

Figure 6-21. Transient heating rates to the PCM across the three Ga60/Cu40 thicknesses for a peak heat load of 55 W. Numbers 1-4 correspond to specific states in Figure 6-22.

phase. This coincided with the drop in liquid PCM temperature as this heat was removed and steady state was reached with a fully melted PCM which was at a much lower average temperature of ~35°C as evidenced in state (4). The thickest (2 mm) PCM resulted in a similar heat buffering effect to the 1 mm Ga95/Ni5 case, and thus the peak temperatures of those were similar. In this case, the heat drawn from the PCM reached a minimum of about 15 W before decaying slowly back to a net zero as the additional sensible heat was removed. The net negative heating (or heat extraction from the PCM) did not occur in the Ga95/Ni5 cases because the PCM was not fully melted after the peak temperature had been reached, and the additional sensible heating that may have occurred there was spread into melting the remaining PCM volume along the way to steady state. Nevertheless, increasing the thickness of the Ga60/Cu40 composite led to a greater relative improvement in peak temperature compared with the Ga95/Ni5 composite due to the increase in

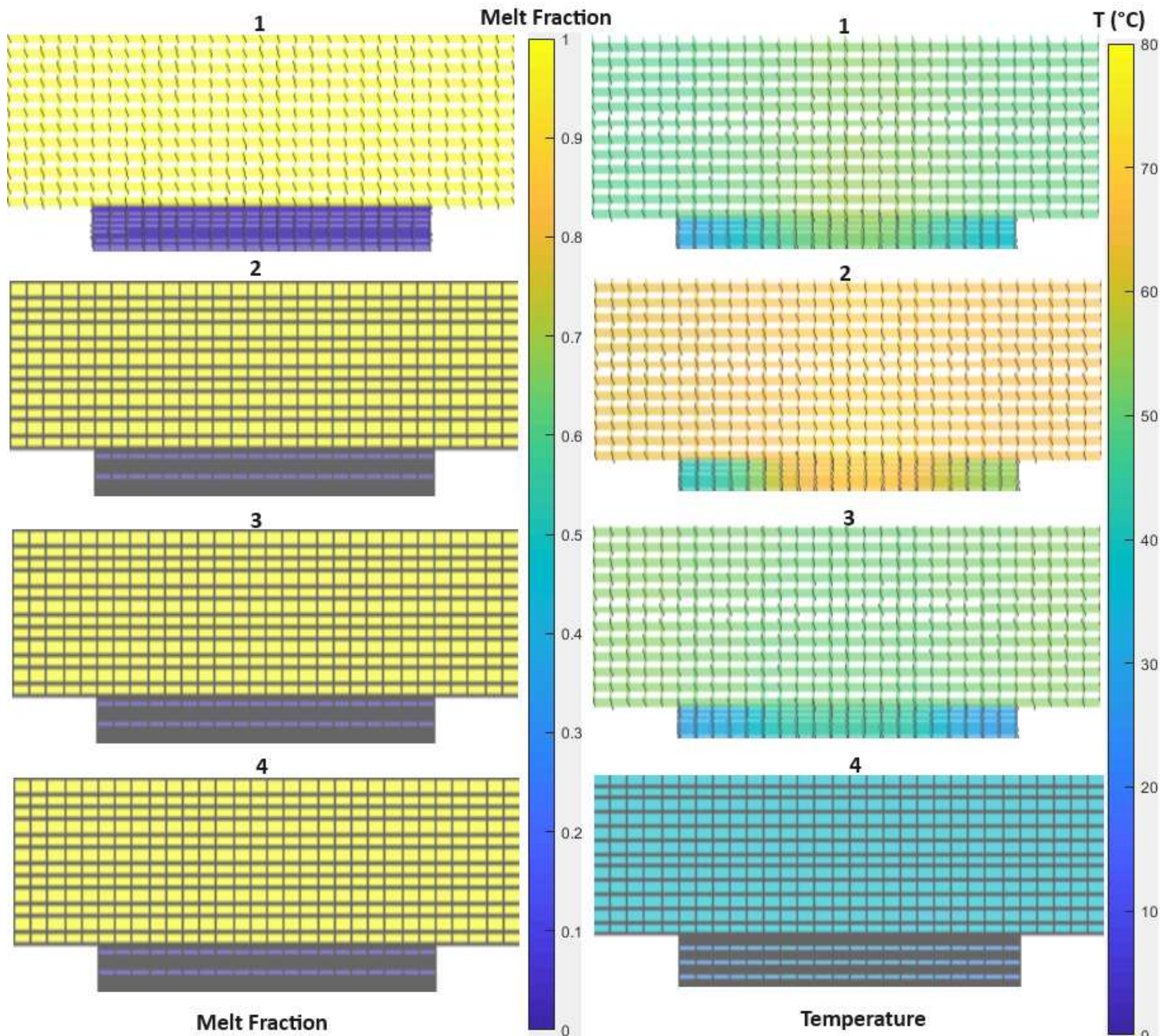

Figure 6-22. Nodal melt fractions and temperatures in PCM at 55 W peak heating with a 0.5 mm Ga60/Cu40 PCM. (1) PCM is fully melted at the ONB, (2) at the peak temperature, sensible heating has occurred in the PCM, (3) the PCM temperature drops as sensible heat is removed, (4) steady state is reached with fully melted PCM and a significantly lowered PCM temperature.

overall heat capacity and the larger thermal conductivity that made transient heat storage in the PCM during the backflow regime more effective.

6.4.3.3. Overall Comparison of PCM Impact at 55 W

As before, the trials with the lowest and highest peak temperatures were run through the model to extract the backflow parameters and bound the potential benefits of including PCM. The results are compared to the baseline peak temperature range across both PCMs and at the three

different modeled thicknesses in Figure 6-23. Given the higher peak heat load, the peak temperature range was much smaller (~5°C) than for the 35.4 or 37.5 W scenarios, representing less stochastic results. Thus, the impact of including the PCMs did not translate to large differences across the different backflow conditions, with a <3°C maximum range. Furthermore, as the PCM thickness increased, this difference decreased even more to ~1°C, thus showcasing the enhanced effect of the PCM in producing more uniform peak temperatures despite the initial range of peak temperature variability.

As shown in Figure 6-24 and in Table 6-3, there were significant reductions in peak temperature when adding the PCMs regardless of thickness or PCM type. The Ga95/Ni5 PCMs

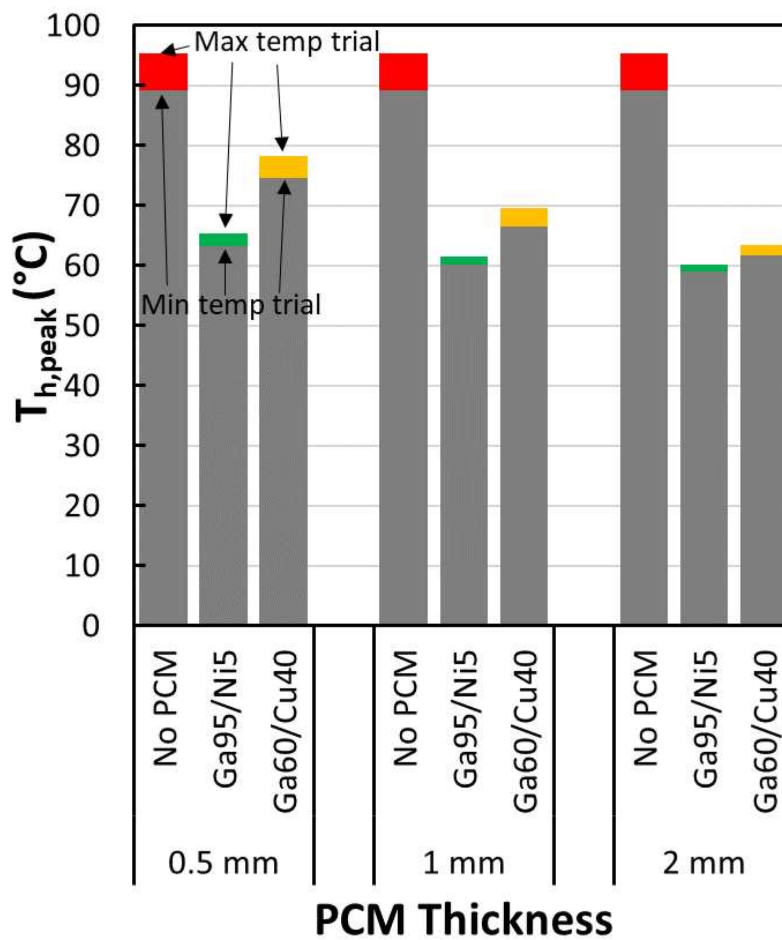

Figure 6-23. Comparison of peak temperature ranges obtained with best- and worst-case trials at a 55 W peak heat load using both PCM types and across the thickness range, with significant reduction in peak temperature observed for all PCM cases.

Table 6-3. Temperature reduction range across PCM types and thicknesses at 55 W.

		0.5 mm	1 mm	2 mm
Ga95/Ni5	Min (°C)	25.89	29.08	30.16
	Max (°C)	29.89	33.80	35.24
Ga60/Cu40	Min (°C)	14.58	22.73	27.38
	Max (°C)	17.06	25.81	31.92

outperformed the Ga60/Cu40 PCMs at this heat load since due to the higher heat load, the latter had already had its latent heat storage exhausted and instead utilized sensible heating during the backflow transient. However, the Ga60/Cu40 PCMs offered a larger margin of effect with increased thickness due to the increase in available latent heat within the high conductivity copper foam matrix and quickly approached the effect afforded by the Ga95/Ni5 PCM. In addition, the

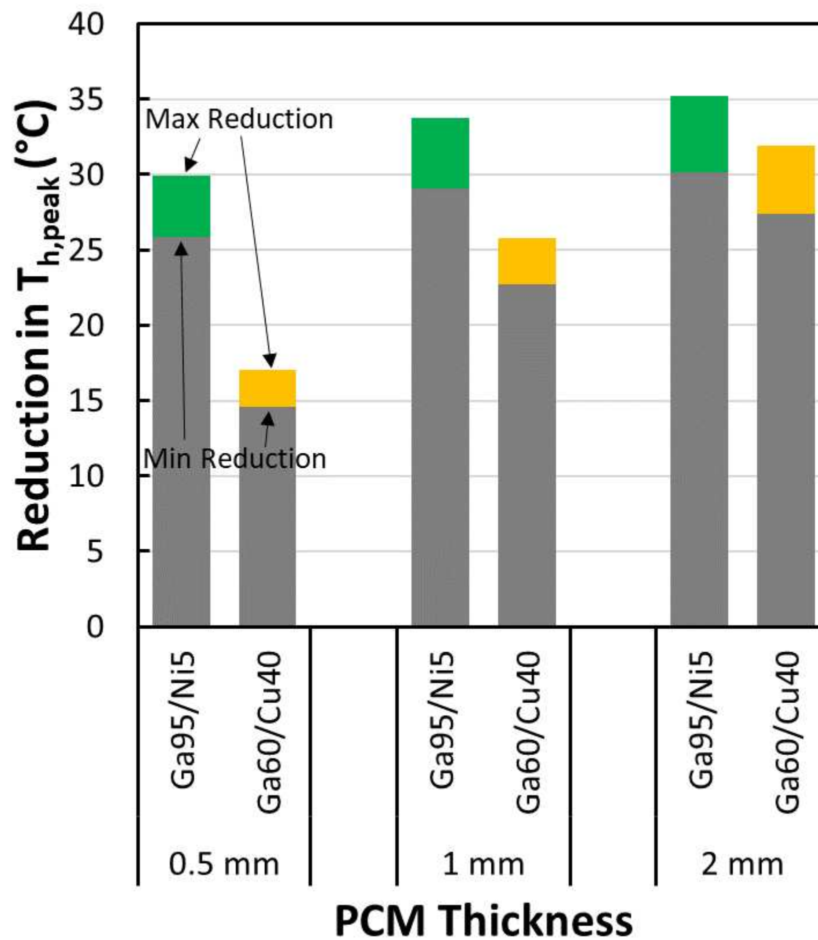

Figure 6-24. Comparison of peak temperature reduction ranges obtained with best- and worst-case trials at a 55 W peak heat load using both PCM types and across the thickness range, with significant reductions which depended heavily on PCM thickness and type.

buffering effect did not level off when increasing the thickness with the Ga60/Cu40 PCM. It is possible that further increasing the thickness would result in the Ga60/Cu40 PCM surpassing the thermal buffering effect of the Ga95/Ni5 PCM. For example, at 0.5 mm of PCM thickness, the peak temperature reductions for Ga60/Cu40 ranged from 14.6 to 17°C, while for Ga95/Ni5, the reductions ranged 26-30°C. However, at the 2 mm thickness, temperature reductions ranged from about 27.5 to 32°C with Ga60/Cu40, to 30 to 35°C for the Ga95/Ni5. Overall, at this 55 W peak heat load, the addition of PCM significantly reduces the peak temperature and improves the transient thermal response even given possible variations in backflow intensity which would result in a larger variation in peak temperature without a PCM than with one.

6.5. Chapter Summary

In this chapter, the potential effect of incorporating different types and volumes of phase change materials (PCMs) on the microchannel evaporator transient thermal response was investigated semi-empirically and through simulations. First the potential buffering impact of including a PCM on this evaporator was studied comprehensively at 35.4 W of peak heating using a large range of PCM thicknesses, areas, and PCM materials. It was found that the larger volumes of PCM along with the higher thermal conductivity PCMs elicited a stronger buffering response by keeping the device temperature lower for longer, demonstrating trade-offs in power and energy density. Higher power density resulted in stronger buffering effects, while higher energy density resulted in longer overall durations of buffering.

To emulate the effects of the PCM experimentally, the heating rate to the fluid in the simulations was extracted and applied as an arbitrary waveform to the experimental test section heater. This was a valid approach due to the small thermal capacitance of the microchannel test section which resulted in a nearly immediate transfer of heat to the fluid when compared with the

addition of PCM. After running the experiments, it was found that, on average, most of the PCMs did not reduce the ONB or peak temperatures compared with the baseline response but in some cases resulted in higher average peak temperatures. The higher thermal conductivity PCMs did reduce the ONB temperatures by ~5°C, but given the already large ONB temperatures and subsequently the wall superheat, it is plausible that a 5°C reduction was not enough to measurably impact the peak temperature. In addition, the PCM heating rate that was simulated assumed single-phase heating conditions throughout, and the inclusion of a PCM would likely reduce the peak temperature by absorbing an increased amount of heat during the vapor backflow phase. This can be explained by considering that the heat transfer coefficient dropped dramatically during the backflow as conduction to vapor ensued, which increased the thermal resistance to the coolant fluid and drove more heat into the PCM.

This effect was studied in the NavyHHF model by incorporating PCM into the three heat load test case models developed in Chapter 5. Two gallium composite metal foam PCMs, one a copper foam, and the other a nickel foam, in thicknesses between 0.5 and 2 mm, were investigated subject to several assumptions. Because the real PCM could not be investigated directly in this work, and based off the variable reduction in ONB temperatures, the models were assumed to retain the same ONB temperatures and vapor backflow durations and time constants as the baseline case without PCM. This would ensure at least a relative comparison of the PCM performance. In addition, to bound the expected performance impact, the trials with the highest and lowest peak temperatures were both run through the models to determine their corresponding backflow and ONB conditions, and then the PCM models were run with both these scenarios for each peak heat load model.

The results showed marked reductions in peak temperatures with the inclusion of PCM, with the reduction in peak temperature generally increasing as the peak heat load increased. Slight differences in performance were observed across the PCM type, with in general the copper foam composite offering a slight edge due to its increased thermal conductivity. In addition, increases in thickness were met with diminishing returns on reducing the peak temperature, though the extent of this improvement was overall higher with the copper foam composite due to its higher conductivity and its lower latent heat. Investigating the transient PCM heating rate and melting fraction revealed that a large spike in heat transfer to the PCM occurred during the backflow phase and was mostly in the form of sensible heat storage for the lower volume PCMs, thus offsetting the rise in peak temperature which would otherwise occur.

CHAPTER 7. Conclusions and Recommendation for Further Work

In this research effort, an extensive study was conducted investigating the transient thermal performance of two <100 μm hydraulic diameter, low thermal resistance, silicon, microchannel evaporators with distinct flow geometry. Knowledge of the impact that transient heating has on flow boiling in a microchannel device is crucial for maintaining high performance devices with reliable operation. The current study investigated the transient performance of these two devices under a large range of fluid inlet and heating conditions to characterize parametric trends in behavior and develop strategies for improving the transient performance observed. In addition, novel predictive models of the transient behavior were created and validated with the experimental results to provide tools for future design and tradeoff studies in these devices. Furthermore, impact of using phase change materials to buffer thermal transients was investigated via simulation and experiment.

Two microchannel evaporators were tested and modeled. Under stepped heat loads, large wall superheats were followed by violent vapor generation at the Onset of Nucleate Boiling (ONB) which resulted in vapor backflow into the inlet plenum of the device. The ONB was followed by a rapid drop to a much lower steady state temperature as the efficient phase change process greatly increased the heat transfer performance, and therefore resulted in a large temperature overshoot. The temperature at the ONB increased as the peak heat load increased. Reducing the transient heating rate by ramping the heat load greatly improved the peak temperature and reduced the vapor backflow due to the decreased wall superheat under which boiling conditions occurred; however, an asymptotic reduction in peak temperature with reduced ramping rate was observed, suggesting an optimal rate. The combination of smaller channel dimensions with a smaller channel to inlet

restriction ratio resulted in larger temperature spikes after boiling inception with peak temperatures higher than the device with larger channels at similar nominal heat loads despite improved steady state performance. In the evaporator with smaller channels, a shift in observed behavior was observed below 35 W, where the device reached a transient steady state in a metastable liquid state, and boiling initiated stochastically as heat loads were low enough to limit the possible range of nucleation cavities with low activation energies.

The differences in observed behavior between the devices provide insights into the effects of device geometry, surface conditions, and inlet restriction ratios on performance. The microfabrication etching process creates channels with a smaller distribution of possible nucleation sites, the small channel dimensions result in high liquid heat transfer coefficients, and the combination of these effects resulted in high wall superheats. High wall superheats at nucleation resulted in violent vapor generation, and combined with the small channel dimensions, increased the chance of flow reversal. While the inlet restrictions reduced backflow at steady state, they were insufficient during the transient. Furthermore, the channel to restriction ratio of 1.3:1 on the 38 μm hydraulic diameter evaporator resulted in significantly worsened vapor backflow than the 2:1 ratio on the 52 μm hydraulic diameter device. Although the smaller channels improved steady state performance, their transient behavior was significantly worse, and additional constraints on channel and inlet restriction design may be required to optimize both transient and steady state performance. Higher pressure drop would be expected with higher inlet ratio restriction, but transient performance may be favorably impacted.

The parametric study identified trends in transient behavior. ONB temperatures increased with peak heat load in a sublinear manner, with a power law dependence on heat load of ~0.5, consistent with literature observations. ONB heater temperatures were not strongly affected by

flow rate or inlet subcooling, though it is possible that the use of the average heater temperature or the large number of channels masked possible localized differences. Increasing inlet subcooling from 2.5 to 10°C resulted in more stochastic peak temperatures below 35 W, likely due to suppression of nucleation cavities, but for higher heat loads where more energy was available to more nucleation sites, resulted in significantly lower peak temperatures of up to 22°C. This was likely due to less vapor generation from increased subcooling that lessened the severity of the vapor backflow.

Higher mass flow rates resulted in a nearly parabolic relationship with heat load with a minimum peak temperature which was shifted to higher heat loads as flow rate was increased. This behavior was suspected to be the result of competing mechanisms which varied in effect as heat load was increased. At low heat loads, more time was spent in a metastable liquid state, and possible nucleation quenching led to significant liquid superheating which in turn intensified vapor backflow. However, at higher heat loads as the duration of time in this metastable state rapidly decreased, a transition to an inertially dominant mechanism was likely responsible which partially mitigated the backward vapor force by a higher incoming fluid inertial force. This was observed experimentally as the duration of vapor backflow in the inlet plenum was significantly reduced with higher flow rates. Peak temperatures at the higher heat loads were reduced by up to 36°C, or 33%, but the tradeoff was higher peak temperatures at heat loads below the minimum optimal heat load.

Novel computational models were created and validated off the transient experimental results for both evaporators in the NavyHHF-ParaPower design and simulation software. A superheat-heat flux relationship was determined semi-empirically for both devices which delayed nucleation to the appropriate temperatures. Then, a modified logistic growth model was used to

dictate the transition time between different heat transfer coefficient phases. The models showed reasonable agreement with experimental results and provided additional functionality for predicting the transient behavior in the computational design tool.

Based on experimental results and the model simulations, it was posited that reducing the rate under which heat was added to the fluid facilitated increased growth of the thermal boundary layer and allowed nucleation to occur at lower temperatures. Heating rates which added heat to the fluid faster than the kinetics of thermal boundary layer growth and bubble nucleation could occur resulted in elevated temperatures prior to boiling. A corollary to this hypothesis suggested that the use of phase change materials (PCMs) to reduce the rate of heat transfer to the fluid and buffer the transient thermal response of a microchannel evaporator would result in improved behavior due to the increased thermal capacitance. Gallium and gallium-metal foam composite PCM structures offer low melting temperatures consistent with the operating temperatures of typical high heat flux devices cooled by microchannel flow boiling while also offering high latent heats and thermal conductivities. The addition of these PCMs could improve the thermal mass of the devices and in turn reduce some of the rapid transient behaviors observed.

The transient microchannel flow boiling model developed in NavyHHF was employed to model the impact of incorporating gallium and several different types of gallium-nickel or gallium-copper composite PCMs with different volumes. Assuming the ONB temperature and backflow characteristics remained unchanged with the addition of PCM, models were created for the transitional heat load case of 35 W, an intermediate case at 37.5 W, and a higher heat load case at 55 W. To bound PCM performance, the trials which experience the least and most backflow were run through the models The results showed marked reductions in peak temperatures by up to 32°C with the inclusion of PCM, with the reduction in peak temperature generally increasing as the peak

heat load increased, thereby supporting the hypothesis. Slight differences in performance were observed across the PCM type. In general, the copper foam composite offered slightly superior transient thermal buffering due to its increased thermal conductivity.

Overall, this research investigation:

- ✓ Investigated the transient thermal response of two <100 μm hydraulic diameter multi-microchannel evaporators
- ✓ Observed large wall superheats, temperature overshoots, peak temperatures, and vapor backflow at and following the Onset of Nucleate Boiling conditions (ONB) in low thermal resistance, low thermal capacitance microchannel evaporators
- ✓ Established novel, experimentally-validated models in a computational design tool for transient heating in microchannel evaporators
- ✓ Quantified the potential thermal buffering effect of including Gallium-based phase change materials on microchannel flow boiling under transient heating
- ✓ Provides practical strategies towards improving and predicting the transient thermal response in low thermal resistance, microchannel evaporators.

7.1. Recommendations for Future Work

The current study focused on two, specific microchannel evaporators and studied the transient thermal behavior under a limited set of conditions. The transient behavior was highly dependent on the microchannel geometry and inlet restriction dimensions. PCMs were studied only semi-empirically. The following work is proposed to expand upon the results of this study:

- The two evaporators experienced differential transient behavior related to their channel dimensions and channel to inlet restriction area ratios. While smaller channels are desirable for improving steady state performance, a more critical approach to designing the channel

inlet orifices may be required to reduce vapor backflow during the transients as well as during steady state. An in-depth investigation into the interplay between inlet restriction and channel dimensions should be conducted to understand these tradeoffs. In addition, the differences observed across different channel dimensions highlight the need for conducting more studies on the different observed transient behavior across different microchannel geometries.

- Wall superheats and temperature overshoots were large at the onset of boiling and led to intensified vapor backflow behaviors. The superheats were suspected in part to be due to a small size distribution of nucleation cavities resulting from the micromachining process. Future studies should investigate the effects of adjusting the characteristic sidewall roughness or adding additional area-enhancement features to promote nucleation at lower superheats in a microchannel evaporator operating under transient heating.
- Since an important feature of flow boiling is flexibility in adjusting the saturation temperature, changes in saturation temperature should be investigated. A broader range of testing conditions is therefore suggested to develop a further understanding of key parameters which impact the transient boiling response.
- The transient microchannel flow boiling models were created for a limited set of conditions. In addition, behavioral differences were observed across multiple trials at the same nominal testing conditions. Future efforts should expand the number of parameters included in the models along with incorporating a statistical approach for addressing the observed variation across trials. Future efforts should also work on determining if non-dimensional relationships and correlations may be found between fluid parameters, device geometry, operating conditions, and possibly surface conditions. Knowledge of nucleation

site density would be very important but may not be practical. Improved simulations using molecular dynamics or similar high-resolution software may help provide additional support but may be limited by high computational demand. Finally, with the rise of AI tools, additional patterns or insights may be gleaned which help form the basis of additional predictive functionality for these models.

- Phase change materials were investigated semi-empirically using a computational tool to model the expected PCM behavior. However, the assumptions of constant backflow behavior and onset of boiling conditions may not hold, and it is likely that experimental results using PCMs will deviate from the current modeling results. Future experimental investigations using composite PCMs on the tested microchannel devices are therefore warranted and recommended to truly capture the potential thermal buffering effects provided by including a PCM.

REFERENCES

[1] F.X. Daiminger, F. Dorsch, D. Lorenzen, High-power laser diodes, laser diode modules, and their applications, in: Laser Optics '98: Solid State Lasers, SPIE, 1998: pp. 13–23. https://doi.org/10.1117/12.334785.

[2] X. Liu, W. Zhao, L. Xiong, H. Liu, Packaging of High Power Semiconductor Lasers, Springer-Verlag, New York, 2015. https://doi.org/10.1007/978-1-4614-9263-4.

[3] P. Sprangle, B. Hafizi, A. Ting, R. Fischer, High-power lasers for directed-energy applications, Appl. Opt., AO 54 (2015) F201–F209. https://doi.org/10.1364/AO.54.00F201.

[4] Mid–infrared laser applications in medicine and biology | Philosophical Transactions of the Royal Society of London. Series A: Mathematical, Physical and Engineering Sciences, (n.d.). https://royalsocietypublishing.org/doi/abs/10.1098/rsta.2000.0747?casa_token=rqUn5xIAyJsAAAAA:hn3YwQluqWh6vzPXznZ4Vm30M27oqMsxkNHex1GK9dw4zP6ew5Q5bPFdyfYov4sU2SG-v9hruVE (accessed November 10, 2021).

[5] R. Betti, O.A. Hurricane, Inertial-confinement fusion with lasers, Nature Phys 12 (2016) 435–448. https://doi.org/10.1038/nphys3736.

[6] J.J. Huddle, L.C. Chow, S. Lei, A. Marcos, D.P. Rini, S.J. Lindauer, M. Bass, P.J. Delfyett, Thermal management of diode laser arrays, in: Sixteenth Annual IEEE Semiconductor Thermal Measurement and Management Symposium (Cat. No.00CH37068), 2000: pp. 154–160. https://doi.org/10.1109/STHERM.2000.837078.

[7] A. Bar-Cohen, P. Wang, Thermal Management of On-Chip Hot Spot, Journal of Heat Transfer 134 (2012). https://doi.org/10.1115/1.4005708.

[8] A. Bar-Cohen, M. Asheghi, T.J. Chainer, S.V. Garimella, K. Goodson, C. Gorle, R. Mandel, J.J. Maurer, M. Ohadi, J.W. Palko, P.R. Parida, Y. Peles, J.L. Plawsky, M.D. Schultz, J.A. Weibel, Y. Joshi, The ICECool Fundamentals Effort on Evaporative Cooling of Microelectronics, IEEE Transactions on Components, Packaging and Manufacturing Technology 11 (2021) 1546–1564. https://doi.org/10.1109/TCPMT.2021.3111114.

[9] K. Matin, A. Bar-Cohen, J.J. Maurer, Modeling and Simulation Challenges in Embedded Two Phase Cooling: DARPA's ICECool Program, in: American Society of Mechanical Engineers Digital Collection, 2015. https://doi.org/10.1115/IPACK2015-48334.

[10] P. Palm, J. Moisala, A. Kivikero, R. Tuominen, A. Iihola, Embedding Active Components Inside Printed Circuit Board (PCB) - a Solution for Miniaturization of Electronics, Proceedings. International Symposium on Advanced Packaging Materials: Processes, Properties and Interfaces, 2005. (2005) 1–4. https://doi.org/10.1109/ISAPM.2005.1432034.

[11] C.H. Amon, J. Murthy, S.C. Yao, S. Narumanchi, C. Wu, C. Hsieh, MEMS-enabled thermal management of high-heat-flux devices EDIFICE : embedded droplet impingement for integrated cooling of electronics, 25 (2001).

[12] T. Bevis, High Heat Flux Phase Change Thermal Management of Laser Diode Arrays, PhD Thesis, Colorado State University, 2016.

[13] J.A. Skidmore, B.L. Freitas, J. Crawford, J. Satariano, E. Utterback, L. DiMercurio, K. Cutter, S. Sutton, Silicon monolithic microchannel-cooled laser diode array, Applied Physics Letters 77 (2000) 10–12. https://doi.org/10.1063/1.126860.

[14] S.-M. Kim, I. Mudawar, Universal approach to predicting saturated flow boiling heat transfer in mini/micro-channels – Part II. Two-phase heat transfer coefficient, International Journal

of Heat and Mass Transfer 64 (2013) 1239–1256. https://doi.org/10.1016/j.ijheatmasstransfer.2013.04.014.
[15] S.S. Bertsch, E.A. Groll, V.S. Garimella, A composite heat transfer correlation for saturated flow boiling in small channels, International Journal of Heat and Mass Transfer 52 (2009) 2110–2118.
[16] T.M. Bandhauer, T.A. Bevis, High Heat Flux Boiling Heat Transfer for Laser Diode Arrays, in: American Society of Mechanical Engineers Digital Collection, 2016. https://doi.org/10.1115/ICNMM2016-7947.
[17] J. Richey, Transient Experimentation and Modeling of a Multi-Microchannel Evaporator, M.S., Colorado State University, 2020.
[18] B. Agostini, A. Bontemps, Vertical flow boiling of refrigerant R134a in small channels, International Journal of Heat and Mass Transfer 26 (2005) 296–306. https://doi.org/10.1016/j.ijheatfluidflow.2004.08.003.
[19] L.E. O'Neill, I. Mudawar, Review of two-phase flow instabilities in macro- and micro-channel systems, International Journal of Heat and Mass Transfer 157 (2020) 119738. https://doi.org/10.1016/j.ijheatmasstransfer.2020.119738.
[20] J.A. Boure, A.E. Bergles, L.S. Tong, REVIEW OF TWO-PHASE FLOW INSTABILITY, Nuclear Engineering and Design 25 (1973) 165–192.
[21] H.J. Lee, D.Y. Liu, S. Yao, Flow instability of evaporative micro-channels, International Journal of Heat and Mass Transfer 53 (2010) 1740–1749. https://doi.org/10.1016/j.ijheatmasstransfer.2010.01.016.
[22] J. Xu, J. Zhou, Y. Gan, Static and dynamic flow instability of a parallel microchannel heat sink at high heat fluxes, Energy Conversion and Management 46 (2005) 313–334.
[23] A. Kosar, C.-J. Kuo, Y. Peles, Suppression of Boiling Flow Oscillations in Parallel Microchannels by Inlet, Journal of Heat Transfer 128 (2006) 251–260. https://doi.org/10.1115/1.2150837.
[24] S.G. Kandlikar, D.A. Willistein, J. Borrelli, Experimental Evaluation of Pressure Drop Elements and Fabricated Nucleation Sites for Stabilizing Flow Boiling in Minichannels and Microchannels, in: American Society of Mechanical Engineers Digital Collection, 2008: pp. 115–124. https://doi.org/10.1115/ICMM2005-75197.
[25] S. Halon, Z. Krolicki, R. Revellin, B. Zajaczkowski, Heat transfer characteristics of flow boiling in a micro channel array with various inlet geometries, International Journal of Heat and Mass Transfer 187 (2022) 122549. https://doi.org/10.1016/j.ijheatmasstransfer.2022.122549.
[26] S. Szczukiewicz, N. Borhani, J.R. Thome, Fine-resolution two-phase flow heat transfer coefficient measurements of refrigerants in multi-microchannel evaporators, International Journal of Heat and Mass Transfer 67 (2013) 913–929. https://doi.org/10.1016/j.ijheatmasstransfer.2013.08.078.
[27] C.T. Lu, C. Pan, Stabilization of flow boiling in microchannel heat sinks with a diverging cross-section design, J. Micromech. Microeng. 18 (2008) 075035. https://doi.org/10.1088/0960-1317/18/7/075035.
[28] A.K.M.M. Morshed, F. Yang, M. Yakut Ali, J.A. Khan, C. Li, Enhanced flow boiling in a microchannel with integration of nanowires, Applied Thermal Engineering 32 (2012) 68–75. https://doi.org/10.1016/j.applthermaleng.2011.08.031.
[29] J. Carter, D. Snyder, J. Reichenbaugh, Transient thermal modeling of high-power pulsed laser diode arrays, in: Ninteenth Annual IEEE Semiconductor Thermal Measurement and

Management Symposium, 2003., 2003: pp. 276–283. https://doi.org/10.1109/STHERM.2003.1194374.
[30] N.R. Jankowski, F.P. McCluskey, Modeling transient thermal response of pulsed power electronic packages, in: 2009 IEEE Pulsed Power Conference, 2009: pp. 820–825. https://doi.org/10.1109/PPC.2009.5386368.
[31] N.R. Jankowski, F.P. McCluskey, A review of phase change materials for vehicle component thermal buffering, Applied Energy 113 (2014) 1525–1561. https://doi.org/10.1016/j.apenergy.2013.08.026.
[32] P.J. Shamberger, N.M. Bruno, Review of metallic phase change materials for high heat flux transient thermal management applications, Applied Energy 258 (2020) 113955. https://doi.org/10.1016/j.apenergy.2019.113955.
[33] R.C. McAfee, M.C. Fish, A.A. Wilson, H.H. Tsang, J.A. Boltersdorf, S. Kim, N. Miljkovic, W.P. King, Fabrication and Thermal Properties of a Gallium and Porous Foam Composite Phase Change Material, ACS Appl. Eng. Mater. (2023). https://doi.org/10.1021/acsaenm.3c00366.
[34] T. Yang, J.G. Kang, P.B. Weisensee, B. Kwon, P.V. Braun, N. Miljkovic, W.P. King, A composite phase change material thermal buffer based on porous metal foam and low-melting-temperature metal alloy, Appl. Phys. Lett. 116 (2020) 071901. https://doi.org/10.1063/1.5135568.
[35] D. Gonzalez-Nino, L.M. Boteler, D. Ibitayo, N.R. Jankowski, D. Urciuoli, I.M. Kierzewski, P.O. Quintero, Experimental evaluation of metallic phase change materials for thermal transient mitigation, International Journal of Heat and Mass Transfer 116 (2018) 512–519. https://doi.org/10.1016/j.ijheatmasstransfer.2017.09.039.
[36] J. Hollis, D.J. Sharar, T. Bandhauer, Effect of Phase Change Material On Dynamic Thermal Management Performance for Power Electronics Packages, Journal of Electronic Packaging (2021). https://doi.org/10.1115/1.4052669.
[37] F. TACHIBANA, M. AKIYAMA, H. KAWAMURA, Heat Transfer and Critical Heat Flux in Transient Boiling, (I): An Experimental Study in Saturated Pool Boiling, Journal of Nuclear Science and Technology 5 (1968) 117–126. https://doi.org/10.1080/18811248.1968.9732415.
[38] M.W. Rosenthal, An Experimental Study of Transient Boiling, Nuclear Science and Engineering 2 (1957) 640–656. https://doi.org/10.13182/NSE57-A25431.
[39] G.-Y. Su, M. Bucci, T. McKrell, J. Buongiorno, Transient boiling of water under exponentially escalating heat inputs. Part I: Pool boiling, International Journal of Heat and Mass Transfer 96 (2016) 667–684. https://doi.org/10.1016/j.ijheatmasstransfer.2016.01.032.
[40] Y. Yan, E. Brown, W. Marcum, Experimental study of the transient boiling phenomenon on a vertically placed ribbon, Nuclear Engineering and Design 390 (2022) 111705. https://doi.org/10.1016/j.nucengdes.2022.111705.
[41] L.L. Giventer, J.L. Smith, Transient Pool Boiling of Liquid Nitrogen Due to a Square-Wave Heat Flux, in: K.D. Timmerhaus (Ed.), Advances in Cryogenic Engineering, Springer US, Boston, MA, 1995: pp. 259–270. https://doi.org/10.1007/978-1-4757-0513-3_31.
[42] M.-C. Duluc, B. Stutz, M. Lallemand, Transient nucleate boiling under stepwise heat generation for highly wetting fluids, International Journal of Heat and Mass Transfer 47 (2004) 5541–5553. https://doi.org/10.1016/j.ijheatmasstransfer.2004.04.038.

[43] S. Héas, H. Robidou, M. Raynaud, M. Lallemand, Onset of transient nucleate boiling from a thick flat sample, International Journal of Heat and Mass Transfer 46 (2003) 355–365. https://doi.org/10.1016/S0017-9310(02)00267-3.
[44] S.G. Kandlikar, W.J. Grande, Evolution of Microchannel Flow Passages–Thermohydraulic Performance and Fabrication Technology, Heat Transfer Engineering 24 (2003) 3–17. https://doi.org/10.1080/01457630304040.
[45] S.S. Mehendale, A.M. Jacobi, R.K. Shah, Fluid Flow and Heat Transfer at Micro- and Meso-Scales With Application to Heat Exchanger Design, Applied Mechanics Reviews 53 (2000) 175–193. https://doi.org/10.1115/1.3097347.
[46] P.A. Kew, K. Cornwell, Correlations for the prediction of boiling heat transfer in small-diameter channels, Applied Thermal Engineering 17 (1997) 705–715. https://doi.org/10.1016/S1359-4311(96)00071-3.
[47] V.V. Kuznetsov, A.S. Shamirzaev, I.A. Kozulin, S.P. Kozlov, Correlation of the Flow Pattern and Flow Boiling Heat Transfer in Microchannels, Heat Transfer Engineering 34 (2013) 235–245. https://doi.org/10.1080/01457632.2013.703564.
[48] T. Harirchian, S.V. Garimella, A comprehensive flow regime map for microchannel flow boiling with quantitative transition criteria, International Journal of Heat and Mass Transfer 53 (2010) 2694–2702. https://doi.org/10.1016/j.ijheatmasstransfer.2010.02.039.
[49] G.-Y. Su, M. Bucci, T. McKrell, J. Buongiorno, Transient boiling of water under exponentially escalating heat inputs. Part II: Flow boiling, International Journal of Heat and Mass Transfer 96 (2016) 685–698. https://doi.org/10.1016/j.ijheatmasstransfer.2016.01.031.
[50] V. Scheiff, N. Baudin, P. Ruyer, J. Sebilleau, C. Colin, Transient flow boiling in a semi-annular duct: From the Onset of Nucleate Boiling to the Fully Developed Nucleate Boiling, International Journal of Heat and Mass Transfer 138 (2019) 699–712. https://doi.org/10.1016/j.ijheatmasstransfer.2019.04.069.
[51] R. Visentini, C. Colin, P. Ruyer, Experimental investigation of heat transfer in transient boiling, Experimental Thermal and Fluid Science 55 (2014) 95–105. https://doi.org/10.1016/j.expthermflusci.2014.02.026.
[52] W.J. Van den Bergh, J. Dirker, C.N. Markides, J.P. Meyer, Influence of non-steady transient heat flux on flow boiling heat transfer and pressure drop in horizontal pipes, International Journal of Heat and Mass Transfer 182 (2022) 121927. https://doi.org/10.1016/j.ijheatmasstransfer.2021.121927.
[53] S.G. Kandlikar, Nucleation characteristics and stability considerations during flow boiling in microchannels, Experimental Thermal and Fluid Science 30 (2006) 441–447. https://doi.org/10.1016/j.expthermflusci.2005.10.001.
[54] M.E. Rahman, J.A. Weibel, Influence of convective heat transfer and wall thermal capacity on dynamic interactions between wall temperature and pressure drop oscillations during microchannel flow boiling, International Journal of Heat and Mass Transfer 221 (2024) 125111.
[55] S. Basu, B. Werneke, Y. Peles, M.K. Jensen, Transient microscale flow boiling heat transfer characteristics of HFE-7000, International Journal of Heat and Mass Transfer 90 (2015) 396–405. https://doi.org/10.1016/j.ijheatmasstransfer.2015.06.038.
[56] G. Chen, P. Cheng, Nucleate and film boiling on a microheater under pulse heating in a microchannel, Internation Communications in Heat and Mass Transfer 36 (2009).
[57] T.A. Kingston, J.A. Weibel, S.V. Garimella, Time-resolved characterization of microchannel flow boiling during transient heating: Part 1 – Dynamic response to a single heat flux pulse,

International Journal of Heat and Mass Transfer 154 (2020) 119643. https://doi.org/10.1016/j.ijheatmasstransfer.2020.119643.
[58] J. Zhuang, H. Yu, H. Tianbiao, M. Ning, Unsteady characteristics of flow pattern and pressure drop of flow boiling in single straight microchannel under sudden heat flux increase, J Therm Anal Calorim 147 (2022) 14571–14586. https://doi.org/10.1007/s10973-022-11641-9.
[59] H. Huang, N. Borhani, J.R. Thome, Thermal Response of Multi- Microchannel Evaporators During Flow Boiling of Refrigerants Under Transient Heat Loads With Flow Visualization, 138 (2018) 1–13. https://doi.org/10.1115/1.4033487.
[60] B. Markal, A. Evcimen, Transient behavior of flow boiling in structured microchannels under sudden and highly variable heat loads, International Communications in Heat and Mass Transfer 154 (2024) 107431. https://doi.org/10.1016/j.icheatmasstransfer.2024.107431.
[61] S. Basu, B. Werneke, Y. Peles, M.K. Jensen, Thermal Behavior of a microdevice under transient heat loads, International Journal of Heat and Mass Transfer 91 (2015) 1078–1087.
[62] C. Anderson, J. Richey, M. Fish, T. Bandhauer, Peak Temperature Mitigation of a Multimicrochannel Evaporator Under Transient Heat Loads, Journal of Electronic Packaging 143 (2021). https://doi.org/10.1115/1.4052360.
[63] M. Shamssuzzoha, Closed-Loop PI/PID Controller Tuning for Stable and Integrating Process with Time Delay, (n.d.). https://www.academia.edu/12100580/Closed_Loop_PI_PID_Controller_Tuning_for_Stable_and_Integrating_Process_with_Time_Delay (accessed May 1, 2024).
[64] H.W. Coleman, W.G. Steele, Experimentation, Validation, and Uncertainty Analysis for Engineers, Third, Wiley, Hoboken, 2009.
[65] J.L. Riddle, G.T. Furukawa, H.H. Plumb, Platinum Resistance Thermometry, National Bureau of Standards, 1973.
[66] F.P. Incropera, D.P. Dewitt, T.L. Bergman, A.S. Lavine, Fundamentals of Heat and Mass Transfer, 7th ed., John Wiley & Sons, 2011.
[67] M. Deckard, P. Shamberger, M. Fish, M. Berman, J. Wang, L. Boteler, Convergence and Validation in ParaPower: A Design Tool for Phase Change Materials in Electronics Packaging, in: 2019 18th IEEE Intersociety Conference on Thermal and Thermomechanical Phenomena in Electronic Systems (ITherm), 2019: pp. 878–885. https://doi.org/10.1109/ITHERM.2019.8757334.
[68] L.M. Boteler, S.M. Miner, M. Fish, M. Berman, Integrating Heat Sinks into a 3D Co-Design Network Model for Quick Parametric Analysis, in: 2019 18th IEEE Intersociety Conference on Thermal and Thermomechanical Phenomena in Electronic Systems (ITherm), 2019: pp. 518–524. https://doi.org/10.1109/ITHERM.2019.8757416.
[69] L. Boteler, M. Fish, M. Berman, ARL ParaPower Fundamentals, (2019).
[70] S. Hodson, K. McCarthy, P. McCarthy, M. Issam, A Dynamic Two-Phase Component Model Library for High Heat Flux Applications, SAE International (2019) 1–11. https://doi.org/10.4271/2019-01-1386.
[71] R.K. Shah, A.L. London, Laminar Flow Forced Convection in Ducts: A Source Book for Compact Heat Exchanger Analytical Data, Academic Press, 2014.
[72] H.R. Shanks, P.D. Maycock, P.H. Sidles, G.C. Danielson, Thermal Conductivity of Silicon from 300 to 1400\ifmmode^\circ\else\textdegree\fi{}K, Phys. Rev. 130 (1963) 1743–1748. https://doi.org/10.1103/PhysRev.130.1743.
[73] EES: Engineering Equation Solver | F-Chart Software : Engineering Software, (n.d.). https://www.fchartsoftware.com/ees/ (accessed April 25, 2024).

[74] P.-S. Lee, S.V. Garimella, Saturated flow boiling heat transfer and pressure drop in silicon microchannel arrays, International Journal of Heat and Mass Transfer 51 (2008) 789–806. https://doi.org/10.1016/j.ijheatmasstransfer.2007.04.019.
[75] F.L. Levy, A modified Maxwell-Eucken equation for calculating the thermal conductivity of two-component solutions or mixtures, International Journal of Refrigeration 4 (1981) 223–225. https://doi.org/10.1016/0140-7007(81)90053-0.
[76] J. Wang, J.K. Carson, M.F. North, D.J. Cleland, A new structural model of effective thermal conductivity for heterogeneous materials with co-continuous phases, International Journal of Heat and Mass Transfer 51 (2008) 2389–2397. https://doi.org/10.1016/j.ijheatmasstransfer.2007.08.028.
[77] Torquato S.,. Author, Haslach HW ,. Jr, Random Heterogeneous Materials: Microstructure and Macroscopic Properties, Applied Mechanics Reviews 55 (2002) B62–B63. https://doi.org/10.1115/1.1483342.
[78] A. Bhattacharya, V.V. Calmidi, R.L. Mahajan, Thermophysical properties of high porosity metal foams, International Journal of Heat and Mass Transfer 45 (2002) 1017–1031. https://doi.org/10.1016/S0017-9310(01)00220-4.
[79] Y.Y. Hsu, On the Size Range of Active Nucleation Cavities on a Heating Surface, Journal of Heat Transfer 84 (1962) 207. https://doi.org/10.1115/1.3684339.
[80] H. Steiner, A. Kobor, L. Gebhard, A wall heat transfer model for subcooled boiling flow, International Journal of Heat and Mass Transfer 48 (2005) 4161–4173. https://doi.org/10.1016/j.ijheatmasstransfer.2005.03.032.
[81] B.E. Burk, T.P. Grumstrup, T.A. Bevis, J. Kotovsky, T.M. Bandhauer, Computational examination of two-phase microchannel heat transfer correlations with conjugate heat spreading, International Journal of Heat and Mass Transfer 132 (2019) 68–79. https://doi.org/10.1016/j.ijheatmasstransfer.2018.11.068.
[82] S.M. Ghiaasiaan, R.C. Chedester, Boiling incipience in microchannels, International Journal of Heat and Mass Transfer 45 (2002) 4599–4606. https://doi.org/10.1016/S0017-9310(02)00167-9.
[83] S.L. Qi, P. Zhang, R.Z. Wang, L.X. Xu, Flow boiling of liquid nitrogen in micro-tubes: Part II – Heat transfer characteristics and critical heat flux, International Journal of Heat and Mass Transfer 50 (2007) 5017–5030. https://doi.org/10.1016/j.ijheatmasstransfer.2007.08.017.
[84] N. Basu, G.R. Warrier, V.K. Dhir, Onset of Nucleate Boiling and Active Nucleation Site Density During Subcooled Flow Boiling, Journal of Heat Transfer 124 (2002) 717–728. https://doi.org/10.1115/1.1471522.
[85] J.R.S. Thom, W.M. Walker, T.A. Fallon, G.F.S. Reising, Paper 6: Boiling in Sub-Cooled Water during Flow up Heated Tubes or Annuli, Proceedings of the Institution of Mechanical Engineers, Conference Proceedings 180 (1965) 226–246. https://doi.org/10.1243/PIME_CONF_1965_180_117_02.
[86] A. Rabhi, I. Aslanidou, K. Kyprianidis, R. Bel Fdhila, Onset of Nucleate Boiling Model for Rectangular Upward Narrow Channel: CFD Based Approach, International Journal of Heat and Mass Transfer 165 (2021) 120715. https://doi.org/10.1016/j.ijheatmasstransfer.2020.120715.
[87] D. Liu, P.-S. Lee, S.V. Garimella, Prediction of the onset of nucleate boiling in microchannel flow, International Journal of Heat and Mass Transfer 48 (2005) 5134–5149. https://doi.org/10.1016/j.ijheatmasstransfer.2005.07.021.

[88] X. Lu, J. Liu, X. Xu, Contact angle measurements of pure refrigerants, International Journal of Heat and Mass Transfer 102 (2016) 877–883. https://doi.org/10.1016/j.ijheatmasstransfer.2016.06.099.
[89] V.G. Baidakov, V.P. Skripov, Experimental study of cryogenic liquids in the metastable superheated state, Experimental Thermal and Fluid Science 5 (1992) 664–678. https://doi.org/10.1016/0894-1777(92)90022-W.
[90] T. Okawa, ONSET OF NUCLEATE BOILING IN MINI AND MICROCHANNELS: A BRIEF REVIEW, Frontiers in Heat and Mass Transfer 3 (2012). https://doi.org/10.5098/hmt.v3.1.3001.
[91] H. Huang, N. Borhani, J.R. Thome, Thermal Response of Multi- Microchannel Evaporators During Flow Boiling of Refrigerants Under Transient Heat Loads With Flow Visualization, 138 (2018) 1–13. https://doi.org/10.1115/1.4033487.
[92] P. Gregorčič, M. Zupančič, I. Golobič, Scalable Surface Microstructuring by a Fiber Laser for Controlled Nucleate Boiling Performance of High- and Low-Surface-Tension Fluids, Sci Rep 8 (2018) 7461. https://doi.org/10.1038/s41598-018-25843-5.
[93] X. Cheng, H. Wu, Impact of inlet subcooling on flow boiling in microchannels, Experimental Thermal and Fluid Science 142 (2023) 110805. https://doi.org/10.1016/j.expthermflusci.2022.110805.

APPENDIX A. Arduino Synchronization Control Switch

To achieve synchronization between the power supply and flow visualization camera, a simple Arduino-controlled switch was constructed which contained a push button to trigger the power supply and high-speed camera. To do this, an N-channel Metal Oxide Field Effect Transistor (MOSFET) was used with several resistors to act as a switch driven by the Arduino Uno. Figure A-1 shows a schematic of the wiring diagram of the setup, while Figure A-2 shows the real device layout. The logic works as follows. The devices are initially in a LOW state, and

Figure A-1. Schematic of Arduino-controlled synchronization and trigger switch.

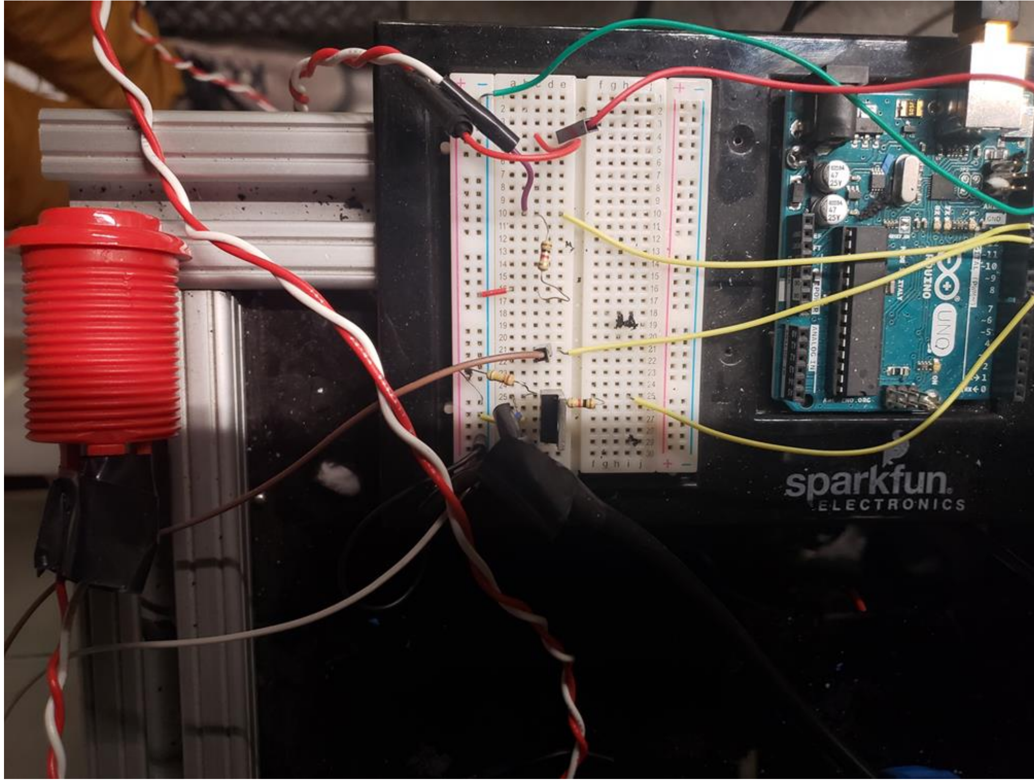

Figure A-2. Arduino-controlled trigger and synchronization switch setup.

the MOSFET switch is therefore open. The power supply is set to trigger via an external voltage source and in the DAQ software waits for the external source from the Arduino to switch on power to the test section. Once the push button is pressed, the sense pin reads HIGH, and the Arduino is programmed to send a HIGH voltage signal to the N7953A power supply and the MOSFET switch. Once a HIGH signal is supplied to the gate of the MOSFET, the circuit between source and drain is closed. This closed switch then allows a 5 V internal signal in the Pixelink camera to be supplied to an internal optocoupling diode via a pull-up resistor which then triggers the Pixelink camera to start recording frames.

APPENDIX B. Pressure Drop Correction Models

COMSOL MultiPhysics v5.6 was used to create pressure drop correction models for the complex plenum and inlet restriction geometries in the test piece to determine the appropriate pressure to use at the inlet or outlet of the test section. The following section details the model setup and equations, mesh sensitivity, and some representative data for each.

B.1. Model Equations and Assumptions

Adiabatic, isothermal flow was assumed in these models, with no viscous dissipation or flow heating. Steady, incompressible flow was assumed due to the liquid state and the steady nature of the pressure drop in the test section under steady state conditions. The resulting Navier-Stokes equations are as follows

$$\nabla \cdot \vec{u} = 0 \tag{B-1}$$

$$\vec{u} \cdot \overrightarrow{\nabla u} = -\frac{1}{\rho}\nabla P + \nu \nabla^2 \vec{u}. \tag{B-2}$$

Because of sharp bends and likely flow separation, the two-equation k-ω SST turbulence model was also incorporated to capture any turbulence effects. This model is preferred over the standard k-ω model for improved stability. The default first order Lagrange elements were used for discretizing the model equations. COMSOL's GMRES solver was used with F-Multigrid preconditioning for the pressure and velocity, while for the turbulence variables the direct PARDISO solver was used. An absolute tolerance of 10^{-4} was used as the target solution residual.

B.2. Inlet Plenum Pressure Drop Model

The inlet plenum model was the first pressure drop model created, and the computational domain was shown in Figure 3-8, with an additional inlet tube region set to precondition the

velocity profile since it may not be fully developed at the pressure transducer location. A uniform inlet velocity profile was set based off the mass flow rate, and a zero-gauge pressure condition was set at the outlet such that the local pressure was the local pressure drop through the inlet plenum model. Up to 12 high orthogonal quality hexahedral elements were used near the walls of the device to capture the large velocity gradients in the boundary layer, while the rest of the model was meshed with tetrahedral elements due to the complex geometry. A mesh sensitivity study was conducted to determine if the mesh was satisfactorily fine to capture the pressure drop accurately. The mesh sensitivity study is shown in Figure B-1 and shows that the pressure drop changed less than 3% between the fine and medium meshes, with a total pressure drop of about 1.53 kPa in this case. Therefore, the fine mesh with ~800,000 elements was used.

A velocity streamline plot for a sample set of conditions is shown in Figure B-2. From this figure, the 90° bend followed by a large contraction from the inlet tube into the five narrower channels results in a large increase in velocity and thus a large pressure drop relative to the rest of

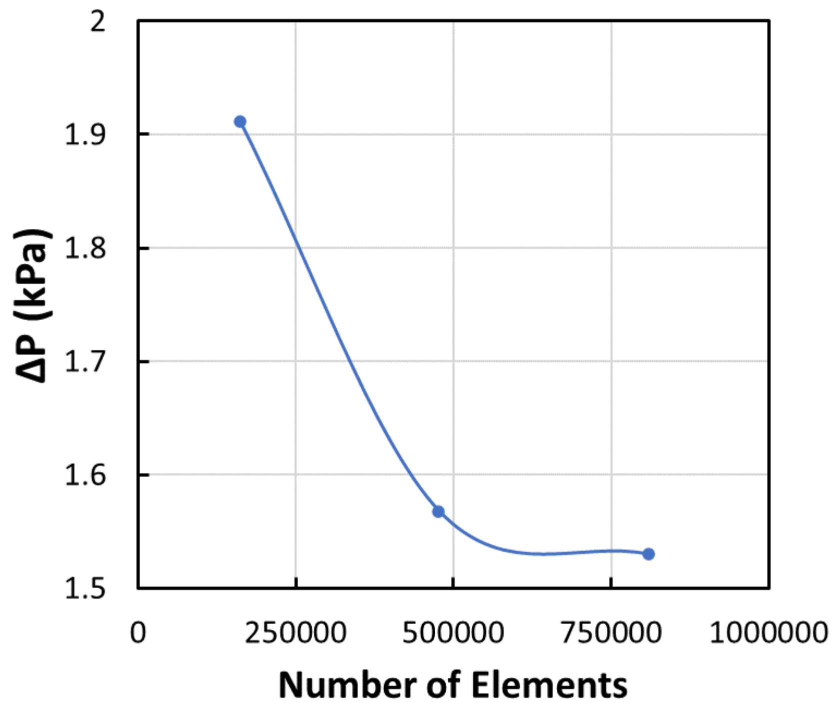

Figure B-1. Mesh sensitivity study for inlet plenum pressure drop model at 50 g/min.

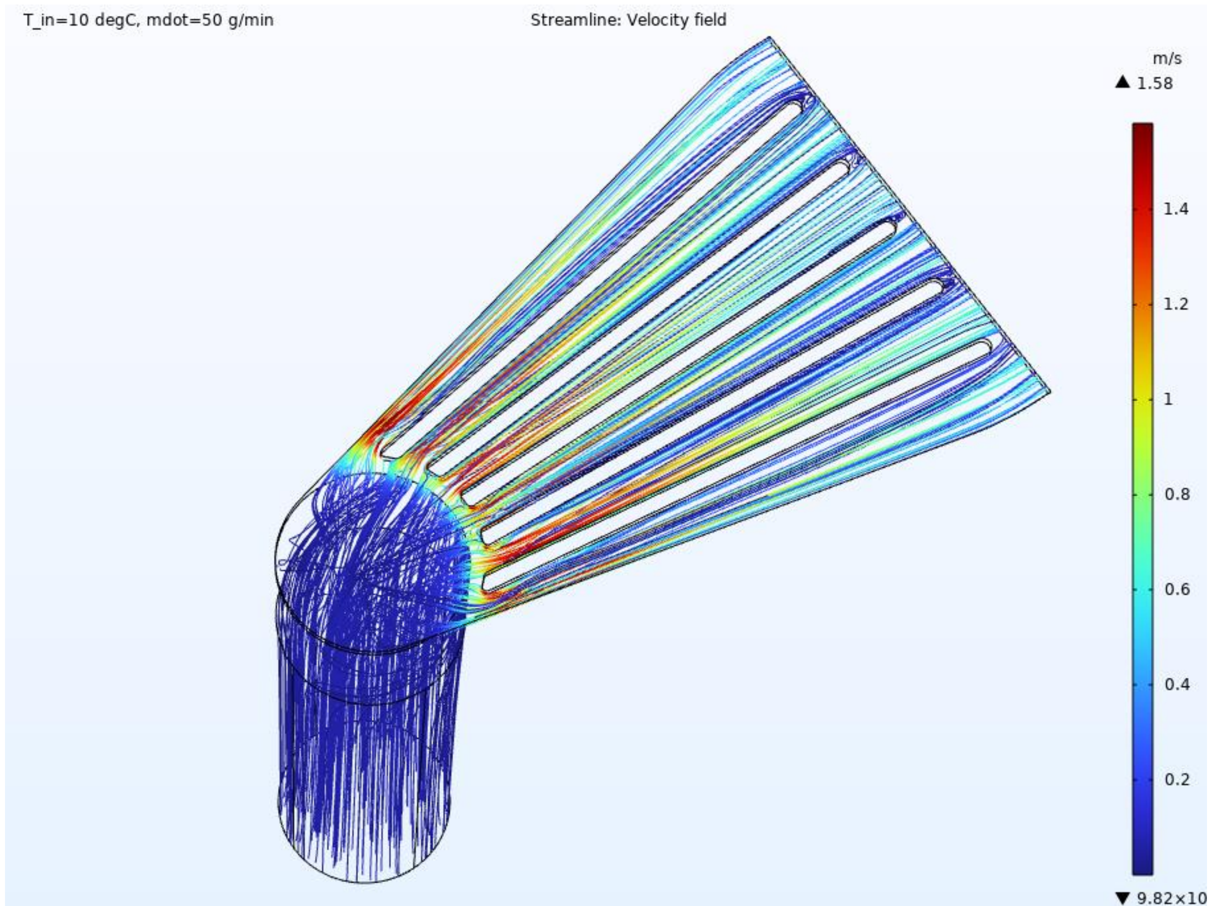

Figure B-2. Example velocity streamline profiles for inlet plenum pressure drop model, where large velocity changes occur when moving from the inlet tube to the 90° bend with contraction into the five channels.

the model. Previous attempts at correcting for this pressure drop made geometric assumptions or assumptions about the order in which to apply pressure drop correlations from the literature. This model clearly shows that a large fraction of the pressure drop occurs in this contraction region into the five supporting feature channels.

B.3. Inlet Restriction Pressure Drop Model

After the inlet plenum model was completed, another model for the inlet restriction was created based on microscopic inspection. A half-channel model was set up with the complex inlet restriction profile and is shown in Figure B-3. An additional inlet conditioning region was used since this region improved the model convergence. Symmetry boundary conditions were applied

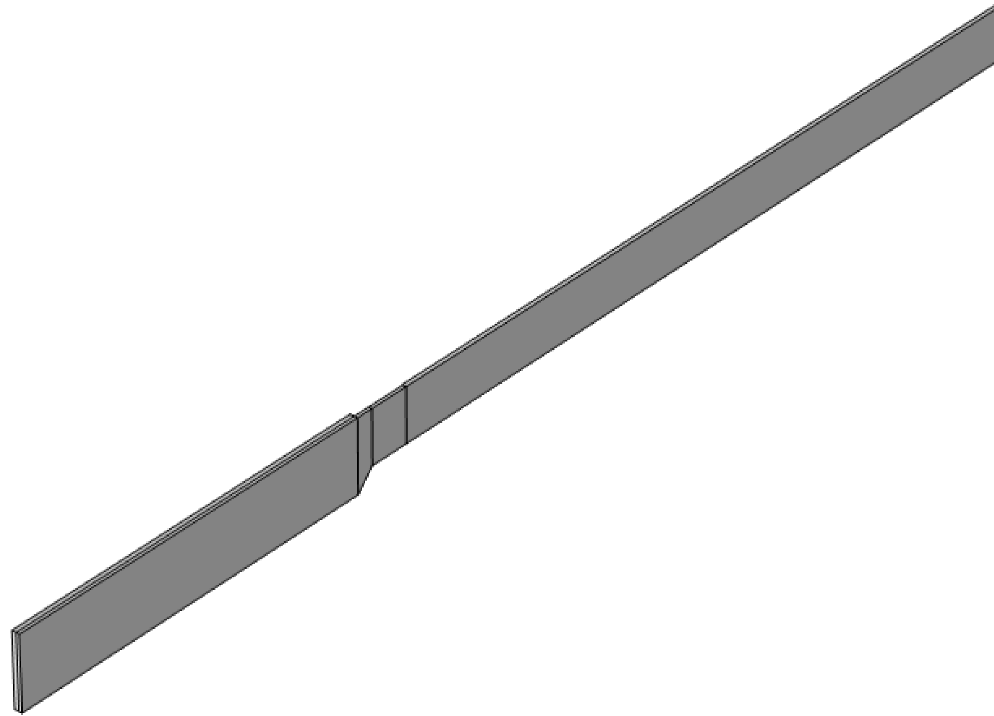

Figure B-3. Computational domain for half-channel inlet restriction and channel geometry.

at the midplanes that divided the channel. A mass flow rate boundary condition was provided at the inlet, normalized to the half-channel domain, while again a zero-gauge pressure was set at the

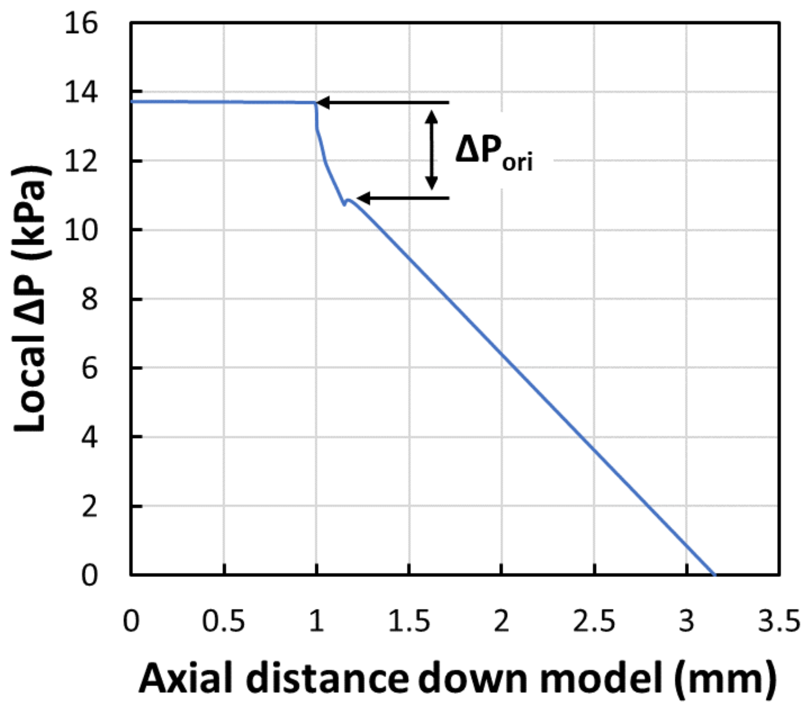

Figure B-4. Determination of local pressure drop in inlet restriction model at 50 g/min.

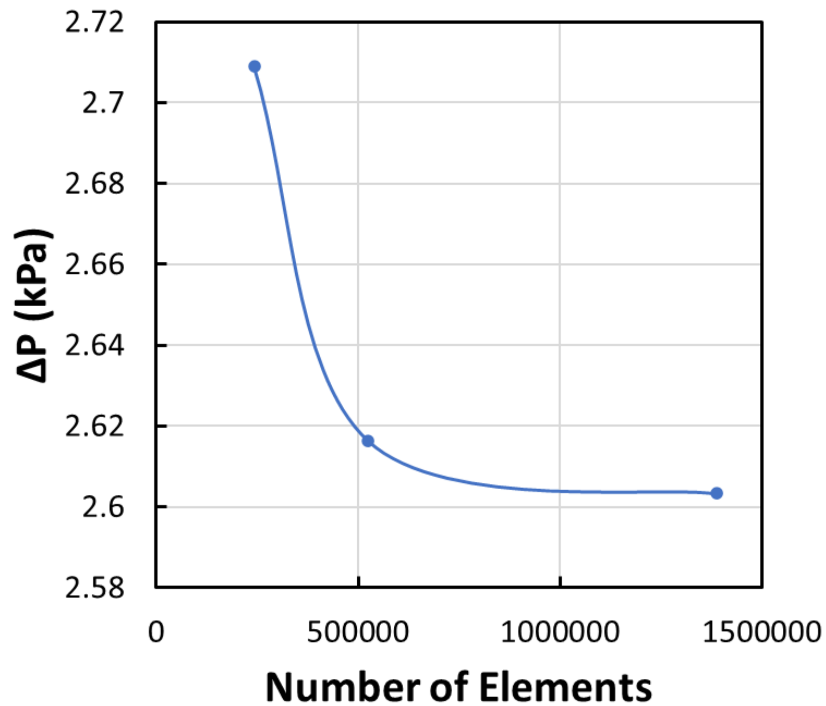

Figure B-5. Mesh sensitivity study for inlet restriction model at 50 g/min.

channel outlet. The mesh procedure and sensitivity study was performed similarly to the inlet plenum model; however, only the pressure drop through the orifice was considered. To determine this, the axial pressure distribution was calculated in the model and extracted. Figure B-4 shows a representative pressure drop profile down the length of the channel. There is a large pressure drop in the orifice due to contraction and friction, then pressure recovery as the fluid expands back into the channel. The pressure drop was extracted outside of these regions at the location where pressure drop changed <0.01 kPa as shown in the figure. The resulting mesh sensitivity results are shown in Figure B-5. Because the pressure drop changed <0.5% between the ~500,000 and ~1,400,000 element mesh, the 500,000-element mesh was used for the simulations.

B.4. Outlet Plenum Pressure Drop Model

The outlet plenum model was used to compensate for pressure drop between the channel outlet and the pressure transducer measurement spot downstream. A similar model to the inlet plenum model was created in COMSOL MultiPhysics and solved at the same nominal testing

conditions. A mass flow inlet and a zero-gauge pressure outlet were used as boundary conditions. A mesh sensitivity was again conducted for this model and is shown in Figure B-6. The pressure drop changed <0.025 kPa, which is <1.5%, between the fine and medium fine models. Thus, the medium dense mesh was used due to its much lower computational demand. This model calculates pressure drop from the downstream transducer to the outlet of the channels but does not account for the pressure recovery which occurs due to expansion out of the channels into the plenum. Therefore, this additional pressure drop was calculated using the following equation from Ref [74]

$$\Delta P_{e,sp} = \frac{1}{2\rho_l} K_{e,sp} G_{ch}^2 \tag{B-3}$$

$$K_{e,sp} = -2 \times 1.33 \left(\frac{N_{ch} A_{ch}}{A_{plen}}\right)\left(1 - \left(\frac{N_{ch} A_{ch}}{A_{plen}}\right)\right) \tag{B-4}$$

Then the channel outlet pressure provided to the model was determined by

$$P_{ch,out} = P_{out} + \Delta P_{plen} + \Delta P_e. \tag{B-5}$$

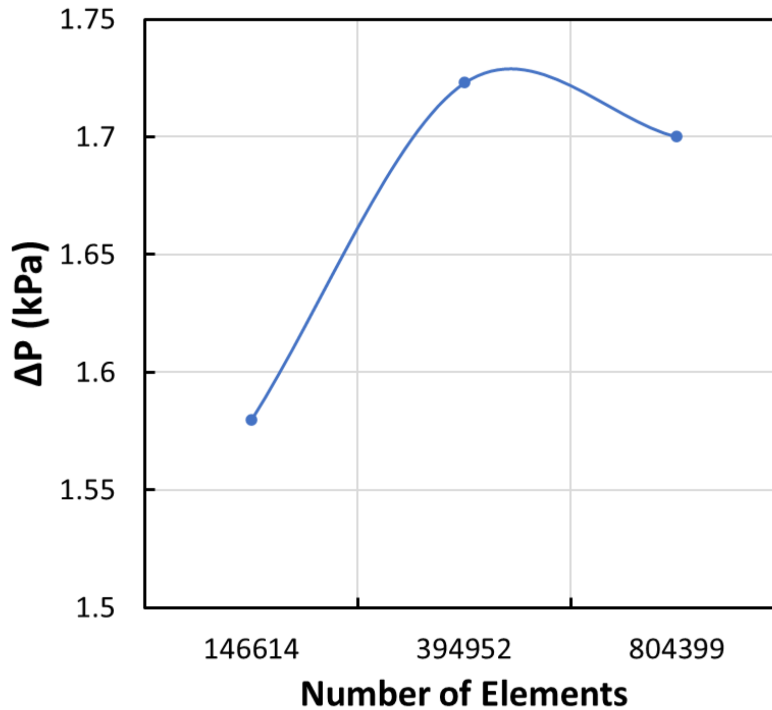

Figure B-6. Mesh sensitivity study for outlet plenum model at 50 g/min.

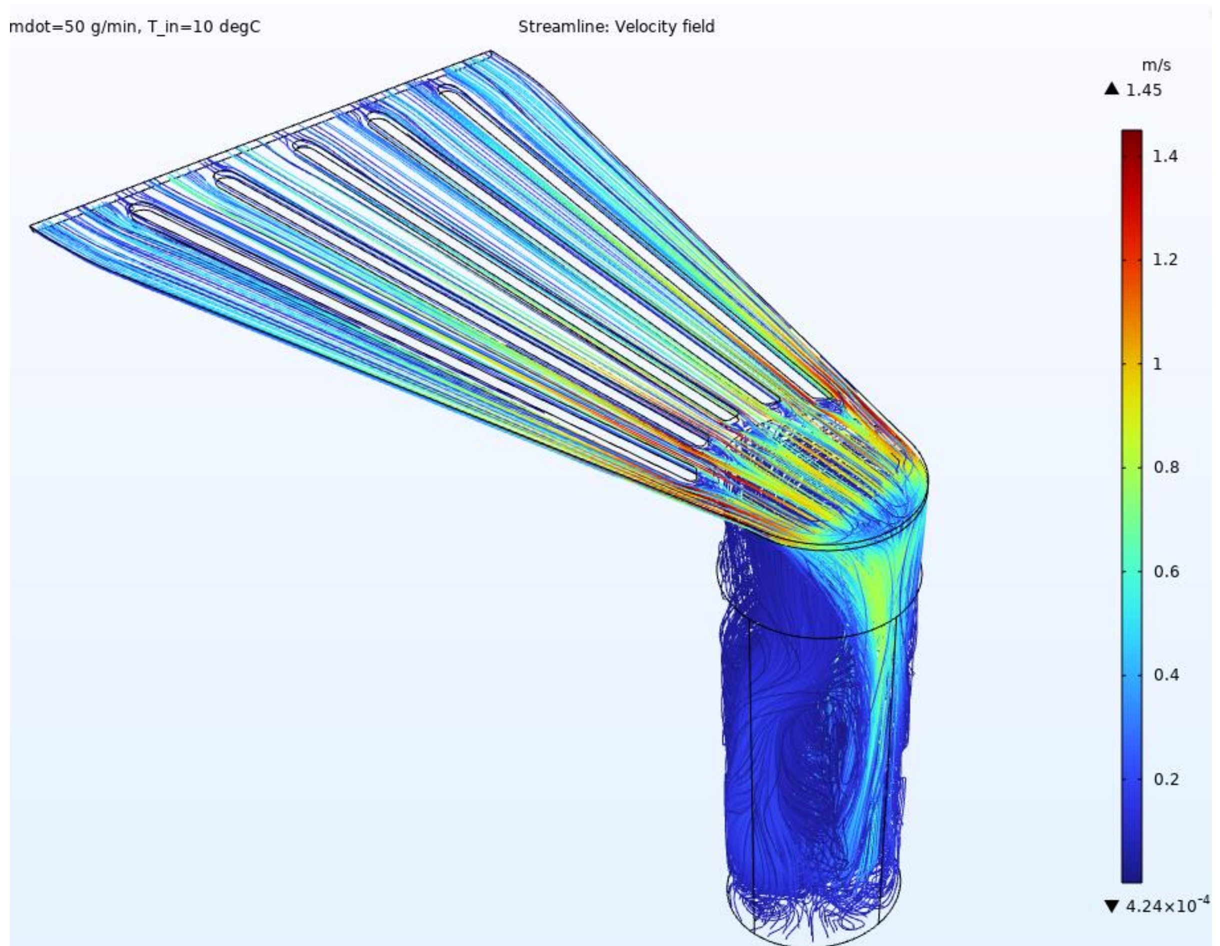

Figure B-7. Example velocity streamline profiles for outlet plenum pressure drop model, where large velocity changes occur due to the contraction at the end of the supporting rib features, and due to expansion and a 90°-bend into the outlet tube.

A sample image of the velocity field in the outlet plenum region is shown in Figure B-7. Flow is accelerated towards the contracting downstream region in the supporting silicon rib features and results in large pressure drop in that region. In addition, the combined 90°-bend and expansion into the downstream outlet tube also results in a large pressure change. Notably, much of the flow appears to ram into the back edge of the tube before it turns down into the tube. It is likely that this behavior also results in a significant amount of the pressure drop in this plenum.

APPENDIX C. Derivation of Exponential Growth Model for the Evolution of the Flow Boiling Heat Transfer Coefficient

In this Appendix, a derivation of the particular solution for the exponential growth model used in Chapters 4 and 5 for the evolution of the transient boiling heat transfer coefficient in the NavyHHF model will be presented.

Assuming a quasi-steady state value for h_{sp} and h_{tp} at each node for a given time step, the (ordinary nonlinear) differential equation for a logistic growth curve model reaching a maximum carrying capacity with growth rate κ_{tp} and with single-phase initial condition h_{sp} is

$$\frac{dh}{dt} = \kappa_{tp} h \left(1 - \frac{h}{h_{tp}}\right) \tag{C-1a}$$

$$h(t \leq t_{ONB}) = h_{sp} \tag{C-1a}$$

where t_{ONB} is the time when the onset of nucleate boiling occurs. This can be solved via separation of variables

$$\int_{h_{sp}}^{h} \frac{dh}{h\left(1 - \frac{h}{h_{tp}}\right)} = \int_{t_{ONB}}^{t} \kappa_{tp} dt \tag{C-2}$$

which leads to the following solution:

$$h(t) = \frac{h_{sp} h_{tp} e^{\kappa_{tp} t}}{h_{sp}\left(e^{\kappa_{tp} t} - e^{\kappa_{tp} t_{ONB}}\right) + h_{tp} e^{\kappa_{tp} t_{ONB}}} \tag{C-3}$$

This can further be simplified to obtain the following

$$h(t) = \frac{h_{tp}}{1 + \left(\frac{h_{tp}}{h_{sp}} - 1\right) e^{-\kappa_{tp}(t - t_{ONB})}}, \tag{C-4}$$

which is Equation (4-3).